



DISSERTATION

Bioanalytical challenges for AAV8 application in gene therapy

carried out for the purpose of obtaining the academic degree of

Doctor in Natural Science

under the direction of

Univ.Prof. Mag. Dr. Günter **Allmaier**[†]

Univ.Prof.in Mag. Dr.in Martina **Marchetti-Deschmann**

Assoc. Prof. Mag. Dr. Victor U. **Weiss**

E 164 – Institute of Chemical Technologies and Analytics

Research Unit of Instrumental and Imaging Analytical Chemistry

Research Group for Mass spectrometric Bio and Polymer Analytics

Submitted to the **Technical University of Vienna**

Faculty of Technical Chemistry

by

Samuele **Zoratto**, MSc.

01429304

Vienna, January 2024

"Never underestimate the power of vision and direction. These are irresistible forces, able to transform what might appear to be unconquerable obstacles into traversable pathways and expanding opportunities."

Jordan B. Peterson

Contents

Abstract	9
Zusammenfassung.....	11
Aim of the Thesis.....	13
1 Introduction	15
1.1 General Overview of Adeno-Associated Virus (AAV).....	15
Introduction to Adeno-Associated Viruses.....	15
Classification and Serotypes of AAV	16
AAV Life Cycle and Replication Process.....	17
Molecular Structure of AAV Capsids	18
Non-Pathogenic Nature and Immune Responses to Adeno-Associated Virus (AAV)	20
1.2 Understanding Virus-Like Particles (VLPs).....	21
1.3 Use of AAV8 VLPs in Gene Therapy.....	23
2 Analytical Techniques	27
2.1 nano Electrospray Gas-Phase Electrophoretic Mobility Molecular Analysis (nES GEMMA)	27
How nES GEMMA works.....	27
nES GEMMA and Its Application for Virology and AAV8	30
Strengths and Limitations of nES GEMMA	31
2.2 Atomic Force Microscopy (AFM)	33
How AFM works	33
AFM Applications in Virology and AAV8 VLP Analysis.....	34
Strengths and Limitations of AFM in Virological Studies.....	35
2.3 Asymmetrical Flow Field-Flow Fractionation (AF4)	37
How AF4 works.....	37
AF4 and its application in virology and AAV8 VLPs	38
Strengths and Limitations of AF4	39
2.4 Native Mass Spectrometry (Native MS)	41
How native MS works.....	41

The role of native MS in virology and AAV8 VLPs applications	42
Challenges and limitations of native MS in AAV8 VLP analysis	42
2.5 Cryogenic Transmission Electron Microscopy (cryo-TEM)	45
How cryo-TEM works.....	45
Cryo-TEM in the study of viral particles	45
Specific applications of cryo-TEM with AAV8 VLPs	46
Strengths and limitations of cryo-TEM in the context of AAV8 VLP study.....	47
2.6 Complementary Use of Analytical Techniques in AAV8 VLPs Study.....	49
3 Publications.....	51
Adeno-associated Virus Virus-like Particle Characterization via Orthogonal Methods: Nanoelectrospray Differential Mobility Analysis, Asymmetric Flow Field-Flow Fractionation, and Atomic Force Microscopy 	51
Molecular Weight Determination of Adeno-Associate Virus serotype 8 Virus-like Particle either carrying or lacking genome via native nES Gas-phase Electrophoretic Molecular Mobility Analysis (GEMMA) and nESI QTOF Mass Spectrometry	71
Adeno-Associated Virus-like Particles' Response to pH Changes as Revealed by nES-DMA	81
4 Additional publications	105
N-terminal VP1 Truncations Favor T = 1 Norovirus-Like Particles.....	105
Virus-like particle size and molecular weight/mass determination applying gas-phase electrophoresis (native nES GEMMA)	141
5 Conclusions	159
References	163
Abbreviations	175
Curriculum Vitae.....	177
Acknowledgments	181

Abstract

This thesis methodically investigates the properties of Adeno-Associated Virus 8 Virus-Like Particles (AAV8 VLPs), a key player in the evolving field of gene therapy. The research work presented here is divided into three publications, each addressing a unique aspect of AAV8 VLPs, crucial for their characterization and application in gene therapy.

The first publication (ACS Omega) establishes the feasibility of nano Electro-spray Gas-phase Electrophoretic Mobility Molecular Analyzer (nES GEMMA) for measuring AAV8 VLPs, and its ability to differentiate between empty and filled capsids. It then applies Asymmetrical Flow Field-Flow Fractionation (AF4) to fractionate these bio-nanoparticles and investigate their response after exposure to specific environmental stressors, such as temperature and shear stress. The subsequent analysis of the fractions using nES GEMMA and Atomic Force Microscopy (AFM) reveals the formation of dimers, trimers, and oligomers, thus enhancing our understanding of the VLPs' aggregation behavior under these stress conditions.

The second publication (J Mass Spectrom) focuses on determining the molecular weight of empty and filled AAV8 VLPs. This was accomplished by initially employing nES GEMMA, followed by native Mass Spectrometry (nMS), and by integrating the results from both techniques. This integrated approach resulted in an improved molecular weight estimation for empty and filled AAV8 VLPs. These findings not only enrich scientific knowledge but also support the development of gene therapy applications.

The third publication (Viruses) investigates the response of AAV8 VLPs to pH variations, specifically focusing on changes in diameter and aggregation behavior. Interestingly, nES GEMMA and AFM suggest specific trends, whereas Cryogenic Transmission Electron Microscopy (cryo-TEM) shows contrasting results. This discrepancy emphasizes the impact of the analytical environment on the behavior of these bio-nanoparticles, thus highlighting the necessity and importance of employing a multi-analytical approach. This strategy is essential for a comprehensive and accurate characterization of AAV8 VLPs and advancing our understanding of other bio-nanoparticles.

To conclude, the studies presented in this thesis demonstrate the significant value of employing diverse analytical techniques, each with unique strengths and limitations, and collectively contribute to expanding our understanding of AAV8-based viral vectors.

Zusammenfassung

Diese Arbeit untersucht systematisch die Eigenschaften des Adeno-assoziierten Virus 8 und Virus-ähnlicher Partikel (AAV8 VLPs), die als Schlüsselement im aufstrebenden Bereich der Gentherapie gelten. Die vorliegende Forschungsarbeit ist in drei Publikationen gegliedert, die jeweils einen einzigartigen Aspekt der AAV8-VLPs behandeln, welcher für deren Charakterisierung und den Einsatz in der Gentherapie von zentraler Bedeutung ist.

Die erste Veröffentlichung (in ACS Omega) demonstriert die Anwendbarkeit des Nano-Elektrospray-Gasphasen-Elektrophorese-Mobilitäts-Molekularanalysators (nES GEMMA) zur Größenbestimmung von AAV8-VLPs und dessen Fähigkeit, zwischen leeren und gefüllten Kapsiden zu differenzieren. Weiters wird die asymmetrische Fluss-Feldflussfraktionierung (AF4) genutzt, um diese Bio-Nanopartikel zu trennen und ihre Reaktionen auf verschiedene Umweltstressfaktoren, wie Temperatur und Scherkräfte, zu analysieren. Die nachfolgende Untersuchung der Fraktionen mit nES GEMMA und Rasterkraftmikroskopie (AFM) ermöglicht die Identifizierung der Bildung von Dimeren, Trimeren und Oligomeren und erweitert damit unser Verständnis des Aggregationsverhaltens der VLPs unter Stressbedingungen.

Die zweite Publikation (in Journal of Mass Spectrometry) setzt sich mit der vergleichenden Bestimmung des Molekulargewichts von leeren und gefüllten AAV8-VLPs auseinander. Dies wurde durch den Einsatz von nES GEMMA in Kombination mit nativer Massenspektrometrie (nMS) erzielt, wobei die Ergebnisse beider Methoden integriert wurden. Dieser kombinierte Ansatz ermöglichte eine präzisere Schätzung des Molekulargewichts für beide VLP-Typen. Die gewonnenen Erkenntnisse bereichern nicht nur das wissenschaftliche Verständnis, sondern unterstützen auch die Entwicklung von Gentherapien.

Die dritte Veröffentlichung (in Viruses) untersucht die Reaktion von AAV8-VLPs auf pH-Veränderungen, insbesondere hinsichtlich Veränderungen des Durchmessers und Aggregationsverhaltens. Interessanterweise zeigen nES GEMMA und AFM spezifische Trends, während die kryogene Transmissionselektronenmikroskopie (Kryo-TEM) gegenteilige Ergebnisse liefert. Diese Diskrepanz betont den Einfluss der analytischen Umgebung auf das Verhalten dieser Bio-Nanopartikel und hebt die Bedeutung eines multi-analytischen Ansatzes hervor. Diese Strategie ist für eine umfassende und genaue Charakterisierung von AAV8-VLPs sowie für das vertiefte Verständnis anderer Bio-Nanopartikel essenziell.

Zusammenfassend zeigen die in dieser Dissertation vorgestellten Studien den erheblichen Wert des Einsatzes verschiedener analytischer Techniken, jeweils mit ihren spezifischen Stärken und Einschränkungen, auf und tragen gemeinsam dazu bei, unser Verständnis von AAV8-basierten viralen Vektoren zu erweitern.

Aim of the Thesis

This thesis aims to comprehensively characterize the properties and behaviors of Adeno-Associated Virus 8 Virus-Like Particles (AAV8 VLPs), an emerging vector for gene therapy applications.

At the heart of this work is the exploration into the physical and chemical properties of AAV8 VLPs. A range of advanced analytical techniques, including gas-phase electrophoretic methods (nES GEMMA), Asymmetric Flow Field-Flow Fractionation (AF4), Atomic Force Microscopy (AFM), and cryogenic transmission electron microscopy (cryo-TEM), are employed to investigate aspects such as particle size, purity, and aggregation states.

In detail, techniques such as nES GEMMA and AF4 have been instrumental in understanding the structural integrity and aggregation behavior, while AFM and cryo-TEM provide high-resolution imaging that reveals detailed structural differences. Additionally, the research examines how environmental factors, like pH changes and physical stress, impact these bio-nanoparticles, a crucial aspect for their application in gene therapy.

Contributing to the broader field of gene therapy, the findings of this thesis offer valuable insights into the properties of AAV8 VLPs. While highlighting the importance of employing diverse analytical methods, the work acknowledges each technique's unique strengths and limitations. The enhanced understanding of AAV8 VLPs acquired from this research supports the ongoing development and optimization of gene therapy applications.

In conclusion, this thesis extensively explores AAV8 VLPs through novel and state-of-the-art analytical techniques. It contributes to the broader understanding of viral vectors in gene therapy, highlighting the complexity and versatility of AAV8 VLPs.

1 Introduction

1.1 General Overview of Adeno-Associated Virus (AAV)

Introduction to Adeno-Associated Viruses

Adeno-associated viruses (AAVs) belong to the genus *Dependoparvovirus* of the *Parvoviridae* family and, thanks to their non-pathogenic nature and versatility as gene delivery vectors, have emerged as a powerful tool for gene therapy applications. [1-4] These viruses are small, approximately 25 nm in diameter, and have a single-stranded DNA structure. They are non-enveloped and require a helper virus, like an adenovirus or baculovirus, for replication. This dependence on another virus categorizes them as dependoparvoviruses. [5-7]

AAVs have a pH-dependent lifecycle, with their replication and interaction with the host cell environment being tightly linked to specific pH conditions. Specifically, host cell infection, uncoating of the capsid, and genome replication depend on acidic pH conditions, which is crucial for triggering the necessary capsid modification. [8, 9]

Additionally, AAV serotypes are classified based on their viral protein (VP) sequences and antigenic profiles. They replicate with the help of a helper virus and display specific distinct tissue tropisms and host ranges. This diversity in serotypes allows for customized approaches in gene therapy, targeting specific tissues and addressing different disease mechanisms. [4, 10, 11]

The genome of the wild-type AAV (wtAAV) is packaged within a protein capsule and carries approximately 4.7 kb of DNA. It contains the instructions for the rep (replication) and cap (capsid) genes flanked by inverted terminal repeats (ITRs). [10, 12] The rep gene is crucial for the virus's replication and integration into the host's genome, while the cap gene codes for the proteins that form the virus's outer shell. In recombinant AAV (rAAV) vectors, the original viral genome is replaced with an engineered version for gene therapy applications. [13] Indeed, rAAVs have shown promising results in clinical tests, as seen in their successful use in several phase I/II clinical trials. These rAAVs have been used to develop gene therapies like Glybera, Luxturna, and Zolgensma, which have gained approval for commercialization by regulatory bodies such as the U.S. Food and Drug Administration (FDA) and the European Medicine Agency (EMA). [14, 15]

Since the EMA's first approval of an AAV-based product in 2012, AAV-based gene therapy has advanced quickly. About over 100 clinical trials, as listed on clinicaltrials.gov, have been conducted using these methods. AAV vectors constitute a significant part of gene delivery in these trials, and their popularity is due to their effectiveness in delivering genes into cells to treat genetic disorders. [16, 17]

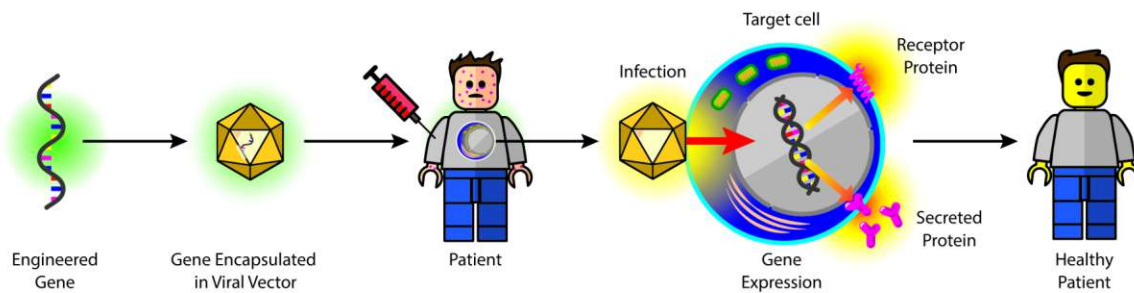


Figure 1.1.1. Simplified scheme for the gene therapy process. An engineered gene, encapsulated within a vector, is administered to the patient. The vector then facilitates the delivery of the gene into the target cells. Once inside, the cell's machinery utilizes the gene to produce the therapeutic agent (e.g., a protein, an enzyme, or other molecule), potentially curing or alleviating the symptoms of the genetic disorder.

In summary, rAAVs are a versatile and safe option in gene therapy, supported by their non-pathogenic nature, low immunogenicity, and capacity to target different cell types and tissues. The significant advancements in their clinical use and the ongoing trials highlight the potential of rAAVs to revolutionize gene therapy and tackle a wide range of genetic disorders. [2, 18, 19]

Classification and Serotypes of AAV

The classification of AAV's serotypes is based on serological reactions and amino acid homology, leading to the identification of over 100 AAV variants and at least 13 distinct serotypes, including AAV1 through AAV12 and AAV[VR-942]. [2, 4, 12]

The serotypes of AAV, derived from both human and nonhuman primates, are classified into eight clades and clonal isolates (AAV1/AAV6, AAV2, AAV2/AAV3, AAV4, AAV5, AAV7, AAV8, and AAV9) and are known for their 55–99% sequence homology. However, despite these genetic similarities, they display varied tissue tropism and transduction efficiency, which are largely determined by the specific amino acids in each serotype. These structural dynamics and tissue specificity play a crucial role in their utility in gene therapy. [7, 20]

Among the AAV serotypes, AAV2 has been most extensively evaluated in preclinical studies and was the first serotype to be fully characterized. This extensive study of AAV2 has laid the foundation for the understanding and application of other AAV serotypes in gene therapy. AAV8, in particular, stands out for its high homology to other AAVs, with a notable structural similarity of 83% with AAV2 capsids. AAV8 was initially isolated from rhesus monkey tissue and has become significant for its applications in gene delivery. [16, 21]

The ability to combine AAV2-based genomic constructs with cap genes from different serotypes has led to the creation of pseudotyped rAAVs. This innovation has expanded the range of tissues that can be targeted by AAV vectors, with packaging systems for about 10 different serotypes currently available for vector construction. The primate AAVs, classified into six genetic groups (clades A to F) and two clonal isolates, highlight AAV vectors' expansive diversity and adaptability in gene therapy applications. [7, 14]

In summary, the classification and serotypes of AAVs form the backbone of their application in gene therapy, with each serotype offering unique advantages in terms of tissue specificity and transduction efficiency. The ongoing exploration and characterization of these serotypes continue to broaden the scope and effectiveness of AAV-based gene therapies.

AAV Life Cycle and Replication Process

The life cycle and replication process of AAVs is a complex and highly coordinated series of events; its genome includes two major open reading frames (ORFs), the rep and cap genes. The rep ORF encodes four replicating proteins essential for genome replication and packaging, while the cap gene encodes the three capsid proteins (VPs) that form the virus's protective shell. [4, 20]

Upon entering the host cell, AAVs undergo a multistep infection process. Initially, the AAV particles bind to specific cell receptors and are then endocytosed. Once inside the cell, these particles are transported towards the nucleus. Although the exact mechanism of their nuclear entry is not yet fully understood, it is known that the ssDNA genome is released from the capsid in a process termed uncoating. Likely, the acidic environment of the endocytic pathway causes the externalization of the unique N-terminal region of the minor capsid viral protein 1 (VP1), known as VP1u, which contains a phospholipase A2 (PLA2) domain. This domain enables the virus to escape from the endo/lysosomal pathway and reach the nucleus, where genome uncoating and replication occur. [2, 9, 14]

The AAV capsid is comprised of three proteins—VP1, VP2, and VP3—generated through alternative initiation. All three proteins share the VP3 sequence, but VP1 and VP2 include additional N-terminal domains. This capsid structure is critical for the packaging and delivery of the AAV genome. Packaging typically initiates from the 3' end of the genome into a preassembled capsid through a pore at a 5-fold symmetry axis. If the genome length exceeds the capsid's packaging capacity, the packaging continues until the capsid is full, after which any remaining unpackaged DNA is truncated by cellular nucleases. [13]

During replication, an important event is the formation of episomal concatemers within transduced cells. An episomal concatemer is an independent chain of repeated units of the viral genome that

remains separate from the cell's DNA, existing as an episome. This formation limits the risk of insertional mutagenesis, which is a major safety concern in gene therapy. [22, 23]

Regarding rAAV vectors, these are produced using DNA-based vectors containing transgene expression cassettes. The two ends of these cassettes carry two ITRs from AAV2, which are crucial for initiating replication and packaging of the rAAV genome. Functional rAAV particles are produced by cotransfecting the recombinant vector with a helper plasmid, which is necessary for the expression of AAV's rep and cap genes (See Figure 1.1.2). [7]

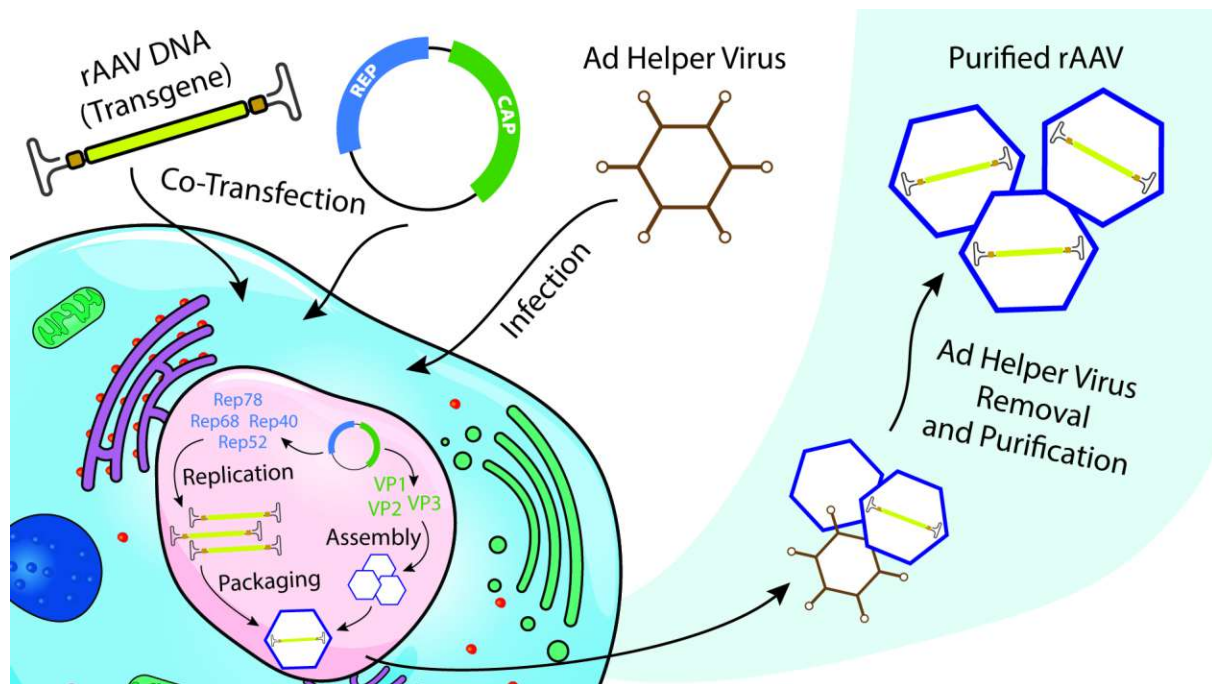


Figure 1.1.2. Scheme for the production of rAAV vectors.

In summary, the life cycle and replication process of AAV involve several crucial steps, critical for its function in gene therapy. Thus, a detailed understanding of these processes is essential for optimizing rAAV vectors for gene therapy applications.

Molecular Structure of AAV Capsids

The proteinaceous capsid of AAV is a protective shell that encapsulates the virus's genetic material, playing a crucial role in the delivery of its cargo and its subsequent application in gene therapy.

Each AAV capsid is composed of 60 capsid monomers arranged in a T=1 icosahedral symmetry, forming a non-enveloped virion approximately 25 nm in diameter. These capsids encapsulate the virus's single-stranded DNA genome, which is about 4.7 kb in length and flanked by "T"-shaped inverted terminal repeats (ITRs) (see Figure 1.1.3). [16, 20]

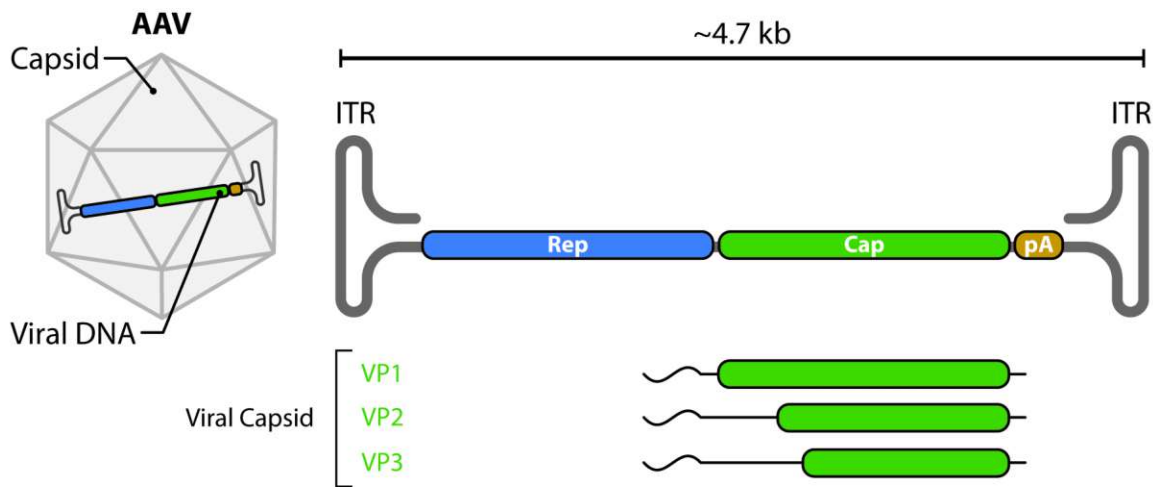


Figure 1.1.3. AAV Genome Structure. The major genetic components include the Rep and Cap genes and the ITRs regions, essential for replication and packaging.

Three viral proteins are central to the capsid's structure—VP1, VP2, and VP3. These proteins are present in a ratio of approximately 1:1:10, amounting to a total of 60 proteins that form the pseudo-icosahedral symmetry of the capsid. The VP1 protein is the largest, containing approximately 137 additional amino acids at the N-terminus compared to VP2. This unique extension of VP1, known as VP1u, contains a phospholipase A2 (PLA2) domain, a calcium-binding domain, and a nuclear localization signal, all essential for AAV infectivity. Both VP1 and VP2 also feature distinct N-terminal sequences folded inside the capsid, playing a role in their binding activities. The VP3 region, common to all three proteins and comprising ~534 amino acids, is crucial in determining the virus's receptor binding. [12, 14, 15, 17]

The molecular architecture of the AAV capsid, forming its inner surface, is characterized by a core structure complemented by various loop regions. These loops contribute to the capsid's surface features and are crucial for the virus's functionality. The variability in these regions is important, as it contributes to the distinct surface features of different AAV serotypes, influencing their tissue tropism and immune responses. [4, 14, 16]

Noticeably, AAV capsids undergo amino side chain rearrangements and DNA compaction in response to environmental stimuli, such as changes in pH. This adaptive feature is vital for the virus's life cycle, particularly during the endosomal escape and genome uncoating processes. [9]

In summary, AAV capsids' molecular structure, intricate protein arrangements, and adaptive capabilities are fundamental to the virus's role in effective cell targeting and gene delivery. Understanding AAVs' structure is key to harnessing its full potential for medical applications.

Non-Pathogenic Nature and Immune Responses to Adeno-Associated Virus (AAV)

The non-pathogenic nature of AAV and its interaction with the immune system represent a significant aspect of its utility and safety in gene therapy applications. AAV vectors, well-known for their ability to transduce a variety of cell types *in vivo*, have facilitated stable transgene expression in post-mitotic tissues, a crucial aspect for effective gene therapy treatments. [2] Their use in over 150 clinical trials proves their safety profile, as no AAV-related severe toxicities have been reported, validating their efficacy and security in clinical settings. [12, 17]

Compared to other viral vectors, AAV requires a lower viral load to be effective, making it particularly suitable for targeting rare diseases. [16] This advantage is further enhanced by its lack of pathogenicity and low immunogenicity, coupled with its ability to target multiple cell types, rendering AAV a highly versatile system for gene delivery. [20]

Another advantage of AAV is its interaction with the immune system. Typically, AAV infections elicit only mild immune responses and are considered non-pathogenic. This reduced immunogenic profile has led to lower biosafety level requirements for working with recombinant AAVs compared to other viral vector systems. [7]

However, immune responses to AAV can vary and are an area of active research. For instance, in clinical trials involving AAV2, no CD8⁺ cytotoxic T lymphocyte (CTL) response to the encoded therapeutic agent was detected. However, lymphocyte activation was observed in response to peptides from the AAV2 capsid. This suggests that capsid-specific CTLs might target and destroy AAV2-transduced cells, potentially leading to treatment failure. In other cases, such as with AAV8, a capsid-specific CTL response was noted in all patients at various time points following AAV delivery, with some patients showing elevated immune response. [12]

Furthermore, the immunogenicity of AAVs can be influenced by factors such as glycosylation of the capsid components. This post-translational modification can affect how the immune system perceives the virus, potentially altering its immunogenic profile. [20]

Essentially, the non-pathogenic nature of AAV, combined with its typically mild immune response, positions it as a safe and effective vector for gene therapy. However, understanding the nuances of its interaction with the immune system, particularly in response to variations in capsid composition and patient-specific factors, remains crucial for optimizing its use in clinical applications.

1.2 Understanding Virus-Like Particles (VLPs)

Virus-like particles (VLPs) have emerged as a significant innovation in biomedical research, offering non-infectious, nanoscale structures composed of viral proteins without viral genetic material. These nanostructures are found across various biological systems, including mammals, plants, insects, and bacteria. [24-26] VLPs represent a significant advancement in the field of vaccinology, emerging as nanostructures that mimic the physical characteristics of viruses. Indeed, comprising one or more structural proteins, VLPs can be arranged in multiple layers, some including a lipid outer envelope, hence closely resembling the structural complexity of natural viruses. [27]

Structurally, VLPs are categorized into enveloped and non-enveloped types, depending on whether they possess a lipid envelope. This structural classification, further characterized by the specific arrangement of capsid proteins, not only contributes to their functional diversity but also presents specific production challenges. Enveloped VLPs, for instance, require more complex production methods due to their structural intricacies and the necessity for proper folding and glycosylation of viral surface antigens. [25-27]

Despite these challenges, the absence of viral genomic material in VLPs essentially eliminates the risk of infection while preserving their ability to elicit robust immune responses. This unique combination of safety, high functionality, versatility, and efficacy has positioned VLPs at the forefront of modern vaccine research and development, extending their reach into gene therapy applications. [25-27]

In the realm of VLP production, the yields and culture modes vary significantly among different systems, each catering to the specific requirements of the VLP being produced. Bacteria and yeast systems offer high-concentration production capabilities, suitable for simpler VLPs, whereas the baculovirus-insect cell (B/IC) system and mammalian cells are preferred for more complex, enveloped VLPs due to their ability to perform sophisticated post-translational modifications. [27]

Furthermore, the assembly of VLPs in vitro offers several advantages over traditional in vivo methods, primarily in avoiding host-derived contaminants and allowing for precise cargo loading. This controllable and defined assembly enables the creation of multi-vaccine candidates and controlled therapeutic delivery systems, avoiding potential unpredictability associated with host-related contaminants. [28]

In terms of vaccine development, VLPs structurally resemble the viruses from which they are derived, possessing highly immunostimulatory physical characteristics, making them effective stand-alone vaccines or versatile platforms for vaccine development. [29] Their size allows for efficient entry into lymphatic vessels, facilitating optimal uptake by antigen-presenting cells. The geometry of VLPs,

featuring multivalent and often rigid structures, contributes significantly to their remarkable ability to activate B cells, leading to robust and enduring antibody responses. [29]

Engineering VLPs to display diverse antigens has been a key focus in vaccine research, maximizing the immunogenic potential of particle platform technologies. Strategies include generating recombinant fusions where foreign antigens are inserted into sites within the viral structural protein, allowing their display on the VLP surface. [29] In some instances, engineering more thermodynamically stable versions of the subunits that comprise VLPs has significantly increased the success rate of peptide insertion. [29] Developing more stable VLPs is also crucial for their practical application. VLPs that can withstand variations in temperature and other conditions are advantageous for both manufacturing and distribution. This is particularly important in developing regions where maintaining a cold chain is challenging. Enhancements in particle stability reduce vaccine costs by allowing longer shelf-life and reducing cold-storage energy requirements. Techniques like introducing inter-subunit disulfide bonds have been employed to increase the stability of various VLPs, such as MS2 and Hepatitis B core antigen VLPs. [29]

The enveloped VLPs (eVLPs) present unique challenges due to their structural complexity and sensitivity to external conditions, necessitating robust computational design and innovative bioprocessing modalities. The intricate assembly process and the need for precise control over the assembly environment are crucial to maintaining the formation and integrity of such VLPs. [30] For this reason, computational modeling tools are increasingly being employed to predict the compatibility of peptides with the VLP assembly process, thereby enhancing the efficiency of VLP-based vaccine design. These challenges highlight the continuous evolution of methodologies aimed at enhancing the understanding and efficient production of VLPs. [29, 30]

In conclusion, VLPs, through their structural properties and biomedical applications, have revolutionized the landscape of vaccine development and gene therapy. Their strong immunogenic profile and repetitive antigenic epitopes effectively engage the immune system, marking them as safer alternatives to conventional vaccines. The dynamic nature of VLP-based vaccine development positions VLPs as a shining example of innovation in the field of immunology and vaccine technology. [24-26]

Moreover, the exploration of VLPs for gene therapy applications has shown immense promise. As highly adaptable and safe nanocarriers, VLPs facilitate the delivery of therapeutic genes to specific cells, offering innovative treatments for genetic disorders and chronic diseases. This capability enhances their effectiveness in combating diseases such as COVID-19, influenza, malaria, AIDS, and various neurodegenerative diseases. [24, 25, 31-36]

Furthermore, the extended reach of VLPs into therapeutic domains, targeting chronic inflammation, pain, allergy, and cancer, highlights their versatility beyond traditional vaccine applications. [24, 25, 37-39]

It is clear that the future of VLPs in biomedical applications is bright. Constant advancements in VLP engineering and production will further expand their applicability, thus revolutionizing both vaccine and gene therapy treatments.

1.3 Use of AAV8 VLPs in Gene Therapy

The use of AAV8 VLPs in gene therapy has seen considerable advances, and this final introductory chapter is dedicated to exploring their application. It summarizes the latest research and ongoing studies to provide a comprehensive look at the role and potential of AAV8 VLPs. The key areas of focus include the distinctive structural properties of AAV8 VLPs, their tissue tropism, and the various challenges encountered in their clinical usage.

Structural Uniqueness and Tissue Tropism

AAV8, isolated from rhesus monkey tissue, is distinguished by its high homology to other AAVs. Crystal structure analysis has highlighted distinct capsid surface topologies between AAV8 and AAV2. Specifically, AAV8 shows an 83% structural similarity to AAV2 capsids. [40] However, the small differences are crucial in determining the efficiency with which AAV8 VLP transduces cells and evades immune recognition. Unlike AAV2, which uses heparan sulfate proteoglycan as its primary receptor, AAV8 binds to the laminin receptor (LamR)[41], a distinction that influences its cellular uptake and nuclear transport, ultimately impacting the vector's infectivity and cell transfection efficiency. [14]

The broad tissue tropism of AAV8 VLP is one of its most notable features, enabling it to target various tissues, including the brain, liver, heart, retina, lung, and muscle cells. It is particularly noted for its hepatophilic nature, as evidenced by nearly 10-to-100-fold higher gene expression in the liver compared to other serotypes. [42] This affinity for liver cells has been demonstrated in various studies, including those where all hepatocytes converted the single-stranded vector genome into double-stranded DNA, achieving nearly 100% transfection rate without hepatotoxicity. [42]

In animal models, AAV8 VLP vectors have shown extensive and persistent transduction in tissues like skeletal and myocardial muscle, with long-lasting expression in the heart. [43] Interestingly, AAV8 VLP also efficiently transfects pancreatic cells, with significant expression levels observed in pancreatic follicular cells. [44] Moreover, AAV8 VLP can transduce brain cells effectively, with notable expression in glial cells and neurons in different regions of the spinal cord. [7, 45]

Challenges and Opportunities in Clinical Applications

The presence of pre-existing neutralizing antibodies (NAb) against AAV8 can significantly hinder gene therapy's effectiveness. Even low titers of anti-AAV8 NAb can reduce transgene expression efficiency. The presence of such NAb varies in the population, with studies reporting a range of from 30% to 50%. [46-48] Clearly, this immunity barrier negatively affects the successful rate of gene therapy applications. [47, 48] Strategies to overcome anti-AAV8 NAb include: immunosuppression, plasma replacement, increasing the vector dose, or introducing an empty coat. [49]

Consequently, the field of gene therapy is witnessing an increasing number of clinical trials employing AAV-mediated gene therapy, reflecting growing confidence in the safety and efficacy of these vectors. For reference, Table 1 summarizes AAV8 VLP projects currently in clinical phase. Continuous advancements in vector technology and gene therapy methodologies are crucial for addressing the existing challenges and expanding the therapeutic applications of AAV8 VLPs.

Table 1. Ongoing Clinical Projects Involving AAV8 VLPs, adapted from Zhao et al. (2023). [16] Data updated as of December 30th, 2023, from ClinicalTrials.gov.

Disease	Transgene	Clinical stage	Company
Achromatopsia	CNGB3	Phase I, II	MeiraGTx
Achromatopsia	CNGA3	Phase I, II	STZ eyetrial
AIDS	VRC07	Phase I	NIH
BCD	CYP4V2	Phase I, II	Chigenovo
Choroideremia	CHM	Phase III	NightstaRx
Cocaine Use Disorder	CocH	Phase I	Mayo Clinic
Congenital Retinoschisis	RS1	Phase I, II	NEI
Diabetic Retinopathy	Anti-VEGF antibody	Phase II	AbbVie
DMD	DMD	Phase I, II	REGENXBIO
GSD1a	G6PC	Phase I, II	Ultragenyx
Haemophilia A	FVIII	Phase I, II	Takeda
Haemophilia B	FIX	Phase I, II	Takeda
HIV	VRC07	Phase I	NIAID
MPS-VI	ARSB	Phase I, II	Fondazione Telethon
Myotubular myopathy	MTM1	Phase II, III	Astellas Gene Therapies
nAMD	Anti-VEGF antibody	Phase II, III	AbbVie
OTC	OTC	Phase III	Ultragenyx
Phenylketonuria	PAH	Early Phase I	FAHBMC
Pompe Disease	AT845	Phase I, II	Astellas Gene Therapies
Pompe Disease	GAA	Phase I, II	Asklepios
Retinal Degeneration	LCA5	Phase I, II	Opus Genetics
Retinitis Pigmentosa	RLBP1	Phase I, II	Novartis
Tay-Sachs disease	HEXA and HEXB	Phase I	Axovant Sciences
wAMD	Anti-VEGF antibody	Phase I, II	Neuracle Genetics
wAMD	Anti-VEGF antibody	Phase I	Regenxbio

AIDS, Acquired Immune Deficiency Syndrome; BCD, Bietti's Crystalline Dystrophy; DMD, Duchenne Muscular Dystrophy; FAHBMC, First Affiliated Hospital Bengbu Medical College; GSD1a, Glycogen Storage Disease Type 1a Disease; MPS-VI, Mucopolysaccharidosis Type VI; nAMD, Neovascular Age-Related Macular Degeneration; NEI, National Eye Institute; NIAID, National Institute of Allergy and Infectious Diseases; OTC, Ornithine Transcarbamylase Deficiency; VEGF, Vascular Endothelial Growth Factor; wAMD, wet Age-related Macular Degeneration; XLRS, X-linked Juvenile Retinoschisis.

In-depth research into the tissue specificity and transduction efficiency of AAV8 VLPs is ongoing. Studies are exploring the mechanisms behind AAV8's selective tissue targeting and its ability to achieve high transduction rates without inducing significant immunogenic responses or hepatotoxicity. These studies are critical for developing more targeted and efficient gene therapy strategies. [50-53]

Looking ahead, the potential of AAV8 VLPs in gene therapy is vast. Future research is expected to focus on refining the vector delivery mechanisms, enhancing tissue specificity, and reducing immunogenicity. Understanding the interactions between AAV8 VLPs and various cell types at the molecular level will be key to unlocking new therapeutic applications. [16, 54-57]

In conclusion, AAV8 VLP stand as a promising and versatile tool in the field of gene therapy. Its unique structural properties and broad tissue tropism, coupled with evolving strategies to overcome challenges in clinical applications, positions it at the forefront of gene therapy research. The development of novel AAV8-based vectors, specifically tailored for certain diseases and patient groups, is an exciting prospect on the horizon. As the field progresses, these vectors are ready to offer transformative treatments for a wide array of genetic disorders, cancers, and other diseases, further strengthening the role of AAV8 VLPs in the development of innovative therapeutic genetic applications.

2 Analytical Techniques

2.1 nano Electropray Gas-Phase Electrophoretic Mobility Molecular Analysis (nES GEMMA)

How nES GEMMA works

Firstly introduced to the scientific community in 1996 by Kaufman and colleagues,[58] and later commercialized by TSI, the nano electropray gas-phase electrophoretic mobility molecular analyzer (nES GEMMA, see Figure 2.1.1) has become an important tool for nanoparticle characterization. [59-70] Often, it is referred in literature by other names, such as nES differential mobility analyzer (nES-DMA), LiquiScan ES, macro ion mobility spectrometer (MacroIMS), and scanning mobility particle sizer (SMPS). [64]

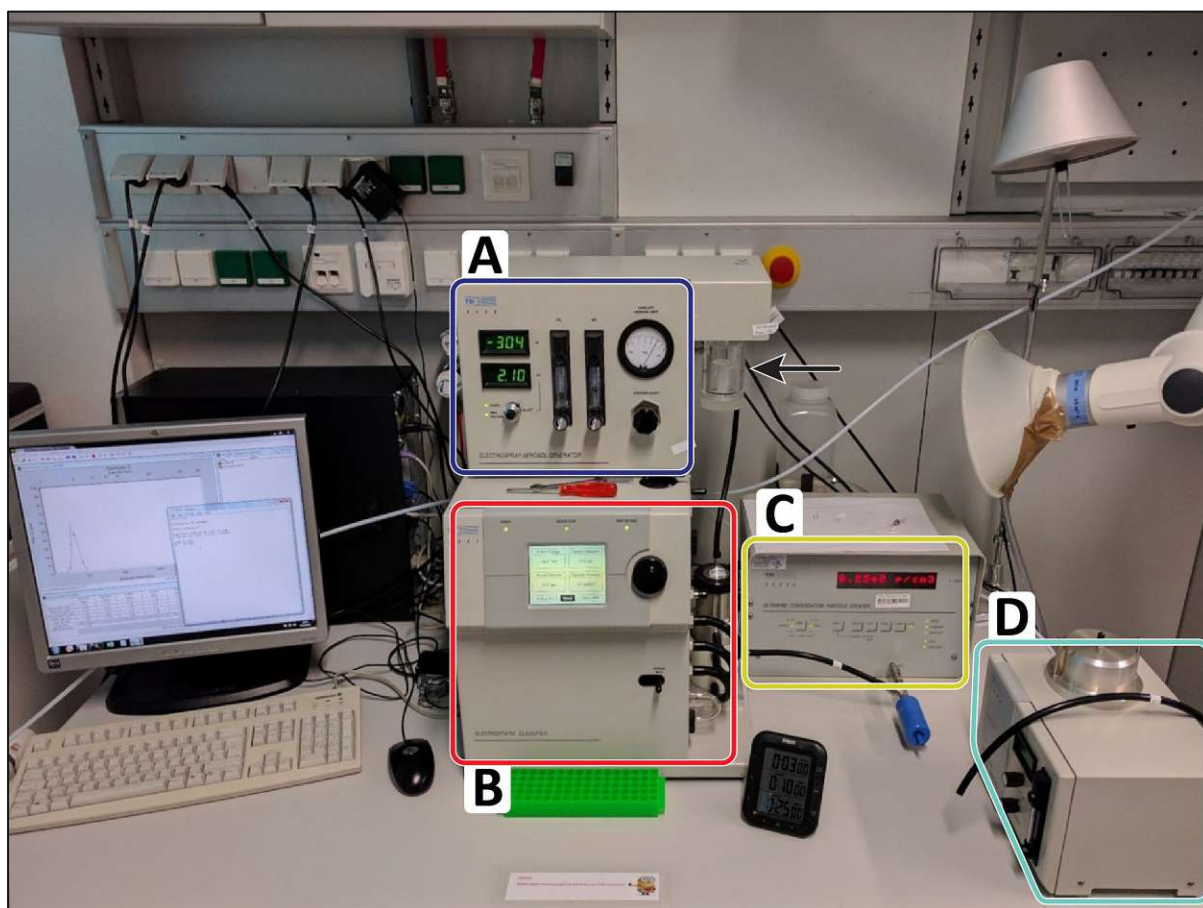


Figure 2.1.1 nES GEMMA System Configuration at TU Wien. A) Nano electropray aerosol generator with charge reduction device, responsible for sample atomization and charge reduction. The black arrow indicates the sample insertion point. B) Electrostatic classifier equipped with a nano differential mobility analyzer, utilized for particle sizing and separation. C) Ultrafine condensation particle counter, which

quantifies the nanoparticles. D) Nanoparticle collector unit, designed for the deposition of nanoparticles onto a substrate for further analysis.

The nES GEMMA device finds its application in the analysis of a multitude of (bio-)nanoparticles, such as proteins, viruses, VLPs, liposomes, extracellular vesicles, and organic and inorganic nanoparticles. [59-70]

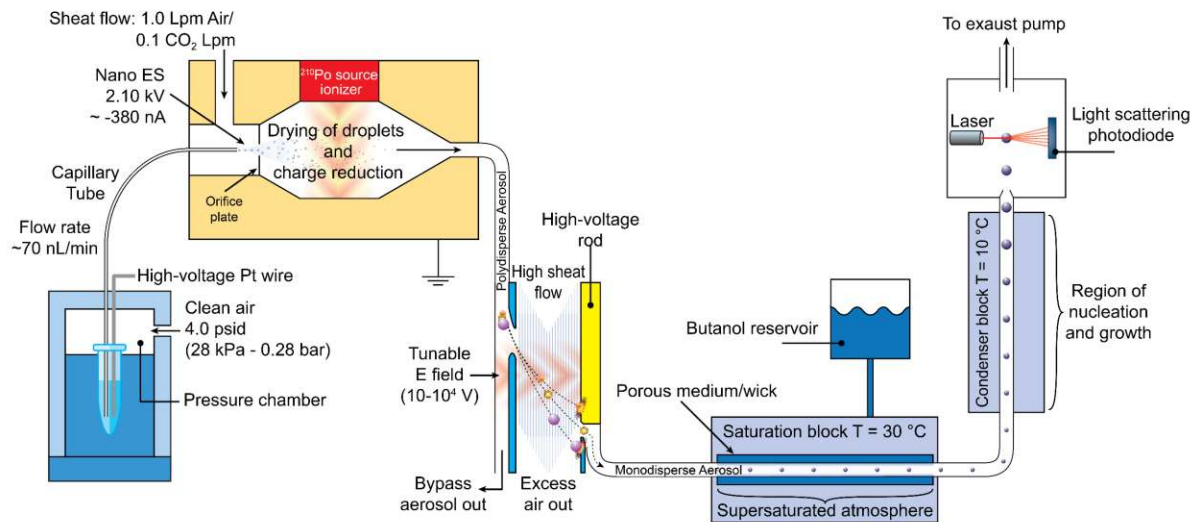


Figure 2.1.2. Schematic view of the working principle of nES GEMMA. Separate devices are not depicted to scale.

The first important step for nES GEMMA analysis, is the transition of the analytes from a liquid state to a gaseous phase. This is achieved using the nano Electro spray (nES) process. Thanks to this method, the samples are sprayed from a volatile electrolyte solution, generating microdroplets into the gaseous phase; these microdroplets are subjected to a drying process, usually aided by a sheath gas flow, generally consisting of dry and particle-free air and CO₂. [58, 71] This ensures the analytes are free from external moisture, preparing them for the next crucial step: charge equilibration. This step is enabled by a carefully induced bipolar atmosphere. This atmosphere can be created by different means, ranging from a ²¹⁰Po α -particle source to soft X-ray radiation, and with a bipolar corona-discharge technique. [59, 62, 67, 70] The purpose here is to regulate the charge on these aerosolized particles. Interestingly, while many particles lose their charges in this transition, few retain a singular charge. This subset of singly-charged analytes proceeds to the heart of the GEMMA separation process: the differential mobility analyzer (DMA). [72, 73]

Initially developed for classifying gas-suspended micro to sub-micro particles, the DMA has roots in aerosol physics and environmental analyses. With advancements in the instrument, the DMA has also gained traction in chemical and biochemical fields. [66, 74-76] The DMA combines a constant high laminar sheath flow of clean, compressed air with a tunable orthogonal electrical field. Size-selective ion separation is achieved by systematically scanning through the entire voltage spectrum. Thanks to this modulation, only particles of a specific electrophoretic mobility diameter (EMD) will navigate successfully to the instrument's detector unit, thus allowing for a detailed size distribution analysis of a given sample. [77]

For detection, the selected analytes are directed into a continuous-flow of n-butanol or water-driven condensation particle counter (CPC), a device that amplifies and counts particles for easier detection. In this critical step, the supersaturated atmosphere within the CPC triggers the condensation of the vapor onto the particles through self-nucleation. This process enlarges the particles to 10-12 μm droplets, making them detectable. Hence, each particle is individually counted using an optical system that measures the scattered light from a laser diode (see Figure 2.1.2). [78] This number-based particle concentrations detection method is in accordance with a recommendation of the European Commission for nanoparticle characterization (2022/C 229/01 from June 10th, 2022).

Alternatively, particles can be collected on various substrates using an electrostatic nanoparticle sampler (ENAS, see Figure 2.1.3). [79, 80] The size-separated positively-charged particles exiting the DMA are attracted to a negatively charged electrode, thus depositing themselves onto a substrate above it. After collection via the ENAS, particles can be analyzed through a multitude of methods, including transmission electron microscopy, atomic force microscopy, MALDI MS, or even immunological assays. [60, 81, 82]

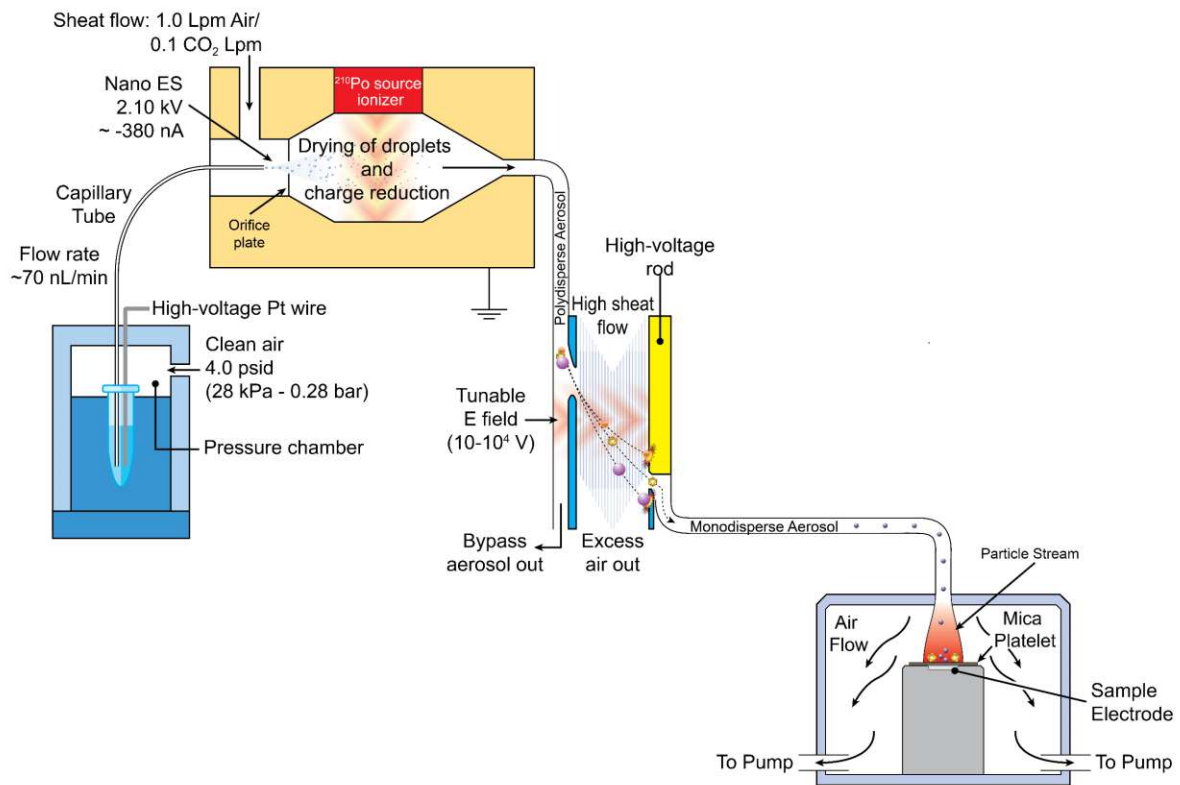


Figure 2.1.3. Schematic view of the working principle of electrostatic nanoparticle sampler (ENAS). The size-separated particles in the monodisperse aerosol (positively charged) will deposit on the support placed above the electrode (negatively charged). Separate devices are not depicted to scale.

nES GEMMA and Its Application for Virology and AAV8

Based on the literature of recent years, nES GEMMA proved to be an invaluable tool in the world of virology, capable of offering unique insights for the analysis of viral particles. Indeed, the soft desorption/ionization nature of the electrospray technique and its separation method, preserve the non-covalent biospecific interactions, making nES GEMMA ideal for analyzing intact viruses and subviral particles, allowing for a detailed look into their size, bioaffinity, and purity. [61, 62, 65, 66, 83-86]

In the studies focused on AAV8 VLPs, as presented in this work, nES GEMMA demonstrated its ability to unveil heterogeneity in particle populations, including empty and fully filled capsids. Hence, shedding light on the variable nature of viral preparations and the importance of understanding their composition for both research and therapeutic applications. [87-89]

Furthermore, important studies involving the human rhinovirus demonstrate the versatility of nES GEMMA. In the work of Weiss et al. in 2015,[65] the HRV serotype 2 (HRV-A2) was studied by employing nES GEMMA not only for purity assessment, but also for the analysis of the subviral HRV-A2 particles; derived from the primary preparation. Followed by native mass spectrometry, the

spectrum of intact HRV-A2 virions and their empty viral capsids –the B-particles– was obtained. This data combination helped draw a correlation between molecular mass and EM diameter.

Moreover, enteroviruses –like HRVs– transition through multiple phases during infection, including the native infective form and the A and B particles. To characterize the evolution of these phases, in the work of Weiss et al. of 2012,[66] nES GEMMA was employed next to capillary electrophoresis to add another layer of understanding to the particle composition of these viral entities.

Overall, with the ability to provide label-free size distributions for particles ranging from approximately 2 nm to less than 150 nm (while using the nano DMA 3085), nES GEMMA has made significant contributions to diagnostics and treatment strategies, from detecting lipoproteins and bacterial infections to assisting in viral clearance and antibody aggregation. Thus proving to be an invaluable tool for advancing both research and medical knowledge.

Strengths and Limitations of nES GEMMA

In the landscape of bio-nanoparticle analysis, nES GEMMA stands out as an efficient and cost-effective tool. However, as with many advanced technologies, it has distinct strengths and inherent limitations. One of the notable advantages of nES GEMMA is its size-separation resolution, which is being further investigated through the work of Fernandez de la Mora et al. in order to enhance peak resolution. [90-93] It can effectively separate a wide array of molecular analytes, from proteins and viruses to VLPs, liposomes, and several nanoparticles and bionanoparticles. As highlighted in this work, nES GEMMA can detect even minor differences among particles. This capability allows for identifying variations within the samples, such as distinguishing between empty and fully filled viral capsids. [88]

Another significant benefit is its ability for label-free characterization. Unlike other methods, nES GEMMA doesn't require fluorescent or radioactive labeling of samples. This approach simplifies the preparation process and avoids potential changes that labeling might introduce to the original analytes. Additionally, in terms of speed, nES GEMMA offers a relatively quick analysis, which is valuable in time-sensitive studies or when working with large sample volumes. Importantly, thanks to the intrinsic gentle nature of the electrospraying process, it manages to preserve non-covalent interactions, which is crucial for native analysis.

However, the application of nES GEMMA is not free from challenges. When utilizing the nano DMA 3085, the instrument's particle range classification is confined to sizes ranging from 2 nm to 150 nm. As a result, the analysis of analytes beyond this size range is limited. Moreover, a potential issue arises as particles transition into the gas phase. The particles potentially undergo shrinkage, which could

compromise the precision of measurements, especially for empty, subviral particles, or proteins. [64, 87, 94]

Lastly, for accurate analysis with nES GEMMA, samples of high purity are essential, which makes purification steps necessary. Additionally, the use of a volatile electrolyte solution requires a buffer exchange process. [87, 95] These combined factors often lead to a reduced sample yield, which should be considered before analysis.

In summary, while nES GEMMA offers a range of impressive strengths, it's essential to be aware of and account for its limitations to fully harness its potential in research.

2.2 Atomic Force Microscopy (AFM)

How AFM works

Atomic Force Microscopy (AFM) is a powerful technique that operates based on the principle of scanning a sharp probe (or "tip") mounted on a cantilever over a sample's surface. As the tip interacts with the surface, it causes the cantilever to deflect. A laser, reflected off the cantilever into a photodetector, measures this deflection. The deflection data is subsequently used to generate a high-resolution 3D image, offering a detailed topographical map of the surface at the nanometer scale. [96-98]

Besides imaging, AFM can also be employed to quantify the forces between the probe and the sample as a function of their mutual separation, a technique known as force spectroscopy. [99] This allows AFM to probe the sample's mechanical properties, such as the sample's Young's modulus - a measure of stiffness. [100] Thus, force spectroscopy also provides critical insights into the mechanical behavior of materials at the nanoscale, enabling the examination of intermolecular forces, protein unfolding, or interactions between biological macromolecules. [99, 101, 102]

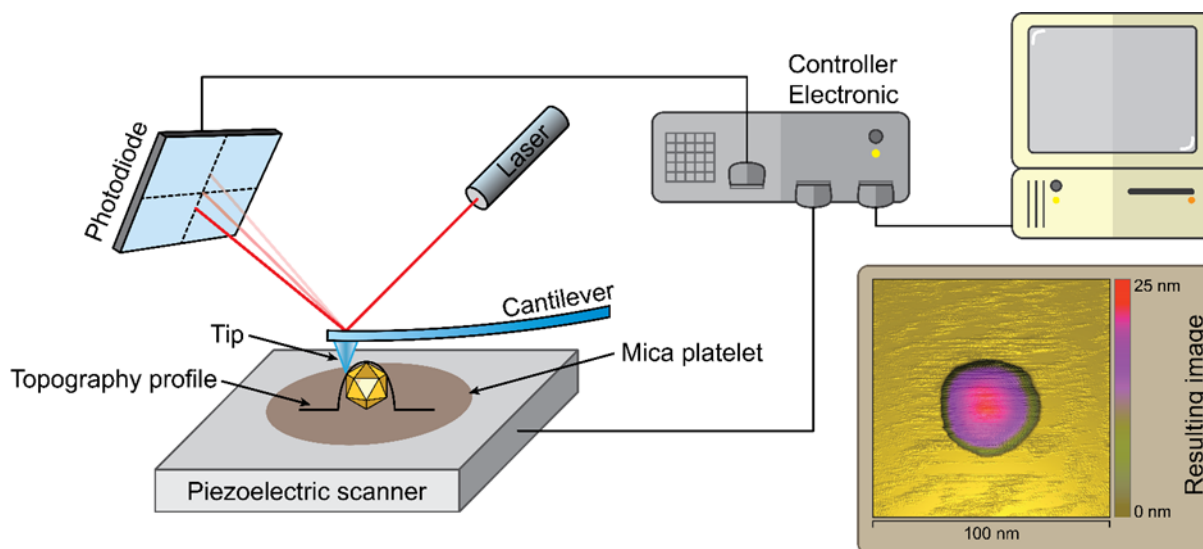


Figure 2.2.1. Schematic overview of the working principle of AFM. The resulting image of a single AAV8 VLP particle is shown in the bottom right.

Key components of an AFM setup include a piezoelectric scanner, a cantilever with a sharp tip, a laser source, a photodiode detector, a control system, and a computer unit (see Figure 2.2.1). The piezoelectric scanner facilitates precise, controlled movement of the sample in relation to the cantilever. The controller adjusts the scanner's height to maintain a constant interaction between the tip and the surface, providing an accurate topography map of the surface or force measurements

depending on the operating mode. Lastly, the computer translates the topographical information or force data into a resulting image or force-distance curves. [103]

AFM operates in various modes, namely contact mode, non-contact mode, and tapping mode. [99] The contact mode maintains constant physical contact between the tip and the sample surface, facilitating both imaging and force spectroscopy measurements. The non-contact mode allows the tip to hover just above the surface, detecting forces without direct contact. The tapping mode combines the previous two, where the cantilever oscillates, and the tip intermittently contacts the surface. [104, 105]

The data collected by AFM is often visualized as 3D images or 2D cross-sections for imaging and as force-distance curves for force spectroscopy. Various software tools can be used for analyzing and interpreting AFM data, allowing the extraction of parameters such as particle size, surface roughness, adhesion forces, and mechanical properties. However, interpretation must be carried out with caution as artifacts can arise due to factors like the tip shape or scan speed. [106, 107]

Lastly, critical parameters that can significantly affect the AFM imaging process, force measurements, and the resulting data include: the cantilever's spring constant and resonance frequency, the tip size and shape, and the scan speed and resolution. Careful selection and control of these parameters are crucial for obtaining reliable and accurate measurements.

AFM Applications in Virology and AAV8 VLP Analysis

Thanks to AFM's high resolution, capability to operate under near-physiological conditions, and adaptability across various environments, from vacuum to liquids, it became an essential tool in the field of virology. [97, 108-112]

One of AFM's primary advantages is its ability to produce high-resolution images of individual viral particles (see Figure 2.2.1). [113] Through this capability, researchers can explore the external morphology of viruses, capturing intricate details of their structures. Moreover, this imaging technique offers a firsthand look at the various stages of viral formation, from initial assembly to their release from host cells. [114]

However, as previously mentioned, AFM is not limited to imaging alone; force spectroscopy is another important feature. For example, it can measure the stiffness or elasticity of viral particles, which are key indicators of their structural integrity, providing insights into their mechanical properties. [115, 116]

Focusing on AAV serotype 8 (AAV8), AFM has helped distinguish between full and empty capsids. [87, 117] It has been used to identify differences in charge and hydrophobicity between these two forms. [118] These variations in properties are thought to arise from the presence of nucleic acids inside the AAV capsid, which may induce subtle but significant structural changes. Other methods, such as nES GEMMA, have been combined with AFM to reveal larger AAV8 VLP aggregates, as highlighted in the first study of this thesis. [87]

Strengths and Limitations of AFM in Virological Studies

AFM undoubtedly offers unique advantages for virological studies. One of its exceptional capabilities is the high-resolution imaging it can generate, allowing for nanoscale exploration of viral morphology. [115] An added advantage of AFM is its non-destructive nature. Unlike techniques such as electron microscopy, there's no need for elaborate sample preparation processes like staining or fixation, which could potentially alter the native properties of the sample. Furthermore, the dynamic observation capacity of AFM means it can actively monitor processes in real time. This is crucial for observing viral assembly or the interactions between viruses and host cells. [119, 120] Adding another layer to its functionality, the force spectroscopy feature of AFM can measure interaction forces, which is essential for quantitative data. [102] Thus, shedding light on aspects such as virus-cell adhesion and the inherent mechanical properties of viral capsids. [98, 99, 120]

However, while AFM offers several advantages, it's not without limitations. One significant challenge lies in its limited field of view, which is smaller than other microscopy methods. Consequently, AFM images are limited to smaller areas, potentially failing to represent the entirety of the sample. Additionally, the scanning speed of AFM can be a limiting factor, especially when striving for high-resolution images, as image acquisition can be time-consuming. There's also the constant risk of potential artifacts affecting the images, stemming from mechanical glitches or instrumental errors, which can impact result accuracy. [106, 107]

Moreover, another source of potential artifacts could arise from the deformation of the particles due to their adhesion on the mica sheet. This adhesion-induced distortion may affect the reliability of the captured images. Furthermore, AFM may produce erroneous size measurements, particularly when analyzing particles' edges, potentially resulting in overestimations. [121]

Despite these challenges, AFM can be less demanding in terms of sample preparation compared to other techniques. However, this convenience sometimes comes at the cost of compromising the native state of the sample when adherence to a substrate is necessary. Additionally, when exploring the internal structures of larger viruses, AFM's depth perception may prove less advantageous compared to techniques offering superior depth resolution, such as electron microscopy.

In conclusion, AFM is a formidable tool for virological studies, providing unparalleled high-resolution images and precise measurements. Yet, it's important to consider its limitations to ensure proper utilization of the technique and correct interpretation of the results. This approach will ensure AFM continues to influence discoveries in virology and biotechnology, especially for gene therapy applications.

2.3 Asymmetrical Flow Field-Flow Fractionation (AF4)

How AF4 works

Asymmetrical Flow Field-Flow Fractionation (AF4) is a versatile size-based separation technique. [122, 123] This method has found its space in various sectors thanks to its compatibility with both aqueous and organic solvents, and its ability to efficiently separate and characterize a wide range of particles, including nanoparticles, polymers, and proteins. [124-126]

The distinguishing feature of AF4 lies in its unique design that utilizes only one semi-permeable wall in the separation channel, hence producing an asymmetrical flow pattern. As a result, the crossflow in AF4 is generated by the carrier liquid, which continuously exits through the semi-permeable membrane at the base of the channel. [122, 123, 127, 128]

In the context of operation, the sample is introduced into the thin, open channel of AF4, where it encounters two interacting flows: a laminar flow that moves the sample forward, and an orthogonal crossflow that pushes the sample against the semi-permeable membrane. These flows interact to create a force field gradient that disperses the particles based on their size and diffusion rates, an intrinsic property dictated by Brownian motion. [122, 123, 127, 128]

In detail, larger particles, with slower diffusion rates due to their size, are pushed closer to the membrane, while smaller particles, with faster diffusion rates, distribute evenly across the channel's height. The laminar flow – that carries the sample through the chamber – has a parabolic profile; thus, its speed varies across the height of the channel (see Figure 2.3.1). The flow is faster in the center of the channel and slower near the walls. Here is where the size-based separation occurs: due to the higher degree of Brownian motion, smaller particles will position themselves away from the membrane and experience faster laminar flow. Consequently, they will be the first to elute. On the contrary, larger particles closer to the membrane will encounter a slower laminar flow and, therefore, elute later. This process, essentially dictated by the interaction between the particles' Brownian motion and the channel's varying laminar flow velocity, results in an effective size-based separation of the particles. [122, 123, 127, 128]

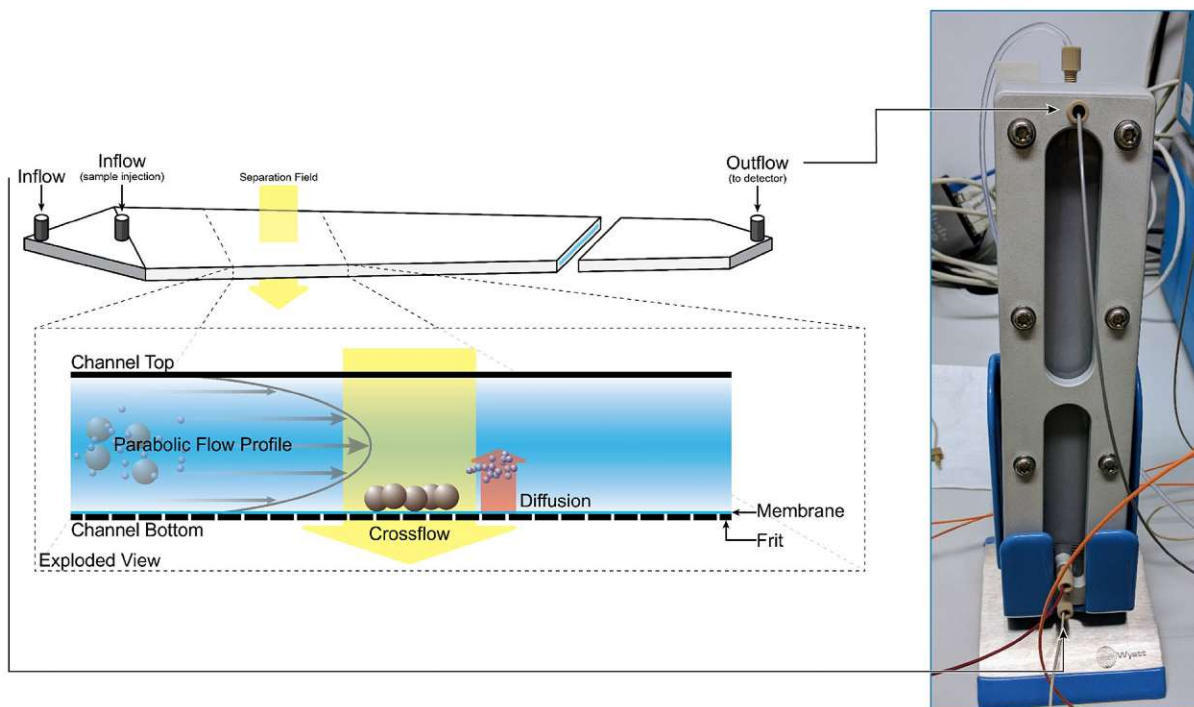


Figure 2.3.1. Schematic representation of the AF4 channel, accompanied by a photograph of the AF4 device used for separation of AAV8 VLP oligomers at Takeda, Orth/Donau, Austria.

Lastly, AF4 can be coupled with a multitude of detection methods, such as UV-absorbance, light scattering, or mass spectrometry. Furthermore, manual or automatized fractionation can also be performed, thus allowing for more exhaustive analysis, as explored in the first study of this thesis. This versatility of AF4 with various detection methods makes it a powerful tool for research and development. [125, 129-132]

AF4 and its application in virology and AAV8 VLPs

AF4 has proven to be an important tool in the field of virology due to its non-destructive nature. [133-137] Unlike other separation methods that rely on stationary phases, which can disrupt the delicate structures of viral particles, AF4's working principle does not rely on a column or stationary phase; thus, it allows for minimal interaction between the particles and the surfaces. This becomes crucial when dealing with viral particles or VLPs, which are often vulnerable to aggregation or disassembly. By minimizing interactions, AF4 not only preserves the integrity of the particles but also limits the loss of sample due to adsorption. [134, 138]

For the analysis of AAV8 VLPs, AF4 provides a significant advantage. Indeed, AAV8 VLPs come in different forms - empty, partially filled, and completely filled particles - that present slight variations in their size. Hence, AF4 can easily be employed to differentiate between these forms. This feature

allows for a comprehensive characterization of AAV8 VLP preparations, proving particularly useful in quality control processes where the ratio of filled to empty particles may be critical. [87, 135]

Strengths and Limitations of AF4

As highlighted in the previous section (2.3.1), AF4 offers numerous strengths for the analysis of viral particles like AAV8 VLPs. The gentle, non-destructive nature of AF4 and its capability for size-based separation are particularly advantageous for AAV8 VLPs. [134, 135, 138] Moreover, the ability to couple AF4 with various detectors and to manually or automatically collect fractions broadens its utility and provides multiple possibilities for analysis. [124, 139]

However, as with any analytical tool, AF4 also has its limitations. For example, optimizing AF4 methods can be tedious and time-consuming, requiring meticulous fine-tuning of several parameters, such as the crossflow rate and focus time. Moreover, AF4 may present difficulties associated with sample concentration and recovery. Specifically, if the sample concentration is low, the detection sensitivity may be compromised, leading to potentially skewed results. Additionally, due to AF4's specific design, a portion of the sample may be lost during the separation process, affecting the overall recovery rate. Lastly, during fractionation, the collected sample might be excessively diluted. As a result, steps to accumulate and concentrate the sample may be necessary, which could further reduce sample recovery. This specific challenge was encountered during the first study of this thesis. [87]

In conclusion, despite certain limitations, with careful method development, AF4 remains an invaluable tool for virological studies, particularly for the analysis of AAV8 VLPs.

2.4 Native Mass Spectrometry (Native MS)

How native MS works

Mass spectrometry is a versatile analytical technique widely used for identifying, characterizing, and quantifying molecules. Essentially, mass spectrometry operates by transforming analytes into ions and sorting them based on their mass-to-charge ratio (m/z) in vacuum. Once the ions are separated, they're detected, and their respective abundances are recorded. With knowledge of the charge state (z), the mass (m) of the analytes can be calculated. This allows for the calculation of the mass of the analytes, providing invaluable information about their identity and composition. [140] In traditional applications, biomolecules are often denatured, fragmented, and ionized under harsh conditions to improve their detection. However, this approach disrupts the non-covalent interaction and leads to a loss of conformation and disassembly of complex structures and hence to a loss of information concerning the intact biomolecule.

Native MS, instead, aims to address these issues by preserving the native state of the analytes. [141-145] This is often achieved by employing a soft ionization technique, known as nano-Electrospray Ionization (nESI, see Figure 2.4.1). [146] In nESI, the analyte is dissolved in a buffer solution that helps maintain near-physiological conditions. This gentle method favors near-native conditions crucial to holding the conformational structure of the proteins or maintaining together large biomolecular assemblies, such as protein complexes and viral particles. [65, 142, 147-151]

Moreover, native MS also extends its capabilities to studying other key interactions, such as protein-protein and protein-ligand bonds. [141, 143] By preserving the near-native state of these large biological assemblies, it offers a unique opportunity to observe these interactions close to their natural context. Overall, this makes native MS an effective tool for studying and understanding the complexity of biological systems.

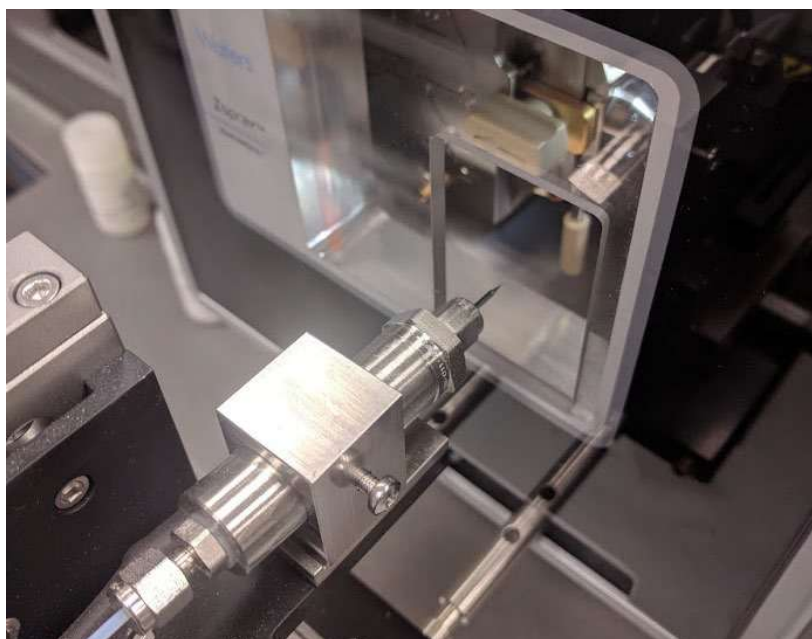


Figure 2.4.1. Picture of the nESI source employed during the analysis of AAV8 VLPs at MSVision (Almere, The Netherlands).

The role of native MS in virology and AAV8 VLPs applications

Native MS has significantly impacted the field of virology by allowing the study and characterization of intact viral capsids. [147, 150, 152-154] By providing direct information about the mass of the viral particles, which can easily span in the MDa range (e.g., Norwalk virus VLP 10 MDa, HK97 bacteriophage 18 MDa), [152, 155] scientists can infer information on the stoichiometry of viral proteins or study the distribution of assembled and unassembled capsids. Moreover, the occupancy state can be derived by the increase in mass, making it possible to distinguish between empty and genome-filled capsids, an interesting feature for gene therapy applications. [17, 88]

In the context of AAV8 VLPs, native MS can be implemented as a tool for understanding their assembly and packaging. [10] As an example, the ability to distinguish between empty and filled forms, which differ in size considerably, can provide insights into the packaging efficiency and potential heterogeneity between sample preparations. [156] This is particularly relevant in the field of gene therapy, where the effective delivery of the vector's cargo largely depends on these characteristics. Therefore, native MS is not only a tool for basic research but also a useful technique for the development and quality control of gene therapies based on AAV vectors. [154, 157]

Challenges and limitations of native MS in AAV8 VLP analysis

Despite its strengths, native MS presents several challenges when it comes to the analysis of viruses. [158] One of the key challenges lies in handling the large size of the analyte, which in the case

of AAV8 VLPs, ranges from approx. 3.7 MDa for empty particles to approx. 5 MDa for filled particles. This large size requires advanced instrumentation specifically modified for high molecular weight analytes. [159]

Sample quality is another significant challenge. High levels of sample purity, homogeneity, and sufficient analyte concentration are crucial for the effective use of native MS. Since contamination, heterogeneity, or sub-optimal concentrations will lead to misleading or ambiguous results. [10, 156, 160] Moreover, handling infectious material introduces additional challenges. Indeed, biosafety protocols and precautions must be followed throughout the entire process to prevent potential exposure and ensure a safe working environment.

Another critical aspect is the requirement for careful sample preparation and optimization of experimental conditions. These measures are necessary to maintain the native state of the VLPs, prevent particle aggregation, and limit disassembly during the measurement process. The selection of a suitable volatile electrolyte is another key factor in sample preparation, as it significantly impacts the effectiveness of the ionization process. [161, 162]

Lastly, data interpretation remains a time-consuming demanding task. Nonetheless, native MS proves to be a crucial technique in studying viral particles, offering unique insights capable of supporting and integrating other analytical methods.

2.5 Cryogenic Transmission Electron Microscopy (cryo-TEM)

How cryo-TEM works

Cryogenic Transmission Electron Microscopy (cryo-TEM) is an advanced imaging technique capable of generating high-resolution images of specimens close to their native state. [163-165] This is achieved by rapidly freezing the biological sample (plunge-freezing method) in a thin layer of vitreous ice (i.e., non-crystalline ice). [166] This method prevents the formation of ice crystals that would disrupt the native structure of the sample.

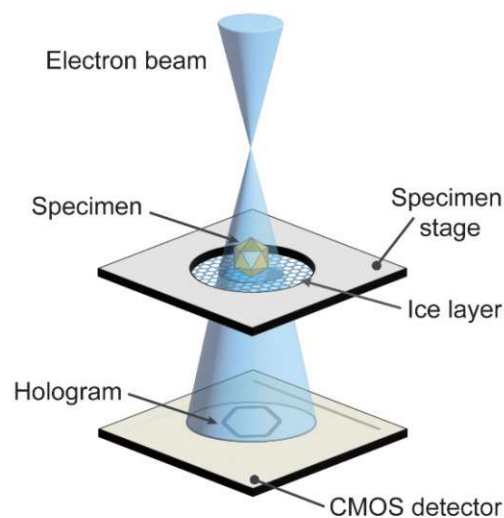


Figure 2.5.1. Schematic drawing of the working principle of cryo-TEM

To generate the images, the frozen sample is exposed to a beam of electrons. As the electrons pass through the sample, they interact with the specimen, and the transmitted electrons are detected to generate a two-dimensional image (see Figure 2.5.1). [165] The contrast of the image is primarily due to differences in electron density within the sample, which allows different components of the sample to be distinguished. Importantly, the native structure of the specimen is preserved because the sample is maintained at cryogenic temperatures during imaging. [165]

The two-dimensional images collected from multiple sample orientations allow for the generation of a three-dimensional reconstruction (i.e., tomogram), thus providing a comprehensive near-atomic resolution view of the specimen's structure. [167, 168]

Cryo-TEM in the study of viral particles

Cryo-TEM's unique capabilities have found extensive application in virology, where it has become a crucial tool for examining the structures of viruses and VLPs. [169-172] The ability of cryo-TEM to

image biological samples in a near-native state offers virologists a 'real-life' view of viruses, helping them understand their composition, morphology, and interactions with proteins or other macromolecules. [173]

In studying viral particles, cryo-TEM provides information about the overall size and shape of the viral capsids, the arrangement of their protein subunits, and genome occupancy. [174-176] Such data are essential for understanding the intricate details of virus architecture, which, in turn, informs us about their mechanisms of infectivity and immune evasion. [177]

In the process of reconstructing viral particles using cryo-TEM, two distinct approaches can be adopted - symmetrical and asymmetrical reconstruction. [163, 175] Symmetrical reconstruction, while faster and simpler, is especially beneficial when investigating highly symmetrical particles. By taking advantage of the natural symmetry, each particle provides multiple data points, enhancing the statistical power of the analysis. However, over-reliance on symmetry may risk overlooking asymmetrical features of the specimen. [163, 178]

Asymmetrical reconstruction, despite being more labor-intensive and time-consuming, delivers a more detailed image of the particle's structure. This technique can reveal unique, asymmetrical features that might be missed otherwise.

Specific applications of cryo-TEM with AAV8 VLPs

Regarding AAV8 VLPs, cryo-TEM provides a multitude of information on their structural details. Indeed, the high-resolution close-up images reveal the shape and size of the viral particles (see Figure 2.5.2). [89, 179] It could give insights into the quality of the VLP preparations, thus informing whether the VLPs have formed correctly or if there are structural abnormalities. [176] For example, the presence of empty or broken capsids can be identified. Information on particle aggregation can also be obtained. All of these factors can influence the efficiency of VLP-based gene delivery and thus are of great interest in the field of gene therapy. [176, 180, 181]

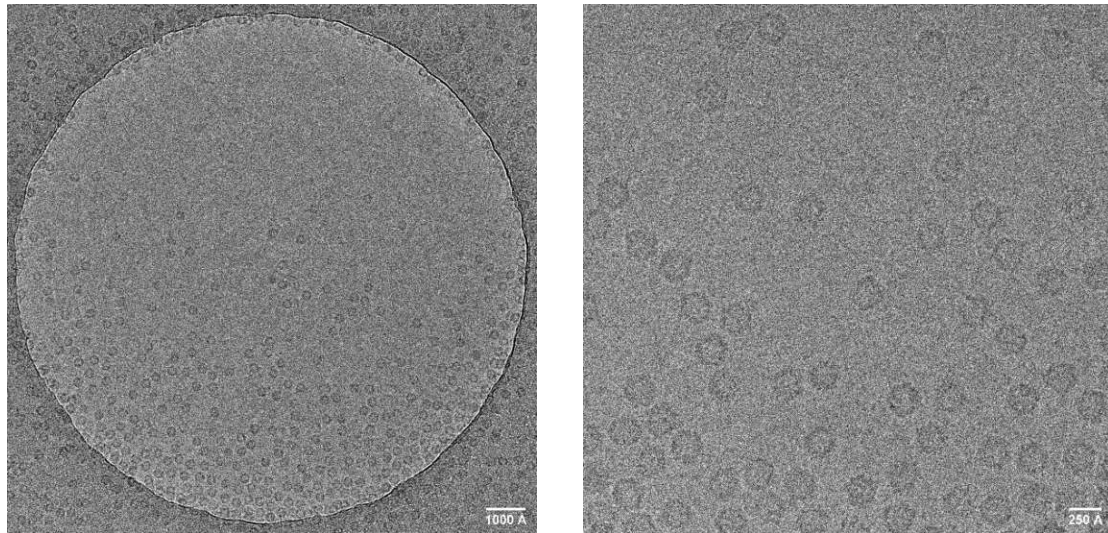


Figure 2.5.2. – Cryo-TEM images of AAV8 VLP filled preparation. Level of magnification: 45K (left), 150K (right)

Strengths and limitations of cryo-TEM in the context of AAV8 VLP study

Despite the many strengths of cryo-TEM, like any other technique, it comes with certain limitations. While cryo-TEM provides unparalleled structural information at high resolution and in a near-native state [163-165, 167, 168], the technique is technically demanding, requiring a high degree of skill to prepare the samples, operate the microscope, and evaluate the data. Moreover, achieving atomic-level resolution with cryo-TEM necessitates extensive image processing and the collection of large datasets, which can be time-consuming and computationally intensive. Despite these limitations, the unique strengths of cryo-TEM make it an indispensable tool in the study of AAV8 VLPs. By providing high-resolution, near-native state structural information, it offers unparalleled insights into these particles, shedding light on their potential as gene delivery vectors. [176, 180, 181]

2.6 Complementary Use of Analytical Techniques in AAV8 VLPs Study

For this research work, a multitude of analytical techniques have been explored. While each offers unique and specific insight, when intertwined, they provide a comprehensive understanding and a holistic view of these viral particles.

In the first study, nES GEMMA, AF4, and AFM were employed. nES GEMMA produced data on the size and genome occupancy of VLPs, while AF4 contributed to additional data on size distribution, aggregation, and allowed for the fractionation of the different oligomer states. These fractions were then analyzed by nES GEMMA and AFM. AFM characterized the topological features of the collected fractions and highlighted their differences.

In the second study, the focus was on the differentiation between empty or filled VLPs via nES GEMMA and nMS. While the former continued to provide valuable data on size distribution, the latter provided crucial insights into the intact mass of AAV8 VLPs. Notably, given the high molecular weight of the capsids, dedicated instrument modifications were necessary. For this purpose, the second study was done in collaboration with MSVision (Almere, The Netherlands).

For the third and final study of this research, the focus was directed towards the effects of pH changes on the aggregation behavior of AAV8 VLPs. The behavior of AAV8 VLPs, empty and filled, was investigated across different pH values. Notable differences linked to pH were highlighted by nES GEMMA analysis. However, AFM and cryo-TEM were employed as complementary techniques to understand these effects fully.

Each of the selected analytical techniques employed in this research provides unique and valuable information on AAV8 VLPs. However, combined, they offer a more complete understanding of AAV8 VLPs. The data from each technique enriches the others, resulting in a comprehensive analysis that can significantly enhance the field's knowledge of AAV8 VLPs and their potential for gene therapy applications.

3 Publications

ACS Omega (2021), 6, 25, 16428–16437

Adeno-associated Virus Virus-like Particle Characterization via Orthogonal Methods: Nanoelectrospray Differential Mobility Analysis, Asymmetric Flow Field-Flow Fractionation, and Atomic Force Microscopy

Samuele Zoratto¹, Victor U. Weiss¹, Gernot Friedbacher¹, Carsten Buengener², Robert Pletzenauer²,
Alexandra Foettinger-Vacha², Michael Graninger², and Guenter Allmaier¹

¹ Institute of Chemical Technologies and Analytics, TU Wien (Vienna University of Technology), Vienna
A-1060, Austria

² Pharmaceutical Sciences, Baxalta Innovations (part of Takeda), Vienna A-1221, Austria

<https://doi.org/10.1021/acsomega.1c01443>

In our study, we developed a comprehensive method to analyze AAV8 VLPs, a vector widely used in gene therapy. We utilized nES GEMMA, AF4, and AFM to examine the VLPs in their native state. These techniques allowed us to determine the size, purity, and aggregation of both types of AAV8 VLPs, those lacking internal material (empty VLPs) and those carrying engineered single-stranded DNA (filled VLPs).

We induced VLP aggregation through a combination of heat and shear stress, which led to the formation of various VLP aggregates. We then size-separated these aggregates using AF4 into monomer, dimer, and oligomer fractions, representing different states of VLP aggregation. Each separated fraction was further analyzed using nES GEMMA and AFM. We found that both techniques confirmed the presence of VLP dimers, trimers, and potential oligomers. Furthermore, our application of AFM revealed even larger AAV8 VLP aggregates, which nES GEMMA could not detect due to its detection limit.

Our study also explored the impact of filling the AAV8 VLPs with engineered DNA. We found that the presence of genomic material inside the capsid affects the overall diameter of the particle. In

conclusion, our research presents a novel and thorough approach to characterizing AAV8 VLPs and their behavior under stress conditions, providing vital insights for their use in gene therapy applications.

INNOVATIVE ASPECTS:

- Development of a comprehensive characterization method for AAV8 VLPs, integrating nES GEMMA, AF4, and AFM, which allows for a detailed understanding of VLP's size, purity, and aggregation behavior.
- Successfully induced VLP aggregation via heat and shear stress and followed by separation into fractions with distinct oligomeric states using AF4.
- New insights into how the presence of genomic material in filled AAV8 VLPs impacts their overall diameter.

OWN CONTRIBUTION

In this work, I

- was involved in planning the experiments.
- conducted the nES GEMMA experiments, evaluated, and interpreted the data.
- assisted AF4 experiments, evaluated, and interpreted the data.
- assisted AFM experiments, evaluated, and interpreted the data.
- drafted and wrote major parts of the manuscript.
- overall data processing.

Adeno-associated Virus Virus-like Particle Characterization via Orthogonal Methods: Nanoelectrospray Differential Mobility Analysis, Asymmetric Flow Field-Flow Fractionation, and Atomic Force Microscopy

Samuele Zoratto, Victor U. Weiss, Gernot Friedbacher, Carsten Buengener, Robert Pletzenauer, Alexandra Foettinger-Vacha, Michael Graninger, and Guenter Allmaier*

Cite This: *ACS Omega* 2021, 6, 16428–16437

Read Online

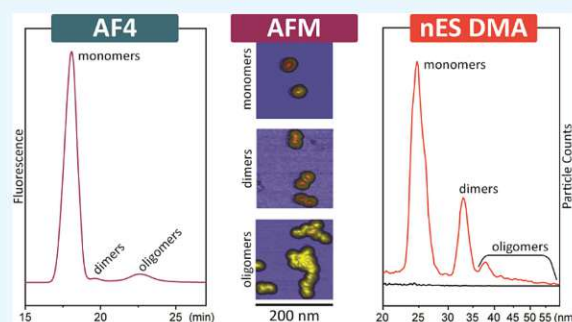
ACCESS |

Metrics & More

Article Recommendations

Supporting Information

ABSTRACT: Adeno-associated virus (AAV)-based virus-like particles (VLPs) are thriving vectors of choice in the biopharmaceutical field of gene therapy. Here, a method to investigate purified AAV serotype 8 (AAV8) batches via a nanoelectrospray gas-phase mobility molecular analyzer (nES GEMMA), also known as an nES differential mobility analyzer, is presented. Indeed, due to AAV's double-digit nanometer scale, nES GEMMA is an excellently suited technique to determine the surface-dry particle size termed electrophoretic mobility diameter of such VLPs in their native state at atmospheric pressure and with particle-number-based detection. Moreover, asymmetric flow field-flow fractionation (AF4, also known as AFFFF) and atomic force microscopy (AFM) techniques were employed as orthogonal techniques for VLP characterization. In addition, AF4 was implemented to size-separate as well as to enrich and collect fractions of AAV8 VLPs after inducing analyte aggregation in the liquid phase. Bionanoparticle aggregation was achieved by a combination of heat and shear stress. These fractions were later analyzed with nES GEMMA (in the gas phase) and AFM (on a solid surface). Both techniques confirm the presence of dimers, trimers, and putative VLP oligomers. Last, AFM reveals even larger AAV8 VLP aggregates, which were not detectable by nES GEMMA because their heterogeneity combined with low abundance was below the limit of detection of the instrument. Hence, the combination of the employed orthogonal sizing methods with the separation technique AF4 allow a comprehensive characterization of AAV8 VLPs applied as vectors.



INTRODUCTION

In the biopharmaceutical field of gene therapy, one of the most investigated carriers is represented by adeno-associated virus (AAV) virus-like particles (VLPs)¹ owing to their low immunogenicity, high efficiency of transduction, and transgene persistence in a broad range of tissues for *in vivo* applications.^{2,3} AAV is a helper-dependent virus of the *Parvoviridae* family, formed by 12 serotypes that show different tissue-specific tropisms.⁴ AAV is based on a non-enveloped, icosahedral capsid with a diameter of approximately 25 nm as related by cryoelectron microscopy reconstruction.⁵ Its cargo capacity is reported to be 4.7 kb of single-stranded DNA (ssDNA).^{6,7} The studies presented here were performed with purified (i.e., VLPs that are homogeneous in size, stable, and lacking aggregates) AAV serotype 8 (AAV8) either lacking (i.e., empty, which means a classical VLP) or carrying engineered ssDNA (i.e., filled particles).

The application of a nanoelectrospray gas-phase electrophoretic mobility molecular analyzer (nES GEMMA aka nES

DMA (differential mobility analyzer), MacroIMS (ion mobility spectrometer), and LiquiScan ES or ES SMPS (scanning mobility particle sizer)) for size characterization of globular proteins has already been demonstrated.⁸ Furthermore, the applicability of this technique for the analysis of viral samples and their complexes (i.e., virus–antibody complexes) has already been confirmed in several studies.^{9–14} As its name suggests, a native nanoelectrospray process is involved in sample droplet formation. Dry analyte separation occurs by means of a differential mobility analyzer (DMA) in the gas phase, and particle detection is conducted using an ultrafine condensation particle counter (CPC) device. In detail, a cone-

Received: March 17, 2021

Accepted: May 27, 2021

Published: June 15, 2021



tipped fused silica capillary, tapered by a homebuilt grinding machine,¹⁵ is used to electrospray a volatile, aqueous electrolyte solution in which the viral analytes are dissolved or suspended. The liquid of the generated nanodroplets evaporates in a mixture of dry particle-free air and carbon dioxide. Simultaneously, charge equilibration is obtained by a bipolar atmosphere produced by, e.g., a radioactive source (i.e., ²⁰¹Po, an α -particle emitter).¹⁶ Thus, a so-called “polydisperse aerosol” composed of surface-dry, single charged bionanoparticles is generated. This polydisperse aerosol is subsequently fed to the nano-DMA via the same air–CO₂ mixture. Here, a well-defined, orthogonal electric field with increasing/decreasing voltage is applied in conjunction with a constant, particle-free, high laminar sheath air flow. Hence, the particles are sorted according to their different electrophoretic mobility diameters (EMDs), the applied voltage, the flow rate, and the DMA’s geometry. Therefore, for a given voltage and a fixed flow rate, a so-called “monodisperse aerosol” is produced, which is composed of nanoparticles with the same EMD. In the case of spherical particles, the EMD corresponds to the nanoparticle diameter. Once in the CPC device, the size-separated nanoparticles act as condensation nuclei in the supersaturated atmosphere of either water or *n*-butanol. Thus, droplet formation occurs. Subsequently, droplets are detected via light scattering optics.¹⁷ When a droplet crosses the focused laser beam, independently from its chemical composition or its original size, a count/signal is added to the spectrum at the relative EMD.¹⁸ Therefore, for a defined flow rate in the DMA, a specific range of EMDs can be explored. By variation of the applied electrical field, a GEMMA spectrum is generated,¹⁹ yielding number-based particle concentrations in accordance with a recommendation of the European Commission for nanoparticle characterization (2011/696/EU from October 18th, 2011). Previous works from Weiss et al.,²⁰ Bereszczak et al.,²¹ Havlik et al.,²² and Pease et al.²³ show that nES GEMMA is a suitable instrumentation for VLP analysis, and in this study, it has been implemented to develop a method to characterize purified AAV8 VLPs either with or without induced bionanoparticle aggregation.

Asymmetric flow field-flow fractionation (AF4, also known as AFFFF) is a soft liquid-phase separation technique that retains the native structure and conformation of the analytes. A detailed overview of the technique and its theory can be found elsewhere.^{24,25} In essence, sample separation is achieved on the intrinsic size-dependent diffusion coefficient of the analytes against an orthogonal crossflow force, and hence the separation is a function of the hydrodynamic radius of the sample components. Its implementation for the separation of bionanoparticles such as viruses and virus-like particles has already been verified in several studies.^{23,26–31} In this study, AF4 was employed to separate and collect the fractions of empty AAV8 VLPs at different hydrodynamic diameters representing monomeric, dimeric, and oligomeric states (formed after treating the original sample with heat and shear stress).

Furthermore, images of both empty and filled AAV8 VLPs samples were produced by means of atomic force microscopy (AFM). This device is capable of measuring in the subnanometer range; hence, it can easily produce images at the viral scale.^{32–34}

A detailed description of the technique is reported elsewhere.³² In principle, a cantilever with an atomically sharp tip interacts with the sample surface. The local forces

between the tip and the structural features of the sample displace the tip vertically. This movement is detected by the instrument and processed to generate an image. In this study, the instrument was set in tapping mode to acquire AFM images due to the softness of the nanoparticles. Thus, the tip is not in continuous contact with the sample surface, but instead, it gently oscillates rapidly on the surface. This approach is particularly indicated for samples that are too soft or too fragile for the continuous contact mode.³³

The implementation of the described analytical techniques to investigate the size characteristics and the aggregation behavior of purified AAV8 VLPs is presented here with two strategies, as outlined in Figure 1. The first approach (see

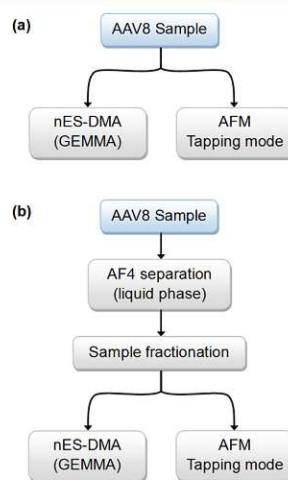


Figure 1. Scheme of the two analytical focuses of this study. (a) Empty and filled AAV8 VLP particles are analyzed via nES GEMMA and AFM. (b) AF4 liquid-phase separation enables AAV8 VLP oligomer analysis by means of nES GEMMA and AFM after fractionation.

Figure 1a) is designed for the investigation of the differences between the two VLP preparations. This approach involves the usage of nES GEMMA and AFM techniques. The second approach (see Figure 1b) focuses mainly on the analysis of empty AAV8 VLPs and their aggregation behavior after bionanoparticle stressing by means of heat and mechanical agitation. With this method, AF4 was used to fractionate and collect the VLPs in different oligomeric states, which were later analyzed via nES GEMMA and AFM. Separately, nES GEMMA and AF4 were performed to prove why a buffer exchange step prior to sample analysis is crucial, even if it comes at the expense of bionanoparticle loss in this process.

RESULTS AND DISCUSSION

Our article aims to demonstrate the strategy for the analysis of an AAV-based VLP by means of nES GEMMA, AF4 with fluorescence detection, and AFM in tapping mode. Two strategies, summarized in Figure 1, have been tested. The first includes the analysis of both empty and filled AAV8 VLPs by means of nES GEMMA and AFM (see Figure 1a). The aim is to investigate and highlight the differences between the two preparations. Whereas, the second strategy (see Figure 1b) aims to investigate different oligomeric states of empty AAV8 VLPs generated under stress conditions. These oligomeric

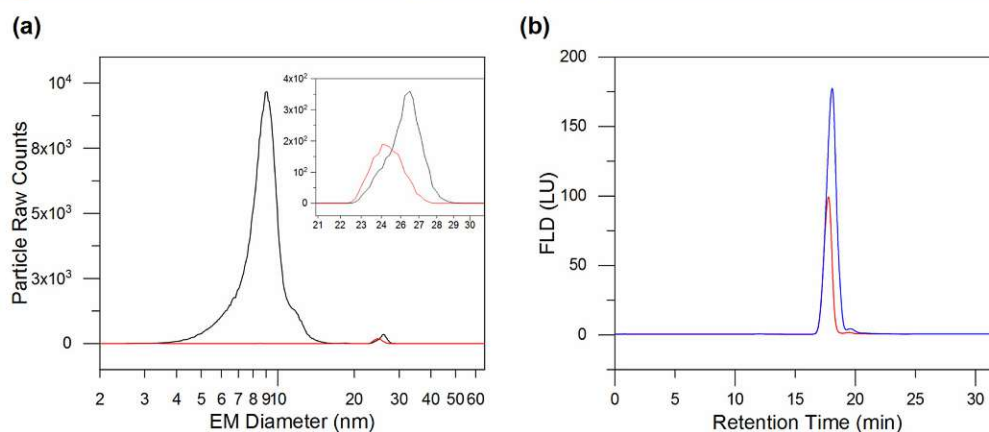


Figure 2. Implications of the buffer exchange treatment. (a) nES GEMMA spectra of the sample before (black trace) and after (red trace) desalting. Nonvolatile salts and other components (3–15 nm) are drastically reduced. The inset shows the shift toward small EM diameter of the AAV8 VLP's peak. (b) AF4 fractogram of the sample with (red trace) or without (blue trace) a buffer exchange procedure. Both nES GEMMA spectra (a) and (b) show reduced signal intensity for the AAV8 VLP's peak due to sample loss during the desalting treatment.

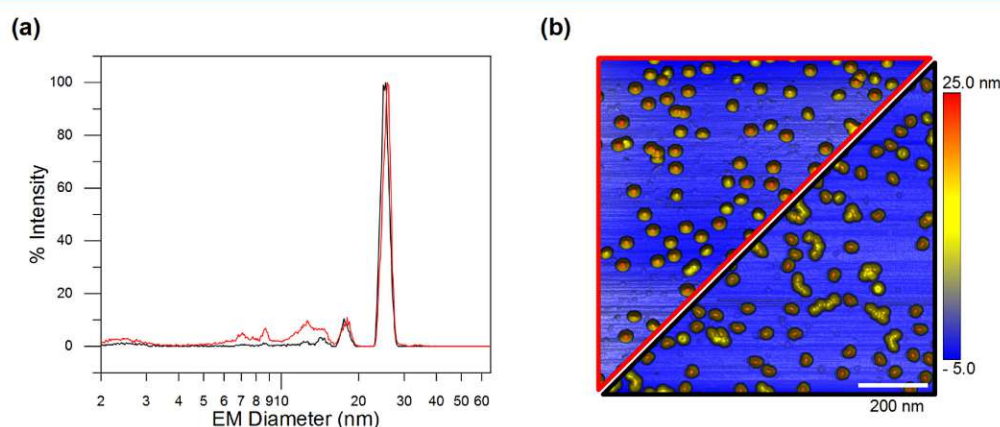


Figure 3. AAV8 VLPs carrying or lacking genomic information. (a) nES GEMMA spectra of empty (black trace) and filled (red trace) AAV8 VLPs. (b) AFM images of empty (right lower black triangle) and filled (left upper red triangle) AAV8 VLPs.

states are separated via AF4. The resulting fractions (representing monomeric, dimeric, and oligomeric bionanoparticles) are collected and later analyzed by nES GEMMA and AFM. Moreover, we also demonstrate the necessity of a volatile electrolyte solution for nES GEMMA. Therefore, frequently, a buffer exchange step is necessary. Hence, we also investigated the sample recovery of this procedure via AF4.

■ BUFFER EXCHANGE AND SAMPLE RECOVERY

Nanoelectrospray gas-phase mobility molecular analyses are based on an electrospray process to transfer analytes from the liquid to the gas phase at atmospheric pressure. Hence, all nonvolatile sample components, e.g., from employed buffer solutions, affect results by generating additional peaks or by forming nonspecific interactions with the intended analyte, i.e., AAV8 VLPs. In the worst case, in terms of gas-phase electrophoresis, other nonvolatile sample components are in a much higher concentration than the analyte in question. Therefore, during the electrospray process, these components are forming nonspecific aggregates, influencing the baseline

and complicating the spectra.³⁵ This effect will be further elaborated in the following paragraph.

The effects of nonvolatile sample components other than the analyte are shown in Figure 2a, where the black profile shows the nES GEMMA signal produced after a 1:100 [v/v] dilution from the stock solution of empty AAV8 VLPs in NH_4OAc . The dominant peak at approximately 9 nm EM diameter is mainly composed of all the components of the original buffer solution and probably in minor part by capsid's fragments generated by degradation of the sample over time and handling of the stock solution. Moreover, nonspecific interactions between the buffer's components and the sample are noticeable by the EM diameter difference between the two profiles of the peak at 25 nm (see the inset). This peak correlates to the AAV8's capsid surface-dry particle diameter. For the VLP sample after simple dilution, an EM diameter of 25.94 nm with an SD of ± 0.03 nm based on the particle number distribution is obtained. In contrast, when the VLP sample is subjected to buffer exchange (red trace), the EM diameter is reduced by about 1 nm (see data below). This behavior can be explained by the presence of salts and other

nonvolatile components that unspecifically attach to the capsid. Hence, the buffer exchange step is a necessary prerequisite for reliable nES GEMMA. Indeed, our buffer exchange procedure removes efficiently original buffer components or other contaminants and retains AAV8 VLPs as dominating nanoparticle species. Nonetheless, lower signal intensity is evident for AAV8 VLP samples after buffer exchange, despite being allegedly diluted to the same concentration. This behavior is a consequence of the buffer exchange step itself. During this procedure, the capsids may unspecifically interact with the centrifugal filter membrane. Alternatively, by depleting the long-term stabilizing components of the original buffer, the capsids may adsorb on the vials' inner surface or form nonspecific ultralarge aggregates. Most likely, the sample's recovery is affected by all of these interactions, which in the end reflects a lower number of VLPs detected.

AF4 analyses further demonstrate that the lower AAV8 peak intensity is indeed due to incomplete analyte recovery during the buffer exchange step. As shown in Figure 2b, the fractrogram of the desalted sample (red profile) produces a lower fluorescent signal when compared with the fractrogram of the diluted sample (from the original stock, blue profile), despite the fact that for both samples, the same amount of analyte was injected (approximately 10 μ g, based on an assumed total recovery of VLPs from the filter membrane after desalting). However, in contrast to nES GEMMA, buffer exchange is not necessary for AF4 since the sample's buffer components do not interfere with the method of separation. On the other hand, no direct size information can instantly be gathered from AF4 analysis. The results from both GEMMA and AF4 techniques allowed us to estimate that the implementation of the buffer exchange step, although critical for nES GEMMA, causes a loss of 40% of the original AAV8 VLP content. The sample composition in terms of VLP monomers and oligomers remains constant (see Figure S1).

■ EMPTY AND FILLED AAV8 VLPs

Subsequently, we expanded our nES GEMMA method for empty AAV8 VLPs to AAV8 VLPs encapsulating genomically engineered ssDNA (filled AAV8 VLPs). Figure 3a shows nES GEMMA of both empty and filled AAV8 VLPs after buffer exchange. Filled capsids (red profile) show a slight but evident shift toward higher EM diameter values of its peak's apex when compared to the empty capsids (black profile). At the same time, the peak width (i.e., at full width half-maximum) of both bionanoparticles remains constant at approximately 2.2 nm. Ideally, since the proteinaceous structure of the capsid is identical as well as the diameter size, both preparations should yield the same EM diameter regardless of the presence or absence of the cargo material.

Differences in surface drying during the nES GEMMA electrospray/charge reduction process at atmospheric pressure might account for the EM diameter difference between empty and filled AAV8 VLPs. Especially for biological samples, the lack of the water solvation layer might destabilize capsids' proteins by leading to a slight shrinking effect of nanoparticles and thus a decrease in EM diameter. The absence or presence of encapsulated ssDNA might enhance or minimize this shrinkage effect accordingly, leading to the observed difference between the two nanoparticle types. In addition, the genome occupancy in the capsid will likely act as a supporting agent, thus providing counter-acting force against shrinking. In detail, nES GEMMA measurements with a statistical

population of over 5000 detected capsids report EM diameters of 25.10 ± 0.18 nm for empty AAV8 VLPs and 25.93 ± 0.07 nm for the filled ones (see Table 1).

Table 1. nES GEMMA and AFM Statistical Analysis of AAV8 VLPs

	empty	filled
nES GEMMA		
total VLP count	5189	5611
average EM diameter (nm)	25.10 ± 0.18	25.93 ± 0.07
AFM		
total VLP count	557	525
average diameter (nm)	30.7 ± 2.4	25.8 ± 2.4
average height (nm)	22.6 ± 1.7	23.2 ± 1.3

Based on the assumption that the ssDNA acts as a scaffold agent for filled capsids, we also investigated via AFM instrumentation if noticeable differences were present between empty and filled AAV8 VLPs. Due to the dry environment conditions during AFM measurements, deformation effects (e.g., shrinking and deflation) should likely happen in the same fashion as we observed in nES GEMMA, especially for empty capsids. The results of this analysis are depicted in Figure 3b (Figure 3b is composed of two separate experiments). On top (i.e., red border triangle), filled AAV8 VLPs are shown, meanwhile empty ones are depicted on the bottom display (i.e., black border triangle).

As reported in Table 1, the statistical analysis on more than 500 capsids via AFM reports that the average diameter for empty capsids is 30.7 ± 2.4 nm, while that for the filled ones is 25.8 ± 2.4 nm. Moreover, average heights are 22.6 ± 1.7 and 23.2 ± 1.3 nm for empty and filled capsids, respectively. Considering that the only difference between the two preparations is the presence (or absence) of a genomic cargo, this further supports the assumption that the encapsulated genome in filled AAV8 VLPs has the effect of making the capsids more firm and less prone to size changes or shape distortions caused by different interactions with the mica surface or by the AFM tip. Empty capsids, in contrast, appear to be flexible and capable of forming numerous interactions with the mica surface, causing the sphere-like shape of the VLP to flatten and deform into an ellipsoid shape.²² In addition, the flattening value f measures the compression of a circle, or a sphere, along a diameter to form an ellipse, or an oblate spheroid, respectively ($f = 0$ for a circle or sphere). This property is determined by the following expression:

$$f = \frac{a - b}{b} \quad (1)$$

where a is the larger dimension (e.g., semimajor axis) and b is the smaller dimension (e.g., semiminor axis). By using the values reported in Table 1, where a is the average diameter and b is the average height, we can calculate that for the filled capsids $f_{\text{filled}} = 0.11$, while for the empty ones $f_{\text{empty}} = 0.36$. Hence, filled VLPs are more spherical than empty VLPs. Therefore, the encapsulated genome is likely to act as an obstacle against capsids' distortion, causing the filled capsids to retain a closer sphere-like structure than their empty counterparts, which is reflected in nES GEMMA data and AFM results alike.

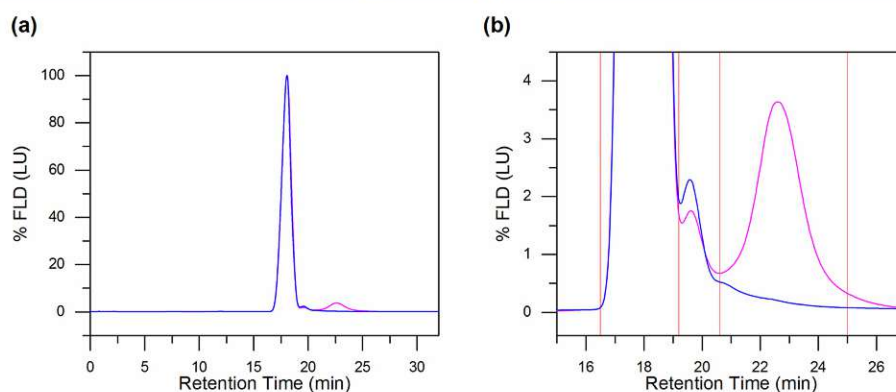


Figure 4. Stressing procedure and fractionation of the sample. (a) AF4 fractogram of control (blue trace) and heat/mechanical-stressed (magenta trace) sample. (b) The red vertical lines mark the collected fractions: 16.5–19.2 min monomer fraction; 19.2–20.6 min dimer and trimer fraction; 20.6–25.0 min higher oligomeric fraction.

■ AF4 FRACTIONATION FOLLOWED BY SUBSEQUENT NES GEMMA AND AFM ANALYSIS

The last aim of this work was to show the strategy outlined in Figure 1b, performing a cross-platform analysis of empty AAV8 VLPs over AF4, nES GEMMA, and AFM, especially under conditions of thermal/mechanical stress exerted on the bionanoparticles. Figure 4a shows the fractogram obtained by AF4, where purified samples, either stressed (i.e., magenta trace) or unstressed (i.e., blue trace), were analyzed. Samples' stress conditions were achieved by means of agitation along with temperature alteration according to the Experimental Section. A magnification of Figure 4a is shown in Figure 4b. Here, it is easier to distinguish the fractogram peaks. The blue trace is composed of two peaks, a dominant one, which has a signal generated by the VLPs' monomer, and a second smaller peak. Although its oligomeric state is not completely resolved, as it will be shown later in this work, this peak is characterized by a high abundance of VLPs' dimers. Last, the magenta trace, besides showing comparable peak shapes as the blue trace, shows an extra peak at a retention time of 23 min. This peak, as it will be shown later, is composed of a heterogeneous mixture of VLPs in a higher oligomeric state. From now on, we will refer to these three peaks as monomer, dimer, and oligomer fractions, accordingly. Moreover, in Figure 4b, the vertical lines mark the time windows for the collection of the respective fractions. Hence, between retention times of 16.5–19.2 min, the monomer fraction was collected; from 19.2 to 20.6 min, the dimer fraction was collected; and last, the oligomer fraction was collected from retention times 20.6–25 min.

After fraction collection, aliquots of each fraction were subsequently analyzed by means of AF4 in order to verify the correct separation and their quality (see Figures S2–S4 in the Supporting Information).

The last step, as shown in Figure 1b, is the analysis of the collected fraction via nES GEMMA and AFM. The results are presented in Figure 5. For both instruments, the operating conditions are reported in the Experimental Section.

For the monomer fraction (retention time 16.5–19.2 min), Figure 5,ba presents nES GEMMA and AFM analyses on the monomer fraction of empty AAV8 VLPs, respectively. The nES GEMMA spectrum shows, as expected, a dominant peak with an EM diameter of 24.82 nm (i.e., label m), which matches the results reported in Table 1 and Figure 3a for both peak's shape

and apex center. In addition, from the AFM measurements, we can observe the presence of solely single nanoparticles, which corroborates our expectation.

For the following fraction (retention time 19.2–20.6 min), the nES GEMMA spectrum, as shown in Figure 5c, reports the presence of two further peaks after the monomer peak. These peaks are reported at EM diameters of 33.03 nm (i.e., label d) and 37.69 nm (i.e., label t), and they likely represent dimeric and trimeric AAV8 VLP nanoobjects, respectively. This interpretation is further validated by the AFM analysis reported in Figure 5d. Here, both monomers and dimers are nicely represented; trimers, as expected, are present to a lower degree, and few unresolved oligomers can also be found. The latter species, in particular, are likely to be responsible for the tailing signal after 40 nm EM diameter in the nES GEMMA spectrum (see Figure 5c). The presence of such species is due to the partial overlap of the oligomer fraction with the dimer fraction during AF4 separation.

For the final fraction (retention time 20.6–25 min), the analysis of this fraction by nES GEMMA (see Figure 5e) shows the signal associated with the residues of monomers, dimers, and trimers (i.e., labels m, d, and t) as dominating peaks in the spectrum. A fourth peak, with an apex center at 41.77 nm, might be associated with a tetrameric nanoobject; this and further oligomeric nanoobjects are sure to be present (i.e., label o in the inset of Figure 5e). However, due to the high heterogeneity of the sample and low abundance, these peaks become too broad and too low to be resolved under the selected device conditions. Moreover, based on the AFM structures visible in Figure 5f of this fraction, it is corroborated that plenty of these oligomeric nanoobjects are either simply out of the employed nES GEMMA instrument sizing settings (e.g., white arrow in Figure 5f, average section diameter 104 nm) or not abundant enough to generate a detectable peak.

Interestingly, in all of the three fractions analyzed by nES GEMMA, the monomer peak is ubiquitous; this could be explained by the fact that some capsids might have formed only weak interaction within the oligomeric nanoobjects; hence aggregation is reversible and the VLPs return in solution as single entities after AF4-based collection or during sample storage.

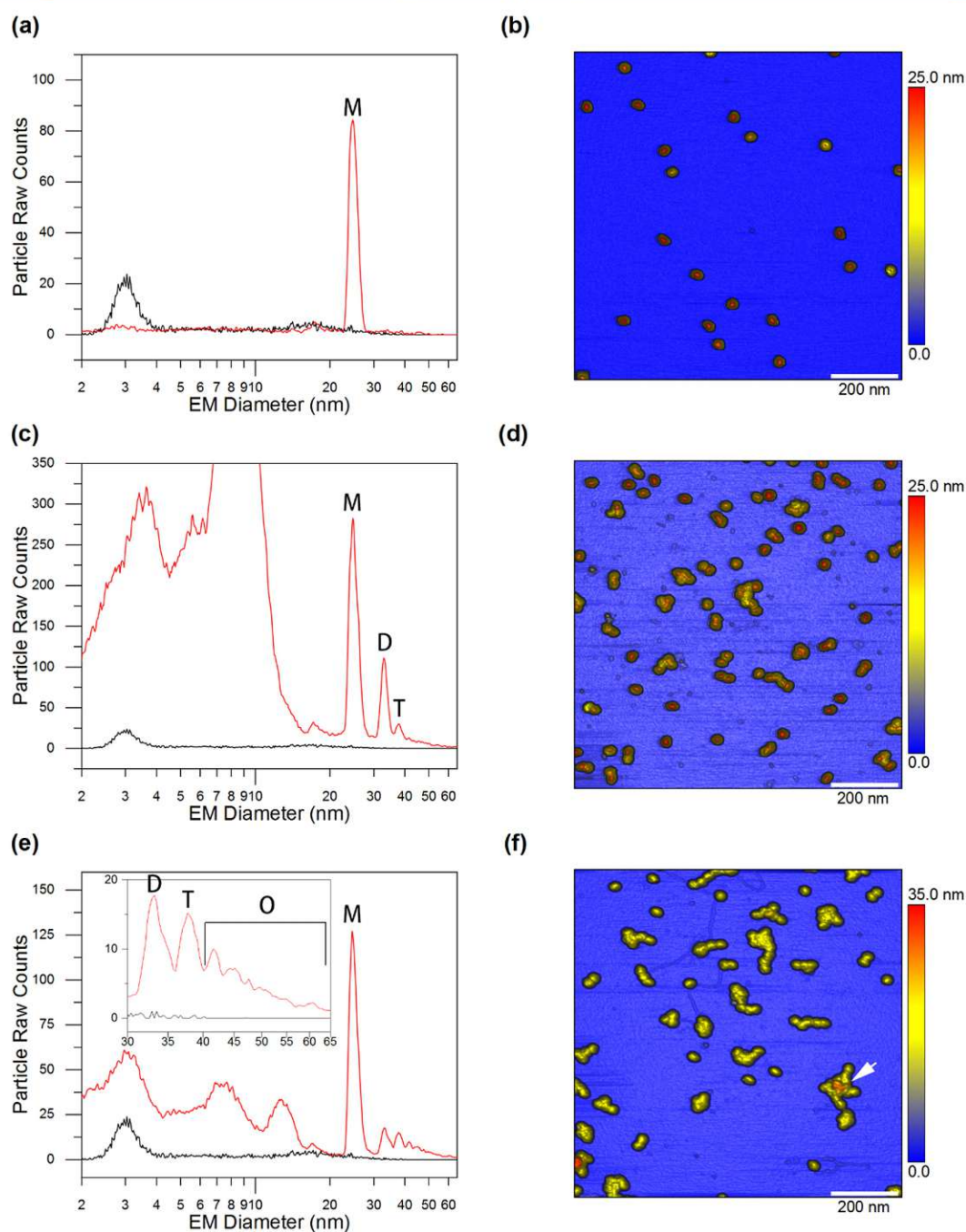


Figure 5. nES GEMMA spectra and AFM images of the three fractions collected with the AF4 technique (see Figure 4b). (a, b) Monomer (M) fraction; (c, d) dimer (D) and trimer (T) fraction; and (e, f) higher oligomeric (O) fraction. nES GEMMA spectra compare signals obtained for VLP-containing samples (red traces) and blanks recorded for a NH_4OAc blank (black traces), respectively. nES GEMMA signals below 20 nm EM diameter putatively correspond to incompletely removed, aggregating AF4 buffer components. In (f), the arrow indicates an AAV8 VLP higher oligomer with a height of 35 nm.

CONCLUDING REMARKS

In this work, we presented a cross-platform analysis of purified AAV8 VLPs, which have been analyzed by three orthogonal techniques, namely, nES GEMMA, AF4, and AFM. Especially

for nES GEMMA, removal of nonvolatile buffer components via buffer exchange is a critical step to ensure accurate measurements and to improve signal reliability. In this respect, nES GEMMA proved to be a valuable and suitable technique

for AAV8 VLP characterization, and it can provide consistent and reproducible sizing data.

The AF4 technique, although in this case not able to fully resolve the oligomeric nanoobjects derived from the heat/mechanic-stressed AAV8 VLP empty preparation, was relatively easy to implement. Especially, its ability to fractionate the three different detected peaks has to be highlighted; the collected fractions were later successfully analyzed by means of nES GEMMA and AFM. Both techniques were able to detect monomeric, dimeric, and oligomeric AAV8 VLP nanoobjects. Moreover, AFM images confirm nES GEMMA findings and also show further larger oligomeric nanoobjects that were not analyzable with nES GEMMA due to the selected conditions focused on analyte resolution.

Moreover, nES GEMMA statistical evaluation over the EM diameter for both empty and filled AAV8 VLPs reveals the impact of the genomic material packed inside the capsid on the overall diameter of the particle. This characteristic is even more noticeable in the statistical analysis obtained by the applied AFM technique. Here, the lack of genomic material in the empty VLPs produces an even higher deformation of the capsids and thus corroborates nES GEMMA findings.

AF4, AFM, and nES GEMMA all proved to be valuable methods for the characterization of VLP and for gathering information in terms of surface-dry bionanoparticle size, sample purity, and VLP aggregation. These results are important to further expand our knowledge about the behavior of these particles during analytical investigations.

■ EXPERIMENTAL SECTION

Chemicals, Electrolyte Solutions, and Buffers. Ammonium acetate (NH_4OAc , $\geq 99.99\%$) and ammonium hydroxide (ACS reagent) were both purchased from Sigma-Aldrich (Steinheim, Germany). The GEMMA electrolyte solution was prepared by dissolving 40 mM ammonium acetate with water of ultrahigh quality (UHQ) delivered by a Simplicity UV apparatus ($18.2 \text{ M}\Omega \times \text{cm}$ at 25°C , Millipore, Billerica, MA, USA). The solution was adjusted to pH 7.0 with ammonium hydroxide and filtered through a surfactant-free cellulose acetate membrane with $0.20 \mu\text{m}$ pore size syringe filters (Sartorius, Göttingen, Germany).

AF4 carrier buffer (PBS) was prepared by dissolving sodium chloride ($\geq 99.5\%$), monopotassium phosphate ($\geq 99.0\%$), potassium chloride ($\geq 99.5\%$, all from Sigma-Aldrich), and disodium phosphate ($\geq 99.5\%$, Merck, Darmstadt, Germany) in UHQ water. The elution buffer additionally included 0.02% (w/v) sodium azide (Merck) as an antimicrobial agent. The pH was adjusted to 7.4 with ammonium hydroxide and filtered through a $0.1 \mu\text{m}$ pore size polyethersulfone membrane filter (VacuCap, Pall, NY, USA).

Sample preparation for AFM measurements required UHQ water and nitrogen gas ($\geq 99.999\%$, Messer Austria GmbH, Gumpoldskirchen Austria) for rinsing and drying.

Samples. Purified AAV8 VLP samples were provided by Baxalta Innovations (Orth/Donau, Austria, part of Takeda). Two different batches were provided: (i) so-called empty AAV8 VLPs ($3776 \mu\text{g}/\text{mL}$, i.e., 7.3×10^{14} capsids/mL), with 93% of capsids not carrying any genomic information, and (ii) so-called filled AAV8 VLPs ($85 \mu\text{g}/\text{mL}$, i.e., 1.6×10^{13} capsids/mL), where 66% of all the capsids were carrying a genomic load. The percentage of capsid filling was assessed via cryo transmission electron microscopy (CryoTEM).

Stressing Conditions. The purified empty and filled AAV8 VLPs preparations, either after the buffer exchange step or directly from the stock, were subjected to a temperature stress of 65°C and to mechanical shear conditions (i.e., 850 rpm agitation) by means of a thermomixer device (Model 22331, Eppendorf, Hamburg, Germany) for a fixed time of 10 min.

Instrumentation. Nanoelectrospray gas-phase mobility molecular analyses were carried out on a TSI Inc instrument (Shoreview, MN, USA), which consisted of a nanoelectrospray charge reduction source unit (model 3480) including a ^{210}Po charge equilibration device, an electrostatic classifier control unit equipped with a nanodifferential mass analyzer (nanoDMA; model 3080), and an *n*-butanol-driven ultrafine condensation particle counter (CPC; model 3025A) for AAV8 VLP detection. For the spraying process, the nES unit is equipped with a 24 cm long polyimide coated fused-silica capillary with an inner diameter of $25 \mu\text{m}$ (Molex, Lincolnshire, IL, USA). The capillary is manually cut and tapered with a homebuilt grinding machine based on the work of Tycova et al.¹⁵

AF4 experiments were performed on an Agilent 1200 system (Agilent Technologies, Santa Clara, CA, USA, auto sampler, pump, and detector), which consisted of an auto sampler, HPLC pumps, an AF4 separation device (Wyatt Technology, Santa Barbara, CA, USA), and a fluorescence detector ($\lambda_{\text{ex/em}} = 280/340 \text{ nm}$). Wyatt Eclipse 3+ A4F (Wyatt Technology, Santa Barbara, CA, USA) was coupled to the system to control the AF4 channel, which was equipped with a 30 kDa molecular weight cutoff cellulose membrane (Superon, Wyatt Technology, Santa Barbara, CA, USA).

AFM experiments of the samples were imaged with a NanoScope III Multimode SPM instrument (Veeco Instruments, Santa Barbara, CA, USA) using silicon cantilevers with integrated silicon tips (NanoWorld, Neuchâtel, Switzerland, Arrow type: NC).

nES GEMMA Operating Conditions. For nanoparticle separation and detection, the filtered air flow on the nES generator was set to $1.6 \times 10^{-5} \text{ m}^3/\text{s}$ (1 liter per minute, Lpm), the CO_2 gas flow to $1.6 \times 10^{-6} \text{ m}^3/\text{s}$ (0.1 Lpm, 99.5% from Messer, Gumpoldskirchen, Austria), and the differential capillary pressure at 27.58 kPa (4 pounds per square inch differential). Capillary conditioning was performed by pre-spraying each sample for at least 3 min before starting the measurement. Capillary rinsing was performed by infusing the electrolyte solution until no signal from the previous sample was detectable. The sample was infused at a flow rate of 70 nL/min. The voltage at the capillary tip was set in order to have a stable Taylor cone (approximately 2 kV voltage and -380 nA current). The electrostatic classifier was set in automatic scanning mode (up scan time 120 s, retrace time 30 s) with a sheath gas flow rate of $2.5 \times 10^{-4} \text{ m}^3/\text{s}$ (15 Lpm), which yielded a standard range of measurable electrophoretic mobility (EM) diameters between 1.95 and 64.9 nm. A total of 10 scans for each sample were used to generate a median spectrum. Mathematical and statistical calculations on the nES GEMMA spectra were made with the software OriginPro 9.1 (OriginLab, Northampton, MA, USA).

nES GEMMA Sample Preparation. Buffer exchange against 40 mM NH_4OAc for nES GEMMA was carried out by means of 10 kDa MWCO centrifugal filters (polyethersulfone membrane from VWR, Vienna, Austria). After three repetitions of spin filtration at 9000g each, the estimated final

concentration for empty AAV8 VLPs was 22 $\mu\text{g}/\text{mL}$, while for filled AAV8 VLPs, it was 8.5 $\mu\text{g}/\text{mL}$.

AF4 Operating Conditions. The AF4 method employed consists of three main steps: sample injection, sample focusing, and elution. The sample was injected for 2 mins at a constant flow rate of 0.2 mL min^{-1} ; this flow was kept constant also during the focusing step. The flow for the focusing step was set to 3.0 mL min^{-1} . The focusing step was prolonged after the sample injection for an additional minute in order to reduce the lateral distribution of the sample itself. Last, the elution was performed with a crossflow decreasing in a linear fashion from 6 to 1 mL min^{-1} during 16 min of analysis. At all times, a baseline crossflow (i.e., detector flow) of 1 mL min^{-1} was present in the AF4 channel.

AF4 Sample Preparation and Fraction Collection. Due to the limited sample concentration and availability of filled AAV8 preparation, AF4 analyses were carried out only with empty AAV8 VLPs. Empty capsids were either simply diluted from the stock solution or treated with the same procedure required for nES GEMMA. From the diluted stock solution, the concentration used was 377 $\mu\text{g}/\text{mL}$, while, after the buffer exchange step, the estimated concentration was 189 $\mu\text{g}/\text{mL}$ (calculated via a calibration curve obtained from stock dilutions, data not shown).

For the aggregation experiment, aliquots from the stock solution were stressed as previously described. Following AF4 separation, a total of seven fractions from each peak-specific oligomeric state were manually collected: 24.5 mL for the monomer fraction, 8.4 mL for the dimer and trimer fraction, and 37.1 mL for the oligomeric fraction. The fractions were accumulated with 10 kDa MWCO centrifugal filters (cellulose membrane, Amicon Ultra-4, Merck Millipore, Darmstadt, Germany), at 9.0×10^3 g ranging from 10 to 20 min. Once all collected fractions were accumulated into a single centrifugal filter, the buffer exchange against 40 mM NH_4OAc was performed twice. As a final step, the same centrifugal filter was used to further concentrate the sample, by setting the centrifuge at 9.0×10^3 g and by periodically checking until the volume of the retentate was at the 100 μL mark of the filter unit.

AFM Operating Conditions. The images were acquired in tapping, constant amplitude mode at a scanning rate of 1.99 Hz, over a scan area of 1 μm^2 .

AFM Sample Preparation. The freshly split mica platelet was first tested by AFM to verify the smoothness and homogeneity of its surface. The sample deposition method involves spotting 10–20 μL of the sample (5–20 $\mu\text{g}/\text{mL}$ solutions) on the platelet's surface at room temperature; to allow adsorption of the analytes, the sample is left resting for 5 min undisturbed before being gently rinsed with UHQ water and successively dried under a soft stream of nitrogen gas (outlet pressure 3.5 bar). Last, the mica platelet is reinserted on the AFM's piezoelectric scanner and it is ready for analysis.

AFM Image Analysis. The AFM images have been analyzed by NanoScope Analysis 1.5 software (Bruker, Santa Barbara, CA, USA) by applying the same approach used elsewhere for AFM characterization of AAV VLPs.³⁶ In particular, the monomeric AAV8 particles' height and diameter have been characterized by selecting all the particles above a defined height (i.e., half of the maximal height of the entire single particle population) and by excluding boundary nanoparticles, small ones (i.e., under 18 nm of diameter),

and aggregates. A demonstration of particle selection is available in Figure S5 in the Supporting Information.

■ ASSOCIATED CONTENT

Supporting Information

The Supporting Information is available free of charge at <https://pubs.acs.org/doi/10.1021/acsomega.1c01443>.

Additional AF4 fractograms acquired to confirm the quality of the collected fractions and example of particle selection for AFM image analysis (PDF)

■ AUTHOR INFORMATION

Corresponding Author

Guenter Allmaier – Institute of Chemical Technologies and Analytics, TU Wien (Vienna University of Technology), Vienna A-1060, Austria; orcid.org/0000-0002-1438-9462; Phone: +43 1 58801 15160; Email: guenter.allmaier@tuwien.ac.at; Fax: +43 1 58801 16199

Authors

Samuele Zoratto – Institute of Chemical Technologies and Analytics, TU Wien (Vienna University of Technology), Vienna A-1060, Austria

Victor U. Weiss – Institute of Chemical Technologies and Analytics, TU Wien (Vienna University of Technology), Vienna A-1060, Austria; orcid.org/0000-0002-0056-6819

Gernot Friedbacher – Institute of Chemical Technologies and Analytics, TU Wien (Vienna University of Technology), Vienna A-1060, Austria

Carsten Buengener – Pharmaceutical Sciences, Baxalta Innovations (part of Takeda), Vienna A-1221, Austria

Robert Pletzenauer – Pharmaceutical Sciences, Baxalta Innovations (part of Takeda), Vienna A-1221, Austria

Alexandra Foettinger-Vacha – Institute of Chemical Technologies and Analytics, TU Wien (Vienna University of Technology), Vienna A-1060, Austria; Present Address: Present address: Boehringer Ingelheim, Vienna, Austria (A.F.-V.).

Michael Graninger – Pharmaceutical Sciences, Baxalta Innovations (part of Takeda), Vienna A-1221, Austria

Complete contact information is available at: <https://pubs.acs.org/doi/10.1021/acsomega.1c01443>

Notes

The authors declare the following competing financial interest(s): Carsten Buengener, Robert Pletzenauer, Alexandra Foettinger-Vacha and Michael Graninger are or were employees of Baxalta Innovations (part of Takeda).

■ ACKNOWLEDGMENTS

We thank Takeda for providing the AAV8 samples, and Carsten Buengener for the access to the AF4 instrumentation and his support during the corresponding analysis. The authors acknowledge TU Wien Bibliothek for financial support through its Open Access Funding Programme.

■ REFERENCES

- (1) Naso, M. F.; Tomkowicz, B.; Perry, W. L., III; Strohl, W. R. Adeno-Associated Virus (AAV) as a Vector for Gene Therapy. *BioDrugs* 2017, 31, 317–334.

- (2) Pierson, E. E.; Keifer, D. Z.; Asokan, A.; Jarrold, M. F. Resolving Adeno-Associated Viral Particle Diversity With Charge Detection Mass Spectrometry. *Anal. Chem.* **2016**, *88*, 6718–6725.
- (3) Colella, P.; Ronzitti, G.; Mingozzi, F. Emerging Issues in AAV-Mediated In Vivo Gene Therapy. *Mol. Ther. Methods Clin. Dev.* **2018**, *8*, 87–104.
- (4) Zincarelli, C.; Soltys, S.; Rengo, G.; Rabinowitz, J. E. Analysis of AAV serotypes 1–9 mediated gene expression and tropism in mice after systemic injection. *Mol. Ther.* **2008**, *16*, 1073–1080.
- (5) Agbandje-McKenna, M.; Kleinschmidt, J. AAV capsid structure and cell interactions. *Methods Mol. Biol.* **2011**, *807*, 47–92.
- (6) Nam, H. J.; Gurda, B. L.; McKenna, R.; Potter, M.; Byrne, B.; Salganik, M.; Muzyczka, N.; Agbandje-McKenna, M. Structural studies of adeno-associated virus serotype 8 capsid transitions associated with endosomal trafficking. *J. Virol.* **2011**, *85*, 11791–11799.
- (7) Horowitz, E. D.; Rahman, K. S.; Bower, B. D.; Dismuke, D. J.; Falvo, M. R.; Griffith, J. D.; Harvey, S. C.; Asokan, A. Biophysical and ultrastructural characterization of adeno-associated virus capsid uncoating and genome release. *J. Virol.* **2013**, *87*, 2994–3002.
- (8) Kaufman, S. L.; Skogen, J. W.; Dorman, F. D.; Zarrin, F.; Lewis, K. C. Macromolecule analysis based on electrophoretic mobility in air: globular proteins. *Anal. Chem.* **1996**, *68*, 1895–1904.
- (9) Bacher, G.; Szymanski, W. W.; Kaufman, S. L.; Zoellner, P.; Blaas, D.; Allmaier, G. Charge-reduced nano electrospray ionization combined with differential mobility analysis of peptides, proteins, glycoproteins, noncovalent protein complexes and viruses. *J. Mass Spectrom.* **2001**, *36*, 1038–1052.
- (10) Laschober, C.; Wruss, J.; Blaas, D.; Szymanski, W. W.; Allmaier, G. Gas-phase electrophoretic molecular mobility analysis of size and stoichiometry of complexes of a common cold virus with antibody and soluble receptor molecules. *Anal. Chem.* **2008**, *80*, 2261–2264.
- (11) Weiss, V. U.; Subirats, X.; Pickl-Herk, A.; Bilek, G.; Winkler, W.; Kumar, M.; Allmaier, G.; Blaas, D.; Kennedler, E. Characterization of rhinovirus subviral A particles via capillary electrophoresis, electron microscopy and gas-phase electrophoretic mobility molecular analysis: Part I. *Electrophoresis* **2012**, *33*, 1833–1841.
- (12) Weiss, V. U.; Subirats, X.; Kumar, M.; Harutyunyan, S.; Gosler, I.; Kowalski, H.; Blaas, D. Capillary electrophoresis, gas-phase electrophoretic mobility molecular analysis, and electron microscopy: effective tools for quality assessment and basic rhinovirus research. *Methods Mol. Biol.* **2015**, *1221*, 101–128.
- (13) Weiss, V. U.; Bereszczak, J. Z.; Havlik, M.; Kallinger, P.; Gosler, I.; Kumar, M.; Blaas, D.; Marchetti-Deschmann, M.; Heck, A. J.; Szymanski, W. W.; Allmaier, G. Analysis of a common cold virus and its subviral particles by gas-phase electrophoretic mobility molecular analysis and native mass spectrometry. *Anal. Chem.* **2015**, *87*, 8709–8717.
- (14) Allmaier, G.; Blaas, D.; Bliem, C.; Dechat, T.; Fedosyuk, S.; Gosler, I.; Kowalski, H.; Weiss, V. U. Monolithic anion-exchange chromatography yields rhinovirus of high purity. *J. Virol. Methods* **2018**, *251*, 15–21.
- (15) Tycova, A.; Prikryl, J.; Foret, F. Reproducible preparation of nanospray tips for capillary electrophoresis coupled to mass spectrometry using 3D printed grinding device. *Electrophoresis* **2016**, *37*, 924–930.
- (16) Fuchs, N. A. On the stationary charge distribution on aerosol particles in a bipolar ionic atmosphere. *Geofis. Pura Appl.* **1963**, *56*, 185–193.
- (17) TSI Incorporated *Model 3025A Ultrafine Condensation Particle Counter Manual*. 2002.
- (18) Agarwal, J. K.; Sem, G. J. Continuous flow, single-particle-counting condensation nucleus counter. *J. Aerosol Sci.* **1980**, *11*, 343–357.
- (19) Weiss, V. U.; Golesne, M.; Friedbacher, G.; Alban, S.; Szymanski, W. W.; Marchetti-Deschmann, M.; Allmaier, G. Size and molecular weight determination of polysaccharides by means of nano electrospray gas-phase electrophoretic mobility molecular analysis (nES GEMMA). *Electrophoresis* **2018**, *39*, 1142–1150.
- (20) Weiss, V. U.; Pogan, R.; Zoratto, S.; Bond, K. M.; Boulanger, P.; Jarrold, M. F.; Lykтей, N.; Pahl, D.; Puffler, N.; Schelhaas, M.; Selivanovitch, E.; Utrecht, C.; Allmaier, G. Virus-like particle size and molecular weight/mass determination applying gas-phase electrophoresis (native nES GEMMA). *Anal. Bioanal. Chem.* **2019**, *411*, 5951–5962.
- (21) Bereszczak, J. Z.; Havlik, M.; Weiss, V. U.; Marchetti-Deschmann, M.; van Duijn, E.; Watts, N. R.; Wingfield, P. T.; Allmaier, G.; Steven, A. C.; Heck, A. J. R. Sizing up large protein complexes by electrospray ionisation-based electrophoretic mobility and native mass spectrometry: morphology selective binding of Fabs to hepatitis B virus capsids. *Anal. Bioanal. Chem.* **2014**, *406*, 1437–1446.
- (22) Havlik, M.; Marchetti-Deschmann, M.; Friedbacher, G.; Winkler, W.; Messner, P.; Perez-Burgos, L.; Tauer, C.; Allmaier, G. Comprehensive size-determination of whole virus vaccine particles using Gas-Phase Electrophoretic Mobility Macromolecular Analyzer, Atomic Force Microscopy, and Transmission Electron Microscopy. *Anal. Chem.* **2015**, *87*, 8657–8664.
- (23) Pease, L. F., III; Lipin, D. I.; Tsai, D.-H.; Zachariah, M. R.; Lua, L. H. L.; Tarlov, M. J.; Middelberg, A. P. J. Quantitative characterization of virus-like particles by Asymmetrical Flow Field Flow Fractionation, Electrospray Differential Mobility Analysis, and Transmission Electron Microscopy. *Biotechnol. Bioeng.* **2009**, *102*, 845–855.
- (24) Litzen, A. Separation speed, retention, and dispersion in asymmetrical flow field-flow fractionation as functions of channel dimensions and flow rates. *Anal. Chem.* **1993**, *65*, 461–470.
- (25) Fraunhofer, W.; Winter, G. The use of asymmetrical flow field-flow fractionation in pharmaceuticals and biopharmaceuticals. *Eur. J. Pharm. Biopharm.* **2004**, *58*, 369–383.
- (26) Eskelin, K.; Lampi, M.; Meier, F.; Moldenhauer, E.; Bamford, D. H.; Oksanen, H. M. Asymmetric flow field flow fractionation methods for virus purification. *J. Chromatogr. A* **2016**, *1469*, 108–119.
- (27) Eskelin, K.; Poranen, M. M.; Oksanen, H. M. Asymmetrical Flow Field-Flow Fractionation on Virus and Virus-Like Particle Applications. *Microorganisms* **2019**, *7*, 555–575.
- (28) Chen, Y.; Zhang, Y.; Zhou, Y.; Luo, J.; Su, Z. Asymmetrical flow field-flow fractionation coupled with multi-angle laser light scattering for stability comparison of virus-like particles in different solution environments. *Vaccine* **2016**, *34*, 3164–3170.
- (29) Citkowitz, A.; Petry, H.; Harkins, R. N.; Ast, O.; Cashion, L.; Goldmann, C.; Bringmann, P.; Plummer, K.; Larsen, B. R. Characterization of virus-like particle assembly for DNA delivery using asymmetrical flow field-flow fractionation and light scattering. *Anal. Biochem.* **2008**, *376*, 163–172.
- (30) Wagner, M.; Holzschuh, S.; Traeger, A.; Fahr, A.; Schubert, U. S. Asymmetric flow field-flow fractionation in the field of nanomedicine. *Anal. Chem.* **2014**, *86*, S201–S210.
- (31) Yohannes, G.; Jussila, M.; Hartonen, K.; Riekkola, M. L. Asymmetrical flow field-flow fractionation technique for separation and characterization of biopolymers and bioparticles. *J. Chromatogr. A* **2011**, *1218*, 4104–4116.
- (32) Kuznetsov, Y. G.; McPherson, A. Atomic Force Microscopy in Imaging of Viruses and Virus-Infected Cells. *Microbiol. Mol. Biol. Rev.* **2011**, *75*, 268–285.
- (33) Baclayon, M.; Wuite, G. J. L.; Roos, W. H. Imaging and manipulation of single viruses by atomic force microscopy. *Soft Matter* **2010**, *6*, 5273–5285.
- (34) Dufrene, Y. F.; Ando, T.; Garcia, R.; Alsteens, D.; Martinez-Martin, D.; Engel, A.; Gerber, C.; Muller, D. J. Imaging modes of atomic force microscopy for application in molecular and cell biology. *Nat. Nanotechnol.* **2017**, *12*, 295–307.
- (35) Weiss, V. U.; Kerul, L.; Kallinger, P.; Szymanski, W. W.; Marchetti-Deschmann, M.; Allmaier, G. Liquid phase separation of proteins based on electrophoretic effects in an electrospray setup during sample introduction into a gas-phase electrophoretic mobility molecular analyzer (CE-GEMMA/CE-ES-DMA). *Anal. Chim. Acta* **2014**, *841*, 91–98.

(36) Bernaud, J.; Rossi, A.; Fis, A.; Gardette, L.; Aillot, L.; Buning, H.; Castelnovo, M.; Salvetti, A.; Faivre-Moskalenko, C. Characterization of AAV vector particle stability at the single-capsid level. *J. Biol. Phys.* **2018**, *44*, 181–194.

Adeno associated virus-like particle characterization via orthogonal methods: nES-DMA, AF4, and AFM

Samuele Zoratto¹, Victor U. Weiss¹, Gernot Friedbacher¹, Carsten Buengener², Robert Pletzenauer², Alexandra Foettinger-Vacha^{2#}, Michael Graninger², Guenter Allmaier^{1,*}

¹ Institute of Chemical Technologies and Analytics, TU Wien (Vienna University of Technology), Vienna, Austria

² Pharmaceutical Sciences, Baxalta Innovations (part of Takeda), Vienna, Austria

Current affiliation: Analytical Development, Böhringer Ingelheim, Vienna, Austria

Keywords: Gene therapy platform, AAV 8, VLP, nES GEMMA, DMA, AF4, AFM.

Correspondence (*): Guenter Allmaier, Institute of Chemical Technologies and Analytics, TU Wien, Getreidemarkt 9/164, A-1060 Vienna, Austria

E-mail: guenter.allmaier@tuwien.ac.at

Tel: +43 1 58801 15160

Fax: +43 1 58801 16199

The supplementary material includes:

- (i) an additional AF4 fractogram (relative plot) demonstrating that the sample composition in terms of AAV8 VLP monomers and oligomers remains constant upon buffer exchange.
- (ii) fractograms of AAV8 VLP monomer, dimer, trimer and higher oligomer fractions.
- (iii) an example of particle selection for AFM image analysis.

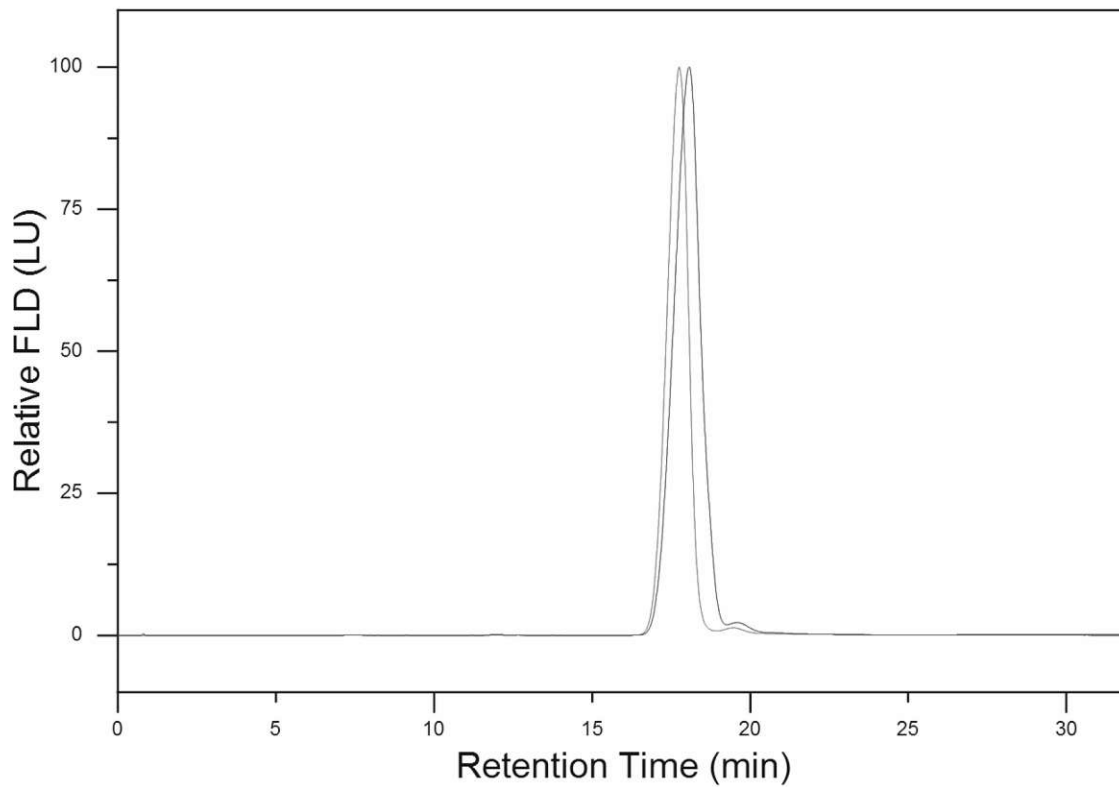


Figure S1. Fractogram overlay of empty AAV8 VLPs either from simple dilution (blue trace) or after buffer exchange step (red trace).

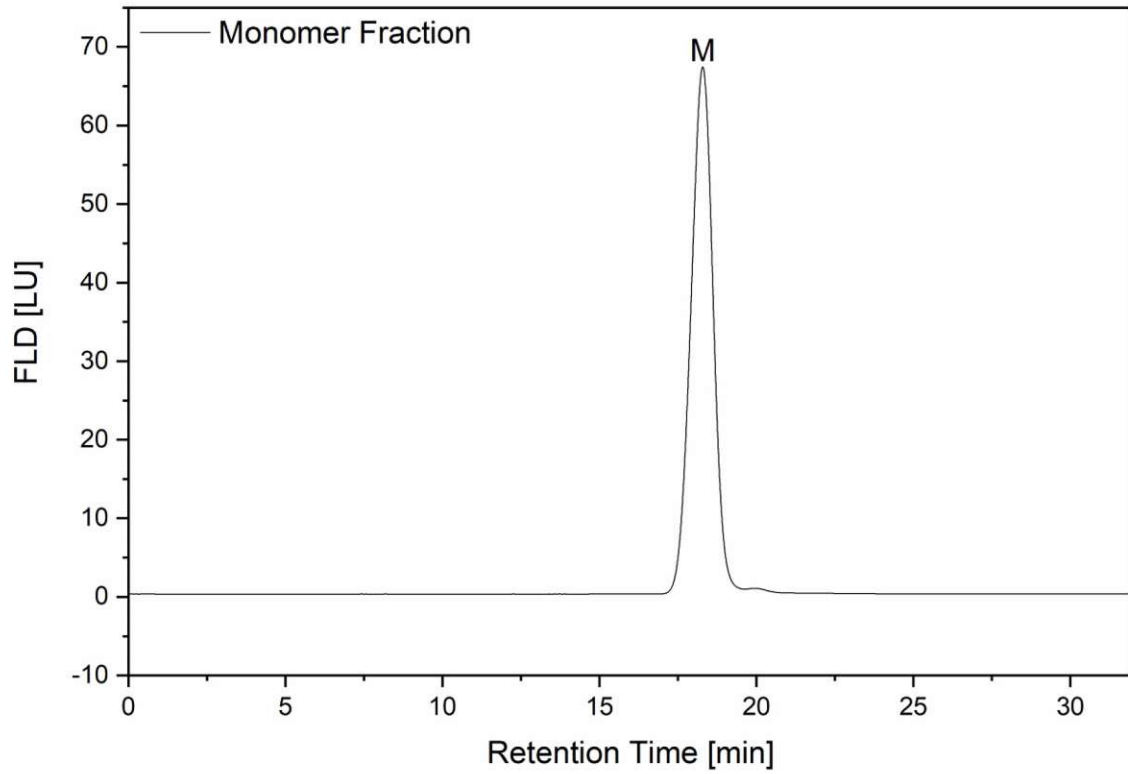


Figure S2. Fractogram of the monomer fraction (empty AAV8 VLPs) after collection and concentration steps (M, monomer).

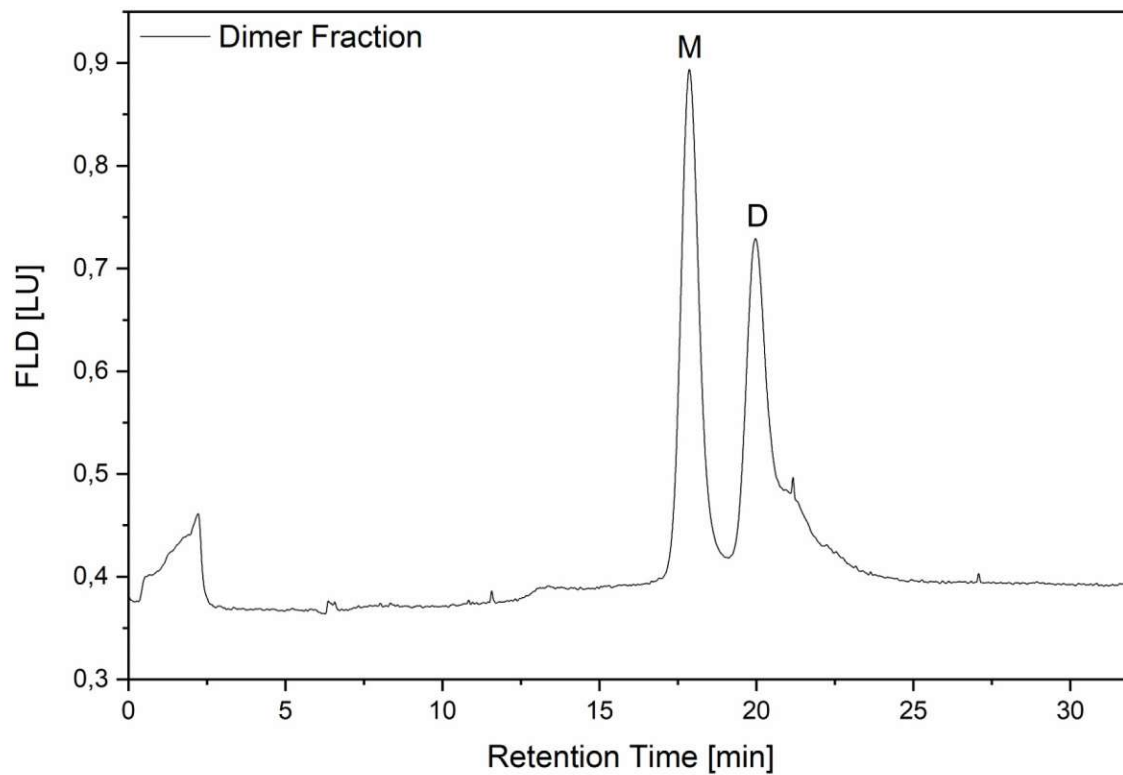


Figure S3. Fractogram of the dimer/trimer fraction (empty AAV8 VLPs) after collection and concentration steps (M, monomer, D, dimer).

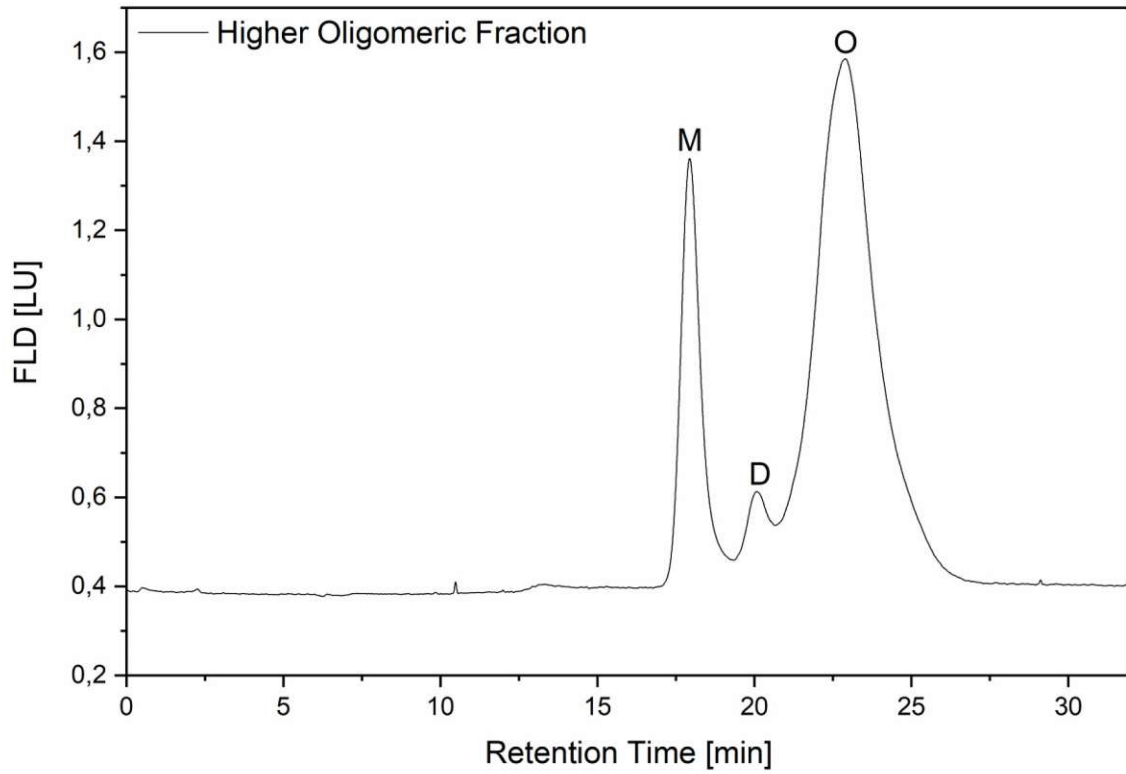


Figure S4. Fractogram of the higher oligomeric fraction (empty AAV8 VLPs) after collection and concentration steps (M, monomer, D, dimer, O, oligomer).

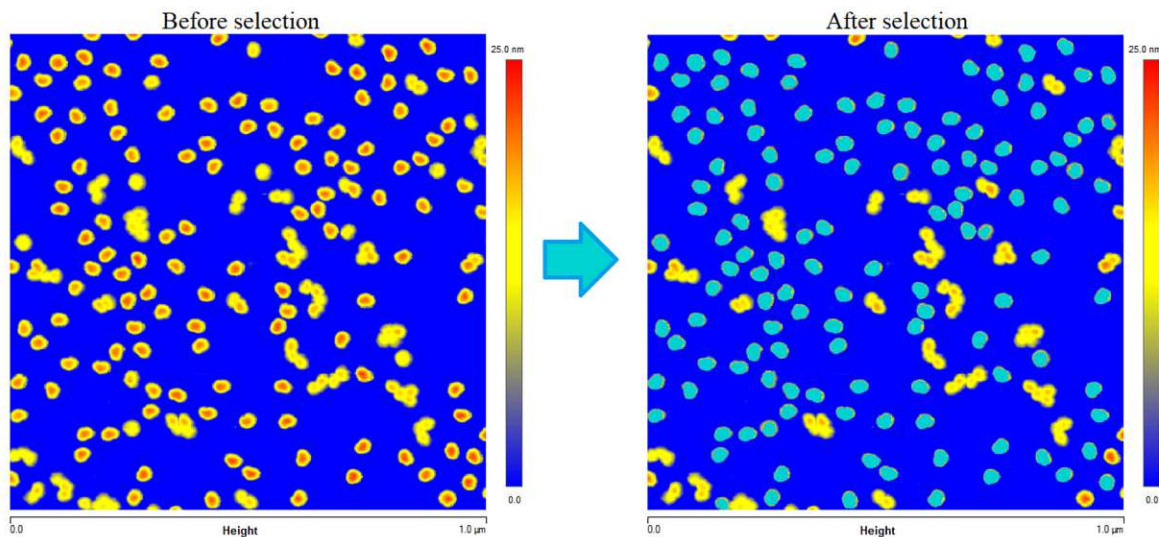


Figure S5. Example of particle selection with NanoScope Analysis 1.5 software. Only particles meeting the criteria described in the materials and methods section (colored in light blue) are used for the statistical analysis.

Molecular Weight Determination of Adeno-Associate Virus serotype 8 Virus-like Particle either carrying or lacking genome via native nES Gas-phase Electrophoretic Molecular Mobility Analysis (GEMMA) and nESI QRTOF Mass Spectrometry

Samuele Zoratto¹, Victor U. Weiss¹, Jerre van der Horst², Jan Commandeur², Carsten Buengener³, Alexandra Foettinger-Vacha³, Robert Pletzenauer³, Michael Graninger³, Guenter Allmaier¹

¹ Institute of Chemical Technologies and Analytics, TU Wien (Vienna University of Technology), Vienna A-1060, Austria

² MS Vision, Almere, The Netherlands

³ Pharmaceutical Sciences, Baxalta Innovations (part of Takeda), Vienna A-1221, Austria

<https://doi.org/10.1002/jms.4786>

In our research, we focused on two preparations of AAV8 VLPs; one with an engineered genome and the other lacking completely the presence of a genomic cargo. We employed two techniques for our investigation, nES GEMMA and native nESI QRTOF MS.

With nES GEMMA – based on existing correlations – we can translate the electrophoretic mobility diameter into an approximate molecular weight. [61, 84] With native MS instead, the molecular weight can be easily determined based on the mass-to-charge ratio of the detected analyte. However, we encountered some challenges while using native MS to analyze such large species, which hindered exact molecular weight determination.

Our research aimed to solve this problem by combining the results of both native nES GEMMA and native ESI QRTOF MS. By doing so, we estimated the molecular weight of the VLPs. We found a molecular weight of 3670 ± 69 kDa and 4751 ± 47 kDa for AAV8 VLPs either lacking or carrying an engineered genome, respectively. Those values correspond perfectly to data calculated from VLP building blocks.

In conclusion, our study demonstrated the potency of combining native nES GEMMA and native nESI QRTOF MS techniques to provide an accurate estimation of molecular weight. Furthermore, it raised doubts about the homogeneity of AAV8 VLP vectors, thereby opening new questions for future research.

INNOVATIVE ASPECTS:

- Successfully combination of nES GEMMA and native nESI QRTOF MS techniques. Combining these two techniques has allowed us to circumvent the limitations of each method and estimate with greater accuracy the molecular weight of the two AAV8 VLPs.
- By using the combined methods, we obtained an estimation of 3670 ± 69 kDa and 4751 ± 47 kDa for the empty and filled AAV8 VLPs, respectively.
- This study has raised important questions about the heterogeneity of AAV8 VLP vectors, which opens new pathways for future research.

OWN CONTRIBUTION

In this work, I

- was involved in planning the experiment,
- conducted the nES GEMMA experiments, evaluated, and interpreted the data.
- assisted native MS experiments at MSVision (Almere, The Netherland), evaluated, and interpreted the data.
- drafted and wrote major parts of the manuscript.
- overall data processing.

RESEARCH ARTICLE

Molecular weight determination of adeno-associate virus serotype 8 virus-like particle either carrying or lacking genome via native nES gas-phase electrophoretic molecular mobility analysis and nESI QRTOF mass spectrometry

Samuele Zoratto¹ | Victor U. Weiss¹ | Jerre van der Horst² | Jan Commandeur² | Carsten Buengener³ | Alexandra Foettinger-Vacha³ | Robert Pletzenauer³ | Michael Graninger³ | Guenter Allmaier¹ 

¹Institute of Chemical Technologies and Analytics, TU Wien (Vienna University of Technology), Vienna, Austria

²MS Vision, Almere, The Netherlands

³Pharmaceutical Sciences, Baxalta Innovations (part of Takeda), Vienna, Austria

Correspondence

Guenter Allmaier, Institute of Chemical Technologies and Analytics, TU Wien (Vienna University of Technology), Getreidemarkt 9, A-1060 Vienna, Austria.
Email: guenter.allmaier@tuwien.ac.at

Funding information

TU Wien University Library

Abstract

Virus-like particles (VLPs) are proteinaceous shells derived from viruses lacking any viral genomic material. Adeno-associated virus (AAV) is a non-enveloped icosahedral virus used as VLP delivery system in gene therapy (GT). Its success as vehicle for GT is due to its selective tropism, high level of transduction, and low immunogenicity. In this study, two preparations of AAV serotype 8 (AAV8) VLPs either carrying or lacking completely genomic cargo (i.e., non-viral ssDNA) have been investigated by means of a native nano-electrospray gas-phase electrophoretic mobility molecular analyzer (GEMMA) (native nES GEMMA) and native nano-electrospray ionization quadrupole reflectron time-of-flight mass spectrometry (MS) (native nESI QRTOF MS). nES GEMMA is based on electrophoretic mobility principles: single-charge nanoparticles (NPs), that is, AAV8 particle, are separated in a laminar sheath flow of dry, particle-free air and a tunable orthogonal electric field. Thus, the electrophoretic mobility diameter (EMD) of a bio-NP (i.e., diameter of globular nano-objects) is obtained at atmospheric pressure, which can be converted into its M_w based on a correlation. First is the native nESI QRTOF MS's goal is to keep the native biological conformation of an analyte during the passage into the vacuum. Subsequently, highly accurate M_w values are obtained from multiple-charged species after deconvolution. However, once applied to the analysis of megadalton species, native MS is challenging and requires customized instrumental modifications not readily available on standard devices. Hence, the analysis of AAV8 VLPs via native MS in our hands did not produce a defined charge state assignment, that is, charge deconvolution for exact M_w determination was not possible. Nonetheless, the method we present is capable to estimate the M_w of VLPs by combining the results from native nES GEMMA and native ESI QRTOF MS. In detail, our findings show a M_w of 3.7 and 5.0 MDa for AAV8 VLPs either lacking or carrying an engineered genome, respectively.

This is an open access article under the terms of the Creative Commons Attribution License, which permits use, distribution and reproduction in any medium, provided the original work is properly cited.

© 2021 The Authors. *Journal of Mass Spectrometry* published by John Wiley & Sons Ltd.

KEYWORDS

AAV, adeno-associated virus, GEMMA, gene therapy platform, native MS

1 | INTRODUCTION

Gene therapy (GT) aims to treat, or cure, a specific disease whose origin is linked to mutation(s) or incorrect expression of a gene.¹ The approach involves delivering an engineered genomic load to add, replace, or interfere with the genetic layout of a cell in question to modify and correct it.² The genomic cargo delivery relies on specific vehicles, which are generally grouped into viral and non-viral vectors based on their origin. Both groups have advantages and limitations; non-viral vectors are usually easier to synthesize and assemble than viral ones but have lower transduction efficiency.³ Instead, viral vectors can efficiently transport their cargo to the target but are often hindered by higher immunogenicity.⁴

In the vector-mediated gene therapy realm, adeno-associated virus (AAV) is the leading vehicle thanks to its high efficiency of transduction and low immunogenicity, as demonstrated by the growing number of clinical trials based on this delivery system.^{5–8}

AAV is a member of the family of *Parvoviridae*, genus *Dependoparvovirus*. It can accommodate up to 4.7 kb of single-stranded DNA (ssDNA) in a non-enveloped, proteinaceous capsid of approximately 26 nm in diameter. According to several sources, a molar ratio of 1:1:10 of the 60 viral proteins VP1, VP2, and VP3 arranged in a T = 1 icosahedral symmetry forms the protein shell.^{4,5,9–11} In nature, the AAV group is composed of 13 natural serotypes, each with a preferred tropism toward a specific tissue, thus making AAV a robust system for the transduction of specific cell types.^{5,12}

In this study, AAV serotype 8 (AAV8) has been used to produce virus-like particles (VLPs). VLPs are proteinaceous “empty” shells derived from viruses, which can be used as vaccine^{13,14} or as viral vector for the delivery of genetic material or other therapeutics,^{15–17} making them a highly adaptable platform.¹⁸ They are non-infectious because the original viral genome is no longer present; instead, engineered genetic material can be encapsulated. In our study, two AAV8 preparations were available for analysis: (i) a so-called “empty” one composed of solely the proteinaceous capsid lacking any genomic cargo and (ii) a so-called “filled” preparation with an encapsulated engineered (non-viral) genome. These two types of preparations were analyzed via native nano-ES (electrospray) gas-phase electrophoretic mobility molecular analysis (nES GEMMA) and with a native nano-ESI (electrospray ionization) quadrupole reflectron time-of-flight mass spectrometry (nES QTOF MS).

The nES GEMMA device, as first described by Kaufman et al.,¹⁹ is a suitable platform for analyzing proteins, viruses, VLPs, liposomes, and several nanoparticles and bionanoparticles, as demonstrated by various studies.^{20–25} The system is also known under the name of differential mobility analyzer (nES DMA), macro ion mobility spectrometer (macroIMS), LiquidScan ES, or scanning mobility particle sizer

(SMPS), all describing the same concept – the size-separation of surface-dry, single-charged (bio-)nanoparticles in the gas-phase at atmospheric pressure.

The nES GEMMA device is composed of three distinct units: (i) The nES source electrospays the analytes dissolved in a volatile electrolyte solution, while charge equilibration for the production of a polydisperse aerosol of single-charged ions is achieved through a bipolar atmosphere generated by a radioactive source (e.g., ²¹⁰Po α -particle emitter),²⁶ a soft X-Ray charger,^{27,28} or an alternating bipolar corona discharge process.²⁹ (ii) A differential mobility analyzer unit, where a laminar sheath flow of particle-free, dried air at atmospheric pressure, and an orthogonal tunable electric field, are used to achieve nanoparticle separation (i.e., gas-phase electrophoresis). The generated monodisperse (monomobile) aerosol is introduced in (iii), a condensation particle counter, where its elements (i.e., the bio-nanoparticles) act as condensation nuclei for droplet formation due to the supersaturated atmosphere of either n-butanol or water. By means of a laser beam, the formed μ m-sized droplets were detected as well as counted after size separation allowing particle-number concentrations to be obtained. It is important to note that particle size determination occurs in the gas-phase at atmospheric pressure. Hence, nES GEMMA yields the surface-dry particle's size diameter (electrophoretic mobility diameter, EMD).^{30,31} Therefore, for AAV8 VLPs, given the approximately spherical shape (i.e., icosahedral) and non-enveloped origin (proteinaceous-only capsid), the detected EMD can be directly correlated to the nanoparticles' diameter. Hence, the obtained EMD can be easily converted with good approximation in a molecular weight value thanks to an EMD/ M_w correlation based on VLPs MS-derived data.^{22,23} This technology's significant advantages are manifested by its simple use, low operating cost, low sample usage, and well-defined results, especially for analytes with a molecular weight (M_w) ranging from kDa to several MDa. Particle size range coverage is defined mainly by the sheath gas flow rate in the DMA, spanning from 1.95 to 64.4 nm for the highest setting (i.e., 15.0 Lpm, liter per minute), or up to 181.1 nm with the lowest one (i.e., 2.5 Lpm) in the applied instrument.²²

Native MS proved to be essential, and capable, for studying non-covalent protein-ligand³² and protein-protein interactions,³³ protein complexes,³⁴ and supramolecular protein structures like viruses^{23,35} and VLPs.^{22,34–36} The main challenge for this MS approach is to desorb/ionize and detect the multiple-charged analytes while preserving their labile non-covalent interactions and structure. Nonetheless, several VLPs have been successfully analyzed by employing commercially available MS instrumentation, such as nESI orbitrap^{37–40} and nESI charge detection mass spectrometry (CDMS).^{41,42} In our case, we employed a Synapt G1 (Waters Manchester, UK) modified by MS Vision (Almere, The Netherlands) to study AAV8 nanoparticles. The instrument is equipped with a nano-electrospray ionization source for

the production of multi-charged bionanoparticles, and with several custom modifications to properly fine-tune the necessary settings (e.g., application of collision and cooling gas, vacuum levels, and voltage settings) for successful analysis.⁴³ Precise M_w determination can be assessed via deconvolution of the charge state assignment of the detected bionanoparticles.

In this manuscript, our focus is to combine native nES GEMMA and native nESI QTOF MS data as well as an EMD/ M_w correlation to expand, with great accuracy, the knowledge about the nanoparticles' size, sample quality, and molecular weight of AAV8 nanoparticles, either carrying or lacking an engineered genomic cargo.

2 | MATERIALS AND METHODS

2.1 | Chemicals, electrolyte solutions, and buffers

Ammonium acetate (NH_4OAc , $\geq 99.99\%$) and ammonium hydroxide (ACS reagent) were both purchased from Sigma-Aldrich (Steinheim, Germany). The nES GEMMA electrolyte solution was prepared by dissolving 40 mM of ammonium acetate with water of ultra-high quality (UHQ) delivered by a Simplicity UV apparatus ($18.2 \text{ M}\Omega \times \text{cm}$ at 25°C , Millipore, Billerica, MA, USA). The solution was adjusted to pH 7.0 with ammonium hydroxide and filtered through a surfactant-free cellulose acetate membrane with $0.20\text{-}\mu\text{m}$ pore size syringe filters (Sartorius, Göttingen, Germany).

2.2 | Samples

HEK (human embryonic kidney) cell produced, purified AAV8 VLP samples were provided by Baxalta Innovations (Orth/Donau, Austria, part of Takeda). Two different batches were provided: (i) so-called "empty" AAV8 VLPs ($3776 \mu\text{g/ml}$, i.e., 7.3×10^{14} capsids/ml) with 93% of capsids not carrying any genomic information and (ii) so-called "filled" AAV8 VLPs ($85 \mu\text{g/ml}$, i.e., 1.6×10^{13} capsids/ml), where 66% of all capsids were carrying the full genomic load (an engineered genome). The percentage of capsid filling was assessed via transmission electron cryomicroscopy (CryoTEM).

For nES GEMMA as well as nESI QTOF MS analysis, a buffer exchange step against 40-mM NH_4OAc was carried out employing 10-kDa MWCO centrifugal filters (polyether sulfone membrane from VWR, Vienna, Austria). After three spin filtration repetitions ($9.0 \times 10^3 \text{ g}$ for 5 min each), the retentate was collected. Based on asymmetric flow field-flow fractionation (AF4 also known as AFFFF) analysis, the estimated final sample concentration for "empty" AAV8 VLPs was $22 \mu\text{g/ml}$, while for "filled" AAV8 VLPs it valued $8.5 \mu\text{g/ml}$.

2.3 | nES GEMMA

nES GEMMA analyses were carried out on a TSI Inc instrument (Shoreview, MN, USA), which consisted of a nano-electrospray unit

with a charge reduction source (model 3480 including a ^{210}Po charge equilibration device), an electrostatic classifier equipped with a nano-differential mass analyzer (nano-DMA; model 3080) and an *n*-butanol driven ultrafine condensation particle counter (CPC; model 3025A) for particle detection. For the spraying process, the nES unit is equipped with a 24 cm long, polyimide coated, fused-silica capillary with an inner diameter of $25 \mu\text{m}$ (Polymicro Technologies, a subsidiary of Molex; Phoenix, AZ, USA). The capillary is manually cut and tapered with a home-built grinding machine based on the work of Tycova et al.⁴⁴

Nanoparticle separation and detection were achieved by using the following settings: The filtered airflow on the nES generator was set to $1.6 \times 10^{-5} \text{ m}^3/\text{s}$ (1 Lpm), the CO_2 gas flow to $1.6 \times 10^{-6} \text{ m}^3/\text{s}$ (0.1 Lpm, 99.5% from Messer, Gumpoldskirchen, Austria) and the differential capillary pressure at 27.58 kPa (four pounds per square inch differential, PSID). Capillary conditioning was performed by pre-spraying each sample for at least 3 min before starting any measurement. Capillary rinsing was performed by infusing the electrolyte solution until no signal from the previous sample was detectable. The sample was infused at a flow rate of approx. 70 nl/min. The capillary tip voltage was set to have a stable Taylor cone (approximately 2-kV voltage resulting in approximately -380-nA current). The electrostatic classifier was set in automatic scanning mode (up scan time for voltage adjustment 120 s, retrace time to initial voltage values 30 s) with a sheath gas flow rate of $2.5 \times 10^{-4} \text{ m}^3/\text{s}$ (15 Lpm), which yielded a range of measurable electrophoretic mobility (EM) diameters between 2 and 65 nm. A total of 10 scans for each sample was used to generate a median spectrum. Mathematical and statistical calculations on the nES GEMMA spectra were made using OriginPro 9.1 (OriginLab, Northampton, MA, USA).

2.4 | nESI QTOF MS

A Synapt G1 (Waters, Manchester, UK) was modified by MS Vision (Almere, The Netherlands) in order to maximize ion transmission for native nESI MS in the kilodalton to megadalton range. This was achieved by (i) increasing the operating pressure of the first vacuum stage (source region) by a manually controlled throttle valve (i.e., 5 to 10 mbar); (ii) fine tuning of the second vacuum stage (transfer pressure region) by fitting a sleeve that restricts pumping of the gas entering from the source region; (iii) installation of a 32 kDa quadrupole mass filter; (iv) amenities to bleed cooling gas like Ar of Xe into the ion mobility stage of the instrument at optimal pressures for cooling and desolvation as well as for independent control of trap and transfer collision cell pressures; (v) customized data acquisition settings (profile binning) and pusher pulse interval (i.e., 128 μs) were adjusted to improve ion detection at ultrahigh mass range. Sample introduction was performed by a nESI source employing manually opened in-house pulled spray capillary. Sample concentration was chosen in order to achieve best results (i.e., avoid clogging of the tip and allow extremely long acquisition time). Spray capillary voltage was set to obtain ideal spraying condition (i.e., ranging between 1 to 2.5 kV). Gas pressures in

the ion source region and in the ion mobility chamber (specifically the TriWave™ cell) before the orthogonal RTOF were finely tuned in order to increase ion transmission. Moreover, a relative high collision induced dissociation voltage (ranging up to 90 V) was applied to increase desolvation and optimize transmission efficiency.^{45,46} The investigated mass range was between m/z 1000 and 40,000 in the positive ion mode. Mass spectra were analyzed using MassLynx (Waters, Manchester, UK) and OriginPro 9.1 (OriginLab, Northampton, MA, USA).

3 | RESULTS AND DISCUSSION

Focusing on the molecular weight determination of (bio-)nanoparticles in general and AAV serotype 8 in particular, we took interest in AAV8 VLPs either carrying or lacking engineered genomic material in their native state as enclosed proteinaceous capsid in the current manuscript. Instrumentation that was already fitted, or modified, for the purpose of studying protein complexes in their native conformation, such as nES GEMMA and nESI QTOF MS was employed. The results obtained from nES GEMMA were correlated with a literature based EMD/ M_w correlation for VLPs and used to aid the interpretation of native MS data.

3.1 | Native nES GEMMA analysis of AAV8 VLPs

Gas-phase electrophoresis of several VLPs—based on bacteriophages, a norovirus serotype, hepatitis B virus, cowpea mosaic virus and a human rhinovirus—yielding surface dry particle EMDs has already been described.^{22,23,42,47} In addition, AAV8 VLPs have likewise been measured via gas-phase electrophoresis as described in a previous work focusing on VLP aggregation (submitted manuscript). Focusing

on the molecular weight of bionanoparticles in the current manuscript, Figure 1A depicts the nES GEMMA spectra of “empty” (blue profile) and “filled” (red profile) AAV8 VLPs in their native state. In order to better appreciate the fine difference between the two preparations, Figure 1B shows the magnification between 22- and 29-nm EMD of Figure 1A. The slight difference in the EMD size is enough to discriminate between the two sample preparations. To confirm this observation, a statistical evaluation over more than 5000 capsids per preparation ($n = 3$ independent nES GEMMA measurements, each) was made. Results show an average EMD of 25.10 ± 0.18 nm and 25.93 ± 0.07 nm for “empty” and “filled” AAV8 VLPs, respectively. The difference in EMD is based on the stabilizing effect promoted by the genomic material inside the capsid of “filled” AAV8 VLPs. Lack of the genomic material as a scaffold in the working environment condition of nES GEMMA causes the partial shriveling of the capsid, hence reducing its EMD.

3.2 | nES GEMMA-based molecular weight determination

The correlation between EMD data, obtained from nES GEMMA measurements, and the M_w of several VLPs or virus particles, either from literature or measured via MS instrumentation, has already been reported.^{22,23} The application of the EMD/ M_w correlations provided in the studies mentioned above is presented in Figure 2. The data produced via nES GEMMA analysis for AAV8 generate M_w of 3670 ± 69 kDa (Figure 2A) and 4751 ± 47 kDa (Figure 2B) for “empty” and “filled” capsids, respectively. A summary of M_w values is presented in Table 1.

The M_w resulting from the EMD/ M_w correlation for the “empty” capsid highly correlates when compared with data based on crystal structural studies⁴⁸ (i.e., 3746 kDa, difference 2.1%) or based on gel

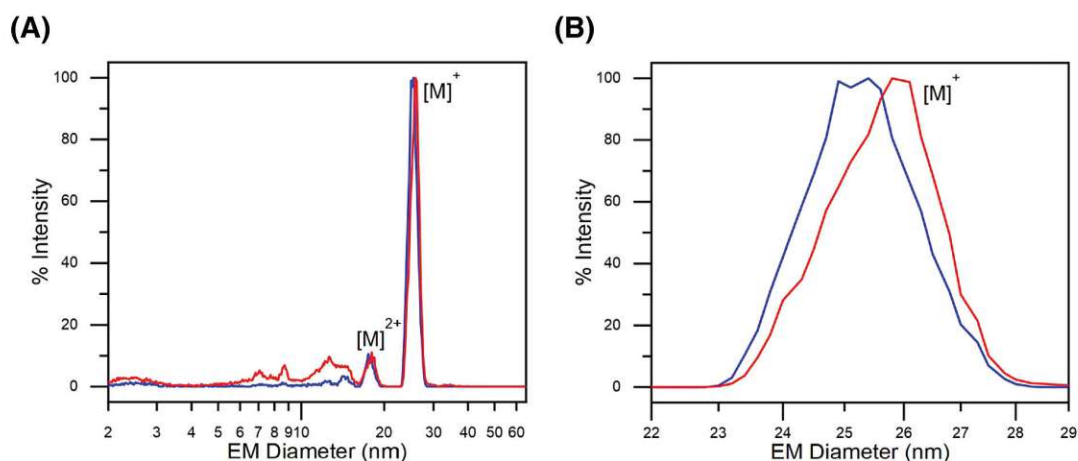


FIGURE 1 Native nano-electrospray gas-phase electrophoretic mobility molecular analyzer (nES GEMMA) analysis of “empty” (blue profile) and “filled” (red profile) AAV8 VLPs. (A) The entire analyzed range is presented. (B) Magnification of the electrophoretic mobility diameter (EMD) range from 22 to 29 nm of panel (A)

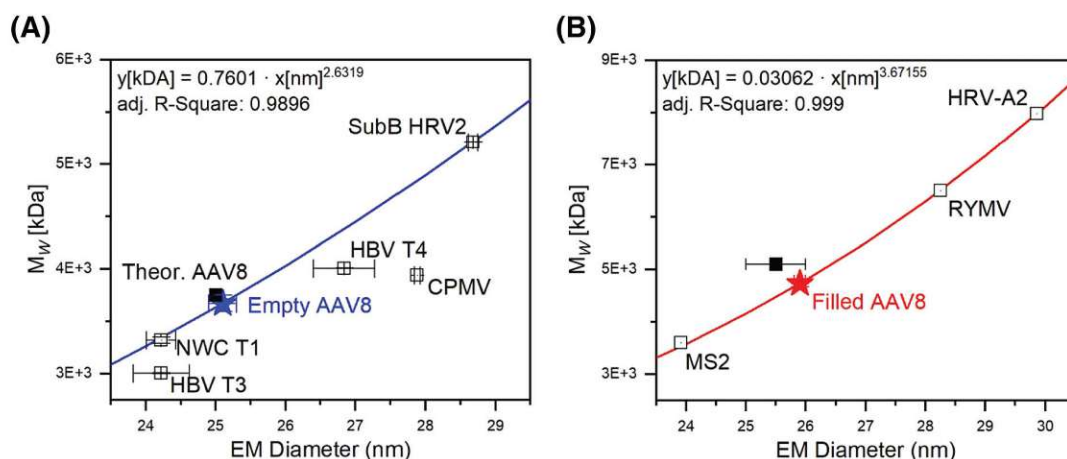


FIGURE 2 Electrophoretic mobility diameter (EMD)/ M_w correlations for (A) “empty” virus-like particles (VLPs) and (B) “filled” VLPs (i.e., intact virus). Readapted with permission from Weiss et al.^{22,23} Legend: NWC T1, Norovirus West Chester T1 VLP; HBV T3, hepatitis B virus T3 VLP; HBV T4, hepatitis B virus T4 VLP; CPMV, cowpea mosaic virus VLP; SubB HRV2, subviral B particle of human rhinovirus 2; MS2, bacteriophage MS2; RYMV, rice yellow mottle virus; HRV-A2, human rhinovirus serotype 2

TABLE 1 Measured size data, theoretical M_w data, derived M_w data and mass spectrometric data of empty and filled AAV8 VLP preparation

Investigative approach:	AAV8 VLP preparations	
	Empty	Filled
nES GEMMA EMD data (nm)	25.10 ± 0.18	25.93 ± 0.07
Theoretical M_w based on 1:1:10 VPs ratio (kDa) ^a	3746	5076
Theoretical M_w based on SDS-PAGE (kDa)	3658	4988
EMD/ M_w correlations (kDa)	3670 ± 69	4751 ± 47
Native MS (kDa) (for $n = 161$ charges)	3710	5005

Abbreviations: EMD, electrophoretic mobility diameter; nES GEMMA, native nano-electrospray gas-phase electrophoretic mobility molecular analyzer; MS, mass spectrometry.

^aBased on the following M_w : VP1 81 kDa; VP2 65 kDa; VP3 60 kDa.⁴⁸

electrophoretic data (i.e., 3658 kDa, difference 0.3%). In both cases, the molecular weight of VP1, VP2, and VP3 is multiplied by the capsid protein ratio; in the first case, with data available in the literature,⁴⁸ while in the second case, the protein ratio is estimated on the basis of SDS-PAGE experiments (data not shown). For the “filled” capsid, the resulting M_w (i.e., 4751 ± 47 kDa) is fitting to a lower degree to the expected value. Precisely, by adding the M_w of the encapsulated genome (i.e., 1330 kDa) to the M_w of the “empty” capsid (3658 kDa), a total molecular weight of 4988 kDa is calculated. This results in a mass difference of 4.75% to the experimental value of 4751 ± 47 kDa as obtained via native nES GEMMA measurements and the application of the corresponding correlation.

3.3 | Native nES QTOF MS analysis of AAV8 VLPs

The analysis of VLPs in their native state is a delicate and laborious job. In this study, megadalton-range species were targeted, which further increased the analytical challenges. The biggest challenge for analyzing such massive species is the passage of desorption/ionization region and transfer into the vacuum part of the mass spectrometer. Parameters like sample concentration, quality and shape of the capillary tip, and the mass spectrometer's pressure in the first two differentially pumped vacuum stages greatly influenced the outcome. The response to each of these settings was rather drastic, to the magnitude where analytes' detection was either successful or not.

In Figure 3A, the positive ion mass spectra of AAV8 VLPs, either “empty” (blue profile) or “filled” (red profile), are shown. The blue profile shows a single dominant peak with an apex center at 23,047 m/z. At the same time, the red profile shows two peaks, a dominant one at 23,205 m/z and a second at 31,092 m/z. Although charge resolution was not achieved and hence no molecular weight determination based on peak charge assignment was possible, it is highly plausible that the detected peaks belong to “empty” (label e) and “filled” (label f) AAV8 VLPs. Further support comes from the presence of a shared peak between the two preparations (i.e., label e, Figure 3B) because the “filled” AAV8 VLPs preparation contains at least 33% of AAV8 VLPs lacking genomic cargo.

Consequently, the peak labeled f, detected only in the “filled” AAV8 preparation (Figure 3C) represents the portion of capsids carrying the genomic cargo. Moreover, although the concentration of “filled” capsids in the sample exceeds “empty” ones' concentration, this is not reflected in the mass spectra. This discrepancy can be explained by a lower transmission efficiency due to the increased

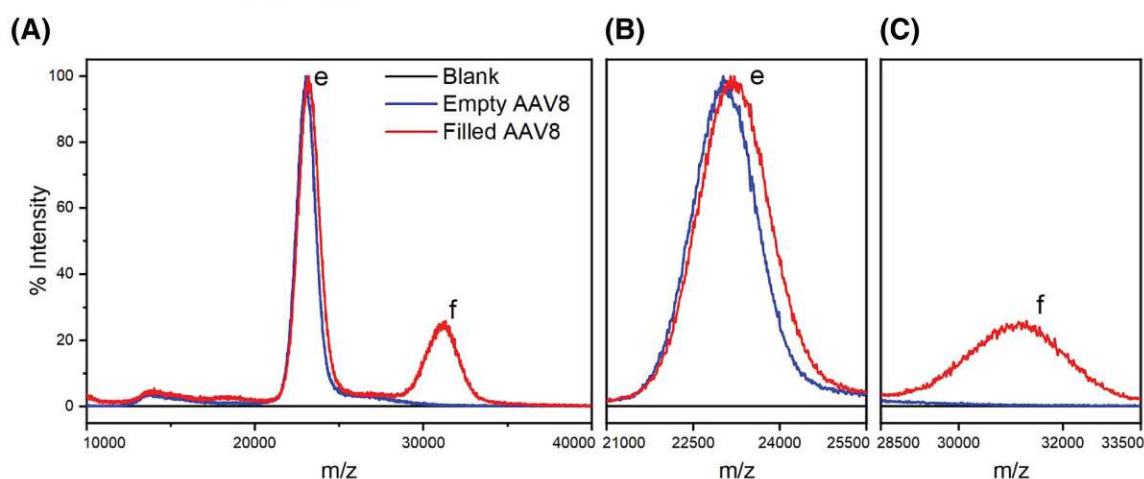


FIGURE 3 Native positive ion mass spectra of “empty” (blue profile) and “filled” (red profile) AAV8 VLPs. The “empty” VLPs preparation shows a dominant peak *e* assigned to monomeric “empty” capsids. The “filled” VLPs preparation contains the shared peak *e* and a second peak *f* assigned to “filled” capsids. The figure comprises (A) the entire *m/z* range and the magnification of the range for (B) peak *e* and (C) peak *f*

mass of the analytes for “filled” VLPs, and/or by an uneven desorption/ionization response between the two VLP species. Lastly, as already mentioned, the lack of charge resolution does not allow to calculate the precise molecular weight of either capsids' preparations. Besides the high amount of resolving power required to obtain charge distribution accurately, it is highly plausible that capsid heterogeneity plays a role in this matter, as already investigated by Snijder et al.³⁹ To overcome this issue, a method that relies on the results generated by nES GEMMA and literature-based EMD/ M_w correlations is proposed to estimate the charges enveloping the capsids.

3.4 | Combining native nES GEMMA and native nESI QTOF MS data for M_w determination of AAV8 VLPs

For the native MS analysis, as already pointed out, charge resolution was not achieved. Therefore, to estimate the M_w of the detected analytes, the following method is proposed: Because the encapsulated genome's size is known and based on the capsids' weight obtained from the EMD/ M_w correlations mentioned earlier, an accurate estimation of the number of charges enveloping the capsids can be made. Therefore, based on (i) the assumption that the apex center of peak *e* (i.e., 23,047 *m/z*) in Figure 3A,B is generated only by “empty” monomeric VLP species, and (ii) given the M_w of 3670 ± 69 kDa obtained from nES GEMMA data as described before is valid, only ions with a number of positive charges ranging from 157 to 162 would generate analytes whose M_w could fit the EMD/ M_w correlation. Consequently, the peak *e* yields a M_w of 3676 ± 58 kDa as an average of calculated values for all charge numbers between 157 and 162 positive charges.

Because the genome encapsulated in the proteinaceous capsid is shielded from the external environment, we suppose that it does not affect the number of charges enveloping the capsid but only its molecular weight. To support this claim, the same range of positive charges assigned to peak *e*, have been applied to peak *f* (i.e. 31,092-*m/z*, Figure 3C). Thus, a M_w of 4959 ± 78 kDa is obtained. As a result, this calculation highly correlates with the molecular weight for “filled” VLPs obtained from the EMD/ M_w correlation (i.e., 4751 ± 47 kDa, difference 4.4%) or from the expected theoretical M_w mentioned before (i.e., 4988 kDa, difference 0.6%). Moreover, because the molecular weight of the encapsulated genome is known, its size can be used to narrow down the range of possible charges of the capsid by comparing the difference in weight between “filled” and “empty” VLPs. As a result, a total of 161 positive charges, for both “empty” and “filled” VLPs, is the value that produces the lowest difference to the genome's molecular weight (i.e., 0.4%).

4 | CONCLUDING REMARKS

In this study, nES GEMMA and native MS spectrometry were applied to analyze and characterize AAV8 VLPs either lacking or carrying a non-viral engineered genomic cargo. The nES GEMMA instrumentation can determine the dry-surface diameter of particles in the nanometer range. This makes nES GEMMA an ideal device for the characterization of nanoparticles and bionanoparticles, for instance, VLPs. Native MS aims to preserve non-covalent interaction, allowing the characterization of proteinaceous complexes such as viral capsids like the one presented in this study. Both techniques do present some limitations; nES GEMMA cannot directly determine the exact

molecular weight of the detected AAV8 nanoparticles but only infer it from EMD/ M_w correlations based on other data (e.g., SDS-PAGE or MS of the individual capsid proteins). Native MS instead generates mass-over-charge results but suffers from low ion transmission efficiency at very high molecular weight and deconvolution challenges.

The EMD obtained from native nES GEMMA analysis results in 25.10 ± 0.18 nm and 25.93 ± 0.07 nm for “empty” and “filled” AAV8 VLPs, respectively. Based on EMD/ M_w correlations, these results directly translate to the molecular weights of 3670 ± 69 kDa and $4,751 \pm 47$ kDa for “empty” and “filled” capsids, respectively.

Although native nESI QRTOF MS was successful for detecting both types of capsid preparations, but charge resolution for exact molecular weight determination was not achieved. To overcome this issue, the data inferred by the EMD/ M_w correlations and the size of the encapsulated genome were used to estimate with high accuracy the number of charges enveloping the capsids, thus deriving the molecular weight of both “empty” and “filled” VLPs. The genomic cargo, since encapsulated in, and protected by, the proteinaceous capsid, is expected to influence solely the overall molecular weight and not the number of charges surrounding the capsid. Therefore, based on the proposed methodology, the detected peaks' apexes are estimated to carry 161 charges, resulting in a M_w of 3710 kDa (1.1% difference from the EMD/ M_w correlation based value) and 5005 kDa (5.4% difference from the EMD/ M_w correlation based value) for “empty” and “filled” VLPs, respectively. These findings corroborate the expected values derived from theoretical calculation and nES GEMMA EMD/ M_w correlations, thus further consolidating the fidelity of EMD/ M_w correlations. Based on our findings, we were able to demonstrate that the combination of native nES GEMMA and native nESI QRTOF MS is very powerful, enabling the in-depth interpretation of data derived from each of these two analysis methods alone to a much higher level of detail (refer to Table 1 for an overview on obtained values).

Noteworthy, SDS-PAGE analysis aimed to determine the viral protein's ratio provided by the manufacturing company of the AAV8 VLPs (data not shown) as well as from the work of Snijder et al.,³⁹ indicate that the VP's ratio is different from the ratio largely listed in the literature, thus indicating that AAV8 VLP vectors are not strictly constrained to the 1:1:10 VPs ratio. This protein ratio heterogeneity might influence, for example, host cell infection and affecting accurate charge detection for molecular weight determination. It is undeniable that further studies to unveil more details about these viral vectors are required, especially as instrumentation (e.g., high-resolution DMAs) and methods for native MS (e.g., CDMS) at high Mw species advance.

ACKNOWLEDGEMENTS

The authors acknowledge TU Wien University Library for financial support through its Open Access Funding Programme. Furthermore we thank Takeda for supporting this investigation.

DATA AVAILABILITY STATEMENT

No additional data are available.

ORCID

Guenter Allmaier  <https://orcid.org/0000-0002-1438-9462>

REFERENCES

- High KA, Roncarolo MG. Gene therapy. *N Engl J Med*. 2019;381(5):455-464.
- Ma CC, Wang ZL, Xu T, He ZY, Wei YQ. The approved gene therapy drugs worldwide: from 1998 to 2019. *Biotechnol Adv*. 2020;40:107502.
- Yin H, Kanasty RL, Eltoukhy AA, Vegas AJ, Dorkin JR, Anderson DG. Non-viral vectors for gene-based therapy. *Nat Rev Genet*. 2014;15(8):541-555.
- Naso MF, Tomkowicz B, Perry WL 3rd, Strohl WR. Adeno-associated virus (AAV) as a vector for gene therapy. *BioDrugs*. 2017;31(4):317-334.
- Wang D, Tai PWL, Gao G. Adeno-associated virus vector as a platform for gene therapy delivery. *Nat Rev Drug Discov*. 2019;18(5):358-378.
- Kotterman MA, Schaffer DV. Engineering adeno-associated viruses for clinical gene therapy. *Nat Rev Genet*. 2014;15(7):445-451.
- Kotterman MA, Chalberg TW, Schaffer DV. Viral vectors for gene therapy: translational and clinical outlook. *Annu Rev Biomed Eng*. 2015;17(1):63-89.
- Li C, Samulski RJ. Engineering adeno-associated virus vectors for gene therapy. *Nat Rev Genet*. 2020;21(4):255-272.
- Naumer M, Sonntag F, Schmidt K, et al. Properties of the adeno-associated virus assembly-activating protein. *J Virol*. 2012;86(23):13038-13048.
- Xie Q, Bu W, Bhatia S, et al. The atomic structure of adeno-associated virus (AAV-2), a vector for human gene therapy. *Proc Natl Acad Sci U S A*. 2002;99(16):10405-10410.
- Nam HJ, Lane MD, Padron E, et al. Structure of adeno-associated virus serotype 8, a gene therapy vector. *J Virol*. 2007;81(22):12260-12271.
- Westhaus A, Cabanes-Creus M, Rybicki A, et al. High-throughput in vitro, ex vivo, and in vivo screen of adeno-associated virus vectors based on physical and functional transduction. *Hum Gene Ther*. 2020;31(9-10):575-589.
- Mohsen MO, Zha L, Cabral-Miranda G, Bachmann MF. Major findings and recent advances in virus-like particle (VLP)-based vaccines. *Semin Immunol*. 2017;34:123-132.
- Zhao L, Seth A, Wibowo N, et al. Nanoparticle vaccines. *Vaccine*. 2014;32(3):327-337.
- Ma Y, Nolte RJ, Cornelissen JJ. Virus-based nanocarriers for drug delivery. *Adv Drug Deliv Rev*. 2012;64(9):811-825.
- Pan Y, Zhang Y, Jia T, Zhang K, Li J, Wang L. Development of a micro-RNA delivery system based on bacteriophage MS2 virus-like particles. *FEBS J*. 2012;279(7):1198-1208.
- Takamura S, Niikura M, Li TC, et al. DNA vaccine-encapsulated virus-like particles derived from an orally transmissible virus stimulate mucosal and systemic immune responses by oral administration. *Gene Ther*. 2004;11(7):628-635.
- Yu M, Wu J, Shi J, Farokhzad OC. Nanotechnology for protein delivery: overview and perspectives. *J Control Release*. 2016;240:24-37.
- Kaufman SL, Skogen JW, Dorman FD, Zarrin F, Lewis KC. Macromolecule analysis based on electrophoretic mobility in air: globular proteins. *Anal Chem*. 1996;68(11):1895-1904.
- Kapellios EA, Karamanou S, Sardis MF, Aivaliotis M, Economou A, Pergantis SA. Using nano-electrospray ion mobility spectrometry (GEMMA) to determine the size and relative molecular mass of proteins and protein assemblies: a comparison with MALLS and QELS. *Anal Bioanal Chem*. 2011;399(7):2421-2433.
- Urey C, Weiss VU, Gondikas A, et al. Combining gas-phase electrophoretic mobility molecular analysis (GEMMA), light scattering, field

- flow fractionation and cryo electron microscopy in a multidimensional approach to characterize liposomal carrier vesicles. *Int J Pharm.* 2016; 513(1-2):309-318.
22. Weiss VU, Pogan R, Zoratto S, et al. Virus-like particle size and molecular weight/mass determination applying gas-phase electrophoresis (native nES GEMMA). *Anal Bioanal Chem.* 2019;411(23): 5951-5962.
 23. Weiss VU, Bereszczak JZ, Havlik M, et al. Analysis of a common cold virus and its subviral particles by gas-phase electrophoretic mobility molecular analysis and native mass spectrometry. *Anal Chem.* 2015; 87(17):8709-8717.
 24. Weiss VU, Wieland K, Schwaighofer A, Lendl B, Allmaier G. Native nano-electrospray differential mobility analyzer (nES GEMMA) enables size selection of liposomal nanocarriers combined with subsequent direct spectroscopic analysis. *Anal Chem.* 2019;91(6): 3860-3868.
 25. Bacher G, Szymanski WW, Kaufman SL, Zollner P, Blaas D, Allmaier G. Charge-reduced nano electrospray ionization combined with differential mobility analysis of peptides, proteins, glycoproteins, noncovalent protein complexes and viruses. *J Mass Spectrom.* 2001; 36(9):1038-1052.
 26. Adachi M, Okuyama K, Kousaka Y. Electrical neutralization of charged aerosol-particles by bipolar ions. *J Chem Eng Japan.* 1983;16(3): 229-235.
 27. Kallinger P, Szymanski WW. Experimental determination of the steady-state charging probabilities and particle size conservation in non-radioactive and radioactive bipolar aerosol chargers in the size range of 5–40nm. *J Nanopart Res.* 2015;17(4):171-182.
 28. Shimada M, Han BW, Okuyama K, Otani Y. Bipolar charging of aerosol nanoparticles by a soft X-ray photoionizer. *J Chem Eng Japan.* 2002;35(8):786-793.
 29. Weiss VU, Frank J, Piplits K, Szymanski WW, Allmaier G. Bipolar corona discharge-based charge equilibration for nano electrospray gas-phase electrophoretic mobility molecular analysis of bio- and polymer nanoparticles. *Anal Chem.* 2020;92(13):8665-8669.
 30. Flagan RC. Differential mobility analysis of aerosols: a tutorial. *KONA Powder Part J.* 2008;26(0):254-268.
 31. Guha S, Li M, Tarlov MJ, Zachariah MR. Electrospray-differential mobility analysis of bionanoparticles. *Trends Biotechnol.* 2012;30(5): 291-300.
 32. Laganowsky A, Reading E, Allison TM, et al. Membrane proteins bind lipids selectively to modulate their structure and function. *Nature.* 2014;510(7503):172-175.
 33. Rostom AA, Fucini P, Benjamin DR, et al. Detection and selective dissociation of intact ribosomes in a mass spectrometer. *Proc Natl Acad Sci U S A.* 2000;97(10):5185-5190.
 34. Uetrecht C, Rose RJ, van Duijn E, Lorenzen K, Heck AJ. Ion mobility mass spectrometry of proteins and protein assemblies. *Chem Soc Rev.* 2010;39(5):1633-1655.
 35. Uetrecht C, Barbu IM, Shoemaker GK, van Duijn E, Heck AJ. Interrogating viral capsid assembly with ion mobility-mass spectrometry. *Nat Chem.* 2011;3(2):126-132.
 36. Leney AC, Heck AJ. Native mass spectrometry: what is in the name? *J Am Soc Mass Spectrom.* 2017;28(1):5-13.
 37. Fort KL, van de Waterbeemd M, Boll D, et al. Expanding the structural analysis capabilities on an Orbitrap-based mass spectrometer for large macromolecular complexes. *Analyst.* 2017;143(1):100-105.
 38. van de Waterbeemd M, Snijder J, Tsvetkova IB, Dragnea BG, Cornelissen JJ, Heck AJ. Examining the heterogeneous genome content of multipartite viruses BMV and CCMV by native mass spectrometry. *J Am Soc Mass Spectrom.* 2016;27(6):1000-1009.
 39. Snijder J, van de Waterbeemd M, Damoc E, et al. Defining the stoichiometry and cargo load of viral and bacterial nanoparticles by Orbitrap mass spectrometry. *J Am Chem Soc.* 2014;136(20):7295-7299.
 40. Worner TP, Bennett A, Habka S, et al. Adeno-associated virus capsid assembly is divergent and stochastic. *Nat Commun.* 2021;12(1):1642.
 41. Pierson EE, Keifer DZ, Asokan A, Jarrold MF. Resolving adeno-associated viral particle diversity with charge detection mass spectrometry. *Anal Chem.* 2016;88(13):6718-6725.
 42. Pogan R, Weiss VU, Bond K, et al. N-terminal VP1 truncations favor T = 1 norovirus-like particles. *Vaccine.* 2021;9:8-24.
 43. van den Heuvel RH, van Duijn E, Mazon H, et al. Improving the performance of a quadrupole time-of-flight instrument for macromolecular mass spectrometry. *Anal Chem.* 2006;78(21):7473-7483.
 44. Tycova A, Prikryl J, Foret F. Reproducible preparation of nanospray tips for capillary electrophoresis coupled to mass spectrometry using 3D printed grinding device. *Electrophoresis.* 2016;37(7-8):924-930.
 45. Krutchinsky AN, Chernushevich IV, Spicer VL, Ens W, Standing KG. Collisional damping interface for an electrospray ionization time-of-flight mass spectrometer. *J Am Soc Mass Spectrom.* 1998;9(6): 569-579.
 46. Sobott F, Hernandez H, McCammon MG, Tito MA, Robinson CV. A tandem mass spectrometer for improved transmission and analysis of large macromolecular assemblies. *Anal Chem.* 2002;74(6):1402-1407.
 47. Havlik M, Marchetti-Deschmann M, Friedbacher G, et al. Comprehensive size-determination of whole virus vaccine particles using gas-phase electrophoretic mobility macromolecular analyzer, atomic force microscopy, and transmission electron microscopy. *Anal Chem.* 2015; 87(17):8657-8664.
 48. Nam HJ, Gurda BL, McKenna R, et al. Structural studies of adeno-associated virus serotype 8 capsid transitions associated with endosomal trafficking. *J Virol.* 2011;85(22):11791-11799.

How to cite this article: Zoratto S, Weiss VU, van der Horst J, et al. Molecular weight determination of adeno-associate virus serotype 8 virus-like particle either carrying or lacking genome via native nES gas-phase electrophoretic molecular mobility analysis and nESI QTOF mass spectrometry. *J Mass Spectrom.* 2021;56(11):e4786. doi:10.1002/jms.4786

Viruses (2023), 15(6), 1361;

Adeno-Associated Virus-like Particles' Response to pH Changes as Revealed by nES-DMA

Samuele Zoratto¹, Thomas Heuser², Gernot Friedbacher¹, Robert Pletzenauer³, Michael Graninger³,
Martina Marchetti-Deschmann¹, and Victor U. Weiss¹

¹ Institute of Chemical Technologies and Analytics, TU Wien (Vienna University of Technology), Vienna A-1060, Austria

² Electron Microscopy Facility, Vienna BioCenter Core Facilities GmbH, A-1030 Vienna, Austria;

³ Pharmaceutical Sciences, Baxalta Innovations (part of Takeda), Vienna A-1221, Austria

<https://doi.org/10.3390/v15061361>

In this study, we focused on exploring the behavior of AAV8 VLPs under varying pH conditions, employing nES GEMMA as our primary analytical technique. We investigated two types of AAV8 VLPs: one lacking any genomic cargo (empty VLPs) and the other carrying an engineered genome (filled VLPs).

Our research revealed distinctive traits in these preparations. Filled VLPs showed slight size variance across different pH levels, although their detection efficiency was hindered in acidic conditions. Contrarily, empty VLPs exhibited great pH-dependent size variation but their detection remained unaffected by changes in pH. These differences between filled and empty VLPs were further investigated through AFM and cryo-TEM.

AFM provided critical insights into the behavior of filled VLPs under acidic pH, showing the formation of heterogeneous aggregates. This phenomenon was challenging for nES GEMMA to detect due to the size and heterogeneity of these clusters. In contrast, cryo-TEM, revealed that different pH levels did not affect the diameter of empty VLPs or the aggregation behavior for filled ones. This discrepancy

implies that the dry analytical environments of nES GEMMA and AFM might influence the observed changes.

Putatively, nES GEMMA's solvent-free environment could cause structural stress in empty VLPs, leading to collapse, while filled VLPs remain stable due to their genomic content. Cryo-TEM, maintaining capsids in native-like conditions, does not exhibit this effect.

In conclusion, our study offers new insights into VLP behavior under different pH conditions, contributing valuable knowledge to both scientific and biopharmaceutical fields. These findings have potential applications in monitoring drug production phases and emphasize the importance of employing diverse analytical approaches in bio-nanoparticle research.

INNOVATIVE ASPECTS:

- New understanding about the behavior of AAV8 VLPs, both empty and filled, under varying pH conditions with different analytical techniques.
- The pH-dependent size variations and detection efficiency of these VLPs are a new and valuable addition to the existing knowledge about their behavior and stability.
- The combination of nES GEMMA, cryo-TEM, and AFM for the comprehensive analysis of AAV8 VLPs.





OWN CONTRIBUTION

In this work, I

- was involved in planning the experiment,
- conducted the nES GEMMA experiments, evaluated, and interpreted the data.
- assisted cryo-TEM experiments, evaluated, and interpreted the data.
- assisted AFM experiments, evaluated, and interpreted the data.
- developed the python script for 2D to 3D conversion, and planar sectioning.
- drafted and wrote major parts of the manuscript, including the revision process.
- overall data processing.

Article

Adeno-Associated Virus-like Particles' Response to pH Changes as Revealed by nES-DMA

Samuele Zoratto ¹, Thomas Heuser ², Gernot Friedbacher ¹, Robert Pletzenauer ³, Michael Graninger ³,
Martina Marchetti-Deschmann ¹ and Victor U. Weiss ^{1,*}

¹ Institute of Chemical Technologies and Analytics, TU Wien, A-1060 Vienna, Austria; samuele.zoratto@tuwien.ac.at (S.Z.); gernot.friedbacher@tuwien.ac.at (G.F.); martina.marchetti-deschmann@tuwien.ac.at (M.M.-D.)

² Electron Microscopy Facility, Vienna BioCenter Core Facilities GmbH, A-1030 Vienna, Austria; thomas.heuser@vbcf.ac.at

³ Pharmaceutical Sciences, Baxalta Innovations GmbH (Part of Takeda), A-1221 Vienna, Austria; robert.pletzenauer@takeda.com (R.P.); michael.graninger@takeda.com (M.G.)

* Correspondence: victor.weiss@tuwien.ac.at; Tel.: +43-1-58801-151611

Abstract: Gas-phase electrophoresis on a nano-Electrospray Gas-phase Electrophoretic Mobility Molecular Analyzer (nES GEMMA) separates single-charged, native analytes according to the surface-dry particle size. A volatile electrolyte, often ammonium acetate, is a prerequisite for electrospraying. Over the years, nES GEMMA has demonstrated its unique capability to investigate (bio-)nanoparticle containing samples in respect to composition, analyte size, size distribution, and particle numbers. Virus-like particles (VLPs), being non-infectious vectors, are often employed for gene therapy applications. Focusing on adeno-associated virus 8 (AAV8) based VLPs, we investigated the response of these bionanoparticles to pH changes via nES GEMMA as ammonium acetate is known to exhibit these changes upon electrospraying. Indeed, slight yet significant differences in VLP diameters in relation to pH changes are found between empty and DNA-cargo-filled assemblies. Additionally, filled VLPs exhibit aggregation in dependence on the applied electrolyte's pH, as corroborated by atomic force microscopy. In contrast, cryogenic transmission electron microscopy did not relate to changes in the overall particle size but in the substantial particle's shape based on cargo conditions. Overall, we conclude that for VLP characterization, the pH of the applied electrolyte solution has to be closely monitored, as variations in pH might account for drastic changes in particles and VLP behavior. Likewise, extrapolation of VLP behavior from empty to filled particles has to be carried out with caution.

Keywords: AAV8; VLP; nES GEMMA; DMA; cryo-TEM; gene therapy



Citation: Zoratto, S.; Heuser, T.; Friedbacher, G.; Pletzenauer, R.; Graninger, M.; Marchetti-Deschmann, M.; Weiss, V.U. Adeno-Associated Virus-like Particles' Response to pH Changes as Revealed by nES-DMA. *Viruses* **2023**, *15*, 1361. <https://doi.org/10.3390/v15061361>

Academic Editors: Ottmar Herchenröder, Brigitte Pützer and Kenneth Lundstrom

Received: 3 May 2023

Revised: 29 May 2023

Accepted: 8 June 2023

Published: 13 June 2023



Copyright: © 2023 by the authors. Licensee MDPI, Basel, Switzerland. This article is an open access article distributed under the terms and conditions of the Creative Commons Attribution (CC BY) license (<https://creativecommons.org/licenses/by/4.0/>).

1. Introduction

Gene therapy alters the genetic information of an organism, replacing, supplementing, or modifying its genomic profile to enable hereditary disease treatment, as lately reviewed for hemophilia [1], for example. To convey new genomic information to a cell, cargo carriers are necessary to shield nucleotides from the environment and achieve their targeted transport. One possible carrier type is virus-like particles (VLPs), macromolecular assemblies resembling their parent virus but no longer being infectious due to a lack of viral genomic information [2]. Hence, VLPs can be engineered to encapsulate other genomic information in question.

AAV are viruses of the genus *Dependoparvovirus* within the family *Parvoviridae*. They are approximately 26 nm in size, non-enveloped, non-pathogenic, and endemic in humans as well as several vertebrate species. To date, 13 serotypes have been identified in nature, each with a different tissue tropism. The capsid comprises 60 copies of three types of subunits: VP1, VP2, and VP3, arranged in a T = 1 icosahedral symmetry with a molar

ratio of 1:1:10. Due to its small size, only 4.7 kb of single-strand DNA (ssDNA) can be encapsulated [3].

In this work, we took an interest in adeno-associated virus serotype 8 (AAV8) modified to generate VLPs for gene therapy applications. AAV8 VLPs were provided in two different preparations: (i) lacking any genomic cargo (i.e., an ‘empty’ VLP preparation), and (ii) carrying a non-viral engineered genome (i.e., a ‘filled’ VLP preparation).

A possible technique for (bio-)nanoparticle characterization in general and AAV8 in particular is gas-phase electrophoresis on a nano Electrospray Gas-phase Electrophoretic Mobility Molecular Analyzer (nES GEMMA), also known as nES Differential Mobility Analyzer (nES-DMA) [4]. This technique is based on the size separation of single-charged, surface-dry analytes in the gas phase. Transfer of analytes from a liquid sample—a volatile electrolyte solution is a necessary prerequisite for the technique—to the gas-phase is achieved via a nES process, followed by drying of droplets and concomitant charge equilibration of particles in a bipolar atmosphere induced by, for example, a ^{210}Po α -particle source, a soft X-ray charger, or an alternating corona discharge process [5–8]. The majority of particles lose all charges upon passage of the bipolar atmosphere and are not regarded further, whereas a certain percentage of aerosolized analytes remains single-charged and are introduced to the DMA unit of the instrumentation. There, two forces act on the particles during size separation. Firstly, analytes are transported via a high laminar sheath flow of compressed, filtered ambient air through the DMA. At the same time, a tunable electric field exerts a force on charged particles in an orthogonal direction. By variation of the applied field strength and based on electrophoretic principles, only particles of a corresponding surface dry particle diameter (electrophoretic mobility, EM diameter) have the correct trajectory to continue to the detector unit of the instrument. There, particles are counted after a nucleation process in a supersaturated atmosphere as they pass a focused laser beam. This setup guarantees true particle-number-based detection of smaller-sized sample components next to larger ones in accordance with the recommendations of the European Commission (2011/696/EU, 18 October 2011, updated 2022) for nanoparticle characterization. The same instrumentation is also known under several other names, e.g., nES-DMA, macroIMS, SMPS or liquiScan ES (e.g., [9,10]).

Since its first reference in the literature by Kaufman et al. in 1996 [4], gas-phase electrophoresis has been applied for the characterization of a multitude of (bio-)nanoparticle materials, such as viruses [11–13], VLPs [14–17], liposomes and lipoprotein particles [18–22], extracellular vesicles [23–25], and organic and inorganic nanoparticles [26–28]. Frequently, ammonium acetate is employed as an electrolyte solution for the nES process. However, ammonium acetate is no buffer per definition (i.e., ammonium acetate solution), and especially at neutral pH, it exhibits no buffering capacity. Hence, significant changes in pH occur upon drying of droplets generated in the nES process, as reported by Konermann in 2017 [29]. We now took interest in the question how AAV8-based VLPs would behave to such pH changes, focusing on a well-defined in-solution setup. Analyses were carried out via gas-phase electrophoresis, and we corroborated our findings by atomic force microscopy (AFM) and cryogenic transmission electron microscopy (cryo-TEM) as orthogonal analytical techniques. All applied analytical techniques relate a pH dependency of AAV8 particles in aqueous ammonium acetate.

2. Materials and Methods

2.1. Chemicals

Ammonium acetate (NH_4OAc , $\geq 99.99\%$), ammonium hydroxide (ACS reagent), and acetic acid (ACS reagent) were purchased from Sigma-Aldrich (Steinheim, Germany). The electrolyte solution was prepared by dissolving 40 mM of ammonium acetate with water of ultrahigh quality (UHQ) delivered by a Simplicity UV apparatus ($18.2 \text{ M}\Omega \times \text{cm}$ at 25°C , Millipore, Billerica, MA, USA). The solution was adjusted to different pH levels ranging from 4.0 to 9.0 (with 1.0 step increase) with ammonium hydroxide or acetic acid. Lastly, the

solution was filtered through a surfactant-free cellulose acetate membrane with 0.20 μm pore size syringe filters (Sartorius, Göttingen, Germany).

2.2. Sample Description

Purified AAV8 VLP samples were provided by Baxalta Innovations GmbH (Orth/Donau, Austria, part of Takeda). Two different batches were provided: (i) so-called empty AAV8 VLPs (3776 $\mu\text{g}/\text{mL}$, i.e., 7.3×10^{14} capsids/ mL) with 97% of capsids not carrying any genomic information, and (ii) so-called filled AAV8 VLPs (85 $\mu\text{g}/\text{mL}$, i.e., 1.6×10^{13} capsids/ mL), where 66% of all the capsids were carrying a genomic load. The percentage of capsid filling was assessed via cryogenic transmission electron microscopy (cryo-TEM) by Baxalta Innovations GmbH.

2.3. Sample Preparation

Buffer exchange against 40 mM NH_4OAc at pH 7.0 was carried out by means of 10 kDa MWCO centrifugal filters (polyethersulfone membrane from VWR, Vienna, Austria). After three repetitions of spin filtration at 9000 g each, the retentate (approx. 10 μL in volume) was reconstituted in a pH-adjusted electrolyte solution (i.e., ranging from 4.0 to 9.0) to yield 22 $\mu\text{g}/\text{mL}$ and 8.5 $\mu\text{g}/\text{mL}$ final concentration for empty and filled AAV8 VLPs, respectively. Before analysis, the samples were further diluted to yield 250–300 particle counts for the signal at 25 nm at pH 7.0 with nES GEMMA. The respective dilution ratio was then employed for AFM and cryo-TEM analysis.

2.4. Instrumentation

nES GEMMA analyses were carried out on a TSI Inc instrument (Shoreview, MN, USA), which consisted of a nanoelectrospray charge reduction source unit (model 3480) equipped with a ^{210}Po charge equilibration device, an electrostatic classifier control unit employing a nano differential mass analyzer (nano DMA; model 3080) and an n-butanol driven ultrafine condensation particle counter (CPC; model 3025A) for AAV8 VLP detection. The nES unit is equipped with a 24 cm long polyimide-coated fused-silica capillary with an inner diameter of 25 μm (Molex, Lincolnshire, IL, USA). The capillary is manually cut and tapered with a home-built grinding machine based on the work of Tycova et al. [30].

Nanoparticle separation and detection were achieved with the following settings: the filtered airflow on the nES generator was set to 1.6×10^{-5} m^3/s (1 L per minute, Lpm), the CO_2 gas flow to 1.6×10^{-6} m^3/s (0.1 Lpm, 99.5% from Messer, Gumpoldskirchen, Austria) and the differential capillary pressure at 27.58 kPa (4 pounds per square inch differential, PSID). Capillary conditioning was performed by pre-spraying each sample for at least 3 min before starting the measurement. Capillary rinsing was performed by infusing the electrolyte solution until the signal from the previous sample was no longer detectable. The sample was infused at a flow rate of 70 nL/min. The capillary tip voltage was set to have a stable Taylor cone (approx. 2 kV voltage and -380 nA current). The electrostatic classifier was set in automatic scanning mode (up scan time 120 s, retrace time 30 s) with a sheath gas flow rate of 2.5×10^{-4} m^3/s (15 Lpm), which yielded a range of measurable EM diameters between 1.95 nm and 64.9 nm. A total of 10 scans for each sample were used to generate a median spectrum. Mathematical and statistical calculations on the nES GEMMA spectra were made with the software OriginPro ver. 2021 (OriginLab Corporation, Northampton, MA, USA).

AFM experiments were carried out on a NanoScope VIII Multimode SPM instrument (Bruker, Bremen, Germany) using silicon cantilevers with integrated silicon tips (model NCHV from Bruker, resonance frequency: 320 kHz, $L = 125$ μm , $k = 42$ N/m). The images were acquired in tapping, constant amplitude mode at a scanning rate of 1.99 Hz over a scan area of 5 and 1 μm^2 .

The homogeneity of the mica platelet was tested prior to sample analysis. Subsequently, 10–20 μL of sample (5–20 $\mu\text{g}/\text{mL}$ solutions) were spotted on the platelet's surface

at room temperature. The sample was allowed to adsorb for 5 min undisturbed before being gently rinsed with UHQ water and dried with nitrogen gas (outlet pressure 350 kPa).

Lastly, the AFM images have been analyzed by NanoScope Analysis 1.5 software (Bruker, Santa Barbara, CA, USA). Longitudinal and medial plane sections were used to generate profiles of the imaged particles.

Cryo-TEM samples were prepared using Quantifoil (Großlöbichau, Germany) Cu 200 mesh R2/2 holey carbon grids which were glow discharged for 60 s at -25 mA with a Bal-Tec (Balzers, Liechtenstein) SCD005 glow discharger. Grids were mounted on forceps and loaded into a Leica GP (Leica Microsystems, Vienna, Austria) grid plunger with the climate chamber set to 4 °C and 75% relative humidity. Sample aliquots of 4 μ L were applied to the carbon side of the grid and front-side blotted for 2 s with Whatman filter paper #1 (Little Chalfont, Great Britain) and plunge frozen into liquid ethane at approximately -180 °C for instant vitrification. Cryo-samples were transferred to a Glacios cryo-transmission microscope (Thermo Scientific, Waltham, MA, USA) equipped with a X-FEG and a Falcon3 direct electron detector. The microscope was operated in low-dose mode and digital images were recorded using the SerialEM software [31] and the Falcon3 camera in linear mode at a defocus of -6 μ m and 36,000 fold magnification corresponding to a pixel size of 4.124 Å.

2.5. Cryo-TEM Particles Diameter Determination

Individual VLP particles were picked manually from suitable cryo-TEM micrographs and their coordinates were saved as model points using the open-source IMOD processing tool [32]. The particle models were used for alignment and 2D averaging with the Particle Estimation for Electron Tomography (PEET) software, an open-source tool typically used for 3D subtomogram averaging [33,34]. Unbiased diameter determination was achieved by an in-house ad hoc developed Python script (see Supporting information), able to generate 3D graphs from the 2D images; by plotting correlating grey values of each (x,y) image's pixel coordinates. The 3D graphs can be sectioned and exported at different height levels. For each sample, three sections at different levels were extracted. At last, the data points contained in the sections were imported to OriginPro software (ver. 2021), where a circle fitting function was applied to determine the diameter of the particle.

3. Results

Our article aims to expand the knowledge concerning the characteristics and behavior of AAV8-based VLPs suspended in electrolyte solutions at different pH levels. nES GEMMA technology is used as main analytical technique. As previously introduced, nES GEMMA can be easily employed to analyze viruses and deliver robust, high-throughput, and cost-effective analyses. Moreover, orthogonal analytical techniques such as AFM in tapping mode and cryo-TEM have been applied to corroborate our results obtained from gas-phase electrophoresis.

As already demonstrated in our previous work [35], nES GEMMA can discriminate between VLPs either carrying or lacking genomic information for the two individual sample types (Figure 1A). The small, albeit critical, difference in EM diameter between the two VLP preparations originates from the presence, or absence, of an encapsulated cargo (i.e., the genomic material). The discrimination is possible due to the operating conditions of nES GEMMA analysis, which induce evaporation of the hydrodynamic layer surrounding the particles, thus yielding surface-dry analytes. However, the surface drying effect seemingly propagates across the proteinaceous layer of the capsid to its core, as the VLP EM diameter is affected by the content of its cargo. Two possible outcomes can be surmised: in the presence of a payload, the particles mostly retain their original shape thanks to stabilizing forces emerging from protein-genome interactions. In the absence of a genomic load instead, a higher degree of deformation is allowed, thus making the particles more flexible and detectable at smaller EM diameters.

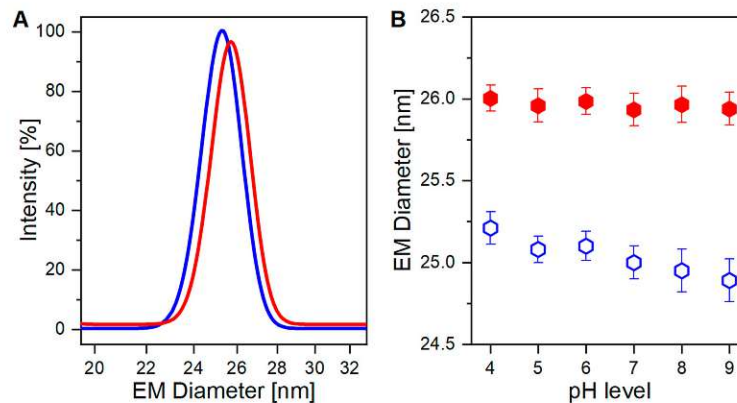


Figure 1. nES GEMMA analysis of empty and filled VLP preparations. (A) Gaussian fitting overlay of empty (blue trace) and filled (red trace) VLPs at pH 7. (Adapted from Zoratto et al., 2021 [35]) (B) EM diameter changes of empty (empty blue hexagons) and filled (filled red hexagons) VLPs according to pH levels ($n = 6$ analyses per pH level, average EM diameters and standard deviations are depicted, $p < 0.0001$).

A mandatory step for nES GEMMA includes the exchange of the original sample buffer to a volatile electrolyte solution. This drastically reduces non-volatile components, which hinder correct and accurate particle EM diameter determination. More details can be found in previous works [36,37]. To some extent, either for nES GEMMA or for ESI MS analysis, aqueous ammonium acetate is applied in that context. However, it has to be considered that ammonium acetate droplets might undergo drastic pH changes upon evaporation, as discussed by Konermann in detail [29]. Thus, we took an interest in investigating the effects of different pH levels on VLP preparations, either carrying a genomic cargo or not, and both suspended in aqueous ammonium acetate. Results are displayed in Figures 1B and 2A, respectively.

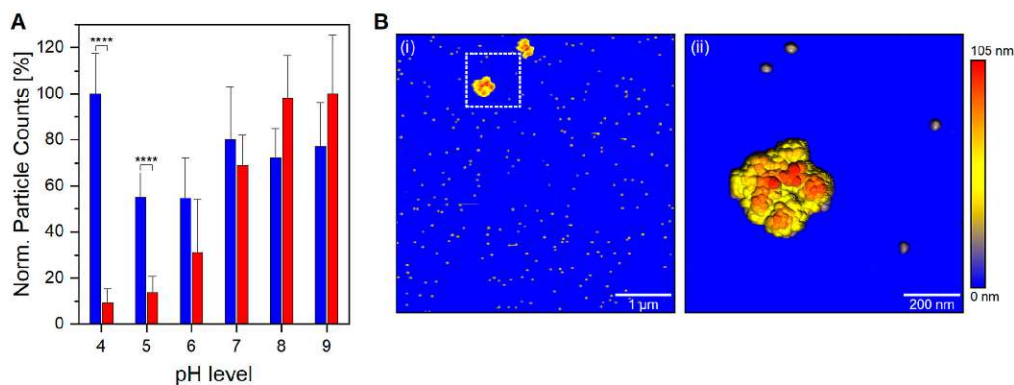


Figure 2. Behavior of VLP preparations at different pH levels. (A) Normalized particle counts detected via nES GEMMA for empty (blue columns) and filled (red columns) preparations at different pH levels ($n = 6$ measurements; average values and standard deviations are depicted; values at a corresponding pH are related to particle counts at pH 4 for empty VLPs and pH 9 for filled VLPs). For filled VLPs a decline in particle numbers with decreasing pH is observed in contrast to empty particles. (B) AFM analysis of filled VLPs at pH 5; (i) the analyzed area shows monomers and two aggregate clusters; (ii) magnification of the white dotted area in (i). **** $p < 0.0001$.

3.1. AAV8 VLPs in Aqueous Ammonium Acetate at Different pH Targeted by Gas-Phase Electrophoresis

Thanks to their distinct size differences, VLP preparations, either carrying or lacking cargo, can be easily discriminated ($p < 0.0001$, Figure 1B). In detail, filled VLPs have a constant higher EM diameter, and show a minimal downward trend towards a smaller EM diameter for alkaline pH. For empty VLPs instead, a sharper pH-dependent trend towards a smaller EM diameter is observed. Reasonably, pH-driven protein modification alters capsid's structural stiffness in both VLP preparations, but empty ones are again more affected.

In addition, below a physiological pH level, a significant contrast in the number of detected particles between filled and empty VLP preparation is noticed ($p < 0.0001$, Figure 2A). A high detection yield for empty VLPs confirms that nES GEMMA capabilities are not hindered in an acidic working environment; hence, the observed difference for VLP preparations is sample-dependent. The unique behavior demonstrated by filled VLPs is of great importance, both for VLP analysis and in the biopharmaceutical field during manufacturing steps. *In vivo*, viruses commonly hijack the cellular uptake mechanism to infect the cells. A number of them take advantage of the acidic environment of late endosomes and endolysosomes to shed their proteinaceous layer to deliver their naked viral load directly into the cytoplasm. Other viruses instead—AAV8 included—need to survive and accomplish endosomal escape intact in order to complete the infection [38,39]. Therefore, it is unlikely that bionanoparticles depletion is caused by viral uncoating. Moreover, capsid fragments would be detected at EM diameters below 25 nm; still, the nES GEMMA signals in this region are negligible and comparable to empty VLP preparations at comparable pH levels. Another viable option is aggregation, where filled VLPs at acidic pH generate clusters outside the operating range of nES GEMMA. To investigate this claim, filled VLPs in acidic conditions have been analyzed via AFM. In fact, VLP aggregates sized >200 nm are clearly visible in the AFM images (Figure 2B(i)). AFM images at higher magnification (Figure 2B(ii)) clearly show aggregate species stemming from monomeric particles. Longitudinal and medial sections of the imaged species match profiles fitting 25 nm monomeric particles (Supporting information, Figure S1). It is of note that particle aggregation yielding such large assemblies cannot be followed by the applied nES GEMMA setup. Furthermore, it has to be stressed that the resulting pH-dependant aggregation is partially reversible as adjusting the pH back to a neutral value restores the corresponding monomer peak in nES GEMMA measurements (Supporting information, Figure S2).

As demonstrated, the presence or absence of an encapsulated cargo significantly alters the capsid's structural characteristics. The novel behavior observed in filled VLPs additionally shows aggregation once exposed to acidic conditions. This pH-driven phenomenon is likely caused by a newly acquired feature linked to an increase in the capsid-to-capsid adherence with or without DNA mediation, and might be caused by fine capsid's structural changes. Although nES GEMMA can determine particles' diameter with both high accuracy and precision with high sample throughput times and good statistics, it can only partially infer the shape details of the sample. For this purpose, analytical techniques capable of imaging at near-atomic levels, such as cryo-TEM, are more fitted, although very time-consuming. Therefore, VLP preparations at both pH extremes (i.e., pH 4 and 9) have been analyzed with cryo-TEM technology to investigate if any distinct features would arise between samples (Figure 3).

3.2. Cryogenic Transmission Electron Microscopy (cryo-TEM) of AAV8 VLPs

Cryo-TEM RAW images have low signal-to-noise contrast between the investigated material and the background. Hence, averaging with software is necessary to increase contrast and highlight the sample's characteristics. In our work, we employed the Particle Estimation for Electron Tomography (PEET) open-source software to catalog, align, and average hundreds of particles per sample (Figure 3A). Originally designed as an averaging program for 3D tomograms, we used it for 2D averaging. To ensure a reliable, biased-free

diameter determination, the averages generated by PEET were processed via a Python script written in-house (included in the Supporting information), where sections at different height were extracted. The data points included in these sections were later fitted with a circle function via the OriginPro (ver. 2021) software. This workflow, providing unbiased, reliable data for PEET-generated cryo-TEM images of VLPs, is summarized in Figure 4 and could be applied to images generated from different analytical techniques.

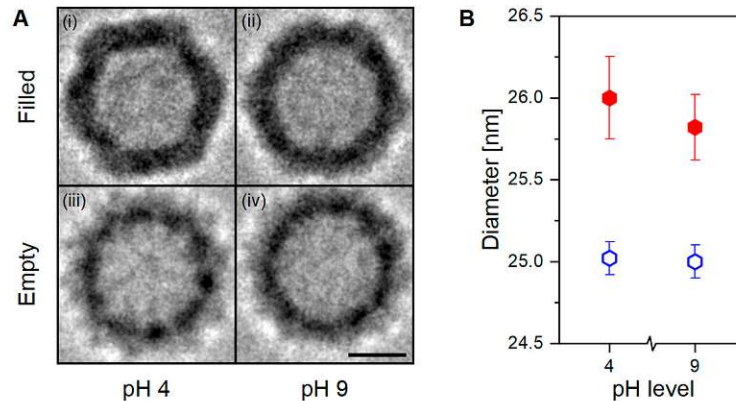


Figure 3. Cryo-TEM analysis of empty and filled AAV8 VLPs. (A) AAV8 VLPs filled at pH 4 (i) and pH 9 (ii), and empty at pH 4 (iii) and pH 9 (iv) after 2D averaging. (B) Particles' diameter determined via Python script from the aligned particles showed in (A). Black bar equals 10 nm.

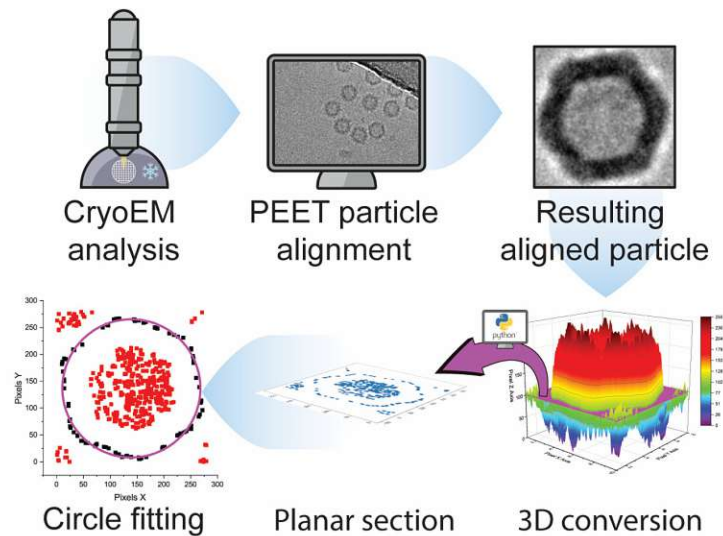


Figure 4. Workflow scheme from cryo-TEM analysis to biased-free diameter determination. In the last tile, the magenta circle represents the fitted function applied to the black data points. Red data points are instead excluded from the fitting process.

Visual comparison of the PEET-generated Cryo-TEM images show remarkable structural differences (Figure 3A). Within the filled VLP preparation, the sample at pH 4 (Figure 3A(i)) shows a well-defined icosahedral capsid's structure with regular, straight edges, and clear vertices; at pH 9 (Figure 3A(ii)) the same characteristics are instead less pronounced. Whereas in the empty VLP preparation, regardless of the pH value, the capsid's structure appears smoother, rounder, and slightly smaller (Figure 3A(iii,iv)). Anticipated

by nES GEMMA results, and now corroborated by cryo-TEM images, the particle's shape is linked with the presence or absence of an encapsulated cargo, and this could affect the capsid's interactions at the macromolecular scale.

Diameter determination results in filled VLPs exhibiting larger diameters than empty ones, in agreement with nES GEMMA observations ($p < 0.001$, Figure 3B). Moreover, new information about the sample's characteristics can be inferred. In detail, empty VLPs report identical diameter values regardless of the solvent's pH, which is contrary to the downward trend observed with nES GEMMA. In hydrated conditions, regardless of the pH, empty VLPs maintain a constant size and shape. Filled VLPs instead show a small diameter variability between pH conditions, probably due to the sharper contours as reflected in the imaged particles (Figure 3A(i,ii)). Nonetheless, this slight visual and diameter difference does not provide any functional proof to explain the observed aggregation behavior.

4. Discussion

In this study, we demonstrated the feasibility of nES GEMMA to discriminate, detect, and characterize novel behaviors of AAV8-based VLP preparations analyzed with nES GEMMA-compatible electrolyte solution adjusted to different pHs. Moreover, to observe the VLP preparations in their hydrated native state, cryo-TEM analysis was performed.

Results from nES GEMMA of the two VLP preparations show peculiar, unique characteristics. Filled VLPs report limited EM diameter deviation across the different pHs, but detection efficiency is hindered in acidic conditions. Instead, the particle detection efficiency of empty VLPs is unperturbed by the electrolyte's pH, but pH-dependent EM diameter variability is observed.

Results from PEET-based cryo-TEM images highlight the structural differences between the two VLP preparations. Moreover, the developed method for biased-free diameter determination via cryo-TEM confirms size-specific differences between empty and filled VLP preparations as observed with nES GEMMA. However, within VLP preparations, pH-dependent variation is observed, contrasting nES GEMMA results—specifically, a constant diameter for empty VLPs and a variable one for filled VLPs. One hypothesis to explain the discrepancy observed between nES GEMMA and cryo-TEM resides in the different working environments of these techniques. In nES GEMMA, the particles are sorted and classified in a solvent-free environment and are in a surface-dry state. Consequently, empty VLPs, lacking an encapsulated cargo, collapse due to structural stress caused by solvent evaporation. Likely, the solvent's pH alters protein conformation, which translates to different degrees of structural stability or stiffness. Therefore, labile structures are detected at smaller EM diameters. Instead, filled VLPs remain unaffected, thanks to the incompressible characteristics of their payload. On the contrary, in cryo-TEM, the VLPs are analyzed in a solubilized native state. Indeed, empty VLPs are not subjected to structural stress from solvent evaporation, and maintain their original form. Filled VLPs instead show a slight difference between the two pH extremes. The origin of this difference is as yet unclear. Putatively, and in addition to pH-induced changes at the protein level in acidic conditions, an osmotic pressure difference is generated at the semipermeable membrane level (i.e., proteinaceous capsid layer) caused by the negative charges of the genomic cargo. Hence, solvent intake is favored to equilibrate the osmotic pressure, causing the particle to swell.

In acidic conditions, nES GEMMA reveals a steep decrease in particle counts for filled VLPs, while empty ones are unaffected. Indeed, AFM analysis of filled VLPs in acidic conditions confirmed our hypothesis: the lower particle count was due to particle aggregation. Although nES GEMMA's working range of detection could be expanded, the heterogeneity of these clusters impedes their detection without an upstream enrichment technique, as observed in previous work [36]. Aggregation could be explained by the shape of the particles, highlighted by cryo-TEM-based PEET averaged images. The well-defined capsid faces of filled VLPs might provide the infrastructure for non-covalent capsid-to-capsid interaction, thus supporting aggregation. However, since no aggregate formation was observed in cryo-TEM averages, it suggests that the onset of aggregation requires

further contributing factors. Once again, the critical factor might lie in the different working environments, dry in both nES GEMMA and AFM, and wet (i.e., plunge frozen in a solvent) for cryo-TEM. Putatively, if aggregation is promoted in a dry environment, it might be an evolutionary adaptation of AAV to increase viral infection transmission efficiency through airborne routes.

The results presented in this study demonstrate the feasibility and resilience of nES GEMMA as a method of analysis for AAV Serotype-8 VLP preparations across different pH levels. This is of great importance, especially in overseeing the different phases of a drug production process, where simple, reliable, and inexpensive control is often sought.

The results observed via AFM and cryo-TEM analysis provided complementary information to investigate the behavior observed with nES GEMMA when filled VLPs are exposed to acidic pH. AFM reveals the formation of heterogeneous aggregate products that could not be directly targeted with nES GEMMA but whose presence could be inferred by the significant drop in particle counts in the EM diameter range characteristic of VLPs in a monomeric state. Initially employed to investigate particle aggregation, cryo-TEM analysis did not confirm cluster formation observation. However, its extreme magnification power provided valuable information, and its application will propel future development toward the characterization of VLPs.

To conclude, the developed method and analytical approaches presented in this study provided new insight and possible applications for both the scientific and the biopharmaceutical field. The observations herein open several discussion points, encouraging further studies to investigate such valuable drug-delivery vectors.

Supplementary Materials: The following supporting information can be downloaded at: <https://www.mdpi.com/article/10.3390/v15061361/s1>, Figure S1: AFM analysis of filled VLPs at pH 5; Figure S2: nES GEMMA reversibility experiment of a filled VLP preparation; Python script to extract a planar section from the cryo-TEM 2D averaged images.

Author Contributions: Conceptualization, V.U.W.; Formal analysis, S.Z.; Investigation, S.Z., T.H. and G.F.; Resources, T.H., G.F., R.P. and M.M.-D.; Writing—original draft, S.Z. and V.U.W.; Writing—review & editing, S.Z., R.P., M.G. and V.U.W.; Supervision, M.M.-D. and V.U.W.; Project administration, M.M.-D. and V.U.W.; Funding acquisition, R.P., M.G. and M.M.-D. All authors have read and agreed to the published version of the manuscript.

Funding: This research was funded by Takeda and received financial support from TU Wien Bibliothek through its Open Access Funding programme. The Vienna BioCenter Core Facilities gratefully acknowledge funding from the Austrian Federal Ministry of Education, Science and Research and the city of Vienna.

Data Availability Statement: Data is available upon request.

Acknowledgments: We thank Takeda for providing the AAV8 samples and supervising this work, Thomas Heuser for the access to the cryo-TEM instrumentation and his support during the corresponding analysis, and Open Access Funding by TU Wien. We dedicate this manuscript to the memory of Günter Allmaier.

Conflicts of Interest: The authors declare no conflict of interest.

References

1. Nathwani, A.C. Gene therapy for hemophilia. *Hematol. Am. Soc. Hematol. Educ. Program.* **2022**, *2022*, 569–578. [[CrossRef](#)] [[PubMed](#)]
2. Mejia-Mendez, J.L.; Vazquez-Duhalt, R.; Hernandez, L.R.; Sanchez-Arreola, E.; Bach, H. Virus-like Particles: Fundamentals and Biomedical Applications. *Int. J. Mol. Sci.* **2022**, *23*, 8579. [[CrossRef](#)] [[PubMed](#)]
3. Sant'Anna, T.B.; Araujo, N.M. Adeno-associated virus infection and its impact in human health: An overview. *Viol. J.* **2022**, *19*, 173. [[CrossRef](#)] [[PubMed](#)]
4. Kaufman, S.L.; Skogen, J.W.; Dorman, F.D.; Zarrin, F.; Lewis, K.C. Macromolecule analysis based on electrophoretic mobility in air: Globular proteins. *Anal. Chem.* **1996**, *68*, 1895–1904. [[CrossRef](#)]
5. Wiedensohler, A.; Fissan, H.J. Aerosol charging in high purity gases. *J. Aerosol Sci.* **1988**, *19*, 867–870. [[CrossRef](#)]

6. Kallinger, P.; Steiner, G.; Szymanski, W.W. Characterization of four different bipolar charging devices for nanoparticle charge conditioning. *J. Nanoparticle Res.* **2012**, *14*, 1–8. [\[CrossRef\]](#)
7. Weiss, V.U.; Frank, J.; Piplits, K.; Szymanski, W.W.; Allmaier, G. Bipolar Corona Discharge-Based Charge Equilibration for Nano Electrospray Gas-Phase Electrophoretic Mobility Molecular Analysis of Bio- and Polymer Nanoparticles. *Anal. Chem.* **2020**, *92*, 8665–8669. [\[CrossRef\]](#)
8. Allmaier, G.; Weiss, V.U.; Engel, N.Y.; Marchetti-Deschmann, M.; Szymanski, W.W. Soft X-ray Radiation Applied in the Analysis of Intact Viruses and Antibodies by Means of Nano Electrospray Differential Mobility Analysis. In *Molecular Technologies for Detection of Chemical and Biological Agents*; Banoub, J., Caprioli, R., Eds.; NATO Science for Peace and Security Series A: Chemistry and Biology; Springer: Dordrecht, The Netherlands, 2017; pp. 149–157. [\[CrossRef\]](#)
9. Carazzone, C.; Raml, R.; Pergantis, S.A. Nanoelectrospray ion mobility spectrometry online with inductively coupled plasma-mass spectrometry for sizing large proteins, DNA, and nanoparticles. *Anal. Chem.* **2008**, *80*, 5812–5818. [\[CrossRef\]](#)
10. Shah, V.B.; Orf, G.S.; Reisch, S.; Harrington, L.B.; Prado, M.; Blankenship, R.E.; Biswas, P. Characterization and deposition of various light-harvesting antenna complexes by electrospray atomization. *Anal. Bioanal. Chem.* **2012**, *404*, 2329–2338. [\[CrossRef\]](#)
11. Weiss, V.U.; Bereszczak, J.Z.; Havlik, M.; Kallinger, P.; Gosler, I.; Kumar, M.; Blaas, D.; Marchetti-Deschmann, M.; Heck, A.J.; Szymanski, W.W.; et al. Analysis of a common cold virus and its subviral particles by gas-phase electrophoretic mobility molecular analysis and native mass spectrometry. *Anal. Chem.* **2015**, *87*, 8709–8717. [\[CrossRef\]](#)
12. Allmaier, G.; Blaas, D.; Bliem, C.; Dechat, T.; Fedosyuk, S.; Gosler, I.; Kowalski, H.; Weiss, V.U. Monolithic anion-exchange chromatography yields rhinovirus of high purity. *J. Virol. Methods* **2018**, *251*, 15–21. [\[CrossRef\]](#)
13. Fernandez de la Mora, J. A singularly narrow 29 nm aerosol size standard based on the ΦX174 bacteriophage. *J. Aerosol Sci.* **2022**, *161*, 105949. [\[CrossRef\]](#)
14. Guha, S.; Pease, L.F., 3rd; Brorson, K.A.; Tarlov, M.J.; Zachariah, M.R. Evaluation of electrospray differential mobility analysis for virus particle analysis: Potential applications for biomanufacturing. *J. Virol. Methods* **2011**, *178*, 201–208. [\[CrossRef\]](#)
15. Bereszczak, J.Z.; Havlik, M.; Weiss, V.U.; Marchetti-Deschmann, M.; van Duijn, E.; Watts, N.R.; Wingfield, P.T.; Allmaier, G.; Steven, A.C.; Heck, A.J. Sizing up large protein complexes by electrospray ionisation-based electrophoretic mobility and native mass spectrometry: Morphology selective binding of Fabs to hepatitis B virus capsids. *Anal. Bioanal. Chem.* **2014**, *406*, 1437–1446. [\[CrossRef\]](#)
16. Havlik, M.; Marchetti-Deschmann, M.; Friedbacher, G.; Messner, P.; Winkler, W.; Perez-Burgos, L.; Tauer, C.; Allmaier, G. Development of a bio-analytical strategy for characterization of vaccine particles combining SEC and nanoES GEMMA. *Analyst* **2014**, *139*, 1412–1419. [\[CrossRef\]](#)
17. Weiss, V.U.; Pogan, R.; Zoratto, S.; Bond, K.M.; Boulanger, P.; Jarrold, M.F.; Lykтей, N.; Pahl, D.; Puffer, N.; Schelhaas, M.; et al. Virus-like particle size and molecular weight/mass determination applying gas-phase electrophoresis (native nES GEMMA). *Anal. Bioanal. Chem.* **2019**, *411*, 5951–5962. [\[CrossRef\]](#)
18. Epstein, H.; Afergan, E.; Moise, T.; Richter, Y.; Rudich, Y.; Golomb, G. Number-concentration of nanoparticles in liposomal and polymeric multiparticulate preparations: Empirical and calculation methods. *Biomaterials* **2006**, *27*, 651–659. [\[CrossRef\]](#)
19. Chattopadhyay, S.; Modesto-Lopez, L.B.; Venkataraman, C.; Biswas, P. Size Distribution and Morphology of Liposome Aerosols Generated By Two Methodologies. *Aerosol Sci. Technol.* **2010**, *44*, 972–982. [\[CrossRef\]](#)
20. Allmaier, G.; Laschober, C.; Szymanski, W.W. Nano ES GEMMA and PDMA, new tools for the analysis of nanobioparticles-protein complexes, lipoparticles, and viruses. *J. Am. Soc. Mass Spectrom.* **2008**, *19*, 1062–1068. [\[CrossRef\]](#)
21. Weiss, V.U.; Urey, C.; Gondikas, A.; Golesne, M.; Friedbacher, G.; von der Kammer, F.; Hofmann, T.; Andersson, R.; Marko-Varga, G.; Marchetti-Deschmann, M.; et al. Nano electrospray gas-phase electrophoretic mobility molecular analysis (nES GEMMA) of liposomes: Applicability of the technique for nano vesicle batch control. *Analyst* **2016**, *141*, 6042–6050. [\[CrossRef\]](#)
22. Weiss, V.U.; Wieland, K.; Schwaighofer, A.; Lendl, B.; Allmaier, G. Native Nano-electrospray Differential Mobility Analyzer (nES GEMMA) Enables Size Selection of Liposomal Nanocarriers Combined with Subsequent Direct Spectroscopic Analysis. *Anal. Chem.* **2019**, *91*, 3860–3868. [\[CrossRef\]](#) [\[PubMed\]](#)
23. Chernyshev, V.S.; Rachamadugu, R.; Tseng, Y.H.; Belnap, D.M.; Jia, Y.; Branch, K.J.; Butterfield, A.E.; Pease, L.F., 3rd; Bernard, P.S.; Skliar, M. Size and shape characterization of hydrated and desiccated exosomes. *Anal. Bioanal. Chem.* **2015**, *407*, 3285–3301. [\[CrossRef\]](#) [\[PubMed\]](#)
24. Steinberger, S.; Karuthedom George, S.; Laukova, L.; Weiss, R.; Tripisciano, C.; Birner-Gruenberger, R.; Weber, V.; Allmaier, G.; Weiss, V.U. A possible role of gas-phase electrophoretic mobility molecular analysis (nES GEMMA) in extracellular vesicle research. *Anal. Bioanal. Chem.* **2021**, *413*, 7341–7352. [\[CrossRef\]](#) [\[PubMed\]](#)
25. Steinberger, S.; Karuthedom George, S.; Laukova, L.; Weiss, R.; Tripisciano, C.; Marchetti-Deschmann, M.; Weber, V.; Allmaier, G.; Weiss, V.U. Targeting the Structural Integrity of Extracellular Vesicles via Nano Electrospray Gas-Phase Electrophoretic Mobility Molecular Analysis (nES GEMMA). *Membranes* **2022**, *12*, 872. [\[CrossRef\]](#)
26. Hinterwirth, H.; Wiedmer, S.K.; Moilanen, M.; Lehner, A.; Allmaier, G.; Waitz, T.; Lindner, W.; Lammerhofer, M. Comparative method evaluation for size and size-distribution analysis of gold nanoparticles. *J. Sep. Sci.* **2013**, *36*, 2952–2961. [\[CrossRef\]](#)
27. Weiss, V.U.; Lehner, A.; Kerul, L.; Grombe, R.; Kratzmeier, M.; Marchetti-Deschmann, M.; Allmaier, G. Characterization of cross-linked gelatin nanoparticles by electrophoretic techniques in the liquid and the gas phase. *Electrophoresis* **2013**, *34*, 3267–3276. [\[CrossRef\]](#)

28. Elzey, S.; Tsai, D.H.; Yu, L.L.; Winchester, M.R.; Kelley, M.E.; Hackley, V.A. Real-time size discrimination and elemental analysis of gold nanoparticles using ES-DMA coupled to ICP-MS. *Anal. Bioanal. Chem.* **2013**, *405*, 2279–2288. [[CrossRef](#)]
29. Konermann, L. Addressing a Common Misconception: Ammonium Acetate as Neutral pH “Buffer” for Native Electrospray Mass Spectrometry. *J. Am. Soc. Mass. Spectrom.* **2017**, *28*, 1827–1835. [[CrossRef](#)]
30. Tycova, A.; Prikryl, J.; Foret, F. Reproducible preparation of nanospray tips for capillary electrophoresis coupled to mass spectrometry using 3D printed grinding device. *Electrophoresis* **2016**, *37*, 924–930. [[CrossRef](#)]
31. Mastronarde, D.N. Automated electron microscope tomography using robust prediction of specimen movements. *J. Struct. Biol.* **2005**, *152*, 36–51. [[CrossRef](#)]
32. Kremer, J.R.; Mastronarde, D.N.; McIntosh, J.R. Computer visualization of three-dimensional image data using IMOD. *J. Struct. Biol.* **1996**, *116*, 71–76. [[CrossRef](#)]
33. Nicastro, D.; Schwartz, C.; Pierson, J.; Gaudette, R.; Porter, M.E.; McIntosh, J.R. The molecular architecture of axonemes revealed by cryoelectron tomography. *Science* **2006**, *313*, 944–948. [[CrossRef](#)]
34. Heumann, J.M.; Hoenger, A.; Mastronarde, D.N. Clustering and variance maps for cryo-electron tomography using wedge-masked differences. *J. Struct. Biol.* **2011**, *175*, 288–299. [[CrossRef](#)]
35. Zoratto, S.; Weiss, V.U.; van der Horst, J.; Commandeur, J.; Buengener, C.; Foettinger-Vacha, A.; Pletzenauer, R.; Graninger, M.; Allmaier, G. Molecular weight determination of adeno-associate virus serotype 8 virus-like particle either carrying or lacking genome via native nES gas-phase electrophoretic molecular mobility analysis and nESI QRTOF mass spectrometry. *J. Mass. Spectrom.* **2021**, *56*, e4786. [[CrossRef](#)]
36. Zoratto, S.; Weiss, V.U.; Friedbacher, G.; Buengener, C.; Pletzenauer, R.; Foettinger-Vacha, A.; Graninger, M.; Allmaier, G. Adeno-associated Virus Virus-like Particle Characterization via Orthogonal Methods: Nanoelectrospray Differential Mobility Analysis, Asymmetric Flow Field-Flow Fractionation, and Atomic Force Microscopy. *ACS Omega* **2021**, *6*, 16428–16437. [[CrossRef](#)]
37. Weiss, V.U.; Kerul, L.; Kallinger, P.; Szymanski, W.W.; Marchetti-Deschmann, M.; Allmaier, G. Liquid phase separation of proteins based on electrophoretic effects in an electrospray setup during sample introduction into a gas-phase electrophoretic mobility molecular analyzer (CE-GEMMA/CE-ES-DMA). *Anal. Chim. Acta* **2014**, *841*, 91–98. [[CrossRef](#)]
38. Wang, D.; Tai, P.W.L.; Gao, G. Adeno-associated virus vector as a platform for gene therapy delivery. *Nat. Rev. Drug. Discov.* **2019**, *18*, 358–378. [[CrossRef](#)]
39. Dhungel, B.P.; Bailey, C.G.; Rasko, J.E.J. Journey to the Center of the Cell: Tracing the Path of AAV Transduction. *Trends Mol. Med.* **2021**, *27*, 172–184. [[CrossRef](#)]

Disclaimer/Publisher’s Note: The statements, opinions and data contained in all publications are solely those of the individual author(s) and contributor(s) and not of MDPI and/or the editor(s). MDPI and/or the editor(s) disclaim responsibility for any injury to people or property resulting from any ideas, methods, instructions or products referred to in the content.

Supporting Information

Adeno-associated virus-like particles' response to pH changes as revealed by nES-DMA

Samuele Zoratto¹, Thomas Heuser², Gernot Friedbacher¹, Robert Pletzenauer³, Michael Graninger³, Martina Marchetti-Deschmann¹, Victor U. Weiss¹

¹Institute of Chemical Technologies and Analytics, TU Wien, Vienna, Austria

²Electron Microscopy Facility, Vienna BioCenter Core Facilities GmbH, Vienna, Austria

³Pharmaceutical Sciences, Baxalta Innovations GmbH (part of Takeda), Vienna, Austria

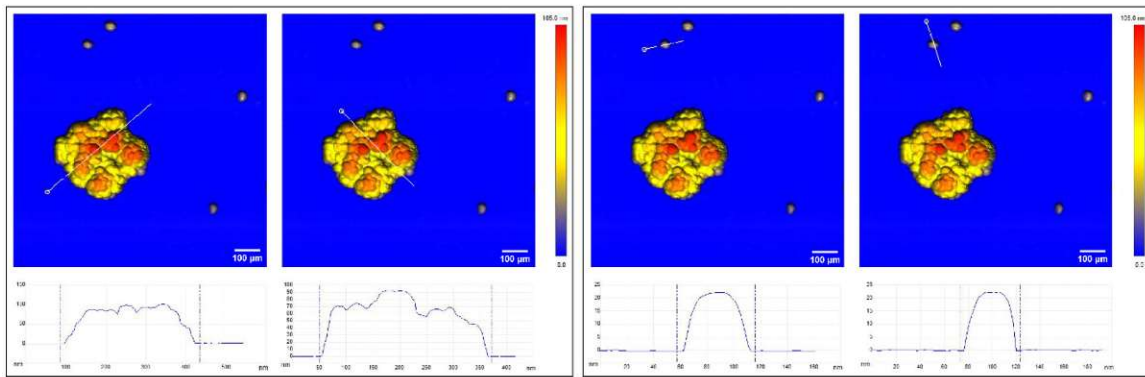
Keywords: nES GEMMA, DMA, VLP, AAV8, cryo-TEM, gene therapy.

Correspondence: Victor Weiss, Institute of Chemical Technologies and Analytics, TU Wien, Getreidemarkt 9/164, A-1060 Vienna, Austria

E-mail: victor.weiss@tuwien.ac.at

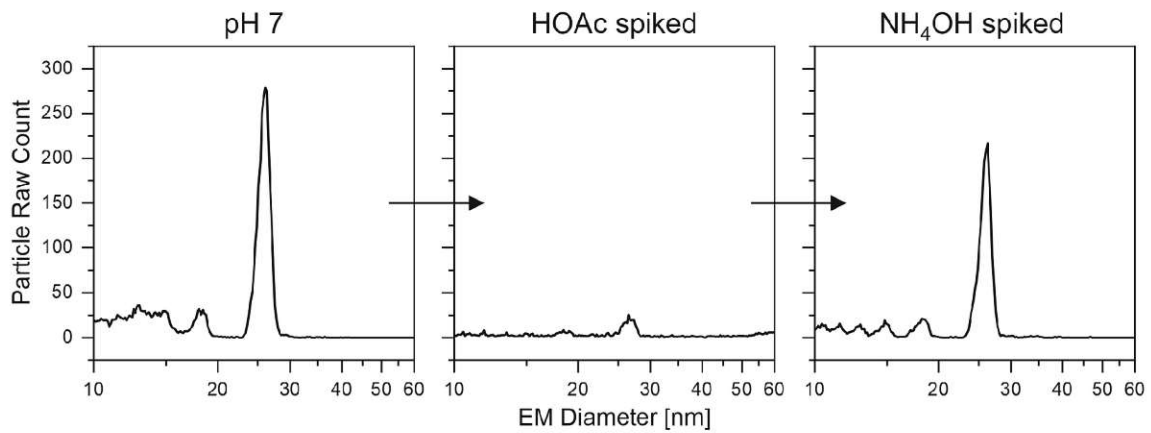
Tel: +43 1 58801 151611

Figure S1



AFM analysis of filled VLPs at pH 5 and relative longitudinal and medial profile section of the cluster (left panel) and one monomeric unit of AAV8 (right panel). Left panel: the profile sections highlight the underlying globular nature of the individual particles forming the cluster.

Figure S2



nES GEMMA reversibility experiment of filled VLP preparation. From left to right: in the first panel the VLP preparation has been analyzed at pH 7. In the middle panel, the aliquot was spiked with 1 μ L of acetic acid, changing the pH to \sim 3.6; substantial loss of particle detection is noticeable. In the last panel, 2 μ L of ammonium hydroxide are added to the aliquot, changing the pH to \sim 8.6 and reestablishing the detection of monomeric VLP particles.

Python script:

The following script was employed to extract planar section from the cryo-TEM 2D averaged images.

```
#!/bin/python3

#Python script created by Samuele Zoratto

#contact: samuele.zoratto@tuwien.ac.at

#import of necessary libraries

import numpy as np

import sys

import os

from PIL import Image

import PIL.ImageOps

import csv

import matplotlib.pyplot as plt

from datetime import datetime

#clean the shell

os.system("cls|clear")

#reads filename of the 2D image to convert to 3D and section
```

try :

```
#check if the file is present from the command line
```

```
image_2D = str(sys.argv[1])
```

```
#check if the filename correspond to an existing file
```

```
if os.path.exists(image_2D):
```

```
    print("File: "+image_2D+" found")
```

```
else:
```

```
    print(">>> Error: File not found! <<<\n\nCheck:\n1- Spelling\n2- Absence of blank characters\n3- If the file is in the same directory of this script!\n\nThe program will terminate")
```

```
    #terminate the script
```

```
    sys.exit(1)
```

```
except IndexError :
```

```
    #if the file was not provided, it asks for it
```

```
    print("No image filename provided in the command line. \nIn the future you can use the following format:\n \n>>> python 3D_section_from_2D_image.py [image name] [section number: 0-255] \n \nEnter the filename to use: ", end = "")
```

```
    image_2D = input()
```

```
    print("\nFilename entered: "+image_2D)
```

```
    #check if the filename correspond to an existing file
```

```
    if os.path.exists(image_2D):
```

```
        print("File "+image_2D+" found! The program will continue\n\n")
```

else:

```
print(">> Error: File not found! <<\n\nCheck:\n1- Spelling\n2- Absence of blank characters\n3- If the file is in the same directory of this script!\n\nThe program will terminate")
```

```
#terminate the script
```

```
sys.exit(1)
```

```
#reads the section number
```

```
try :
```

```
#check if the number has been declared in the command line, if it is valid, and in range
```

```
section_number = str(sys.argv[2])
```

```
if section_number.isnumeric() and -1 < int(section_number) < 256:
```

```
print("Section number in the correct range [0-255]: "+section_number)
```

```
else:
```

```
print(">> Error: Section number not valid! <<\n\nCheck:\n1- Spelling\n2- Number in range [0-255]\n\nThe program will terminate")
```

```
sys.exit(1)
```

```
except IndexError :
```

```
#if the section number was not provided, it asks for it
```

```
print("No section number provided in the command line. \nIn the future you can use the following format:\n \n>> python 3D_section_from_2D_image.py [image name] [section number: 0-255] \n \nEnter the section number to use [0-255]: ", end = "")
```

```
try :
```

```

section_number = input()

print("\nSection number entered: "+section_number)

if -1 < int(section_number) < 256 :

    print("Section number accepted")

else :

    while True :

        print("The section number entered is not valid. Please insert a valid section number
[0-255]: ", end = "")

        section_number = input()

        print("\nSection number entered: "+section_number)

        if -1 < int(section_number) < 256 :

            print("Section number accepted")

            break

    except ValueError :

        print("\n\n>> ERROR <<\nA non-numeric value has been entered. The program will
terminate")

        sys.exit(1)

#generate the filename for the csv file

now = datetime.now()

```

```

datestring = now.strftime("%b-%d-%Y_%H%M%S")

#the filename generated will be in this format: Export_image.jpg_section123_May-30-
2022_125500.csv with current date and time

filename = str("Export_" + image_2D + "_section"+section_number+"_"+datestring+".csv")

try :

    file = open(filename,"w",newline="")

    writer = csv.writer(file)

    print("\nCSV file created: "+ filename)

except :

    print("\n\n>> ERROR <<Impossible to create a file in the directory. Check disk space or
writing permissions.\nThe program will terminate")

    sys.exit(1)

#function to write the exported section in the csv file

def printArrayValuesInCSV(tobeprinted):

    for x in range(len(tobeprinted)):

        writer.writerow(tobeprinted[x])

#function to create a list of scattered points from an array

def createScatteredPoints(dataArray):

    dataList = []

```

```

for x in range(len(dataArray)):

    for y in range(len(dataArray[0])):

        if dataArray[x,y] == True:

            dataList.append([x,y])

return dataList

```

```

#open the 2D image, convert to grayscale, and invert the colors (black = 0 = baseline; white =
255 = highest elevation)

```

```

img = PIL.ImageOps.invert(Image.open(image_2D).convert("L")) #L converts to grayscale

```

```

#the image is converted in a numpy array, each pixel is converted in a value from 0 to 255

```

```

array = np.array(img)

```

```

#arrayBool will contain a True value, if the value of the numpy array in position [x,y] equals
the section number. In other words, for a given section number (height) only those value will
be selected.

```

```

arrayBool = array == int(section_number)

```

```

#conversion of the arrayBool in a list containing the data points (in x and y values) of the
selected section

```

```

newlist = createScatteredPoints(arrayBool)

```

```

#variables for the plot

```

```

x,y = zip(*newlist)

```

```
#writing of the array values in the csv file

printArrayValuesInCSV(newlist)

print("Section correctly exported into the csv file")

#close csv file

file.close()

#visualization of the plot

plt.scatter(x,y)

plt.title("Section n°" + str(section_number) + " of " + str(image_2D))

plt.axis("equal")

print("\n\nTo terminate the program, close the plot window")

plt.show()
```


4 Additional publications

The following chapter presents additional publications to which I contributed, which lay outside the main scope of my thesis.

Vaccines (2021), 9(1), 8

N-terminal VP1 Truncations Favor T = 1 Norovirus-Like Particles

Ronja Pogan^{1,2}, Victor U. Weiss³, Kevin Bond⁴, Jasmin Dülfer¹, Christoph Krisp⁵, Nicholas Lykтей⁴,
Jürgen Müller-Guhl^{1,6}, Samuele Zoratto³, Günter Allmaier³, Martin F. Jarrold⁴, Cesar Muñoz-Fontela⁶,
Hartmut Schlüter⁵, Charlotte Uetrecht^{1,2}

¹ Heinrich Pette Institute, Leibniz Institute for Experimental Virology, 20251 Hamburg, Germany

² European XFEL GmbH, 22869 Schenefeld, Germany

³ Institute of Chemical Technologies and Analytics, TU Wien, 1060 Vienna, Austria

⁴ Department of Chemistry, Indiana University, Bloomington, IN 47405, USA

⁵ Mass Spectrometric Proteomics Group, Institute of Clinical Chemistry and Laboratory Medicine, University Medical Center Hamburg-Eppendorf, 20246 Hamburg, Germany

⁶ Partner Site Hamburg-Lübeck-Borstel-Riems, Bernhard Nocht Institute for Tropical Medicine and German Center for Infection Research (DZIF), 20359 Hamburg, Germany

<https://doi.org/10.3390/vaccines9010008>

In this study, we investigated the self-assembling properties of the human norovirus major capsid protein VP1, which are crucial for developing VLPs for vaccine production. We focused on understanding the factors influencing capsid size variation, as it is important for producing particles of a defined size that present antigens consistent with intact virions. The study revealed that major truncations in the capsid proteins led to the formation of T = 1 particles, a finding significant for vaccine development and other bio-nanotechnological applications.

Our research involved detailed characterization of VLPs from different norovirus variants, produced in insect cells. We employed biophysical and structural tools, including native mass spectrometry, gas-phase electrophoretic mobility molecular analysis, and proteomics. This comprehensive approach allowed us to gain clear insights into the particle size, structure, composition, and stability of the VLPs.

We identified that noroviruses generally form mainly T = 3 particles, but in this study, a major truncation in the capsid proteins was identified as a likely cause for the formation of T = 1 particles. This discovery has significant implications for the production of bio-nanoparticles, as size-homogeneity is highly favored in vaccine design and other applications.

In summary, our findings contribute to a deeper understanding of capsid assembly and size determination in human noroviruses. This knowledge is essential for developing effective vaccines and VLPs for diverse bio-nanotechnological applications.

INNOVATIVE ASPECTS:

- Uncovered truncations in norovirus capsid proteins lead to specific particle formation, aiding vaccine research.
- Employed a range of advanced analytical techniques for the in-depth characterization of VLPs.
- Provided important insights for vaccine development and bio-nanotechnological applications, emphasizing the importance of consistent, size-specific bio-nanoparticle production.

OWN CONTRIBUTION

In this work, I

- assisted in conducting nES GEMMA experiments and aided with data interpretation.

Article

N-Terminal VP1 Truncations Favor $T = 1$ Norovirus-Like Particles

Ronja Pogan^{1,2}, Victor U. Weiss³, Kevin Bond⁴, Jasmin Dülfer¹, Christoph Krisp⁵, Nicholas Lykтей⁴, Jürgen Müller-Guhl^{1,6}, Samuele Zoratto³, Günter Allmaier³, Martin F. Jarrold⁴, Cesar Muñoz-Fontela⁶, Hartmut Schlüter⁵ and Charlotte Uetrecht^{1,2,*}

- ¹ Heinrich Pette Institute, Leibniz Institute for Experimental Virology, 20251 Hamburg, Germany; ronja.pogan@leibniz-hpi.de (R.P.); jasmin.duelfer@leibniz-hpi.de (J.D.); juergen.mueller@leibniz-hpi.de (J.M.-G.)
 - ² European XFEL GmbH, 22869 Schenefeld, Germany
 - ³ Institute of Chemical Technologies and Analytics, TU Wien, 1060 Vienna, Austria; victor.weiss@tuwien.ac.at (V.U.W.); samuele.zoratto@tuwien.ac.at (S.Z.); guenter.allmaier@tuwien.ac.at (G.A.)
 - ⁴ Department of Chemistry, Indiana University, Bloomington, IN 47405, USA; kmbond@iu.edu (K.B.); nalykтей@iu.edu (N.L.); mfj@indiana.edu (M.F.J.)
 - ⁵ Mass Spectrometric Proteomics Group, Institute of Clinical Chemistry and Laboratory Medicine, University Medical Center Hamburg-Eppendorf, 20246 Hamburg, Germany; c.krisp@uke.de (C.K.); hschluet@uke.de (H.S.)
 - ⁶ Partner Site Hamburg-Lübeck-Borstel-Riems, Bernhard Nocht Institute for Tropical Medicine and German Center for Infection Research (DZIF), 20359 Hamburg, Germany; munoz-fontela@bnitm.de
- * Correspondence: charlotte.uetrecht@xfel.eu

Abstract: Noroviruses cause immense sporadic gastroenteritis outbreaks worldwide. Emerging genotypes, which are divided based on the sequence of the major capsid protein VP1, further enhance this public threat. Self-assembling properties of the human norovirus major capsid protein VP1 are crucial for using virus-like particles (VLPs) for vaccine development. However, there is no vaccine available yet. Here, VLPs from different variants produced in insect cells were characterized in detail using a set of biophysical and structural tools. We used native mass spectrometry, gas-phase electrophoretic mobility molecular analysis, and proteomics to get clear insights into particle size, structure, and composition, as well as stability. Generally, noroviruses have been known to form mainly $T = 3$ particles. Importantly, we identified a major truncation in the capsid proteins as a likely cause for the formation of $T = 1$ particles. For vaccine development, particle production needs to be a reproducible, reliable process. Understanding the underlying processes in capsid size variation will help to produce particles of a defined capsid size presenting antigens consistent with intact virions. Next to vaccine production itself, this would be immensely beneficial for bio-/nano-technological approaches using viral particles as carriers or triggers for immunological reactions.

Keywords: norovirus; capsid assembly; native mass spectrometry; nES GEMMA; differential mobility analysis; CDMS



Citation: Pogan, R.; Weiss, V.U.; Bond, K.; Dülfer, J.; Krisp, C.; Lykтей, N.; Müller-Guhl, J.; Zoratto, S.; Allmaier, G.; Jarrold, M.F.; et al. N-Terminal VP1 Truncations Favor $T = 1$ Norovirus-Like Particles.

Vaccines **2021**, *9*, 8. <https://dx.doi.org/10.3390/vaccines9010008>

Received: 25 November 2020

Accepted: 21 December 2020

Published: 24 December 2020

Publisher's Note: MDPI stays neutral with regard to jurisdictional claims in published maps and institutional affiliations.



Copyright: © 2020 by the authors. Licensee MDPI, Basel, Switzerland. This article is an open access article distributed under the terms and conditions of the Creative Commons Attribution (CC BY) license (<https://creativecommons.org/licenses/by/4.0/>).

1. Introduction

A vast number of nonbacterial gastroenteritis cases worldwide is caused by human noroviruses (hNoVs) [1]. Norovirus infection especially poses an acute threat to children, immunocompromised individuals and elderly people. Already a small number of particles is sufficient for infection [2]. Gastroenteritis outbreaks happen worldwide with new hNoV-variants occurring sporadically.

Human noroviruses are non-enveloped and a member of the *Caliciviridae* family. They have a positive sense, single strand, approx. 7.7 kb RNA genome organized into three open reading frames (ORFs) and a poly(A) tail. ORF1 encodes non-structural proteins, ORF2 the major capsid protein VP1, and ORF 3 the minor structural protein VP2 [3,4].

Based on VP1, noroviruses can be classified into up to ten genogroups (GI-GX) and further into genotypes [5]. Genogroups I, II, IV, VIII, and IX infect humans. The prototypical GI.1 Norwalk was isolated from stool samples in Norwalk, Ohio in 1968 [6]. Today, mostly GII.4 and GII.17 strains have been identified as a cause of viral gastroenteritis outbreaks [7,8].

There is no norovirus vaccine available yet. The lack of a robust cell culture system and small animal models as well as the immense genetic diversity of hNoVs have hindered its development to date. Although breakthroughs in developing a cell-culture system have been made in 2016 by Ettayebi et al. [9], hNoV research has mostly been based on virus-like particles (VLPs). Current vaccine candidates are also using VLPs, mostly GI.1 and GII.4 VLPs. hNoVLPs can be produced by expressing VP1 in various systems, including insect cells, yeast, mammalian cells, and plants [10–13].

Generally, VP1 can be divided into two functionally and structurally distinct domains. The shell (S)-domain, forming a scaffold around the genome, and a protruding (P)-domain. In GI.1 Norwalk, the N-terminal 225 amino acids (aa) belong to the S-domain. The P-domain is further divided into subdomains P1 and an insertion P2, with P2 being most variable and involved in host-attachment and immunogenicity [14,15]. Self-assembling properties of VP1 allow for next to fully formed $T = 3$ particles, particles of several other forms [16]. The isolated P-domain expressed in *Escherichia coli* with or without a tag can form P-dimers as well as 12-mer and 24-mer P-particles [17]. Expression of the S-domain in the baculovirus-expression system results in thin-layered, small, and smooth $T = 3$ particles [18]. In full-length VP1 particles, S- and P-domains are connected via a flexible hinge region [14]. When expressed in eukaryotic systems, caliciviruses generally are known to assemble into VP1 180-mers with $T = 3$ icosahedral symmetry. However, VP1 60-mers of $T = 1$ symmetry have been described as byproducts of hNoVLP production coexisting with other particle sizes and independent of the expression system [19]. Recently, VP1 240-mers of $T = 4$ symmetry have also been described so far only for GII.4 variants expressed in insect cells as well as in plants [20,21]. In studies on virions of different norovirus variants $T = 3$ as well as $T = 1$, formations were detected [22].

Thus, hNoVLP particle sizes are polymorphic and dynamic. Native mass spectrometry (MS) is a perfect biophysical tool to characterize these structural dynamics [23]. Previously, VLPs of three different norovirus variants have been investigated with native MS [24,25]. In our previous work, we established the pH stability pattern of two norovirus variants, GI.1 West Chester and GII.17 Kawasaki [25]. Stability was assessed in different ionic strengths as well as pH levels and compared to results on Norwalk VLPs [24]. In all three variants, $T = 3$ particles were identified as the major population. Furthermore, GII.17 Kawasaki was resistant to changing conditions, while both GI variants disassembled upon alkaline treatment.

In order to characterize hNoVLPs in detail and gain more insights into size determination, we extended our previous native MS studies with a set of biophysical methods. Next to charge detection mass spectrometry (CDMS) for mass determination of heterogeneous particle populations and proteomics, we used nano electrospray gas-phase electrophoretic mobility molecular analysis (nES GEMMA) [26], especially suited to measure high-mass particles at low concentrations [27,28]. Notably, this fast technique allows for measurements at low ionic strength and with less concentrated sample.

We described particle preparations from insect cells with sample batches, where only $T = 1$ particles were detected. A major VP1 truncation was identified in all particle preparations forming these $T = 1$ particles. We found that this size-limitation was genogroup- and genotype-independent and could not be rescued in different buffer conditions. This provides great implications for vaccine design and other applications of bio-nanoparticles, where size-homogeneity is highly favored.

2. Materials and Methods

2.1. VLP Production and Preparation

Full-length VP1 genes for GI.1 West Chester, GII.4 Saga 2006, GII.10 Vietnam, GII.17 Kawasaki308, and GII.17 Saitama T87 (GenBank accession numbers: AY502016.1, AB447457.1, AF504671.2, LC037415.1, AII73747.1) were cloned and expressed in a baculovirus system [29,30]. After transfection of a bacmid containing the recombinant VP1 gene in Sf9 insect cells and incubation for 5–7 days, the culture medium was collected and centrifuged for 10 min at 3000 rpm at 4 °C. Subsequently, Hi5 insect cells were infected with recovered baculovirus and incubated for 5 days. After centrifuging the culture medium for 10 min at 3000 rpm at 4 °C and then 1 h at 6500 rpm at 4 °C, VLPs in the supernatant were concentrated by ultracentrifugation at 35,000 rpm (Beckman Ti45 rotor, Krefeld, Germany) for 2 h at 4 °C. Furthermore, VLPs were further purified using CsCl equilibrium gradient ultracentrifugation at 35,000 rpm (Beckman SW56 rotor, Krefeld, Germany) for 18 h at 4 °C. VLPs were pelleted for 2 h at 40,000 rpm (Beckman TLA55 rotor, Krefeld, Germany) at 4 °C and solved in PBS (pH 7.4).

2.2. VP1 Mapping

Trypsin digestion. For tryptic digestion followed by proteomic analysis, VLP samples in PBS at 15 µM VP1 were separated via sodium dodecyl sulfate polyacrylamide gel electrophoresis (SDS-PAGE) following the reported method [31]. After staining with a solution containing 0.5% Coomassie brilliant blue R250, 50% ethanol, and 7% acetic acid, respective gel bands were cut into small pieces and further processed according to Shevchenko et al. [32]. After digestion, the samples were dried and thereafter dissolved in 0.1% formic acid and transferred into the autosampler. Tryptic peptides were either separated on a nano-UPLC system (Dionex Ultimate 3000 UPLC system, Thermo Fisher Scientific, Bremen, Germany) with a 50 cm C18 analytical column (Acclaim PepMap 100, 75, 3 µm, Thermo Fisher Scientific, Darmstadt, Germany) or a nano-UPLC system (nanoAcquity, Waters, Manchester, Great Britain) with a 25 cm C18 analytical column (BEH C18 Column, 75, 1.7 µm, 100 Å, Waters) using a 60 min gradient with increasing acetonitrile concentration from 2% to 30%. Eluting peptides were desorbed and ionized with an electrospray ionization (ESI) source into a Tribrid mass spectrometer consisting of a quadrupole, linear ion-trap, and an Orbitrap (Fusion; Thermo Fisher Scientific, Bremen, Germany) with the Dionex setup or a quadrupole Orbitrap mass spectrometer (QExactive; Thermo Fisher Scientific, Bremen, Germany) with nanoAcquity setup operated in data-dependent acquisition (DDA) mode. MS/MS spectra were searched with the Sequest algorithm integrated in the Proteome Discoverer software version 2.0, against AY502016.1, AB447457.1, AF504671.2, LC037415.1, AII73747, and a common contaminant protein database. Precursor ion mass tolerance was set to 10 ppm, and fragment ion mass tolerances was set to 0.02 (QExactive) or 0.6 Da (Fusion). Carbamidomethylation was set as a fixed modification on cysteine residues. Acetylation of the protein N-terminus, N-terminal methionine loss, the oxidation of methionine, deamidation of asparagine and glutamine, and glutamine to pyroglutamate on the peptide N-terminus were set as variable modifications. Only peptides with a high confidence (FDR of <1%) using a decoy database approach were accepted as identified.

Pepsin digestion. VLP samples were mixed 1:1 with denaturing buffer (300 mM phosphate buffer, pH 2.3, 6 M urea). Pepsin digestion of 100 pmol VP1 was performed online (Agilent Infinity 1260, Agilent Technologies, Waldbronn, Germany) on a home-packed pepsin column (IDEX guard column with an internal volume of 60 µL, Porozyme immobilized pepsin beads, Thermo Scientific, Darmstadt, Germany) at a flow rate of 75 µL/min (0.4% formic acid in water). Peptides were trapped in a trap column (OPTI-TRAP for peptides, Optimize Technologies, Oregon City, OR, USA.) and separated on a reversed-phase analytical column (PLRP-S for Biomolecules, Agilent Technologies) using a 27 min gradient of 8–40% organic solvent (0.4% formic acid in acetonitrile) at 150 µL/min. MS was performed using an Orbitrap Fusion Tribrid in positive ESI data-dependent MS/MS acquisition mode (Orbitrap resolution 120,000, 1 microscan, HCD 30 with dynamic

exclusion). Precursor and fragment ions were searched and matched against a local protein database containing the proteins of interest in MaxQuant (version 1.5.7.0, Max-Planck-Institute, Munich, Germany) using the Andromeda search engine. The digestion mode was set to “unspecific” and N-terminal acetylation, deamidation, oxidation, and disulfide bond formation were included as variable modifications with a maximum number of 5 modifications per peptide. Peptides between 5 and 30 amino acids length were accepted. The MaxQuant default mass tolerances for precursor (4.5 ppm) and fragment (20 ppm) ions defined for the Orbitrap instrument (Thermo Fisher Scientific, Bremen, Germany) were used for data search. The minimum score for successful identifications was set to 20 for unmodified and 40 for modified peptides.

The mass spectrometry proteomics data have been deposited to the ProteomeXchange Consortium via the PRIDE [33] partner repository with the dataset identifier PXD023182.

2.3. Sample Preparation

For mass spectrometry as well as nES GEMMA analysis, hNoVLP sample solutions were exchanged to 40 and 250 mM ammonium acetate solutions. Solution pH was adjusted between 5 and 9 using acetic acid and ammonia. For the solution exchange, Vivaspin 500 centrifugal concentrators (10,000 MWCO, Sartorius, Göttingen, Germany) or Zeba micro spinTM desalting columns 0.5 mL (7000 MWCO, Thermo Fisher Scientific, Rockford, IL, USA) were used. Generally, 5 filtration steps using spin filters and 3 steps using size-exclusion columns were employed. Samples were diluted to 10 μ M VP1 protein or further diluted, if necessary, to obtain spectra.

2.4. Mass Spectrometry

Conventional native MS measurements of VLPs were performed using a quadrupole time-of-flight (QToF) instrument Q-ToF 2 (Waters, Manchester, UK and MS Vision, Almere, the Netherlands) modified for high mass experiments [34]. For ESI, capillaries were handmade by pulling borosilicate glass tubes (inner diameter 0.68 mm, outer diameter 1.2 mm with filament, World Precision Instruments, Sarasota, FL, USA) using a two-step program in a micropipette puller (Sutter Instruments, Novato, CA, USA) with a squared box filament (2.5×2.5 mm). Gold-coating of capillaries was performed using a sputter coater (Quorum Technologies., East Sussex, UK, 40 mA, 200 s, tooling factor of 2.3 and end bleed vacuum of 8×10^{-2} mbar argon or Safematic (Zizers, Switzerland), process pressure 5×10^{-2} mbar, process current 30.0 mA, coating time 100 s, 3 runs to vacuum limit 3×10^{-2} mbar Argon). Capillaries were opened on the sample cone of the mass spectrometer. Using a nanoESI source, ions were introduced into the vacuum at a source pressure of 10 mbar. The positive ion mode was used to record spectra. Generally, voltages of 1.45 kV and 165 V to the capillary and cone, respectively, were used and adjusted during spray-optimization. Xenon was used as a collision gas at a pressure of 1.7×10^{-2} mbar in order to enable better transmission of high-mass ions [35]. MS profile and repetition frequency of the pusher pulse were adjusted to high mass range. For instrument calibration, a cesium iodide spectrum was recorded the same day. Analysis was performed using MassLynx V4.1 SCN 566 (Waters, Manchester, UK) and Massign [36].

Charge detection mass spectrometry (CDMS) was performed on a home-built CDMS instrument described in detail elsewhere [37] in order to enable measurements of heterogeneous complexes in the MDa range or larger. Briefly, charge and m/z of single ions are measured simultaneously using a charge conduction cylinder and electrostatic ion trap. In contrast to conventional QToF MS, CDMS sidesteps the need for charge states to be assigned. Ions were generated using an automated nano-ESI source (Nanomate, Advion, Ithaca, NY, USA) with a capillary voltage of approximately 1.7 kV. After entering a heated metal capillary, ions are transmitted using various ion optics to a dual hemispherical deflection energy analyzer, which selects ions with energies centered on 100 eV/z. Subsequently, ions enter a modified cone trap where they oscillate back and forth in a charge detection

cylinder for 100 ms. Single ion masses were binned to generate mass spectra. Mass spectra were analyzed by fitting Gaussian peaks with Origin software (OriginPro 2016).

Gas-phase electrophoresis was performed on a nES GEMMA instrument (TSI Inc, Shoreview, MN, USA) consisting of a nES aerosol generator (model 3480) including a ^{210}Po α -particle source, an electrostatic classifier (model 3080) with a nano differential mobility analyzer (nDMA), and an n-butanol based ultrafine condensation particle counter (model 3025A). Briefly, particle-size determination is a function of the particles' trajectory in the nDMA chamber. The trajectory of a size-specific particle is based on the sheath flow of particle-free ambient air and an orthogonal electric field applied. Therefore, with a constant high laminar sheath flow of air and a variable electrical field, only specific particle sizes can successfully be transported to the particle counter device for detection. For electrospraying, polyimide-coated fused silica capillaries (25 μm inner diameter, Polymicro, obtained via Optronis, Kehl, Germany) with in-house-made tips [38] were used. Settings for a stable Taylor cone at the nES tip were chosen, typically around 2 kV, resulting in approx. -375 nA current, 0.1 L/min CO_2 (Messer, Gumpoldskirchen, Austria), and 1.0 L/min filtered, dried ambient air. Four pounds per square inch differential (psid, approx. 27.6 kPa) were applied to additionally move the sample through the capillary, and 15 L/min sheath flow filtered ambient air was used to size-separate VLPs in an electrophoretic mobility diameter (EMD) range from 2 to 65 nm. The corresponding EMD size range was scanned for 120 s. Subsequently, the applied voltage was adjusted to starting values within a 30 s timeframe. Seven datasets (raw data obtained from instrument software, MacroIMS manager v2.0.1.0) were combined via their median to yield a corresponding spectrum. Lastly, Gauss peaks were fit to spectra via Origin software (OriginPro 2016) to obtain EMD values. EMD values were correlated to particle mass using MW-correlation either based on proteins [39] or VLPs [28].

2.5. Electron Microscopy

For imaging using transmission electron microscopy (EM), hNoVLPs stored in PBS were adsorbed onto glow discharge-activated carbon-coated grids (Science Services, Munich, Germany). After three consecutive washing steps with distilled water, the sample coated grids were stained with 1% uranyl acetate. Image acquisition was performed using a FEI TecnaiTM G2 transmission electron microscope and wide-angle Veleta CCD camera (FEI, Thermo Fisher Scientific, USA and Olympus, Tokyo, Japan) at 80 kV.

3. Results

3.1. Truncated GII.4 Saga VP1 Forms Homogeneous $T = 1$ Particles

Here, we extended our previous investigations on GI.1 West Chester and GII.17 Kawasaki to other hNoVLP constructs. VLPs of an outbreak strain GII.4 Saga are produced in the same baculovirus-expression system. Native mass spectra reveal the lack of $T = 3$ particles at neutral pH and moderate ionic strength (Figure 1). Notably, the identified peak distribution is almost baseline resolved, indicating a highly homogeneous population annotated to VP1 60-mers or $T = 1$ particles. An additional, unresolved peak distribution around 15,000 m/z relates to metastable ions. Metastable ions are commonly accompanying high-mass ions as these disintegrate partially in the ToF-analyzer, as such they cannot be targeted by selection in the quadrupole, allowing differentiation from ions originating from the sample solution. Figure 1 also illustrates collision-induced dissociation (CID) products for GII.4 Saga. The $T = 1$ ions ($\sim 150+$ charges) dissociate via consecutive losses of VP1 monomers, with at least two subspecies in mass, as well as corresponding high mass ions, VP1 59-mer, 58-mer, and 57-mer. Mass-assignment of the dissociated monomer suggests an N-terminal truncation of 45 amino acids (aa) of the main species and a subpopulation lacking 45 aa. Proteomics data following trypsin-digestion as well as pepsin-digestion (Table 1) results in VP1 sequence coverage of 95 and 90% with the N-terminal coverage starting from residues 25 and 27, indicating additional subpopulations, which are low abundant. Notably, the C-terminus is complete up to several arginine residues (C-terminal

three to six residues), which exclude coverage for both proteins due to small peptides. This suggests exclusive N-terminal truncation. An assembly into a 60-mer of the full-length VP1 would result in a theoretical $T = 1$ mass of 3.54 MDa, and VP1 lacking 45 aa would form 3.28 MDa $T = 1$ particles. The assigned mass of 3.27 MDa using QToF MS and 3.35 MDa using native CDMS (Supplementary Table S1; note, masses in CDMS are always higher, indicating incomplete desolvation) suggests that detected 60-mer particles are indeed formed mainly from VP1 lacking at least 45 aa. To conclude, in this case, heterologous expression of GII.4 Saga VP1 results in a truncated VP1 species with the mere ability to form $T = 1$ but not $T = 3$ particles.

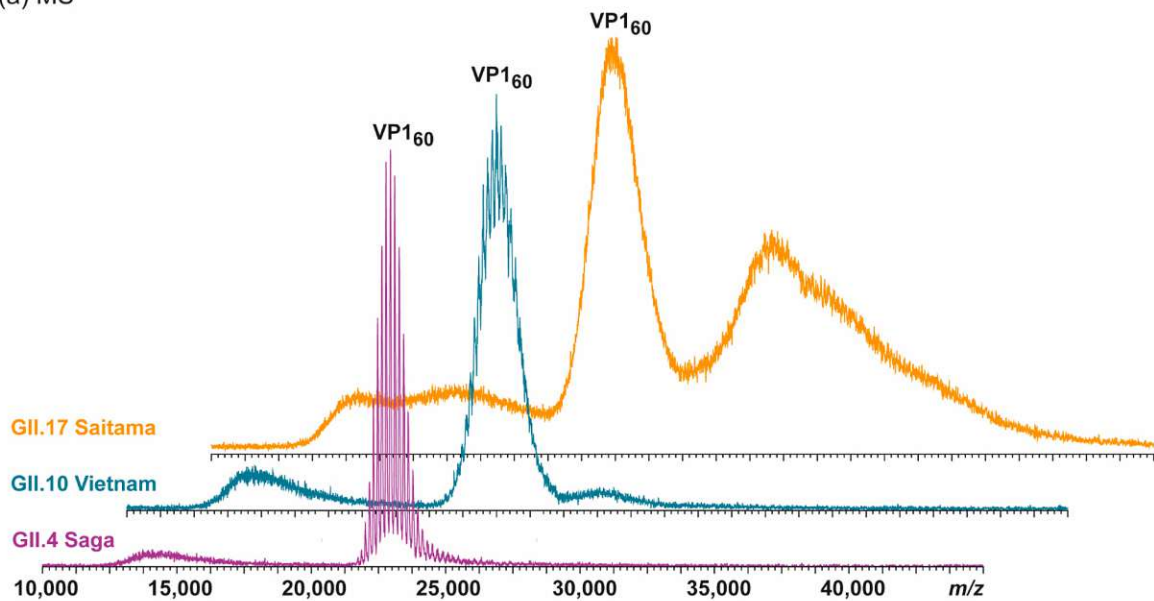
3.2. $T = 1$ Capsid Formation Is Genotype-Independent

Additional hNoVLPs were investigated to pinpoint whether the truncation seen in GII.4 Saga causes $T = 1$ formation. Norovirus-like particle polymorphism has been described as putatively genotype-dependent [20,21,40]. Therefore, we extended our sampling to GII.10 Vietnam and GII.17 Saitama (Figure 1). In line with GII.4 Saga measurements, most abundant peak distributions were assigned to VP1 60-mers for both variants. Notably, more acceleration energy compared to GII.4 Saga was needed to gain charge-resolution for VP1 60-mer peaks, which indicated increased VP1 heterogeneity in these samples (Supplementary Figure S1). Furthermore, $T = 1$ ions in GII.10 Vietnam showed tailing with a non-resolved shoulder peak, indicating either aggregation or a further low-intensity assembly of slightly higher mass. In GII.17 Saitama mass spectra, heterogeneity was even more prominent as multiple higher-mass assemblies gave rise to complex ion distributions between 30,000 and 40,000 m/z . GII.17 Saitama ion distributions were overlapping with the respective $T = 3$ m/z range observed in previous mass spectra, but clear mass assignment was hindered due to high heterogeneity in the sample. Dissociated VP1 monomer species for all listed variants except GII.17 Saitama, where signal intensities were too low for selective dissociation experiments and monomer mass was inferred from CDMS (Table S1), are listed in Table 1. If a similar incomplete desolvation for GII.17 Saitama as for GII.4 Saga was assumed in CDMS, the VP1 monomer mass further reduced by ~1500 Da corresponding to an additional 14 aa missing, resulting in a total of 31 aa, closer to the values observed for the other hNoVLPs. Mutual in most VP1 monomer measurements was a major truncation of at least 45 aa (45 aa in GII.4, 45 aa in GII.10, and 17 aa/31 aa in GII.17). Although VP1 truncation was similar in all three variants, the putative cleavage site did not reside in a conserved region, and a putative protease could not be assigned (Table 1).

3.3. Heterologous Expression of GI.1 West Chester Results in Either $T = 1$ or $T = 3$ Preparations

To provide further evidence of truncation influence, we compared two GI.1 West Chester batches. Batch 1 is identical to the sample used in our previous work [25]. In the second batch, no $T = 3$ particles were detected at neutral pH using native MS (Figure 2). The main peak distribution was assigned to $T = 1$ particles, which was accompanied by a low-intense shoulder peak comparable to GII.10 Vietnam. At increased acceleration voltage, the $T = 1$ ions released VP1 monomers. A close-up of these monomers showed that at least two subspecies were present. This directly contributed to heterogeneity and therefore low peak resolution of higher-mass species. The dominating VP1 species was assigned to $52,760 \pm 10$ Da, or the theoretical VP1 mass lacking 40 N-terminal aa. Proteomics data, which hinted to subspecies with minor truncations, was consistent with other variants tested in this study (Table 1). In our previous study, we could identify GI.1 West Chester VP1 monomers with the major species lacking only three amino acids, forming mainly $T = 3$ particles [25]. Taken together, we can assume that with the VP1 N-terminus of GI.1 West Chester lacking three amino acids the formation of $T = 3$ particles is possible, while with an expanded truncation of 40 amino acids this is no longer the case.

(a) MS



(b) MS/MS GII.4 Saga

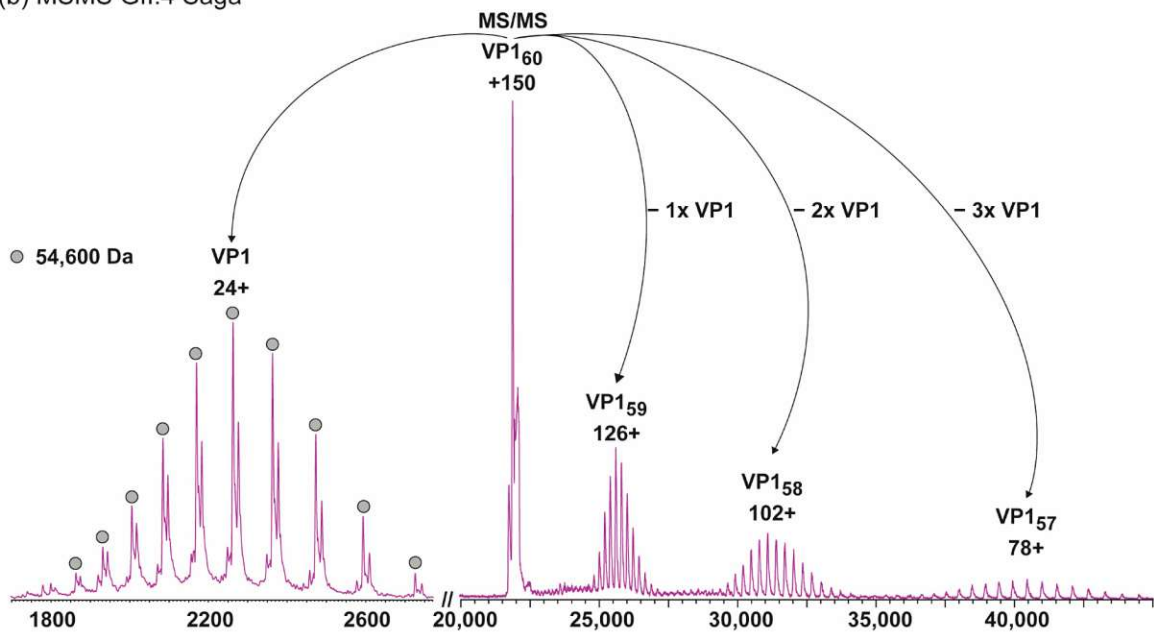


Figure 1. Native MS of different human norovirus-like particles (hNoVLPs) suggests that a major truncation of VP1 leads to $T = 1$ particles. (a) From bottom to top spectra of GII.4 Saga (purple), GII.10 Vietnam (blue), and GII.17 Saitama (orange) in 250 mM ammonium acetate pH 7 at 10 μ M VP1 are shown. All variants have main ion distributions between 20,000 and 25,000 m/z , which are assigned to VP1₆₀ complexes. GII.10 Vietnam and especially GII.17 Saitama also form larger assemblies as indicated by additional signal above 25,000 m/z . (b) Collision-induced dissociation MS/MS is shown exemplarily for GII.4 Saga. The dissociation of the 150+ charged VP1 60-mer into VP1-monomer (top left) and residual VP1 59-, 58-, and 57-mer (top right) is shown. Charge states and average monomer mass are annotated. The MS/MS confirms stoichiometry assignment and reveals monomer truncation.

Table 1. Overview of investigated samples forming mainly $T = 1$ particles. Theoretical (th.) VP1 mass and amino acid (aa) number given for constructs West Chester, Saga, Vietnam, and Saitama constructs. Experimental (exp) mass and truncation given for main observed monomeric species after dissociation in conventional MS for all variants except GII.17 Saitama. For Saitama, mass was approximated using charge detection mass spectrometry (CDMS) (Table S1, for nMS see Table S2). MW: Molecular weight.

Variant	VP1 th.	VP1 exp.	Putative Cleavage Site	Trypsin Digestion	Pepsin Digestion
	MW, Total MW Truncation	Main Species MW Truncation	According to exp. VP1 MW	Sequence Coverage %, Minimal N-terminal Truncation	
GI.1 West Chester	56,609 Da, 530 aa	52,760 Da, −40 aa	LAMDVPVAGSS/TAVATAGQVN	80%, −6 aa	98%, −2 aa
GII.4 Saga	59,005 Da 540 aa	54,600 Da, −45 aa	AIAAPVAGQQ/NVIDPWIRNN	95%, −25 aa	90%, −27 aa
GII.10 Vietnam	59,901 Da 548 aa	55,560 Da, −aa	SLAAPVTGQT/NIIDPWIRMN	95%, −27 aa	94%, −27 aa
GII.17 Saitama	58,957 Da 540 aa	57,300 Da, −17 aa	SNDGATGLVP/EINNETLPLE	91%, −32 aa	99%, −3 aa

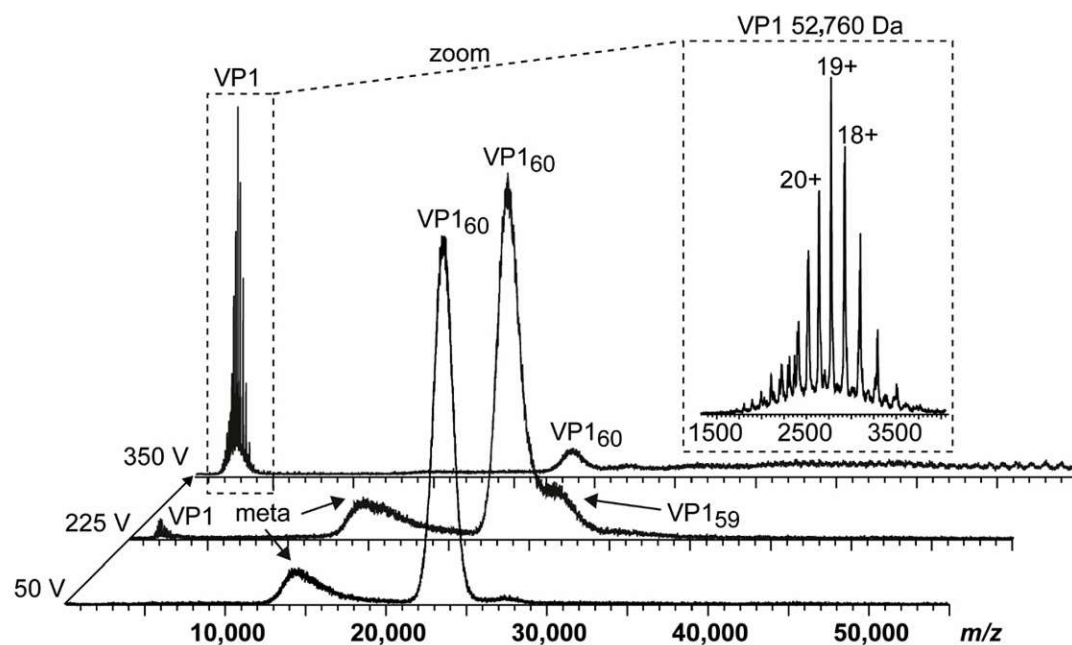


Figure 2. Native MS of a GI.1 West Chester batch forming merely VP1₆₀ complexes. Dissociation pathway without selection in the quadrupole is shown for GI.1 West Chester in 250 mM ammonium acetate pH 7 at 10 μ M VP1. From bottom to top, illustrative mass spectra are shown for 50, 225, and 350 V acceleration into the collision cell. While at 225 V, VP1 monomers dissociate with the main population of VP1 60-mer still intact, the signal ratio of VP1 monomer:60-mer is reversed at 350 V. An insert shows a zoom of dissociated VP1 monomer with annotated charge states and average mass. As lower mass ions at approximately 15,000 m/z are annotated as metastable ions (meta), monomer lacking at least 40 aa most likely dissociate from $T = 1$ species.

Furthermore, we characterized particle size and stoichiometry in further detail using nES GEMMA. Measurements of both GI.1 West Chester preparations are superimposed in Figure 3. In order to exclude artefacts, all samples were measured at different dilutions (Supplementary Figure S2). Putative artefacts included unspecific, nES-based aggregates at high sample concentrations, as well as multiply charged particles obtained at low

percentage values during charge equilibration in the bipolar atmosphere of the spray chamber. Comparison of both batches at neutral pH reveals a clear shift in particle size and their counts. In the first GI.1 West Chester batch, most prominent particle counts were at 34.37 ± 0.13 nm, which was assigned to $T = 3$ particles. Further particle counts at 8.10 ± 0.05 and 24.09 ± 0.27 nm were assigned to VP1 dimer and VP1 60-mer. nES GEMMA spectra of the second batch showed a predominant species at 24.50 ± 0.12 nm equaling $T = 1$, as well as a species with low counts at 30.71 ± 0.17 nm. The population at 30.71 nm was assigned to 6.24 MDa using VLP correlation fitting approximately 120 VP1 (Table S3) [28]. At pH 9, high-mass particles in batch 1 were fragile, complementing our previous findings with native MS [25], while the $T = 1$ VLPs in batch 2 were resistant to pH 9. Other particles in the second batch bigger than 24.18 ± 0.06 nm disappeared. Interestingly, comparing EMDs of this 60-mer species at neutral pH and pH 9 did not indicate swelling or shrinking of the particles. Notably, the VP1 dimers released in alkaline conditions were slightly smaller in the second batch in line with the observed truncation. Moreover, size difference was not observed for $T = 1$ particles in the two batches in line with an N-terminal truncation located at the inner face of the capsids. We can conclude that no $T = 3$ particles were detected with nES GEMMA in the second West Chester batch, which indicated that at least a certain amount of full-length or less truncated VP1 subpopulation was needed to form $T = 3$ particles. Intermediate-sized populations could stem from either truncated, full-length VP1, or a mixture.

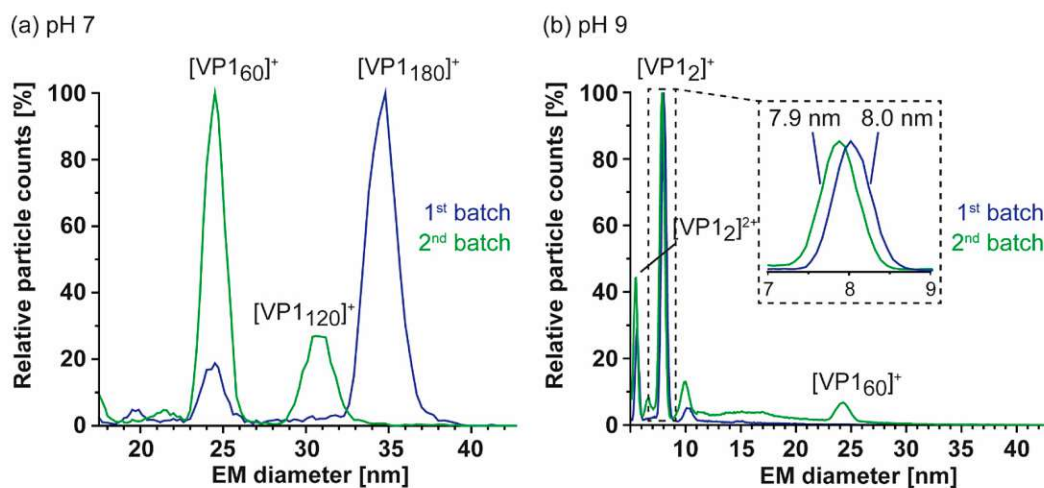


Figure 3. Comparison of two GI.1 West Chester VLP preparations using nano electrospray gas-phase electrophoretic mobility molecular analysis (nES GEMMA). Illustrative spectra are shown for both samples in 40 mM ammonium acetate at pH 7 (a) and pH 9 (b) at approximately 2–10 μ M VP1. Depicted are exemplary spectra for two batches in blue (1) and green (2). (a) Batch 1 shows a clear pattern with a main population of 34.37 ± 0.13 nm and less particle counts at 24.09 ± 0.27 nm, assigned to VP1 180-mer and VP1 60-mer. In batch 2, VP1 60-mer detected at 24.50 ± 0.12 nm is the most abundant species. Furthermore, a species at 30.71 ± 0.17 nm assigned to VP1 120-mer is present and VP1 180-mer is missing. (b) At pH 9, no VP1 complexes other than VP1 dimer were detected for batch 1. The second batch shows a small particle distribution at 24.18 ± 0.06 , indicating higher stability of VP1 60-mers. A zoom at the electrophoretic mobility diameter (EMD) range depicts a minor difference in VP1 dimer size of 8.03 ± 0.01 nm for batch 1 and 7.89 ± 0.01 nm for batch 2. For both conditions, the shown EMD range was adjusted and the complete range including multiply charged species in the low EMD range are shown in Supplementary Figure S2.

3.4. Detailed nES GEMMA and CDMS Profiling

As nES GEMMA is fast and sensitive, all samples were further profiled to see if $T = 3$ assemblies could be rescued and/or $T = 1$ particles from truncated VP1 were in general

more stable at alkaline pH. At neutral pH and low ionic strength, particle size patterns of all variants were in line with conventional native MS. Next to the GI.1 West Chester second batch, GII.4 Saga and GII.10 Vietnam formed $T = 1$ particles but not $T = 3$ particles. GII.17 Saitama showed some signals, which may have originated from $T = 3$ particles. Similar to the low-count species in GI.1 West Chester batch 2 of 30.71 ± 0.17 nm (120-mer), in GII.4 Saga and even more prominent in GII.10 Vietnam, further particles were detected at around 33 nm, equaling 7.7 MDa (VP1 140-mer). In line with native MS data, enormous heterogeneity was observed in GII.17 Saitama, and multiple species other than VP1 60-mer could be distinguished with nES GEMMA (Figure 4). Measurements at pH 5 up to pH 9 revealed that $T = 1$ formations of all samples were mostly resistant to changing solution conditions (Figure 5). Starting from pH 8, free VP1 dimer was detected in all variants in low counts. At pH 9, GII.10 Vietnam and GII.17 Saitama showed reversed particle count ratios of VP1 60-mer and VP1 dimer and larger assemblies did not disintegrate. In GII.4 Saga, no complexes were detected at pH 9 and the employed low VP1 concentrations. However, GII.4 Saga 60-mers remained intact at alkaline pH and low ionic strength in conventional native MS measurements at $10 \mu\text{M}$ VP1 (50 mM ammonium acetate, Supplementary Figure S3). For all samples, particle-size patterns were also consistent at pH 5, although with lower particle counts and with increased background noise. Taken together, this indicated that $T = 1$ particles were highly stable, resisting alkaline pH, and $T = 3$ particle formation could not be rescued by changing solution conditions.

So far, several different size-populations have been detected outside the scope of the Caspar–Klug capsid assembly theory [41], where multiples of 60 (with 120 being formally not allowed) form particles of icosahedral symmetry. CDMS measurements in conditions comparable to our conventional QToF measurements at 250 mM ammonium acetate were used to unambiguously assign such assemblies (Figure 6). For GII.4 Saga, no species but $T = 1$ particles were observed in sufficient counts to fit peaks. Albeit peaks at approximately 33 nm appeared in low-salt nES GEMMA measurements, no respective peak could be assigned to VP1 140-mer with CDMS. At notably lower ion counts, GII.10 Vietnam showed $T = 1$ particles, as well as two further species with approximately 4.5 and 6.9 MDa assigned to VP1 79-mer and VP1 121-mer, respectively. Note that those species were approximations due to very low counts, and stoichiometry was based on assuming that 60 VP1 formed the 3.41 MDa population. For both variants, the VP1 mass inferred from the 60-mer was higher than determined in conventional native MS (CDMS/nMS: GII.4 Saga 55.8/54.6 and GII.10 Vietnam 56.8/55.6 kDa). This indicated mixed subpopulations of different VP1-size forming particles or less efficient desolvation in CDMS compared to QToF measurements. Notably, the species at 4.5 MDa was repetitive in GII.10 Vietnam, as well as GI.1 West Chester batch 1 (Supplementary Figure S4). In GII.17 Saitama, CDMS helped to elucidate mass heterogeneity observed in the other methods. Next to a distinct population of 3.44 MDa assigned to VP1 60-mer, five additional high mass species could be deconvoluted. CDMS clearly showed the absence of fully-formed $T = 3$ particles. Proteomics data for Saitama indicated a subpopulation of VP1 with a minor truncation of 3 aa. This subpopulation would putatively be able to form $T = 3$ particles in low amounts, which would likely be prone to disassemble at varying concentrations, ionic strengths, and pH levels. Given a mass of approximately 57.3 kDa, CDMS Saitama high-mass species fit VP1 71-, 91-, 100-, 108-, and 120-mers. In contrast, the stability at alkaline pH and low concentrations of these species suggested distinct assemblies. Particle size-heterogeneity was also observed using EM (Figure S5), where various larger assemblies were detected in GII.17 Saitama micrographs. Moreover, although formally not allowed according to triangulation theory, observed VP1 intermediates were repeatedly found in all tested variants and with different techniques.

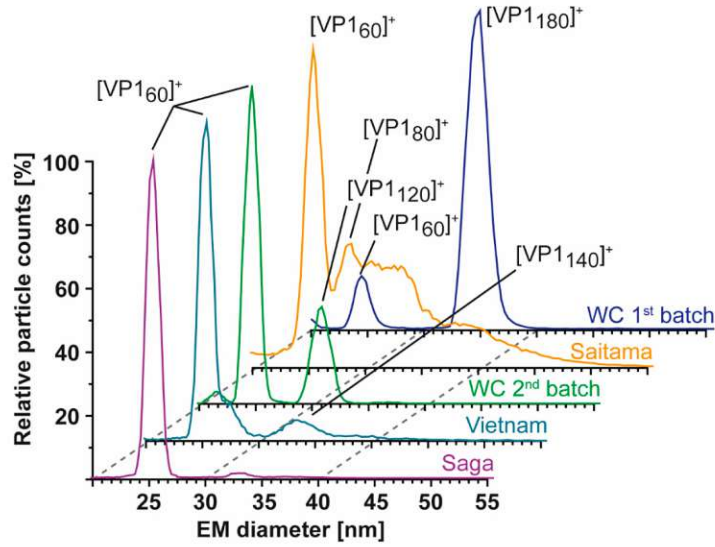


Figure 4. Size-distribution overview of different hNoVLPs with nES GEMMA. All variants are measured at 40 mM ammonium acetate pH 7 and approximately 2–10 μ M VP1. From bottom to top GII.4 Saga (purple), GII.10 Vietnam (light blue), GI.1 West Chester batch 2 (WC, green), GII.17 Saitama (orange), and GI.1 West Chester batch 1 (WC, dark blue). West Chester batch 1 is shown as an indication of the expected EMD range for $T = 3$ particles. Assigned species are annotated. VP1 60-mers were detected in all variants, with less counts in WC batch 1. Next to 60-mers, GII.4 Saga and GII.10 Vietnam show distributions at approx. 33 nm assigned to VP1 140-mer, and WC second batch shows a distinct peak at 30 nm assigned to VP1-120mer. In GII.17 Saitama, at least two peaks can be fitted in the particle distribution accompanying VP1 60-mer annotated as VP1 80-mer and putatively VP1 180-mer.

(a) GII.4 Saga

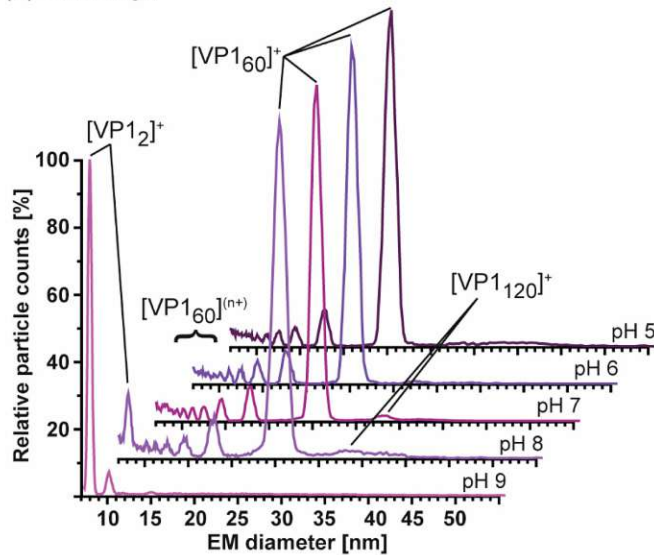


Figure 5. Cont.

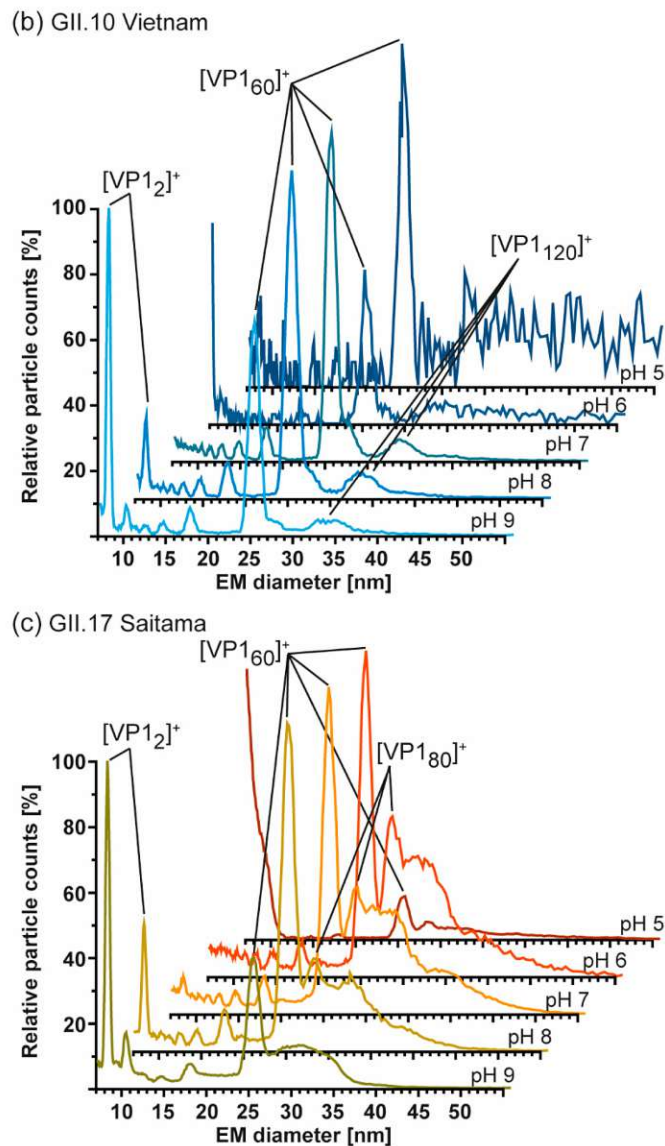


Figure 5. Measurements at different pH of hNoVLPs with GEMMA indicates high pH-resistance of $T = 1$ particles formed from truncated VP1. All measurements were performed at 40 mM ammonium acetate at pH 5–9 from top to bottom at approximately 2–10 μM . (a) GII.4 Saga (purple) shows mainly VP1 60-mer accompanied by multiply charged VP1-60-mer. Particle patterns differ only at pH 8, where VP1 dimers are present in low counts as well as pH 9, where merely VP1 dimer is detected. (b) GII.10 Vietnam (blue) shows intact $T = 1$ particles at all tested pH values. Increased particle counts at pH 7–9 are accompanied with multiply charged VP1 60-mer. Disassembly into VP1 dimer is seen at pH 8 but is only resulting in less VP1-mer counts at pH 9. This pattern is comparable to measurements of GII.17 Saitama (c). Here, main VP1-mers are accompanied by heterogeneous subspecies, which are reduced under alkaline conditions.

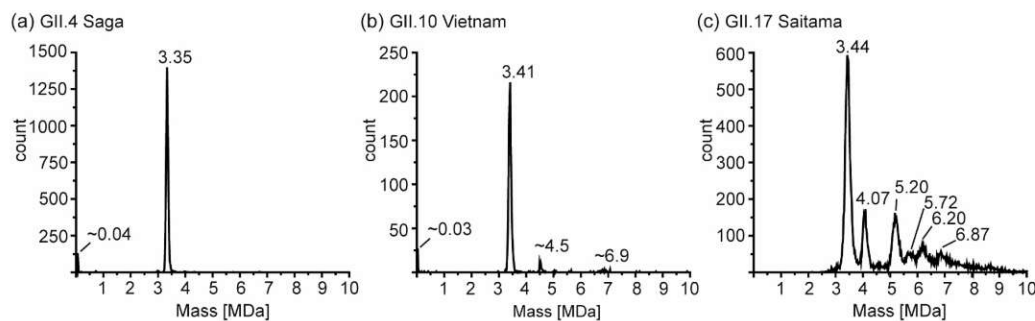


Figure 6. Charge detection mass spectrometry of hNoVLPs at 250 mM ammonium acetate pH 7 and 10 μ M VP1. Illustrative spectra shown for (a) GII.4 Saga (b) GII.10 Vietnam, and (c) GII.17 Saitama. Distinct peaks are annotated; for GII.4 Saga and GII.10 Vietnam low-count species, masses are approximations.

4. Discussion

In this study, different hNoVLP variants were investigated with a set of biophysical tools in order to obtain insights into particle size, stoichiometry, and shape. hNoVLP preparations forming $T = 1$ particles were identified. $T = 1$ particles were repeatedly described in hNoVLP preparations [19,21,24,25]. In our previous study, $T = 1$ and $T = 3$ particles were coexisting in GI.1 West Chester and GII.17 Kawasaki preparations at neutral pH. In line with a former study on GI.1 Norwalk [24], GI.1 West Chester formed $T = 3$ particles, which were prone to disassemble in alkaline pH [25]. Here, we identified a major VP1 N-terminal truncation of more than 40 aa in several hNoV variants, leading to $T = 1$ particles only. The origin of this truncation was unclear. As no clear conserved cleavage motif could be identified, various or unspecific proteases were proposed, likely originating from the insect cell expression system [42,43]. Moreover, this pointed at a structurally defined proteolytic site, which was in line with the flexibility observed in the N-terminal arm. Notably, in all investigated preparations, less populated subspecies with limited truncations building the observed particle formations could not be excluded as proteomics data suggest. This was further supported by a $T = 1$ structure from cryo-EM [21], which showed no electron density for the N-terminal stretch, indicating that it was either flexible or absent in the preparation.

The ability of truncated VP1 to form mainly $T = 1$ particles was genogroup- and genotype-independent, as several hNoV variants were targeted here. This indicated a major truncation was sufficient for VP1 to form $T = 1$ only, and therefore, homogenous, small-sized hNoVLP production was reproducible. Interestingly, several intermediate species were observed repeatedly. In GI.1 West Chester batch 2, GII.4 Saga, and GII.10 Vietnam intermediates were detected in very low proportions. In GII.17 Saitama, spectra suggested a heterogeneous size distribution of several high-mass species with increased counts. A repetitive species that overlapped between preparations was VP1 120-mer. VP1 dimer has been described as a building block for capsid assembly, which suggests that intermediate species must be even integers [14,15,40,44]. Therefore, GII.17 Saitama CDMS measurements resulting in odd numbered complexes were rounded here. Using a combination of characterizing tools like nES GEMMA, conventional MS, and CDMS, VP1 120-mer appeared biologically relevant, although not allowed according to triangulation theory [41]. Moreover, the agreement in GEMMA mass assignment based on a VLP calibration and CDMS revealed that these assemblies resemble hollow spheres like regular capsids. Putative, non-allowed $T = 2$ particles were described for bluetongue virus and brome mosaic virus among others [45–47]. Another intermediate observed in different hNoVLP preparations was VP1 80-mer. Interestingly, it was detected in preparations, in which $T = 3$ particles were also observed like GI.1 Norwalk [24], GI.1 West Chester [25] (Supplementary Figure S4). This indicated different behavior of full-length and truncated

VP1 and mixtures thereof. General observed particle plasticity suggested that these species could be trapped formations or overgrown particles, as observed for hepatitis B virus and woodchuck hepatitis virus [48,49]. However, it has to be noted that assemblies have specific sizes as evident from CDMS, rather than covering a broad distribution. The inability to form full $T = 3$ particles indicated that the N-terminus was required to form flat C/C dimers, leading to lattice expansion. We already proposed an influence of the N-terminus in capsid size determination in our previous study [25]. In turn, the truncated VP1 would likely form mainly bent A/B-like dimers, forming the pentameric vertices present in both VLP formations. This would then likely preclude $T = 2$ capsids. An alternative assembly route would follow octahedral symmetry, which has been described for SV40 polyomavirus [50]. This requires strongly bent dimer interactions and a 24-mer octahedron formed from pentamers exactly matching the VP1 120-mers detected here. This interpretation was further appealing as it offered an explanation for the aberrant GII.17 Saitama assemblies of 70/72, 90/92, 100, and 108/110 VP1 subunits being octahedrons lacking multiple pentamers. Polymorphism in hNoVLP production, independent of the expression system, have been described both for VP1 forming $T = 1$ and $T = 3$ particles at neutral pH levels and intermediates upon changing conditions. In an assembly study on GI.1 Norwalk, three N-terminal deletion mutants were compared [18]. Full-length as well as deletion of N-terminal 20 aa still resulted in $T = 3$ particles. Deletion of 34 and 98 aa N-terminally did not result in any particles detectable with electron microscopy. However, N-terminal 34 aa mutant expression was described as low, hampering the assessment of how this deletion is involved in capsid assembly. Furthermore, N-terminal deletions of 26 and 38 aa were introduced in GII.4 Sydney VLPs. Both constructs were found to form mainly small particles when examined with electron microscopy [51]. Next to deletion itself, culture conditions were also described as a putative reason for size heterogeneity. Another attempt to gain size-homogeneity in hNoVLP preparations was performed by Someya et al. using GI.4 Chiba VLPs [52]. Truncation of 45 aa N-terminally, similar as observed in this study, was identified and the subsequent introduction of a mutation Leu43Val in this region resulted in the formation of merely $T = 3$ particles. However, in a follow-up study, GI.4 Chiba mutants were shown to form 23 nm or $T = 1$ particles, putatively due to freezing and thawing of preparations or pH-dependent processes [53]. Previously, $T = 4$ particles were identified in hNoVLP preparations [20,21]. Interestingly, one study included GII.2 Snow Mountain virus forming $T = 1$ particles [21]. Here, residues 1 to 46 were not covered in electron density maps. Hence, truncation as the origin of small particles similar to our observations could not be excluded.

Next to particle size distribution, the influence of solution pH was investigated. $T = 1$ particles, as well as higher-mass assemblies in GII.17 Saitama, were found to be pH-independent. Moreover, in preparations forming mainly $T = 1$ particles, like GI.1 West Chester batch 2, $T = 1$ particles showed increased stability in alkaline conditions. Therefore, truncated VP1 was able to build particles with increased stability. This implies great advances for bio-nanotechnology, as especially in approaches using VLPs as carrier particles, they need to be stable independently of environmental conditions. The contribution of the N-terminus to pH stability suggests a way to obtain S-particles of increased stability by truncation.

5. Conclusions

There is no hNoV vaccine available yet and hNoVLP size polymorphism could contribute to this circumstance. Therefore, N-terminally truncated particles have great potential to be beneficial as they imply size homogeneity. An N-terminal truncation of VP1 also leaves P-domains and therefore protrusions on assembled particles intact, as evident from EM data on all tested variants. Studies on P-particles imply the necessity of protrusions for antigen recognition and immunogenicity [54]. Furthermore, P-particles were shown to putatively enable other immunological approaches like antigen presentation [55]. There are clear structural differences between $T = 1$ particles of truncated VP1 and P-particles as the

S-domain is missing in the latter. Furthermore, the S-domain is generally more conserved among hNoVs, putatively allowing induction of cross-reactive antibodies. Orientation of dimeric protrusions, and therefore their interaction is likely to be different in P-particles missing the S-domain, truncated VP1 $T = 1$ or full-length $T = 3$ particles. Whether this affects antibody raising and therefore immunogenic reaction needs to be investigated. Additionally, increased stability would likely allow for simplified and prolonged storage. Our results indicate that such small particles from truncated VP1 can be produced independent of genotype by introducing N-terminal deletion mutants.

Supplementary Materials: The following are available online at <https://www.mdpi.com/2076-393X/9/1/8/s1>, Figure S1: Native MS of a GII.10 Vietnam VLPs, Figure S2: GEMMA spectra of different hNoVLPs in 40 mM ammonium acetate at pH 7, 3 different tested dilutions exemplarily shown for (a) West Chester batch 1, (b) West Chester batch 2, (c) GII.4 Saga, (d) GII.10 Vietnam, and (e) GII.17 Saitama, Figure S3: Native mass spectrum of GII.4 Saga VLPs at 50 mM ammonium pH 9 at 10 μ M VP1, Figure S4: Charge detection mass spectra of GI.1 West Chester batch 1 VLPs in 250 mM ammonium acetate at (a) pH 7 and (b) pH 8, Figure S5: Electron micrographs of different hNoVLPs in PBS, Figure S6: VP1 mapping overview of hNoVLP GI.1 West Chester batch 1 after pepsin digestion, Figure S7: VP1 mapping overview of hNoVLP GI.1 West Chester batch 2 after pepsin digestion, Figure S8: VP1 mapping overview of hNoVLP GII.4 Saga after pepsin digestion, Figure S9: VP1 mapping overview of hNoVLP GII.10 Vietnam after pepsin digestion, Figure S10: VP1 mapping overview of hNoVLP GII.17 Saitama after pepsin digestion, Figure S11: VP1 mapping overview of hNoVLP GI.1 West Chester batch 1 after trypsin digestion (coverage 72%), Figure S12: VP1 mapping overview of hNoVLP GI.1 West Chester batch 2 after trypsin digestion (coverage 80%), Figure S13: VP1 mapping overview of hNoVLP GII.4 Saga after trypsin digestion (coverage 95%), Figure S14: VP1 mapping overview of hNoVLP GII.10 Vietnam after trypsin digestion (coverage 95%), Figure S15: VP1 mapping overview of hNoVLP GII.17 Saitama after trypsin digestion (coverage 91%), Table S1: Data mass table for charge detection mass spectrometry measurements, Table S2: Data mass table for conventional QToF measurements, Table S3: GEMMA data mass table for gas-phase electrophoretic molecular mobility analysis.

Author Contributions: Conceptualization, C.U.; methodology, C.U., M.F.J., G.A.; validation, R.P.; formal analysis, R.P., V.U.W.; investigation, R.P., V.U.W., S.Z., K.B., N.L., J.D., C.K., J.M.-G.; resources, C.U., M.F.J., G.A., H.S., C.M.-F.; data curation, R.P.; writing—original draft preparation, R.P., C.U.; writing—review and editing, R.P., V.U.W., K.B., J.D., C.K., N.L., J.M.-G., S.Z., G.A., M.F.J., C.M.-F., H.S., C.U. visualization, R.P.; supervision, C.U.; project administration, C.U.; funding acquisition, C.U., C.M.-F. All authors have read and agreed to the published version of the manuscript.

Funding: The Heinrich-Pette-Institute, Leibniz Institute for Experimental Virology is supported by the Free and Hanseatic City Hamburg and the Federal Ministry of Health (Bundesministerium für Gesundheit, BMG). C.U. acknowledges funding from the Leibniz Association through SAW-2014-HPI-4 grant. R.P., J.M.-G., C.U., and C.M.-F. acknowledge funding from EU Horizon 2020 project VIRUSCAN 731868. R.P. further acknowledges funding from MIN Graduate School Universität Hamburg. J.D. was funded by DFG FOR2327 Virocarb. V.U.W. acknowledges funding of the Austrian Theodor Körner Fonds. V.U.W. and R.P. both acknowledge funding of COST Action BM1403 Native Mass Spectrometry and Related Methods for Structural Biology.

Data Availability Statement: The mass spectrometry proteomics data have been deposited to the ProteomeXchange Consortium via the PRIDE [33] partner repository with the dataset identifier PXD023182. All other data are available on request from the corresponding author.

Acknowledgments: We thank Grant Hansman for providing VLPs. We thank the HPI microscopy technology platform, especially Carola Schneider, for assistance in electron microscopy.

Conflicts of Interest: The authors declare no conflict of interest.

References

- Ahmed, S.M.; Hall, A.J.; Robinson, A.E.; Verhoeve, L.; Premkumar, P.; Parashar, U.D.; Koopmans, M.; Lopman, B.A. Global prevalence of norovirus in cases of gastroenteritis: A systematic review and meta-analysis. *Lancet Infect. Dis.* **2014**, *14*, 725–730. [[CrossRef](#)]
- Teunis, P.F.; Moe, C.L.; Liu, P.; Miller, S.E.; Lindesmith, L.; Baric, R.S.; Le Pendu, J.; Calderon, R.L. Norwalk virus: How infectious is it? *J. Med. Virol.* **2008**, *80*, 1468–1476. [[CrossRef](#)]
- Xi, J.N.; Graham, D.Y.; Wang, K.N.; Estes, M.K. Norwalk virus genome cloning and characterization. *Science* **1990**, *250*, 1580–1583. [[CrossRef](#)]
- Jiang, X.; Wang, M.; Wang, K.; Estes, M.K. Sequence and genomic organization of Norwalk virus. *Virology* **1993**, *195*, 51–61. [[CrossRef](#)]
- Chhabra, P.; de Graaf, M.; Parra, G.I.; Chan, M.C.; Green, K.; Martella, V.; Wang, Q.; White, P.A.; Katayama, K.; Vennema, H.; et al. Updated classification of norovirus genogroups and genotypes. *J. Gen. Virol.* **2019**, *100*, 1393–1406. [[CrossRef](#)]
- Kapikian, A.Z.; Wyatt, R.G.; Dolin, R.; Thornhill, T.S.; Kalica, A.R.; Chanock, R.M. Visualization by immune electron microscopy of a 27-nm particle associated with acute infectious nonbacterial gastroenteritis. *J. Virol.* **1972**, *10*, 1075–1081. [[CrossRef](#)]
- Eden, J.S.; Tanaka, M.M.; Boni, M.F.; Rawlinson, W.D.; White, P.A. Recombination within the Pandemic Norovirus GII.4 Lineage. *J. Virol.* **2013**, *87*, 6270–6282. [[CrossRef](#)]
- De Graaf, M.; van Beek, J.; Vennema, H.; Podkolzin, A.T.; Hewitt, J.; Bucardo, E.; Templeton, K.; Mans, J.; Nordgren, J.; Reuter, G.; et al. Emergence of a novel GII.17 norovirus—End of the GII.4 era? *Eurosurveillance* **2015**, *20*, 8–15. [[CrossRef](#)]
- Ettayebi, K.; Crawford, S.E.; Murakami, K.; Broughman, J.R.; Karandikar, U.; Tenge, V.R.; Neill, F.H.; Blutt, S.E.; Zeng, X.L.; Qu, L.; et al. Replication of human noroviruses in stem cell-derived human enteroids. *Science* **2016**. [[CrossRef](#)]
- Tome-Amat, J.; Fleischer, L.; Parker, S.A.; Bardliving, C.L.; Batt, C.A. Secreted production of assembled Norovirus virus-like particles from *Pichia pastoris*. *Microb. Cell Fact.* **2014**, *13*, 134. [[CrossRef](#)]
- Taube, S.; Kurth, A.; Schreier, E. Generation of recombinant norovirus-like particles (VLP) in the human endothelial kidney cell line 293T. *Arch. Virol.* **2005**, *150*, 1425–1431. [[CrossRef](#)] [[PubMed](#)]
- Diamos, A.G.; Mason, H.S. High-level expression and enrichment of norovirus virus-like particles in plants using modified geminiviral vectors. *Protein Expr. Purif.* **2018**, *151*, 86–92. [[CrossRef](#)] [[PubMed](#)]
- Mason, H.S.; Ball, J.M.; Shi, J.J.; Jiang, X.; Estes, M.K.; Arntzen, C.J. Expression of Norwalk virus capsid protein in transgenic tobacco and potato and its oral immunogenicity in mice. *Proc. Natl. Acad. Sci. USA* **1996**, *93*, 5335–5340. [[CrossRef](#)] [[PubMed](#)]
- Prasad, B.V.; Rothnagel, R.; Jiang, X.; Estes, M.K. Three-dimensional structure of baculovirus-expressed Norwalk virus capsids. *J. Virol.* **1994**, *68*, 5117–5125. [[CrossRef](#)] [[PubMed](#)]
- Prasad, B.V.; Hardy, M.E.; Dokland, T.; Bella, J.; Rossmann, M.G.; Estes, M.K. X-ray crystallographic structure of the Norwalk virus capsid. *Science* **1999**, *286*, 287–290. [[CrossRef](#)]
- Jiang, X.; Wang, M.; Graham, D.Y.; Estes, M.K. Expression, self-assembly, and antigenicity of the Norwalk virus capsid protein. *J. Virol.* **1992**, *66*, 6527–6532. [[CrossRef](#)] [[PubMed](#)]
- Tan, M.; Jiang, X. The p domain of norovirus capsid protein forms a subviral particle that binds to histo-blood group antigen receptors. *J. Virol.* **2005**, *79*, 14017–14030. [[CrossRef](#)]
- Bertolotti-Ciarlet, A.; White, L.J.; Chen, R.; Prasad, B.V.; Estes, M.K. Structural requirements for the assembly of Norwalk virus-like particles. *J. Virol.* **2002**, *76*, 4044–4055. [[CrossRef](#)]
- White, L.J.; Hardy, M.E.; Estes, M.K. Biochemical characterization of a smaller form of recombinant Norwalk virus capsids assembled in insect cells. *J. Virol.* **1997**, *71*, 8066–8072. [[CrossRef](#)]
- Devant, J.M.; Hofhaus, G.; Bhella, D.; Hansman, G.S. Heterologous expression of human norovirus GII.4 VP1 leads to assembly of T = 4 virus-like particles. *Antivir. Res.* **2019**, *168*, 175–182. [[CrossRef](#)]
- Jung, J.; Grant, T.; Thomas, D.R.; Diehnelt, C.W.; Grigorieff, N.; Joshua-Tor, L. High-resolution cryo-EM structures of outbreak strain human norovirus shells reveal size variations. *Proc. Natl. Acad. Sci. USA* **2019**, *116*, 12828–12832. [[CrossRef](#)] [[PubMed](#)]
- Taniguchi, K.; Urasawa, S.; Urasawa, T. Further studies of 35–40 nm virus-like particles associated with outbreaks of acute gastroenteritis. *J. Med. Microbiol.* **1981**, *14*, 107–118. [[CrossRef](#)] [[PubMed](#)]
- Dulfer, J.; Kadek, A.; Kopicki, J.D.; Krichel, B.; Uetrecht, C. Structural mass spectrometry goes viral. *Adv. Virus Res.* **2019**, *105*, 189–238. [[CrossRef](#)] [[PubMed](#)]
- Shoemaker, G.K.; van Duijn, E.; Crawford, S.E.; Uetrecht, C.; Baclayon, M.; Roos, W.H.; Wuite, G.J.; Estes, M.K.; Prasad, B.V.; Heck, A.J. Norwalk virus assembly and stability monitored by mass spectrometry. *Mol. Cell Proteom.* **2010**, *9*, 1742–1751. [[CrossRef](#)] [[PubMed](#)]
- Pogan, R.; Schneider, C.; Reimer, R.; Hansman, G.; Uetrecht, C. Norovirus-like VP1 particles exhibit isolate dependent stability profiles. *J. Phys. Condens. Matter* **2018**, *30*, 064006. [[CrossRef](#)]
- Kaufman, S.L.; Skogen, J.W.; Dorman, F.D.; Zarrin, F.; Lewis, K.C. Macromolecule analysis based on electrophoretic mobility in air: Globular proteins. *Anal. Chem.* **1996**, *68*, 1895–1904. [[CrossRef](#)]
- Weiss, V.U.; Bereszczak, J.Z.; Havlik, M.; Kallinger, P.; Gosler, I.; Kumar, M.; Blaas, D.; Marchetti-Deschmann, M.; Heck, A.J.; Szymanski, W.W.; et al. Analysis of a common cold virus and its subviral particles by gas-phase electrophoretic mobility molecular analysis and native mass spectrometry. *Anal. Chem.* **2015**, *87*, 8709–8717. [[CrossRef](#)]
- Weiss, V.U.; Pogan, R.; Zoratto, S.; Bond, K.M.; Boulanger, P.; Jarrold, M.F.; Lyktye, N.; Pahl, D.; Puffer, N.; Schelhaas, M.; et al. Virus-like particle size and molecular weight/mass determination applying gas-phase electrophoresis (native nES GEMMA). *Anal. Bioanal. Chem.* **2019**, *411*, 5951–5962. [[CrossRef](#)]

29. Hansman, G.S.; Natori, K.; Oka, T.; Ogawa, S.; Tanaka, K.; Nagata, N.; Ushijima, H.; Takeda, N.; Katayama, K. Cross-reactivity among sapovirus recombinant capsid proteins. *Arch. Virol.* **2005**, *150*, 21–36. [[CrossRef](#)]
30. Hansman, G.S.; Saito, H.; Shibata, C.; Ishizuka, S.; Oseto, M.; Oka, T.; Takeda, N. Outbreak of gastroenteritis due to sapovirus. *J. Clin. Microbiol.* **2007**, *45*, 1347–1349. [[CrossRef](#)]
31. Laemmli, U.K. Cleavage of structural proteins during the assembly of the head of bacteriophage T4. *Nature* **1970**, *227*, 680–685. [[CrossRef](#)]
32. Shevchenko, A.; Tomas, H.; Havlis, J.; Olsen, J.V.; Mann, M. In-gel digestion for mass spectrometric characterization of proteins and proteomes. *Nat. Protoc.* **2006**, *1*, 2856–2860. [[CrossRef](#)]
33. Perez-Riverol, Y.; Csordas, A.; Bai, J.; Bernal-Llinares, M.; Hewapathirana, S.; Kundu, D.J.; Inuganti, A.; Griss, J.; Mayer, G.; Eisenacher, M.; et al. The PRIDE database and related tools and resources in 2019: Improving support for quantification data. *Nucleic Acids Res.* **2019**, *47*, D442–D450. [[CrossRef](#)] [[PubMed](#)]
34. Van den Heuvel, R.H.; van Duijn, E.; Mazon, H.; Synowsky, S.A.; Lorenzen, K.; Versluis, C.; Brouns, S.J.; Langridge, D.; van der Oost, J.; Hoyes, J.; et al. Improving the performance of a quadrupole time-of-flight instrument for macromolecular mass spectrometry. *Anal. Chem.* **2006**, *78*, 7473–7483. [[CrossRef](#)] [[PubMed](#)]
35. Lorenzen, K.; Versluis, C.; van Duijn, E.; van den Heuvel, R.H.H.; Heck, A.J.R. Optimizing macromolecular tandem mass spectrometry of large non-covalent complexes using heavy collision gases. *Int. J. Mass Spectrom.* **2007**, *268*, 198–206. [[CrossRef](#)]
36. Morgner, N.; Robinson, C.V. Massign: An assignment strategy for maximizing information from the mass spectra of heterogeneous protein assemblies. *Anal. Chem.* **2012**, *84*, 2939–2948. [[CrossRef](#)]
37. Contino, N.C.; Pierson, E.E.; Keifer, D.Z.; Jarrold, M.F. Charge detection mass spectrometry with resolved charge states. *J. Am. Soc. Mass Spectrom.* **2013**, *24*, 101–108. [[CrossRef](#)]
38. Tycova, A.; Prikryl, J.; Foret, F. Reproducible preparation of nanospray tips for capillary electrophoresis coupled to mass spectrometry using 3D printed grinding device. *Electrophoresis* **2016**, *37*, 924–930. [[CrossRef](#)]
39. Bacher, G.; Szymanski, W.W.; Kaufman, S.L.; Zollner, P.; Blaas, D.; Allmaier, G. Charge-reduced nano electrospray ionization combined with differential mobility analysis of peptides, proteins, glycoproteins, noncovalent protein complexes and viruses. *J. Mass Spectrom.* **2001**, *36*, 1038–1052. [[CrossRef](#)]
40. Caspar, D.L.; Klug, A. Physical principles in the construction of regular viruses. *Cold Spring Harb. Symp. Quant. Biol.* **1962**, *27*, 1–24. [[CrossRef](#)]
41. Gotoh, T.; Miyazaki, Y.; Kikuchi, K.; Bentley, W.E. Investigation of sequential behavior of carboxyl protease and cysteine protease activities in virus-infected Sf-9 insect cell culture by inhibition assay. *Appl. Microbiol. Biotechnol.* **2001**, *56*, 742–749. [[CrossRef](#)]
42. Gotoh, T.; Ono, H.; Kikuchi, K.; Nirasawa, S.; Takahashi, S. Purification and characterization of aspartic protease derived from Sf9 insect cells. *Biosci. Biotechnol. Biochem.* **2010**, *74*, 2154–2157. [[CrossRef](#)] [[PubMed](#)]
43. Uetrecht, C.; Barbu, I.M.; Shoemaker, G.K.; van Duijn, E.; Heck, A.J. Interrogating viral capsid assembly with ion mobility-mass spectrometry. *Nat. Chem.* **2011**, *3*, 126–132. [[CrossRef](#)] [[PubMed](#)]
44. Pogan, R.; Dulfer, J.; Uetrecht, C. Norovirus assembly and stability. *Curr. Opin. Virol.* **2018**, *31*, 59–65. [[CrossRef](#)] [[PubMed](#)]
45. Grimes, J.M.; Burroughs, J.N.; Gouet, P.; Diprose, J.M.; Malby, R.; Zientara, S.; Mertens, P.P.; Stuart, D.I. The atomic structure of the bluetongue virus core. *Nature* **1998**, *395*, 470–478. [[CrossRef](#)] [[PubMed](#)]
46. Baker, T.S.; Olson, N.H.; Fuller, S.D. Adding the third dimension to virus life cycles: Three-dimensional reconstruction of icosahedral viruses from cryo-electron micrographs. *Microbiol. Mol. Biol. Rev.* **1999**, *63*, 862–922. [[CrossRef](#)] [[PubMed](#)]
47. Krol, M.A.; Olson, N.H.; Tate, J.; Johnson, J.E.; Baker, T.S.; Ahlquist, P. RNA-controlled polymorphism in the in vivo assembly of 180-subunit and 120-subunit virions from a single capsid protein. *Proc. Natl. Acad. Sci. USA* **1999**, *96*, 13650–13655. [[CrossRef](#)]
48. Lutowski, C.A.; Lykтей, N.A.; Zhao, Z.; Pierson, E.E.; Zlotnick, A.; Jarrold, M.F. Hepatitis B Virus Capsid Completion Occurs through Error Correction. *J. Am. Chem. Soc.* **2017**, *139*, 16932–16938. [[CrossRef](#)]
49. Pierson, E.E.; Keifer, D.Z.; Kukreja, A.A.; Wang, J.C.; Zlotnick, A.; Jarrold, M.F. Charge Detection Mass Spectrometry Identifies Preferred Non-Icosahedral Polymorphs in the Self-Assembly of Woodchuck Hepatitis Virus Capsids. *J. Mol. Biol.* **2016**, *428*, 292–300. [[CrossRef](#)]
50. Salunke, D.M.; Caspar, D.L.; Garcea, R.L. Polymorphism in the assembly of polyomavirus capsid protein VP1. *Biophys. J.* **1989**, *56*, 887–900. [[CrossRef](#)]
51. Huo, Y.Q.; Wan, X.; Wang, Z.J.; Meng, S.L.; Shen, S. Production of Norovirus VLPs to size homogeneity. *Virus Res.* **2015**, *204*, 1–5. [[CrossRef](#)] [[PubMed](#)]
52. Someya, Y.; Shirato, H.; Hasegawa, K.; Kumasaka, T.; Takeda, N. Assembly of homogeneous norovirus-like particles accomplished by amino acid substitution. *J. Gen. Virol.* **2011**, *92*, 2320–2323. [[CrossRef](#)] [[PubMed](#)]
53. Hasegawa, K.; Someya, Y.; Shigematsu, H.; Kimura-Someya, T.; Nuemket, N.; Kumasaka, T. Crystallization and X-ray analysis of 23 nm virus-like particles from Norovirus Chiba strain. *Acta Crystallogr. F Struct. Biol. Commun.* **2017**, *73*, 568–573. [[CrossRef](#)] [[PubMed](#)]
54. Tan, M.; Fang, P.; Chachiyo, T.; Xia, M.; Huang, P.; Fang, Z.; Jiang, W.; Jiang, X. Noroviral P particle: Structure, function and applications in virus-host interaction. *Virology* **2008**, *382*, 115–123. [[CrossRef](#)]
55. Tan, M.; Jiang, X. Norovirus P particle: A subviral nanoparticle for vaccine development against norovirus, rotavirus and influenza virus. *Nanomedicine* **2012**, *7*, 889–897. [[CrossRef](#)] [[PubMed](#)]

Supplementary information

N-terminal VP1 truncations favor $T=1$ norovirus-like particles

Ronja Pogan ^{1,2}, Victor U. Weiss ³, Kevin Bond ⁴, Jasmin Dülfer ¹, Christoph Krisp ⁵, Nicholas Lykтей ⁴, Jürgen Müller-Guhl ^{1,6}, Samuele Zoratto ³, Günter Allmaier ³, Martin F. Jarrold ⁴, Caesar Muñoz-Fontela ⁶, Hartmut Schlüter ⁵, and Charlotte Uetrecht ^{1,2,*}

¹ Heinrich Pette Institute, Leibniz Institute for Experimental Virology, Hamburg, Germany

² European XFEL GmbH, Schenefeld, Germany

³ Institute of Chemical Technologies and Analytics, TU Wien, Vienna, Austria

⁴ Department of Chemistry, Indiana University, Bloomington, IN, USA

⁵ Institute of Clinical Chemistry and Laboratory Medicine, Mass Spectrometric Proteomics Group, University Medical Center Hamburg - Eppendorf, Hamburg, Germany

⁶ Bernhard Nocht Institute for Tropical Medicine and German Center for Infection Research (DZIF), Partner site Hamburg-Lübeck-Borstel-Riems, Hamburg, Germany.

*Correspondence: charlotte.uetrecht@xfel.eu

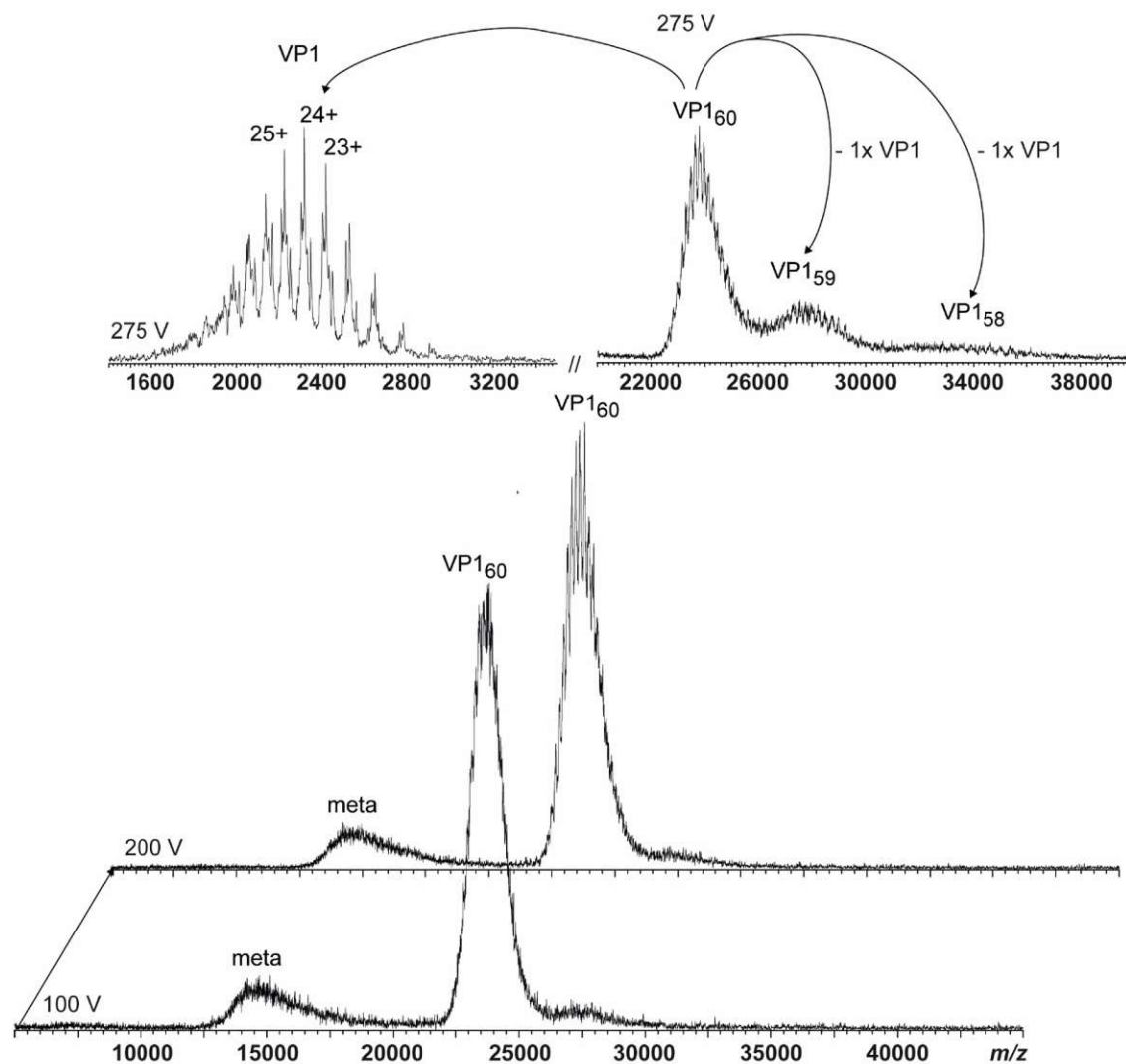
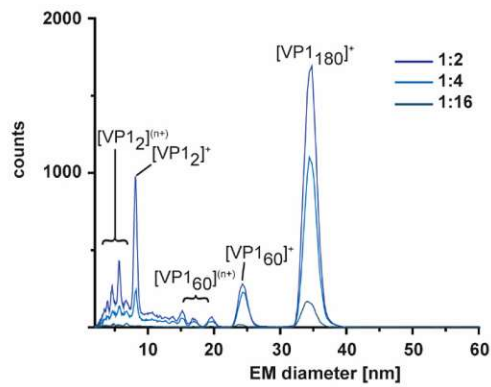
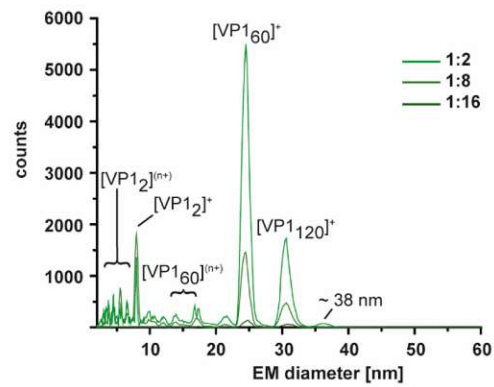


Figure S1. Native MS of a GIL10 Vietnam VLPs. Dissociation pathway without selection in the quadrupole shown for GIL10 Vietnam in 250 mM ammonium acetate pH 7 at 10 μ M VP1. From bottom to top, illustrative mass spectra are shown for 100 V, 200 V, and a zoom in to low m/z (monomer) and high m/z (VP1 60-, 59-, 58-mer) at 275 V acceleration into the collision cell. As lower mass ions at approximately 15,000 m/z are annotated as metastable ions (meta), monomer lacking at least 45 aa most likely dissociate from $T=1$ species.

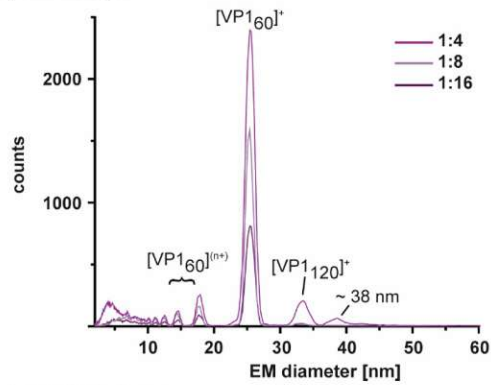
(a) West Chester batch 1



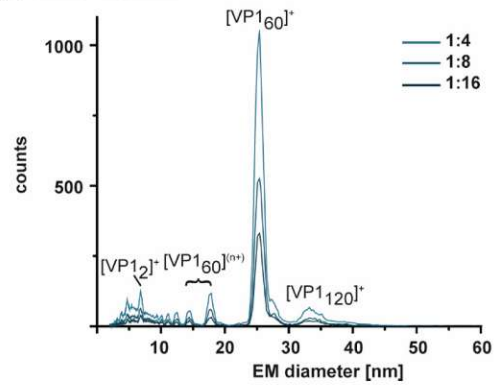
(b) West Chester batch 2



(c) GII.4 Saga



(d) GII.10 Vietnam



(e) GII.17 Saitama

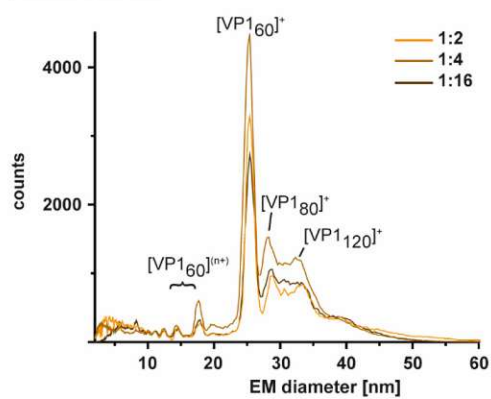


Figure S2. GEMMA spectra of different hNoVLPs in 40 mM ammonium acetate at pH 7, 3 different tested dilutions exemplarily shown for (a) West Chester batch 1 (b) West Chester batch 2 (c) GII.4 Saga (d) GII.10 Vietnam and (e) GII.17 Saitama. In GII.1 West Chester batch 2 and GII.4 Saga, additional species at approximately 38 nm were assigned to aggregation due to their appearance only at higher concentrations.

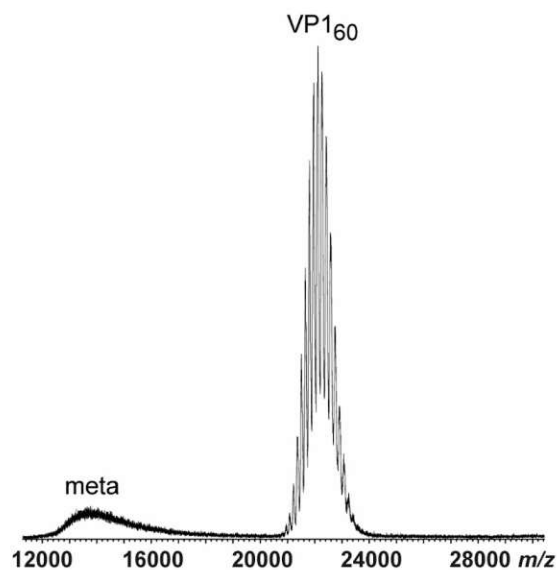


Figure S3. Native mass spectrum of GIL4 Saga VLPs at 50 mM ammonium pH 9 at 10 μ M VP1. In contrast to GEMMA measurements (Figure 5), $T=1$ particles are detected.

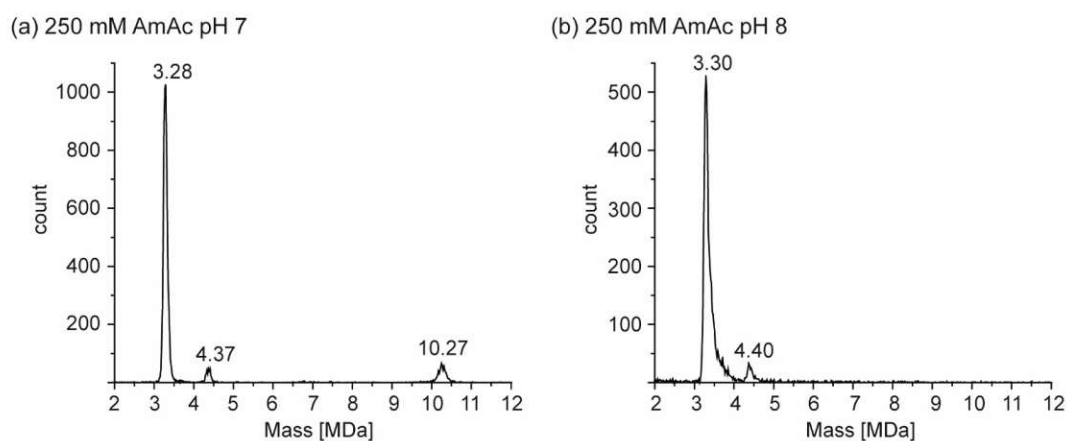
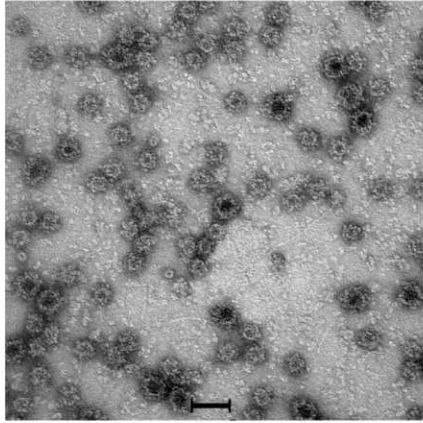
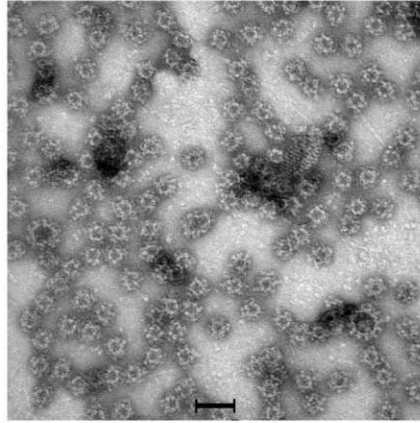


Figure S4. Charge detection mass spectra of GI.1 West Chester batch 1 VLPs in 250 mM ammonium acetate at (a) pH 7 and (b) pH 8. Next to $T=1$ particles, a species at approximately 4.37 MDa at pH 7 and 4.40 MDa at pH 8 is detected. Given the VP1 60-er mass 4.4 MDa species equal VP1 80-mers. At pH 7, further ions at 10.27 MDa or $T=3$ particles are observed.

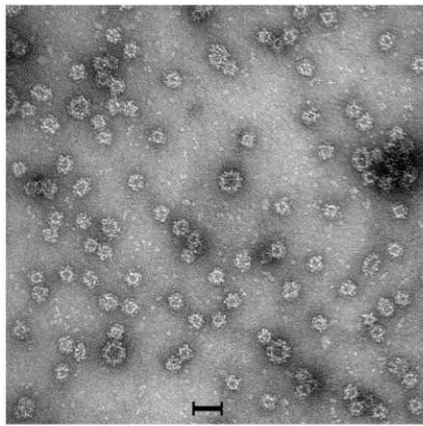
(a) GI.1 West Chester



(b) GII.4 Saga



(c) GII.10 Vietnam



(d) GII.17 Saitama

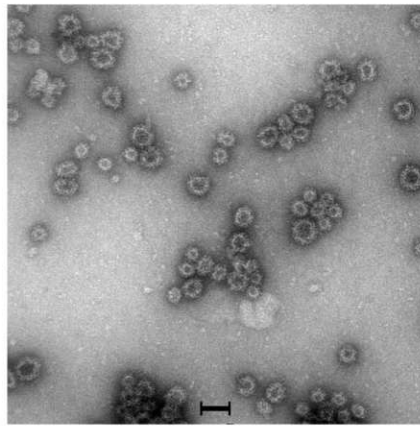


Figure S5. Electron micrographs of different hNoVLPs in PBS. (a) GI.1 West Chester (b) GII.4 Saga (c) GII.10 Vietnam and (d) GII.17 Saitama. The bar represents 50 nm. All images are taken at the same magnification. In some cases, particles of similar size to $T=3$ are observed but the low number precludes detection by other means, moreover our CDMS results suggest that these could also belong to intermediate assemblies in line with the broad GEMMA and native MS distributions.

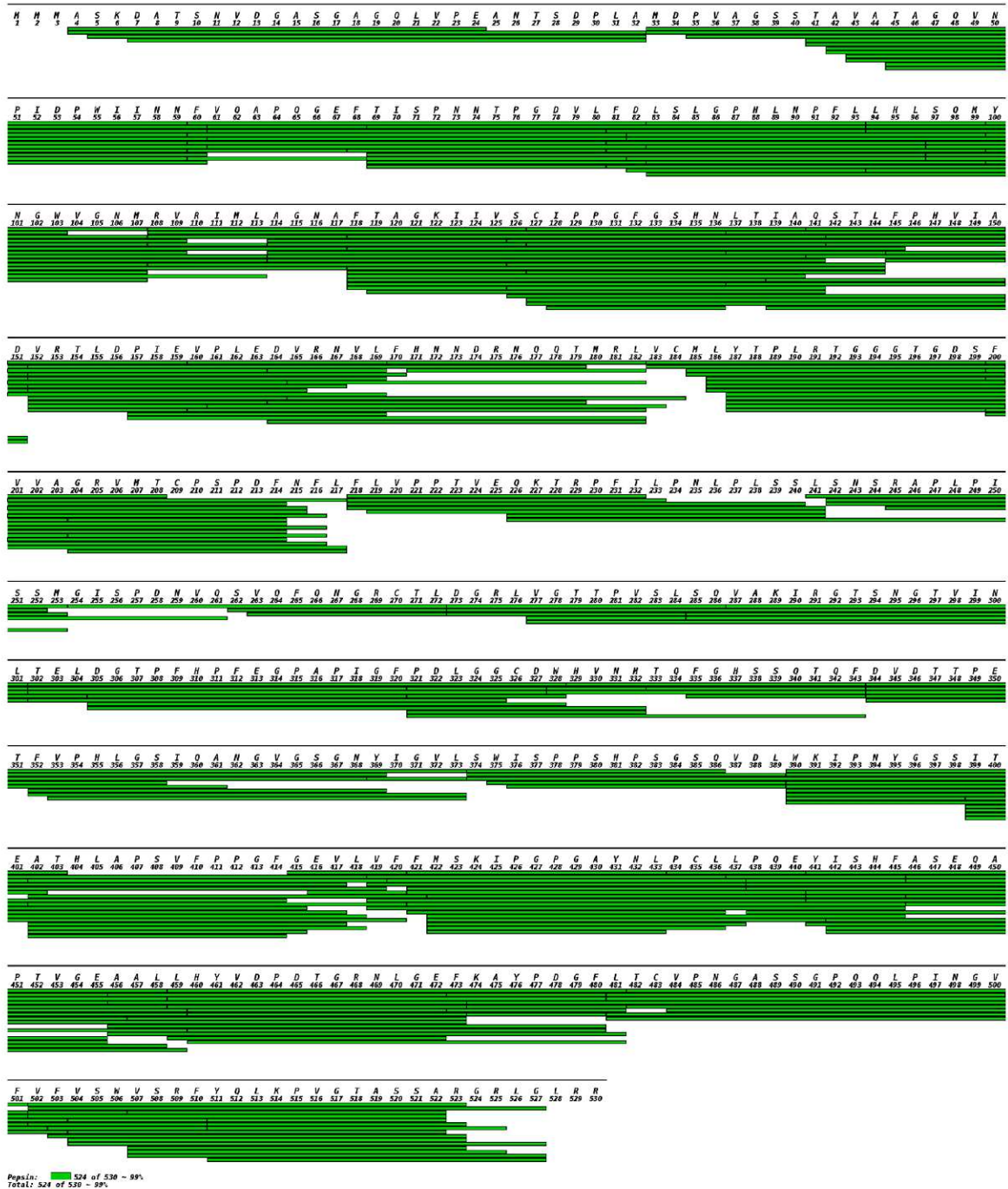
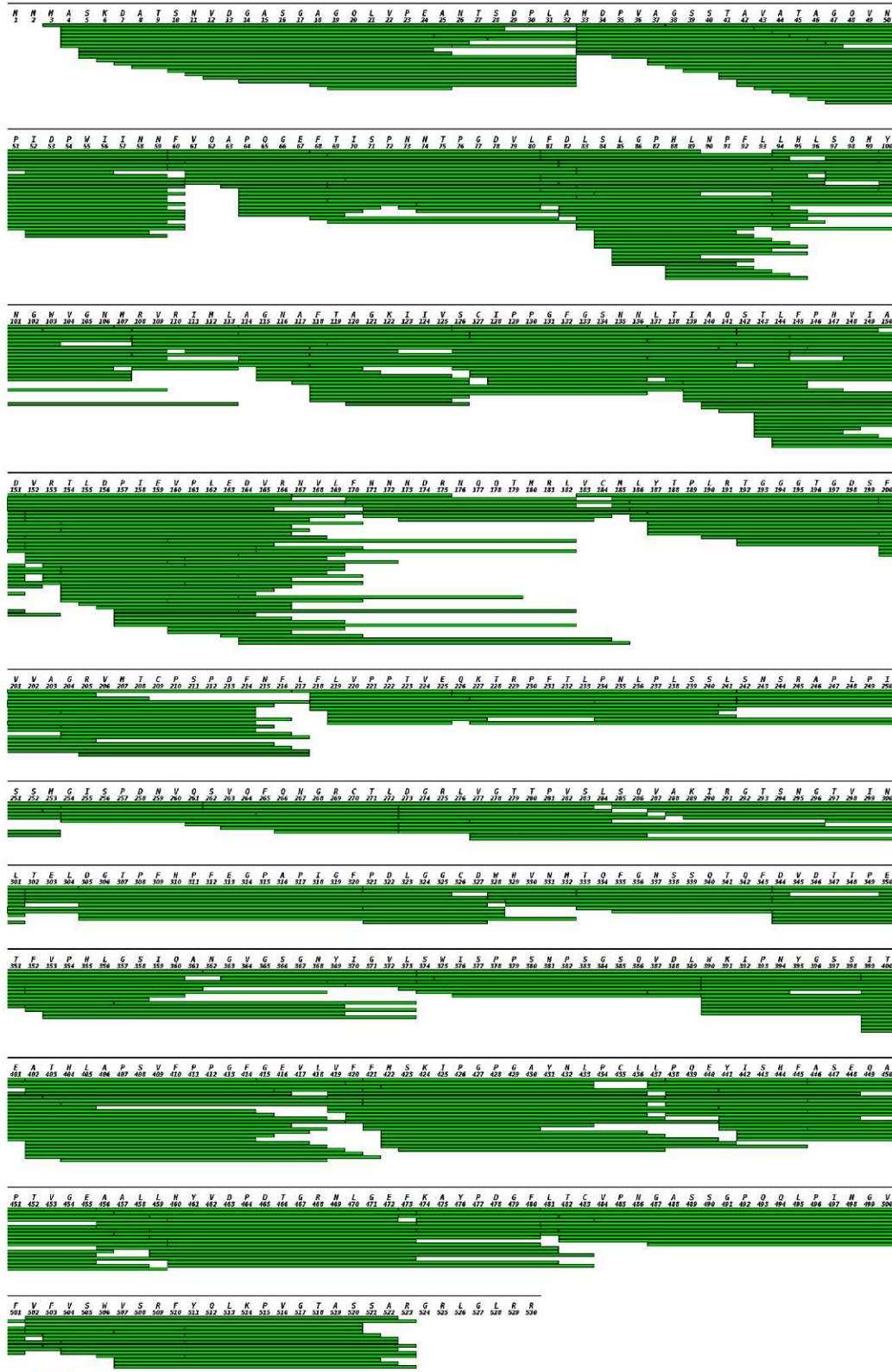
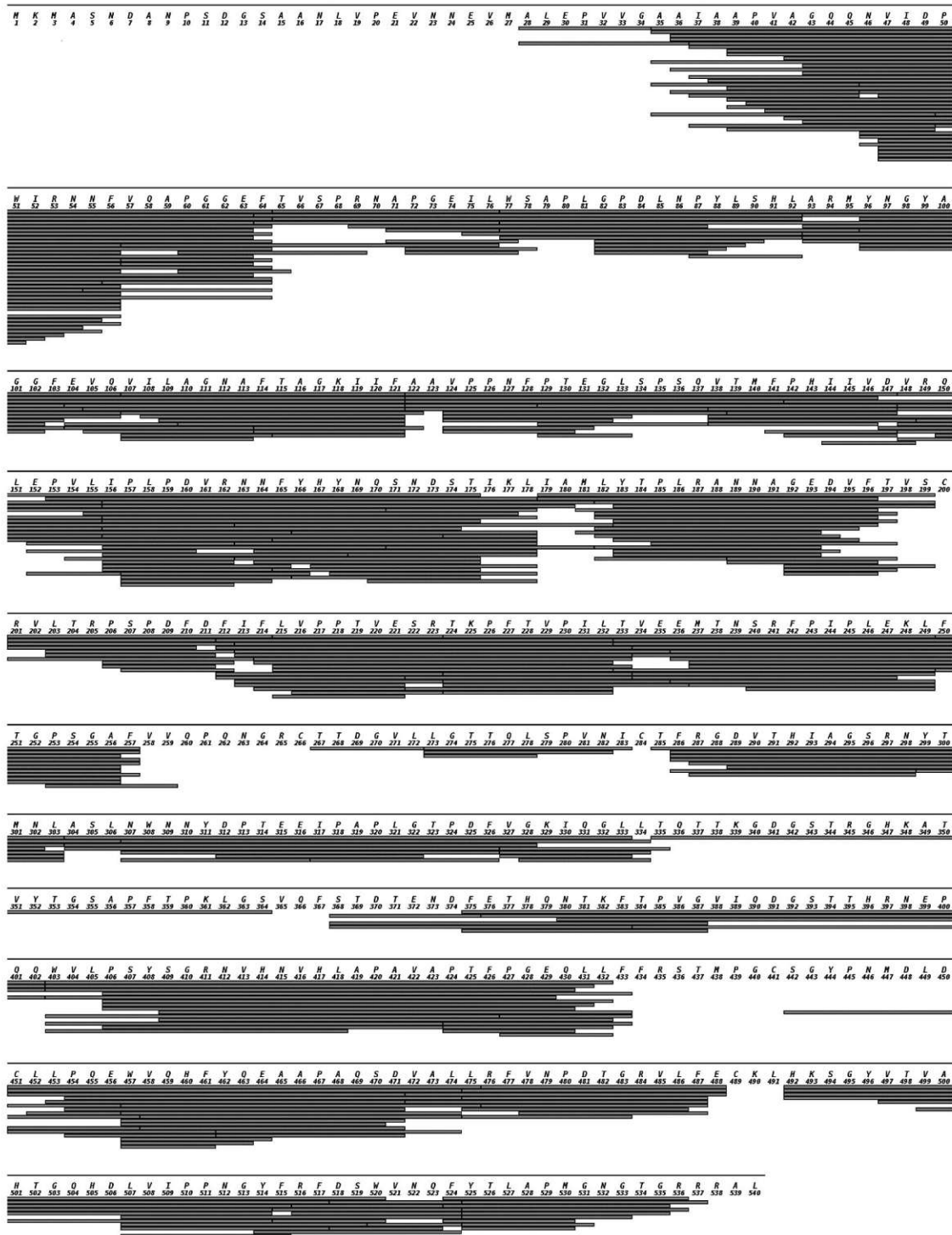


Figure S6. VP1 mapping overview of hNoVLP GI.1 West Chester batch 1 after pepsin digestion. In total 524 of 530 aa are covered (coverage 99 %). The first N-terminal residue covered is Ala4, while C-terminally the triplet Leu528-Arg529-Arg530 is missing.



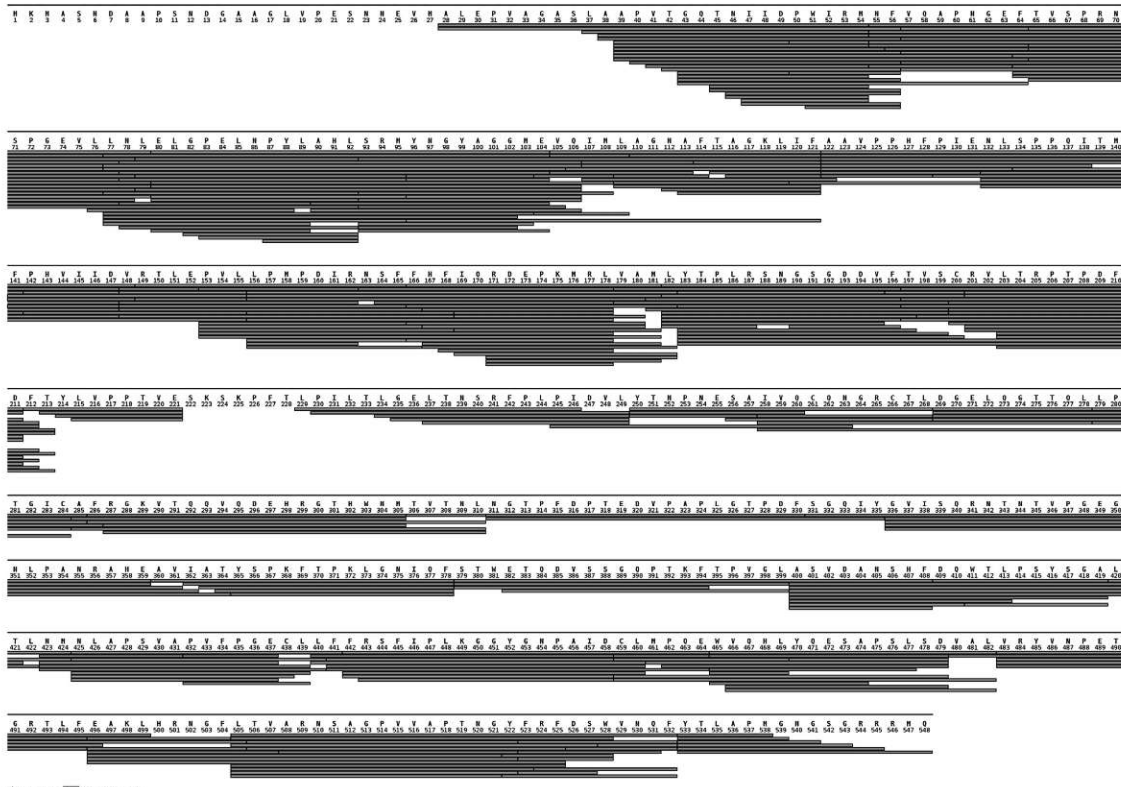
Peptide: 521 of 530 - 98%
 Total: 521 of 530 - 98%

Figure S7. VP1 mapping overview of hNoVLP GI.1 West Chester batch 2 after pepsin digestion. In total 521 of 530 aa are covered (coverage 98 %). The first N-terminal residue covered is Met3 and the C-terminus is covered up to residue Arg523.



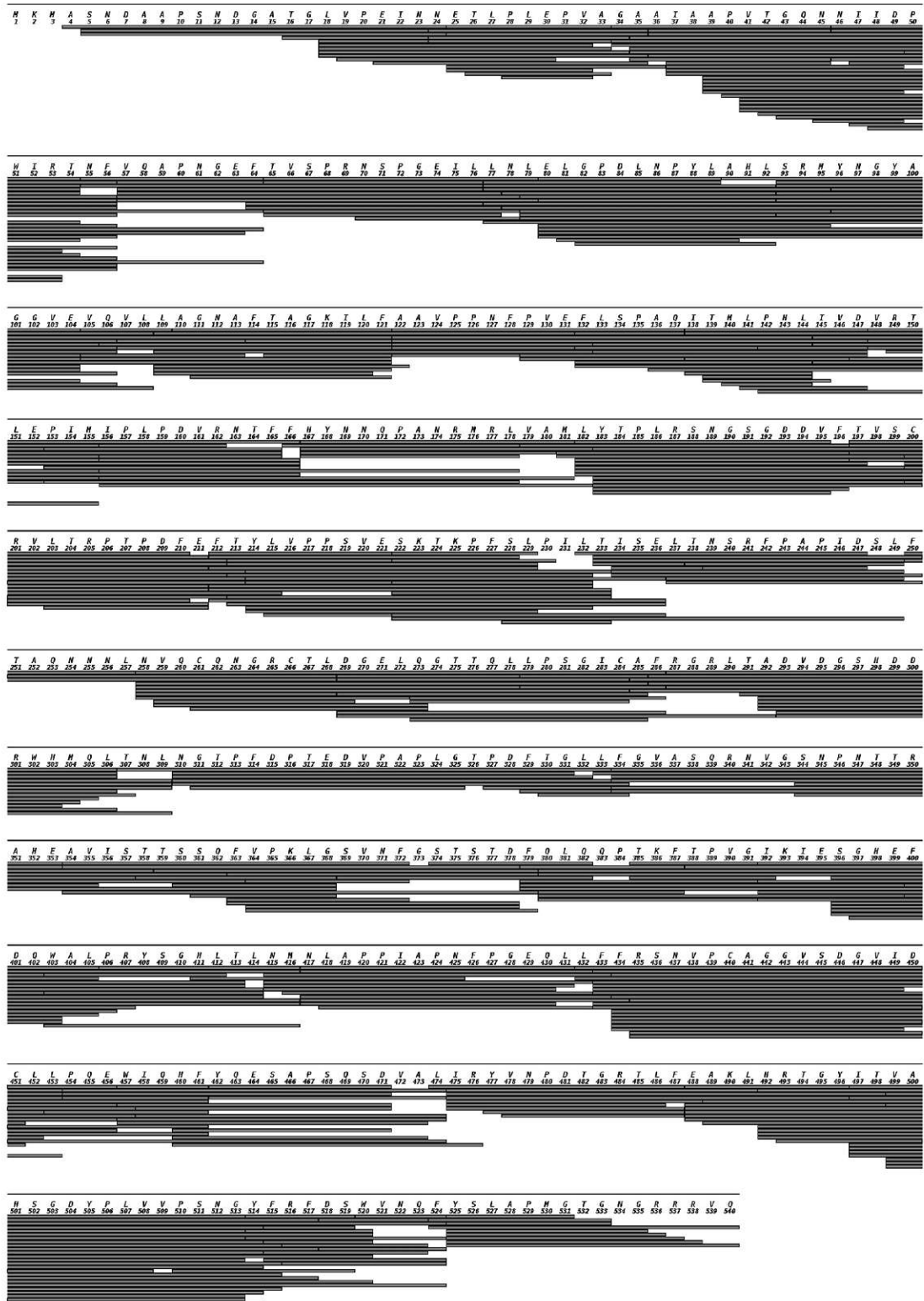
Pepsin_Seq08: 487 of 540 - 90%
 Total: 487 of 540 - 90%

Figure S8. VP1 mapping overview of hNoVLP GII.4 Saga after pepsin digestion. In total 487 of 540 aa are covered (coverage 90 %). The first N-terminal residue covered is Ala28, while C-terminally the triplet Arg538-Ala539-Leu540 is not covered.



System 10, p. 514 of 548 - 94%
 514 of 548 aa

Figure S9. VP1 mapping overview of hNoVLP GIL10 Vietnam after pepsin digestion. In total 514 of 548 aa are covered (coverage 94 %). The first N-terminal residue covered is Ala28, while full-coverage is given for the C-terminus.



Pepsin_Saitama: 537 of 540 - 99%
 Total: 537 of 540 - 99%

Figure S10. VP1 mapping overview of hNoVLP GII.17 Saitama after pepsin digestion. In total 537 of 540 aa are covered (coverage 99 %). The first N-terminal residue covered is Ala4, while full-coverage is given for the C-terminus.

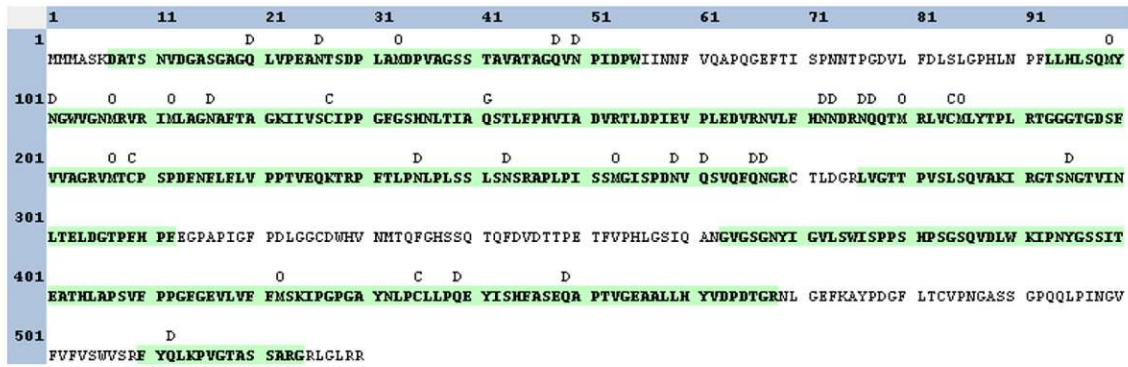


Figure S11. VP1 mapping overview of hNoVLP GI.1 West Chester batch 1 after trypsin digestion (coverage 72 %). The first N-terminal residue covered is Asp7 and C-terminally six residues are not covered.

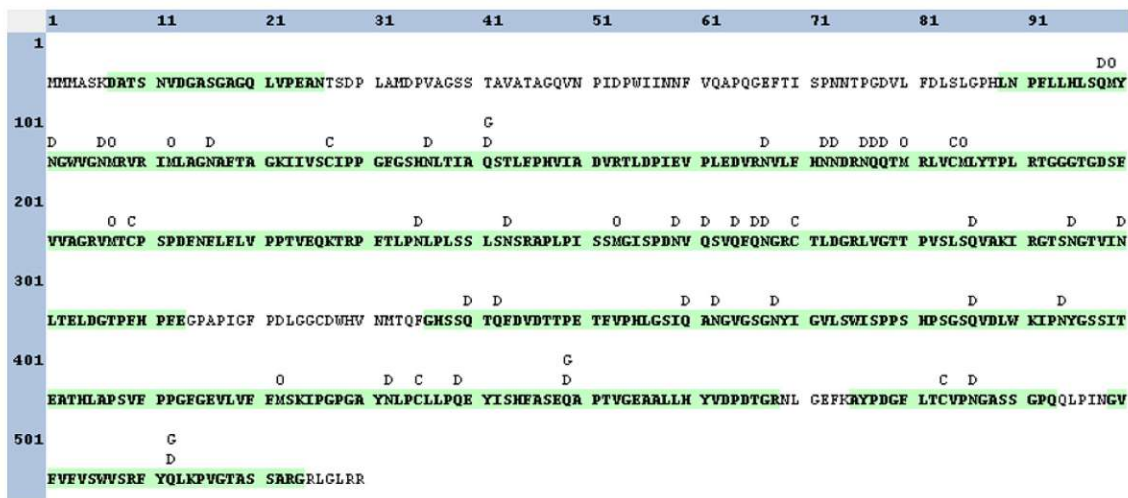


Figure S12. VP1 mapping overview of hNoVLP GI.1 West Chester batch 2 after trypsin digestion (coverage 80 %). The first N-terminal residue covered is Asp7 and C-terminally six residues are not covered.

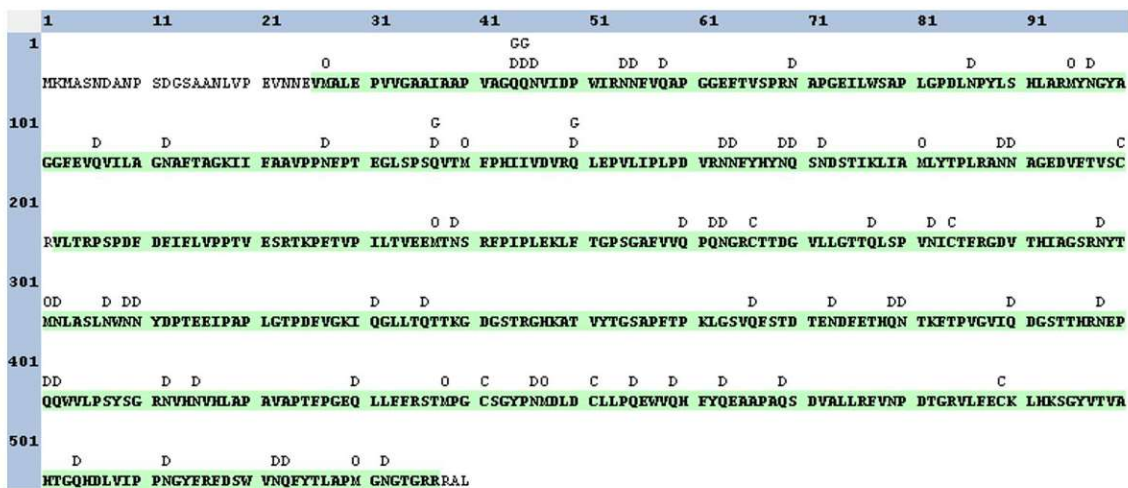


Figure S13. VP1 mapping overview of hNoVLP GII.4 Saga after trypsin digestion (coverage 95 %). Semi-tryptic peptide search identifies Val26 as the first N-terminal residue covered, while C-terminally the triplet Arg538-Ala539-Leu540 is not covered.

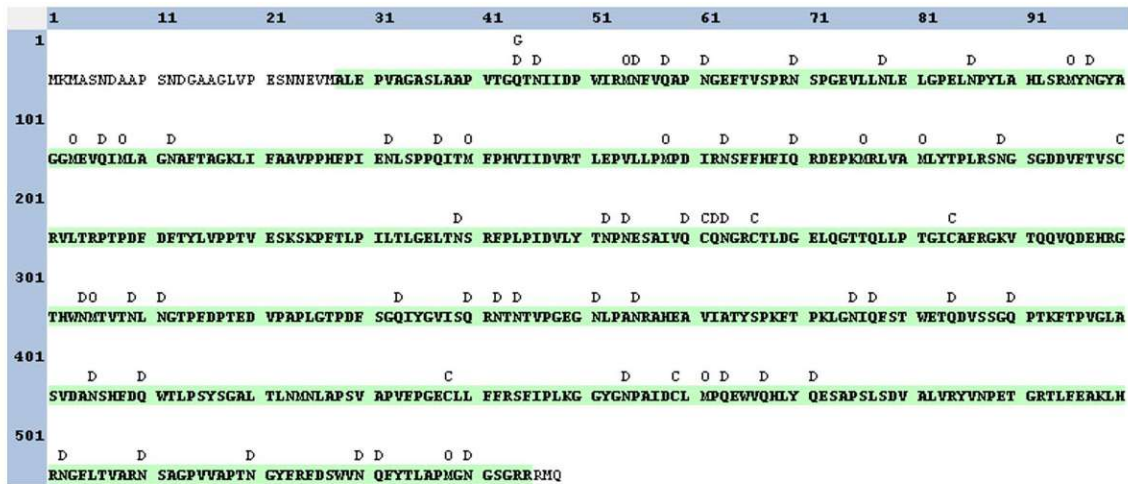


Figure S14. VP1 mapping overview of hNoVLP GII.10 Vietnam after trypsin digestion (coverage 95 %). Semi-tryptic peptide search identifies Ala28 as the first N-terminal residue covered, while C-terminally the triplet Arg546-Met547-Gln548 is not covered. Note that the sequence covered starts indeed with a semi-tryptic peptide.

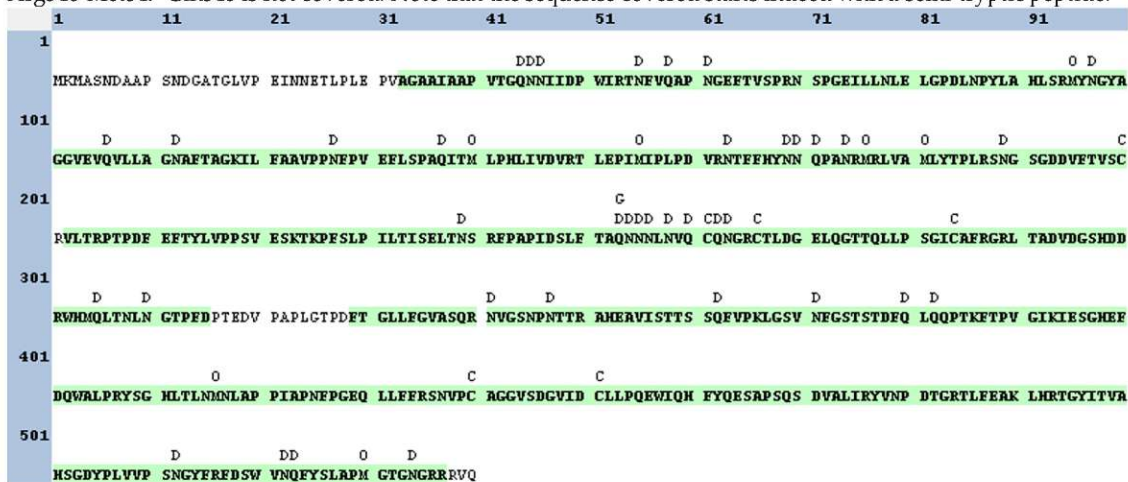


Figure S15. VP1 mapping overview of hNoVLP GII.17 Saitama after trypsin digestion (coverage 91 %). Semi-tryptic peptide search identifies Ala33 as the first N-terminal residue covered, while C-terminally the triplet Arg538-Val539-Gln540 is not covered. Note that the sequence covered starts indeed with a semi-tryptic peptide.

Table S1. Data mass table for charge detection mass spectrometry measurements. Abbreviations Th. theoretical, Exp. experimental, Calc. calculated. VP1 Calc. based on VP1 60-mer mass. For VP1 Th. and VP1 Calc. the total aa-amount and aa truncation according to experimental mass are given, respectively. *N* VP1 given for larger assemblies respective to VP1 Calc. *indicate masses are approximations due to low particle counts.

Variant	VP1 Th.	Complex Exp.	VP1 Calc.	<i>N</i> VP1 Complex
GII.4 Saga	59005 Da 540 aa	3.35 MDa	55800 Da, -31 aa	60
GII.10 Vietnam	59901 Da 548 aa	3.41 MDa ~ 4.5 MDa* ~ 6.9 MDa*	56800 Da, -31 aa	60 79 121
GII.17 Saitama	58957 Da 540 aa	3.44 MDa 4.07 MDa 5.20 MDa 5.72 MDa 6.20 MDa 6.87 MDa	57300 Da, -17 aa	60 71 91 100 108 120

Table S2. Data mass table for conventional QToF measurements. Abbreviations Th. theoretical, Exp. experimental, Calc. calculated. For all tested variants, collision induced dissociation experiments resulted in dissociated VP1 monomer with a main species (VP1 Exp. main) and one or two neighboring species with lower intensity (VP1 Exp. following). VP1 60-mer experimental mass (Complex VP1₆₀ Exp.) assigned where charge state resolution was obtained and given as approximations for GI.1 West Chester due to low desolvation and associated low charge state resolution. *approximation.

Variant	VP1 Th.	VP1 Exp. main	VP1 Exp. following	Complex VP1 ₆₀ Exp.
GI.1 West Chester	56609 Da, 530 aa	52760 ± 10 Da, -40 aa	52540 ± 10 Da, -4 aa-	~3.4 MDa*
GII.4 Saga	59005 Da 540 aa	54600 ± 20 Da, -45 aa	54270 ± 20 Da, -48 aa	3.27 ± 0.02 MDa
GII.10 Vietnam	59901 Da 548 aa	55560 ± 10, -45 aa	55220 ± 20, -48 aa 56290 ± 10, -37aa	3.33 ± 0.02 MDa

Table S3 GEMMA Data mass table for gas phase electrophoretic molecular mobility analysis. Abbreviations, Exp. experimental, Calc. calculated. VP1 oligomers given as experimental EMD values and respective molecular weight calculations for low EMD range (¹ Bacher et al 2001) and high EMD range (² Weiss et al. 2019) *approximation due to low particle counts.

Variant	pH	VP1 dimer	VP1 60-mer Exp.	VP1 80-mer	VP1 120-mer	VP1 140-mer	VP1 180-mer
		Exp. (nm) Calc. ¹ (kDa)	(nm) Calc. ² (MDa)	Exp. (nm) Calc. ² (MDa)	Exp. (nm) Calc. ² (MDa)	Exp. (nm) Calc. ² (MDa)	Exp. (nm) Calc. ² (MDa)
GI.1 West Chester batch 1	6		24.29 ± 0.09 3.37 ± 0.03				34.54 ± 0.05 8.50 ± 0.03
	7	8.10 ± 0.05 112 ± 2	24.09 ± 0.27 3.30 ± 0.10				34.37 ± 0.13 8.40 ± 0.09
	9	8.03 ± 0.01 109 ± 1					
GI.1 West Chester batch 2	6		24.48 ± 0.02 3.44 ± 0.01		30.73 ± 0.05 6.25 ± 0.03		
	7	8.00 ± 0.07 108 ± 3	24.50 ± 0.12 3.45 ± 0.04		30.71 ± 0.17 6.24 ± 0.09		
	9	7.89 ± 0.01 104 ± 1	24.18 ± 0.06 3.33 ± 0.02				
GII.4 Saga	5		25.27 ± 0.01 3.74 ± 0.01				
	6		25.18 ± 0.01 3.70 ± 0.01				
	7		25.38 ± 0.07 3.8 ± 0.03			33.30 ± 0.08 7.72 ± 0.05	
	8	8.03 ± 0.02 109 ± 1	25.44 ± 0.03 3.80 ± 0.01				
	9	7.88 ± 0.01 104 ± 1					
GII.10 Vietnam	5		~ 25*				
	6		25.11 ± 0.01 3.68 ± 0.02				
	7		25.32 ± 0.02 3.75 ± 0.01			33.41 ± 0.09 7.79 ± 0.06	
	8	7.90 ± 0.02 104 ± 1	25.10 ± 0.02 3.67 ± 0.01			33.31 ± 0.05 7.73 ± 0.03	
	9	7.93 ± 0.02 105 ± 1	25.06 ± 0.02 3.66 ± 0.01				
GII.17 Saitama	5		25.47 ± 0.09 3.81 ± 0.04	28.67 ± 0.54 5.21 ± 0.26			
	6		25.20 ± 0.06 3.71 ± 0.03				
	7		25.36 ± 0.06 3.77 ± 0.03	28.48 ± 0.17 5.12 ± 0.08		32.62 ± 0.22 7.31 ± 0.13	
	8	7.99 ± 0.08 108 ± 3	25.14 ± 0.05 3.69 ± 0.02	28.13 ± 0.10 4.96 ± 0.05		32.33 ± 0.08 7.15 ± 0.05	
	9	8.08 ± 0.05 111 ± 2	25.22 ± 0.17 3.72 ± 0.07				

¹ Bacher G, Szymanski WW, Kaufman SL, Zollner P, Blaas D, Allmaier G. Charge-reduced nano electrospray ionization combined with differential mobility analysis of peptides, proteins, glycoproteins, noncovalent protein complexes and viruses. *J Mass Spectrom.* 2001;36(9):1038-52.

² Weiss VU, Pogan R, Zoratto S, Bond KM, Boulanger P, Jarrold MF, et al. Virus-like particle size and molecular weight/mass determination applying gas-phase electrophoresis (native nES GEMMA). *Anal Bioanal Chem.* 2019;411(23):5951-62

Anal Bioanal Chem. 2019; 411(23): 5951–5962.

Virus-like particle size and molecular weight/mass determination applying gas-phase electrophoresis (native nES GEMMA)

Victor U. Weiss¹, Ronja Pogan^{2,3}, Samuele Zoratto¹, Kevin M. Bond⁴, Pascale Boulanger⁵, Martin F. Jarrold⁴, Nicholas Lykтей⁴, Dominik Pahl⁶, Nicole Puffler¹, Mario Schelhaas⁶, Ekaterina Selivanovitch⁴, Charlotte Uetrecht^{2,3}, Günter Allmaier¹

¹ Institute of Chemical Technologies and Analytics, TU Wien, Getreidemarkt 9/164, 1060, Vienna, Austria.

² Heinrich Pette Institute, Leibniz Institute for Experimental Virology, Martinstraße 52, 20251, Hamburg, Germany.

³ European XFEL GmbH, Holzkoppel 4, 22869 Schenefeld, Germany

⁴ Department of Chemistry, Indiana University, 800 E Kirkwood Ave, Bloomington, IN, 47405, USA.

⁵ Institute for Integrative Biology of the Cell, CEA, CNRS, Université Paris-Sud, Université Paris-Saclay, 91198, Gif-sur-Yvette, France.

⁶ Institute of Cellular Virology, WWU Münster, Von-Esmarch-Str. 56, 48149, Münster, Germany.

<https://doi.org/10.1007/s00216-019-01998-6>

In this study, we examined the use of a native nES GEMMA for analyzing (bio-)nanoparticles, focusing on VLPs. We successfully established a correlation between the EMD and molecular weight (MW) for VLPs, which differ significantly from correlations for other analyte classes like proteins or intact virus particles. This correlation enables MW determination of VLPs based on their EMD. Our study highlights the potential of native nES GEMMA as a quick, cost-effective, and less sample-dependent method compared to native MS for analyzing VLPs.

We also encountered challenges in native MS due to the sample's inherent characteristics, which were not present in charge detection mass spectrometry (CDMS). Whereas nES GEMMA proved superior in analysis speed and less dependent on sample purity and homogeneity, offering calculated MW values

in good approximation even when charge resolution was not achieved in native MS. Consequently, both methods (nES GEMMA-based MW determination via an EMD/MW correlation and native MS) provided complementary information in terms of analyte size, MW, sample quality, and particle number concentration.

This comprehensive analysis approach is crucial for biopharmaceutical applications, where in-depth characterization of VLPs in terms of size, MW, sample and analyte heterogeneity, and particle number concentration is essential.

INNOVATIVE ASPECTS:

- Developed a correlation between EMD and MW, specific for VLPs.
- Demonstrated the effectiveness of nES GEMMA in providing faster and more accurate MW determination, with less dependence on sample purity
- Combined native nES GEMMA and native ESI MS for a detailed analysis of VLPs, essential in biopharmaceutical applications.

OWN CONTRIBUTION

In this work, I

- assisted and performed nES GEMMA experiments, with data interpretation.



Virus-like particle size and molecular weight/mass determination applying gas-phase electrophoresis (native nES GEMMA)

Victor U. Weiss¹ · Ronja Pogan^{2,3} · Samuele Zoratto¹ · Kevin M. Bond⁴ · Pascale Boulanger⁵ · Martin F. Jarrold⁴ · Nicholas Lykтей⁴ · Dominik Pahl⁶ · Nicole Puffler¹ · Mario Schelhaas⁶ · Ekaterina Selivanovitch⁴ · Charlotte Uetrecht^{2,3} · Günter Allmaier¹

Received: 16 April 2019 / Revised: 29 May 2019 / Accepted: 24 June 2019 / Published online: 6 July 2019
© The Author(s) 2019

Abstract

(Bio-)nanoparticle analysis employing a nano-electrospray gas-phase electrophoretic mobility molecular analyzer (native nES GEMMA) also known as nES differential mobility analyzer (nES DMA) is based on surface-dry analyte separation at ambient pressure. Based on electrophoretic principles, single-charged nanoparticles are separated according to their electrophoretic mobility diameter (EMD) corresponding to the particle size for spherical analytes. Subsequently, it is possible to correlate the (bio-)nanoparticle EMDs to their molecular weight (M_w) yielding a corresponding fitted curve for an investigated analyte class. Based on such a correlation, (bio-)nanoparticle M_w determination via its EMD within one analyte class is possible. Turning our attention to icosahedral, non-enveloped virus-like particles (VLPs), proteinaceous shells, we set up an EMD/ M_w correlation. We employed native electrospray ionization mass spectrometry (native ESI MS) to obtain M_w values of investigated analytes, where possible, after extensive purification. We experienced difficulties in native ESI MS with time-of-flight (ToF) detection to determine M_w due to sample inherent characteristics, which was not the case for charge detection (CDMS). nES GEMMA exceeds CDMS in speed of analysis and is likewise less dependent on sample purity and homogeneity. Hence, gas-phase electrophoresis yields calculated M_w values in good approximation even when charge resolution was not obtained in native ESI ToF MS. Therefore, both methods-native nES GEMMA-based M_w determination via an analyte class inherent EMD/ M_w correlation and native ESI MS-in the end relate (bio-)nanoparticle M_w values. However, they differ significantly in, e.g., ease of instrument operation, sample and analyte handling, or costs of instrumentation.

Keywords Native nES GEMMA · DMA · VLP · Molecular weight/mass · Size · Mass spectrometry

Victor U. Weiss and Ronja Pogan contributed equally to this work.

Electronic supplementary material The online version of this article (<https://doi.org/10.1007/s00216-019-01998-6>) contains supplementary material, which is available to authorized users.

✉ Victor U. Weiss
victor.weiss@tuwien.ac.at

¹ Institute of Chemical Technologies and Analytics, TU Wien, Getreidemarkt 9/164, 1060 Vienna, Austria

² Heinrich Pette Institute, Leibniz Institute for Experimental Virology, Martinistraße 52, 20251 Hamburg, Germany

³ European XFEL GmbH, Holzkoppel 4, 22869 Schenefeld, Germany

⁴ Department of Chemistry, Indiana University, 800 E Kirkwood Ave, Bloomington, IN 47405, USA

⁵ Institute for Integrative Biology of the Cell, CEA, CNRS, Université Paris-Sud, Université Paris-Saclay, 91198 Gif-sur-Yvette, France

⁶ Institute of Cellular Virology, WWU Münster, Von-Esmarch-Str. 56, 48149 Münster, Germany

Springer

Introduction

Viruses are nanoparticles of biological origin: A proteinaceous capsid protects the viral genome from the exterior. Additional protection can be conveyed by a lipid membrane, which is additionally modified by (glyco-) proteins to enable attachment to target cells (e.g., [1]). Only upon target cell infection, the genomic material of the virus is intended for release. This concept is of interest for pharmacological applications as virus bionanoparticles can be interpreted as carriers enabling the shielded, targeted transport of cargo material. Alternatively, viral particles without any encapsulated cargo can be employed for vaccination. In both cases, corresponding particles are referred to as virus-like particles (VLPs) (e.g., [2]).

To allow for VLP application in the field of pharmaceuticals, their thorough characterization and preparation batch control, e.g., in terms of particle homogeneity, purity of preparations, particle size, and molecular weight (M_W), is of importance. For the latter, native electrospray ionization mass spectrometry (native ESI MS) mostly in combination with time-of-flight (ToF) analyzers evolved as method of choice, yielding M_W values of bionanoparticles after deconvolution of mass spectra. Such, the M_W of dimorphic hepatitis B-based VLPs could be obtained already in 2008 [3]. In addition, several other VLPs or subviral particles [4, 5] up to a maximum M_W of 17.9 MDa with charge state assignment [6] or employing cryodetection with matrix assisted laser desorption/ionization time-of-flight (MALDI TOF) MS [7] could be investigated. ESI with charge detection mass spectrometry (CDMS) [8, 9] even allowed detection of VLPs up to 26.8 MDa, employing bacteriophage P22 as model [10, 11]. Besides enabling the analysis of VLPs, also capsid binding to antibody fragments [12], pH-dependent VLP decomposition [13] or the investigation of VLP capsid assembly [14] was accessible via native ESI MS. However, none of these measurements can be carried out on standard commercial instruments. Employed mass spectrometers are usually customized in terms of, e.g., applied pressures, employed carrier gas or voltage settings, or pose completely new instrumental developments. In 2018, for instance, Dominguez-Medina and coworkers reported the analysis of bacteriophage T5 icosahedral capsids either in their empty VLP form ($M_W \sim 27$ MDa) or in their DNA-filled native form ($M_W \sim 108$ MDa) [15]. For these experiments, nanochemical resonators were employed [16, 17].

As alternative, M_W determination can also be based on gas-phase electrophoresis data employing a nano-electrospray gas-phase electrophoretic mobility molecular analyzer (native nES GEMMA also known as nES differential mobility analyzer, nES DMA) [18]. Bionanoparticles are electrosprayed from a volatile, aqueous electrolyte solution. Subsequently, droplets are dried. At the same time, charge equilibration occurs in a bipolar atmosphere induced by, e.g., an α -particle emitter like ^{210}Po , an alternating corona discharger or a soft X-

ray tube [19, 20]. Hence, singly charged particles are obtained (besides a majority of neutral objects), which are then separated according to electrophoretic principles in the gas phase at ambient pressure. A particle charge of one leads to bionanoparticle separation according only to the surface-dry particle size (electrophoretic mobility diameter, EMD) in a high laminar sheath flow of particle-free, dried air, and a tunable electric field. Variation of the field strength enables size separation of sample components. The obtained monodisperse aerosol is subsequently introduced to the detector unit of the instrument (ultrafine condensation particle counter, CPC), where bionanoparticles act as condensation nuclei in a supersaturated atmosphere of either n-butanol or water. Obtained droplets are counted as they pass a focused laser beam. Such an instrumentation has previously been employed for the analysis of liposomes [21, 22], exosomes [23], viruses [24–29], proteins and protein aggregates [30], polysaccharides [31–33], DNA [34], polymers [35–37], and nanoparticles in general [38–42]. Besides yielding information on analyte surface-dry particle size and size distribution, particle number concentration detection is possible in accordance with recommendations of the European Commission for characterization of nanoparticle material (2011/696/EU from October 18th, 2011). Furthermore, analytes can be size-selected for further analyses employing orthogonal methods for instance electron microscopy [43], atomic force microscopy [44], spectroscopic techniques [45, 46], or antibody-based nanoparticle recognition [44, 47]. It is of note that LiquiScan ES, MacroIMS, and SMPS are synonyms of the same instrument found in literature.

Furthermore, as first demonstrated in great detail by Bacher and colleagues [48] for proteins, obtained EMD results can be related to particle M_W values yielding a corresponding correlation. Hence, based on a protein EMD value, its M_W can be calculated in good approximation. Similar approaches have been demonstrated, e.g., for intact viruses [4] and polysaccharides [32]. It is of note that for the latter two, the obtained EMD/ M_W correlations deviated from the protein case. For instance for polysaccharides, it was reasoned that additional factors might influence the EMD/ M_W correlation, inter alia particle shape, or insufficient characterization of applied, commercially available standards. Likewise, for elongated virus structures (tobacco mosaic virus), effects like bending of analytes due to surface effects of droplets generated during the nES process were observed [49].

In the current manuscript, we focus on nano-objects, namely VLPs, which are approximately spherical (icosahedral) and non-enveloped (empty protein shells). We asked ourselves, if a native nES GEMMA-based EMD/ M_W correlation for VLPs is likewise differing from correlations described for other classes of analytes. In addition, we wanted to investigate if a corresponding EMD/ M_W correlation will allow an approx. M_W determination of this class of bionanoparticles with a

relatively quick, cheap (~ 80.000 €), less challenging (in terms of sample quality) and easy to handle analytical setup in comparison to native ESI MS. Mind however, that a high accuracy M_w determination of VLPs is only possible on the basis of MS-derived data. Hence, both methods have to be regarded as yielding complementary information in terms of analyte size and M_w , sample quality, and particle number concentration.

Materials and methods

Chemicals Ammonium acetate (NH_4OAc , $\geq 99.99\%$) and ammonium hydroxide (ACS reagent) were both purchased from Sigma-Aldrich (Steinheim, Germany).

Electrolyte NH_4OAc , 40 mM ammonium acetate at pH 7.0 was used as electrolyte solution for desalting of VLPs and for sample dilution for nES GEMMA and ESI MS. Electrolyte solutions for CDMS measurements are detailed with corresponding experiments. NH_4OAc solution was filtered (0.2 μm pore size syringe filters, Sartorius, Göttingen, Germany) prior application. Millipore (Billerica, MA, USA) grade water was employed (18.2 $\text{M}\Omega\text{cm}$ resistivity at 25 °C).

Biological material Norovirus West Chester GI.1 VLPs (3 mg/mL in PBS, pH 7.4) were produced in insect cells and kindly provided by Grant Hansman, Heidelberg, Germany, and CPMV VLPs (4 mg/mL in 10 mM sodium phosphate, pH 7.0) were from John Innes Centre (kindly provided by George Lomonosoff, Norwich, UK). Bacteriophage P22 VLPs (2 mg/mL in 50 mM sodium phosphate, pH 7.0 including 100 mM sodium chloride and 200 ppm sodium azide) were obtained from Indiana University Bloomington (Bloomington, IN, USA), bacteriophage T5 VLPs (0.3 mg/mL, i.e., 7×10^{12} empty capsids/mL in PBS) from the Institute for Integrative Biology of the Cell (I2BC), Gif-sur-Yvette, France). Human papillomavirus type 16 (HPV16, 0.3 mg/mL in PBS additionally including 625 mM sodium chloride, 0.9 mM calcium chloride, 0.5 mM magnesium chloride, and 2.1 mM potassium chloride) VLPs were prepared from mammalian cells as previously described [50].

Instrumentation Gas-phase electrophoresis was performed on two setups: a nES GEMMA instrument (TSI Inc., Shoreview, MN, USA) consisting of a nES aerosol generator (model 3480) including a ^{210}Po α -particle source, an electrostatic classifier (model 3080) with a nano-differential mobility analyzer (nDMA) and an n-butanol-based ultrafine condensation particle counter (model 3025A or 3776C) was applied as instrument A. Instrument B consisted of a model 3482 nES aerosol generator including a soft X-ray source, an electrostatic classifier (model 3082) and a water-based ultrafine condensation particle counter (model 3788). Twenty-five μm inner

diameter polyimide coated fused silica capillaries (Polymicro, obtained via Optronis, Kehl, Germany) with in-house made tips [51] were employed to transfer analytes from the liquid to the gas phase. Settings for a stable Taylor cone at the nES tip were chosen, typically around 2 kV voltage resulting in approx. – 375 nA current, 0.1 liters per minute (Lpm) CO_2 (Messer, Gumpoldskirchen, Austria) and 1.0 Lpm filtered, dried ambient air. Four pounds per square inch differential (psid, approx. 27.6 kPa) were applied to additionally move the sample through the capillary. Fifteen Lpm sheath flow filtered ambient air was used to size-separate VLPs in an EMD range from 2 to 65 nm. The corresponding EMD size range was scanned for 120 s. Subsequently, the applied voltage was adjusted to starting values within a 30-s timeframe. Seven datasets (raw data obtained from instrument software, MacroIMS manager v2.0.1.0) were combined via their median to yield a corresponding spectrum. Lastly, Gaussian peaks were fitted to spectra via Origin software (OriginPro v9.1.0) to obtain EMD values.

HPV16 VLPs cannot be produced in high yields. Due to the resulting low VLP concentration, samples were only analyzed between 30 and 65 nm EMD to increase the scanning time in this range. In addition, a 40 μm inner diameter capillary was employed to reduce the surface to volume ratio and hence the probability of analyte loss due to VLP interaction with the fused silica material of the nES capillary. This resulted in significantly higher particle numbers detected per channel and hence a discernible VLP peak.

For CPMV and P22 VLPs, native MS was performed on a Q-ToF 2 instrument (Waters, Manchester, UK, and MS Vision, Almere, the Netherlands) modified for high mass experiments [52, 53] and calibrated with cesium iodide. A nano-ESI source in positive ion mode with a source pressure of 10 mbar was used. Capillaries were produced in-house. Borosilicate glass tubes (inner diameter 0.68 mm, outer diameter 1.2 mm with filament; World Precision Instruments, Sarasota, FL, USA) were pulled using a two-step program in a micropipette puller (model P-1000 from Sutter Instruments, Novato, CA, USA) with a squared box filament (2.5 \times 2.5 mm). Subsequently, the capillaries were gold-coated using a sputter coater (Quorum Technologies, East Sussex, UK, 40 mA, 200 s, tooling factor of 2.3 and end bleed vacuum of 8×10^{-2} mbar argon) and opened directly on the sample cone of the mass spectrometer. Voltages of 1.45–1.65 kV and 145–155 V were applied to the capillary and cone, respectively. Xenon (purity 5.0) was used as collision gas at a pressure of $1.7\text{--}2.0 \times 10^{-2}$ mbar to improve the transmission of large ions [53]. Collision energies were ramped from 10 to 400 V. MS profile and repetition frequency of the pusher pulse were adjusted to high mass range. Mass spectra were analyzed using MassLynx (Waters, Manchester, UK).

Mass spectra of norovirus West Chester VLPs were obtained using a home-built ESI CDMS system, described in detail elsewhere [54]. Briefly, CDMS is a single particle MS technique, which retrieves m/z and z for each ion allowing direct mass determination from a charge conducting cylinder functioning also as electrostatic ion trap. Hence, masses of large, heterogeneous biological complexes can be measured. An automated nano-ESI source (Advion, Ithaca, NY, USA) was used to generate ions with a capillary voltage of 1.7 kV. The ions then enter a heated metal capillary and are transmitted using various ion optics to a dual hemispherical deflection energy analyzer which selects ions with energies centered on 100 eV/ z . These ions then enter a modified cone trap. Here, trapped ions oscillate back and forth in a charge detection cylinder for 100 ms. Mass spectra were generated by binning of the single ion masses. Spectra were subsequently analyzed by fitting Gaussian peaks with Origin software (OriginPro 2016).

Sample preparation In order to enable native nES-based analysis of VLPs, employed storage buffers (often including additional salt components or stabilizing agents) had to be replaced by a volatile electrolyte solution. Else, these additional sample components were shown to lead to an increased peak heterogeneity of the analytes of interest and, in nES GEMMA, an elevated baseline resulting from clustering of small, non-volatile molecules during the nES process [55]. As in previous studies, we opted for ammonium acetate and carried out removal of small, buffer-associated sample components via spin filtration [42] employing 10 kDa M_w cutoff filters (Vivaspin-polyethersulfone membrane, Vivacon-regenerated cellulose membrane-both from Sartorius or centrifugal filters-polyethersulfone membrane, VWR, Vienna, Austria). Between 3 and 5 filtration steps were necessary to remove non-volatile additional sample components. Sample concentration for measurements was typically well below 1 mg/mL protein content (based on originally determined values and sample dilution).

Results and discussion

It was the aim of our investigation to analyze VLP material with gas-phase electrophoresis on a native nES GEMMA instrument and to compare results with data obtained from native ESI MS and from literature. We intended to setup an EMD/ M_w correlation for VLPs to allow for future VLP M_w determination based on gas-phase electrophoresis directed towards analysis of samples not applicable to native ESI ToF MS.

Native nES GEMMA analysis of VLPs In previous work, we had already described the analysis of VLP or VLP-like material

based on hepatitis B virus capsids (HBV) with two icosahedral symmetries [12] and subviral particles of a human rhinovirus serotype (HRV-A2) [4]. We now turned to further VLP material and analyzed bionanoparticles derived from cowpea mosaic virus (CPMV), a norovirus strain and particles from bacteriophage P22 and T5 via gas-phase electrophoresis. Figure 1 depicts corresponding native nES GEMMA spectra. An overview of investigated VLPs and resulting EMD values are listed in Table 1. In order to exclude the possibility of unspecific aggregation of sample components, VLPs were electrosprayed from samples diluted to at least three different concentrations. Unspecific aggregation of components was excluded, if peaks remained at identical EMD values for all investigated dilutions.

Besides information on the surface-dry VLP size and an approximation on the bionanoparticle number concentration, two other pieces of information could be gathered from native nES GEMMA spectra. (i) Especially for norovirus West Chester VLPs (Fig. 1b), detection of material below 10 nm EMD hinted the presence of free proteins. Pogan et al. [13] showed that these particles already disassemble at neutral pH and low ionic strengths, which is in line with our results. Moreover, general particle rupture in the nES process is unlikely, as such peaks were only recorded for norovirus West Chester VLPs. (ii) Especially for bacteriophage P22-based VLPs (Fig. 1c) several additional species with significantly lower abundance than the main VLP peak were detected (e.g., at 34 or 45 nm EMD). If these peaks correspond to species simply carrying a higher number of charges from insufficient charge equilibration in the bipolar atmosphere of the nES unit or are analytes of biological relevance (e.g., capsids losing subunits) cannot be determined based on obtained native nES GEMMA results alone. However, ESI ToF MS also showed at least one additional species, which indicates that the observed peaks correspond to different assemblies present in solution (Fig. 2).

Native ESI MS analysis of VLPs Next to targeting these VLP analytes via native nES GEMMA, we also applied native ESI MS in VLP characterization. Employing Q-ToF instruments, challenges of VLP M_w determination in native ESI MS become obvious. For the same samples as with native nES GEMMA, clear peaks were obtained via native ESI ToF MS (Fig. 2). However, the lack of charge state separation hampered exact mass determination. Common sources for lack of resolution are intrinsic VLP heterogeneity mostly on protein level, e.g., the presence of truncated protein or sequence variants, or simply size resulting in overlapping charge states. As was shown in a previous study, the problems in charge state resolution can be instrument, but as well analyte derived [3]. Furthermore, incomplete desolvation can additionally cause peak broadening, which influences native ESI ToF MS to a higher extent than gas-phase electrophoresis. Nevertheless,

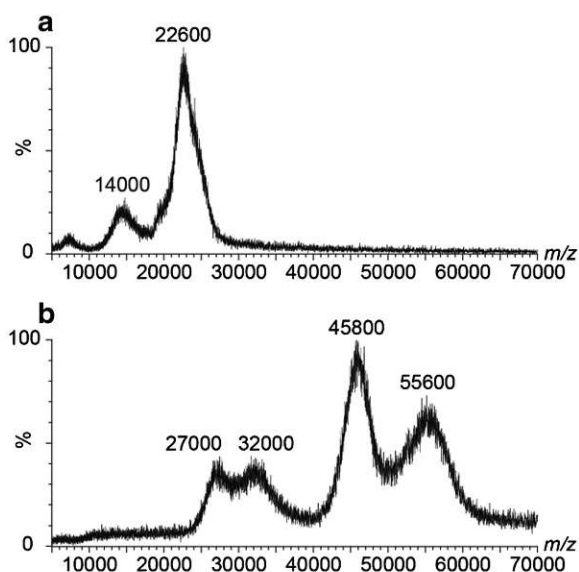


Fig. 2 QTOF native ESI MS data for VLPs: CPMV at 50 V collision energy (a) and bacteriophage P22 at 100 V collision energy (b) are shown. Although in both cases signals are detected, analyte heterogeneity precluded charge state resolution. m/z values at peak apices are given. VLPs were exchanged to 40 mM NH_4OAc , pH 7.0, using 10 kDa M_W cutoff filters. Peaks at 14,000, 27,000, and 32,000 m/z may represent metastable ions

A collapse of VLP particles during gas-phase electrophoresis upon stripping of solvent molecules from their interior seems highly unlikely as AFM and dot-blot analyses of a vaccine VLP demonstrated particle integrity after gas-phase electrophoresis [44]. Instead, due to protein analyte inherent M_W limitations, especially a direct comparison of a protein correlation with an EMD/ M_W correlation for VLPs is to date not feasible. Simply because VLPs are analyzed in an EMD/ M_W range, in which pure protein complexes (in a non-aggregated or structured form) rarely exist, the extrapolation

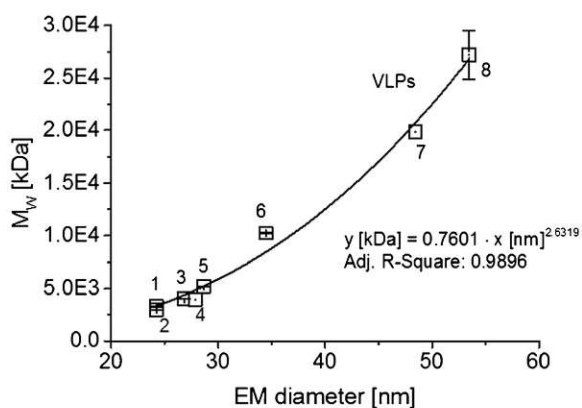


Fig. 3 nES GEMMA and MS data can be related to yield an EMD/ M_W correlation valid for VLPs. The numbering of data points correlates to Table 1

of the protein EMD/ M_W correlation to larger EMD and M_W values has to be taken with extreme caution. It is of note that the largest protein analyzed in [32] was the octamer of β -galactosidase with an EMD of 16.83 nm and a M_W of 931.28 kDa.

In contrast, the VLP-based EMD/ M_W correlation is based on data points for larger EMD/ M_W values. VLPs with low EMD/ M_W value are not reasonable as the proteinaceous sphere has to be of a certain lower size limit (around 20 nm) in order to allow for genome encapsulation within the capsid. Therefore, there is poor overlap between pure protein complex and VLP curves. Extrapolation of either the protein correlation to large or the VLP correlation to lower EMD/ M_W values is problematic. Hence, we advise against taking one single EMD/ M_W correlation for all investigated analyte classes in order to calculate M_W values based on a particle EMD.

EMD/ M_W correlations on different native nES GEMMA instruments As it was our intention to setup an EMD/ M_W correlation for VLPs applicable to as many as possible corresponding native nES GEMMA instrumentations, we asked ourselves, if obtained results can be ported between setups. Laschober and colleagues already reported in 2007 differences of up to 15% in obtained EMD values for globular proteins up to 660 kDa [58]. Especially slight variations in nDMA geometries, length values of connecting tubes between instrument parts or differences in sheath flow values may lead to deviations observed between instruments. Therefore, we analyzed a set of analytes on another gas-phase electrophoretic setup besides our standard native nES GEMMA (instrument A). This instrument corresponded to a next-generation setup with differences in the geometry of the nES source and a soft X-ray source for charge equilibration (instrument B). Detection on the latter instrumentation was carried out on a water-based CPC. We

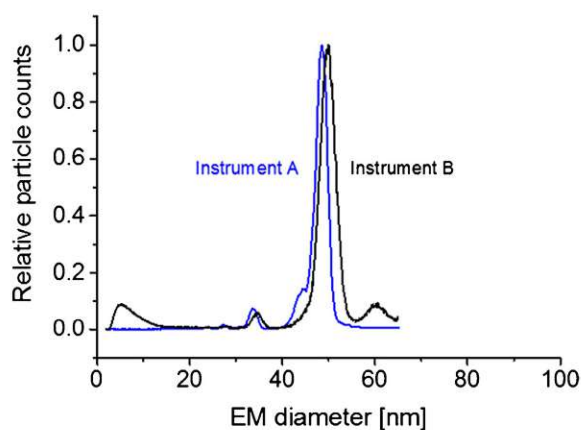
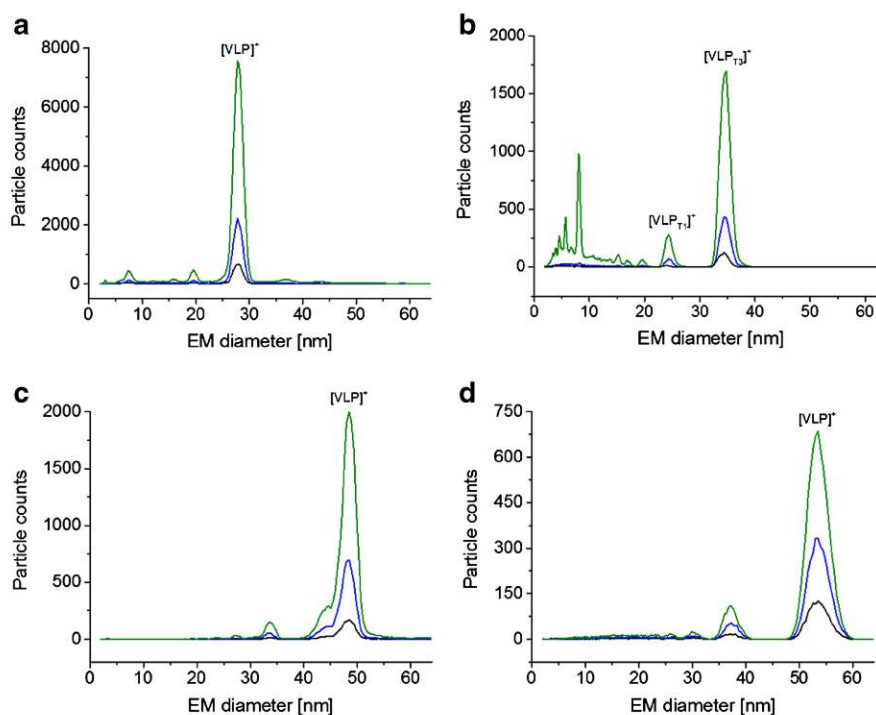


Fig. 4 Comparing gas-phase electrophoresis data obtained on two instrument generations. As shown for bacteriophage P22, a significant shift in obtained EMD values on both instruments is found. Corresponding EMD data is found in Table 2

Fig. 1 nES GEMMA data for VLPs: CPMV (a), norovirus West Chester (b), bacteriophage P22 (c), and bacteriophage T5 capsids (d). All VLPs are shown in three different dilutions of obtained material after solution exchange to 40 mM NH_4OAc , pH 7.0 employing 10 kDa M_W cutoff membrane filters. (Typically, overall dilutions were in the range of 1:10 to 1:250 [v:v] of the original VLP stock solutions resulting from solution exchange and sample dilution steps)



using an experimentally derived equation [57], also in such cases, the M_W can be estimated from the obtained m/z values. Taking for instance m/z of 22,600 for CPMV into consideration, a M_W of 3107 kDa is obtained, for bacteriophage P22, an m/z of 55,600 yields a M_W of 18,807 kDa. Both M_W values are in the same range as data found in literature (see Table 1). In general, the spectra show that the number of different observed sizes is in line with the nES GEMMA results. Moreover, the norovirus VLPs were also analyzed on an ESI CDMS instrument to provide M_W values without the need for charge state resolution and obtain more values for the correlation (Electronic Supplementary Material (ESM) Fig. S1). Additionally, application of an Orbitrap instrument with

higher resolution might help to resolve charge states in a future study.

Combining native nES GEMMA and native ESI MS data yields an EMD/ M_W correlation for VLPs Based on our analyses of VLP material via native nES GEMMA and accurate mass values from native ESI MS including literature values (given in Table 1), we set up a corresponding EMD/ M_W correlation: $y [M_W \text{ in kDa}] = 0.7601 [\text{EMD in nm}]^{2.6319}$ (Fig. 3). Notably, this deviates from a correlation for proteins as was the case for filled virions [32]. Hence, a basic knowledge concerning the analyte class prior EMD-based M_W calculation (but not for gas-phase electrophoresis itself) is necessary.

Table 1 Overview on investigated VLP material as well as data taken from literature as indicated

VLP	EM diameter (nm)	Based on	M_W (kDa)	Based on
1 Norovirus West Chester T1 VLP	24.22 ± 0.21	–	3320 ± 30	CDMS
2 Hepatitis B virus (HBV) T3 VLP	24.22 ± 0.40	[12]	3004 ± 3	MS [12]
3 Hepatitis B virus (HBV) T4 VLP	26.84 ± 0.44	[12]	4006 ± 3	MS [12]
4 Cowpea mosaic virus (CPMV) VLP	27.88 ± 0.04	–	3940 ± n.a.	[56]
5 Subviral B particle of human rhinovirus 2	28.68 ± 0.07	[4]	5210 ± 2	MS [4]
6 Norovirus West Chester T3 VLP	34.47 ± 0.15	–	10,260 ± 40	CDMS
7 Bacteriophage P22 VLP	48.44 ± 0.12	–	19,840 ± n.a.	MS [11]
8 Bacteriophage T5 VLP	53.45 ± 0.09	–	27,200 ± 2300	MS [15]

New data is presented in italics. An exemplary CDMS spectrum of investigated VLPs is shown in the ESM (Fig. S1). At least $N=3$ technical replicates were used per EMD value. Errors provided are standard deviations

Table 2 Comparison of averaged EMD values obtained on several gas-phase electrophoretic instrumentations

Analyte	MW (kDa)	Instrument A			Instrument B	
		EMD (nm)	STDEV	(%) value instrument B	EMD (nm)	STDEV
IgG	M 147.27	9.03	0.10	95.19	9.49	0.04
IgG	D 294.54	11.26	0.10	95.58	11.78	0.04
β -Gal	M 116.41	8.33	0.11	95.76	8.70	0.03
β -Gal	D 232.82	10.57	0.11	95.52	11.07	0.02
Dextran 150	M 147.6	8.17	0.15	98.67	8.28	0.01
Dextran 670	M 667.8	10.05	0.41	92.88	10.82	0.12
Oat β glucan 80	M 81	7.12	0.04	93.81	7.59	0.03
Oat β glucan 1500	M 1508	7.71	0.15	94.83	8.13	0.04
CPMV VLP	M 3940	27.88	0.04	99.32	28.07	0.07
P22 VLP	M 19,840	48.44	0.12	97.21	49.83	0.07

At least $N=3$ measurements were considered per EMD value. M_W values and data for instrument A either taken from [32] or Table 1. M monomer, D dimer; errors provided are standard deviations

opted for immunoglobulin G (IgG), β -galactosidase (β -Gal), several polysaccharides (dextrans and oat β glucans), CPMV VLP, and bacteriophage P22 VLP as analytes.

Resulting spectra from gas-phase electrophoresis carried out on the two instrumentations are depicted in Fig. 4 as exemplified by P22 VLPs. Corresponding data for all analytes is given in Table 2. As can be seen, indeed slight differences between instrumentations were detected. For instance, the EMD of investigated proteins deviated on average by 4.5% at the peak apex between our standard instrumentation (instrument A) and the next-generation setup (instrument B). Less variation was found for VLPs, more for polysaccharides. Based on this data, we strongly suggest calibration of each instrument for corresponding EMD-based M_W calculation: Instrument specific parameters have to be regarded in order to obtain reliable EMD-based M_W

values via gas-phase electrophoresis. A simple porting of EMD/ M_W correlations between instrumentations without considering a corresponding deviation would lead to significant systematic errors in EMD-based particle M_W calculation.

Application of the developed EMD/ M_W correlation in VLP research, an example Following the setup of our EMD/ M_W correlation for VLPs, we turned to another VLP based on HPV16, for which no native MS data was obtained so far. We carried out our analyses on our standard instrumentation (instrument A). Employing native nES GEMMA, we could obtain a peak at 47.78 ± 0.29 nm EM diameter ($N=4$ measurements, Fig. 5). Subsequently, we employed our EMD/ M_W correlation for the calculation of the VLP M_W . A result of 19,975 kDa is in good accordance with the expected value of 20,260 kDa (based on 72 pentamers of coat protein L1, Uniprot data, P03101, retrieved on January 17th, 2019); the deviation is in fact below 1.5%. Reasons for this deviation could be inter alia (i) a still relatively low number of data points available for the VLP EMD/ M_W correlation, (ii) the shape, surface texture, or tightness of the proteinaceous shell itself, (iii) additional material encapsulated within VLPs, or (iv) differences between VLP material measured via native nES GEMMA and material described in the database. Nevertheless, employing HPV16 as an exemplary VLP bionanoparticle, we were able to demonstrate the applicability of native nES GEMMA-based M_W determination of VLP analytes.

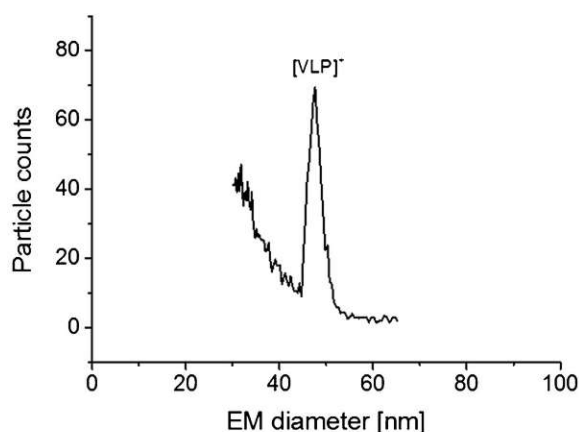


Fig. 5 nES GEMMA yields a peak for HPV16-based VLPs allowing its subsequent M_W determination based on the correlation presented in Fig. 3. The calculated M_W (19,975 kDa) is in good accordance with the theoretically expected M_W value (20,260 kDa, based on VLP stoichiometry and database M_W values for individual viral proteins)

Concluding remarks

For pharmaceutical applications as pointed out above, the thorough characterization of VLPs in terms of particle size,

M_w , sample, and analyte heterogeneity and particle number-based concentration is a necessary prerequisite. In general, it can be seen that ESI MS, whether from ToF or CDMS instruments, is in good agreement with nES GEMMA in terms of species detected. Hence, ESI MS results can be used to interpret nES GEMMA data of unknown samples. However, although native ESI ToF MS is unrivaled in VLP M_w determination, it often experiences problems due to sample specific problems, like heterogeneity or low particle numbers. Even though ESI CDMS is not suffering from sample heterogeneity, it is slow, requiring several hours per mass spectrum, and the home-built instrumentation is not widely accessible. nES GEMMA on the other hand is less prone to the mentioned sample inherent characteristics and is relatively cheap facilitating wide application. Analytes are separated according to electrophoretic principles in the gas-phase at ambient pressure based on their size yielding particle number-based concentrations. As has already been shown for other analyte classes, a subsequent correlation between the nES GEMMA-derived EMD and the particle M_w allows (bio-)nanoparticle M_w calculation in good approximation. We now focused on spherical VLPs and analyzed a variety of these bionanoparticles to setup an EMD/ M_w correlation, which we found significantly different from correlations known for, e.g., proteins or intact virus particles. As such, it is crucial to know the nature of samples prior to M_w determination. As demonstrated, application of this correlation allowed us to calculate the M_w of a VLP, for which native ESI MS data is not available to date. Especially through the combination of both methods, nES GEMMA and native ESI MS, as exemplified here, a thorough VLP characterization will be feasible in the future.

Acknowledgments Open access funding provided by TU Wien (TUW). VUW acknowledges funding of the Austrian Theodor Körner Fonds. VUW and RP both acknowledge funding of COST Action BM1403 - Native Mass Spectrometry and Related Methods for Structural Biology. The Heinrich-Pette-Institute, Leibniz Institute for Experimental Virology is supported by the Freie und Hansestadt Hamburg and the Bundesministerium für Gesundheit (BMG). CU acknowledges funding from the Leibniz Association through SAW-2014-HPI-4 grant. RP acknowledges funding from EU Horizon 2020 project VIRUSCAN 731868 and thanks MINGS. CU, RP, DP and MS further thank the DFG FOR2327 Virocarb for support. We thank Grant Hansman and George Lomonosoff for providing VLPs. ES was supported by the Graduate Training Program in Quantitative and Chemical Biology under Award T32 GM109825 and Indiana University.

Author contributions Initial idea: VUW, GA; nES GEMMA measurements: VUW, RP, SZ; MS measurements: RP, KB, NL; sample preparation: PB, DP, MS, ES; data interpretation: VUW, RP, CU, GA; instrumentation: GA, CU, MFJ; funding: GA, CU, VUW; scientific guidance: GA, CU, VUW; organization: VUW; all authors contributed to the manuscript.

Compliance with ethical standards

Conflict of interest The authors declare that they have no conflict of interest.

Open Access This article is distributed under the terms of the Creative Commons Attribution 4.0 International License (<http://creativecommons.org/licenses/by/4.0/>), which permits unrestricted use, distribution, and reproduction in any medium, provided you give appropriate credit to the original author(s) and the source, provide a link to the Creative Commons license, and indicate if changes were made.

References

1. Sieben C, Kappel C, Zhu R, Wozniak A, Rankl C, Hinterdorfer P, et al. Influenza virus binds its host cell using multiple dynamic interactions. *P Natl Acad Sci USA*. 2012;109(34):13626–31.
2. Zeltins A. Construction and characterization of virus-like particles: a review. *Mol Biotechnol*. 2013;53(1):92–107.
3. Uetrecht C, Versluis C, Watts NR, Roos WH, Wuite GJ, Wingfield PT, et al. High-resolution mass spectrometry of viral assemblies: molecular composition and stability of dimorphic hepatitis B virus capsids. *Proc Natl Acad Sci U S A*. 2008;105(27):9216–20.
4. Weiss VU, Bereszczak JZ, Havlik M, Kallinger P, Gosler I, Kumar M, et al. Analysis of a common cold virus and its subviral particles by gas-phase electrophoretic mobility molecular analysis and native mass spectrometry. *Anal Chem*. 2015;87(17):8709–17.
5. Snijder J, van de Waterbeemd M, Damoc E, Denisov E, Grinfeld D, Bennett A, et al. Defining the stoichiometry and cargo load of viral and bacterial nanoparticles by Orbitrap mass spectrometry. *J Am Chem Soc*. 2014;136(20):7295–9.
6. Snijder J, Rose RJ, Veeler D, Johnson JE, Heck AJR. Studying 18 MDa virus assemblies with native mass spectrometry. *Angew Chem Int Edit*. 2013;52(14):4020–3.
7. Sipe DM, Ozdemir A, Firek B, Hendrix RW, Bier ME. Analysis of viral CapsidHK97 via cryodetection MALDI TOF in the megadalton mass range. In: 56th ASMS Conference on Mass Spectrometry and Allied Topics. June 1st–5th, 2008; Denver, CO, USA(# 571).
8. Keifer DZ, Pierson EE, Jarrold MF. Charge detection mass spectrometry: weighing heavier things. *Analyst*. 2017;142(10):1654–71.
9. Keifer DZ, Motwani T, Teschke CM, Jarrold MF. Measurement of the accurate mass of a 50 MDa infectious virus. *Rapid Commun Mass Spectrom*. 2016;30(17):1957–62.
10. Keifer DZ, Motwani T, Teschke CM, Jarrold MF. Acquiring structural information on virus particles with charge detection mass spectrometry. *J Am Soc Mass Spectrom*. 2016;27(6):1028–36.
11. Keifer DZ, Pierson EE, Hogan JA, Bedwell GJ, Prevelige PE, Jarrold MF. Charge detection mass spectrometry of bacteriophage P22 procapsid distributions above 20 MDa. *Rapid Commun Mass Spectrom*. 2014;28(5):483–8.
12. Bereszczak JZ, Havlik M, Weiss VU, Marchetti-Deschmann M, van Duijn E, Watts NR, et al. Sizing up large protein complexes by electrospray ionisation-based electrophoretic mobility and native mass spectrometry: morphology selective binding of Fabs to hepatitis B virus capsids. *Anal Bioanal Chem*. 2014;406(5):1437–46.

13. Pogan R, Schneider C, Reimer R, Hansman G, Uetrecht C. Norovirus-like VP1 particles exhibit isolate dependent stability profiles. *J Phys Condens Matter*. 2018;30(6):064006.
14. Shoemaker GK, van Duijn E, Crawford SE, Uetrecht C, Baclayon M, Roos WH, et al. Norwalk virus assembly and stability monitored by mass spectrometry. *Mol Cell Proteomics*. 2010;9(8):1742–51.
15. Dominguez-Medina S, Foster S, Defoort M, Sansa M, Stark AK, Halim MA, et al. Neutral mass spectrometry of virus capsids above 100 megadaltons with nanomechanical resonators. *Science*. 2018;362(6417):918–22.
16. Naik AK, Hanay MS, Hiebert WK, Feng XL, Roukes ML. Towards single-molecule nanomechanical mass spectrometry. *Nat Nanotechnol*. 2009;4(7):445–50.
17. Malvar O, Ruz JJ, Kosaka PM, Dominguez CM, Gil-Santos E, Calleja M, et al. Mass and stiffness spectrometry of nanoparticles and whole intact bacteria by multimode nanomechanical resonators. *Nat Commun*. 2016;7:13452.
18. Kaufman SL, Skogen JW, Dorman FD, Zarrin F, Lewis KC. Macromolecule analysis based on electrophoretic mobility in air: globular proteins. *Anal Chem*. 1996;68(11):1895–904.
19. Kallinger P, Szymanski WW. Experimental determination of the steady-state charging probabilities and particle size conservation in non-radioactive and radioactive bipolar aerosol chargers in the size range of 5–40 nm. *J Nanopart Res*. 2015;17(4):171.
20. Allmaier G, Weiss VU, Engel NY, Marchetti-Deschmann M, Szymanski WW. Soft X-ray radiation applied in the analysis of intact viruses and antibodies by means of nano electrospray differential mobility analysis. In: Banoub JH, Caprioli RM, editors. *Molecular technologies for detection of chemical and biological agents*. Dordrecht: Springer Netherlands; 2017. p. 149–57.
21. Epstein H, Afergan E, Moise T, Richter Y, Rudich Y, Golomb G. Number-concentration of nanoparticles in liposomal and polymeric multiparticulate preparations: empirical and calculation methods. *Biomaterials*. 2006;27(4):651–9.
22. Weiss VU, Urey C, Gondikas A, Golesne M, Friedbacher G, von der Kammer F, et al. Nano electrospray gas-phase electrophoretic mobility molecular analysis (nES GEMMA) of liposomes: applicability of the technique for nano vesicle batch control. *Analyst*. 2016;141(21):6042–50.
23. Chernyshev VS, Rachamadugu R, Tseng YH, Belnap DM, Jia YL, Branch KJ, et al. Size and shape characterization of hydrated and desiccated exosomes. *Anal Bioanal Chem*. 2015;407(12):3285–301.
24. Hogan CJ Jr, Kettleton EM, Ramaswami B, Chen DR, Biswas P. Charge reduced electrospray size spectrometry of mega- and gigadalton complexes: whole viruses and virus fragments. *Anal Chem*. 2006;78(3):844–52.
25. TJ J, Bothner B, Traina J, Benner WH, Siuzdak G. Electrospray ion mobility spectrometry of intact viruses. *Spectroscopy*. 2004;18:31–6.
26. Pease LF 3rd. Physical analysis of virus particles using electrospray differential mobility analysis. *Trends Biotechnol*. 2012;30(4):216–24.
27. Pease LF 3rd, Lipin DI, Tsai DH, Zachariah MR, Lua LH, Tarlov MJ, et al. Quantitative characterization of virus-like particles by asymmetrical flow field flow fractionation, electrospray differential mobility analysis, and transmission electron microscopy. *Biotechnol Bioeng*. 2009;102(3):845–55.
28. Pease LF 3rd, Tsai DH, Brorson KA, Guha S, Zachariah MR, Tarlov MJ. Physical characterization of icosahedral virus ultra structure, stability, and integrity using electrospray differential mobility analysis. *Anal Chem*. 2011;83(5):1753–9.
29. Laschober C, Wruss J, Blaas D, Szymanski WW, Allmaier G. Gas-phase electrophoretic molecular mobility analysis of size and stoichiometry of complexes of a common cold virus with antibody and soluble receptor molecules. *Anal Chem*. 2008;80(6):2261–4.
30. Kaddis CS, Lomeli SH, Yin S, Berhane B, Apostol MI, Kickhoefer VA, et al. Sizing large proteins and protein complexes by electrospray ionization mass spectrometry and ion mobility. *J Am Soc Mass Spectrom*. 2007;18(7):1206–16.
31. Malm L, Hellman U, Larsson G. Size determination of hyaluronan using a gas-phase electrophoretic mobility molecular analysis. *Glycobiology*. 2012;22(1):7–11.
32. Weiss VU, Golesne M, Friedbacher G, Alban S, Szymanski WW, Marchetti-Deschmann M, et al. Size and molecular weight determination of polysaccharides by means of nano electrospray gas-phase electrophoretic mobility molecular analysis (nES GEMMA). *Electrophoresis*. 2018;39(9–10):1142–50.
33. Szymanski WW, Bacher G, Allmaier G. Applicability of nanoaerosol techniques for measurements of high-mass biopolymers and complexes. In: Szymanski WW, Wagner P, Itoh M, Ohachi T, editors. *Nanostructured materials and their applications*. Vienna: Facultas; 2004. p. 157–66.
34. Mouradian S, Skogen JW, Dorman FD, Zarrin F, Kaufman SL, Smith LM. DNA analysis using an electrospray scanning mobility particle sizer. *Anal Chem*. 1997;69(5):919–25.
35. Saucy DA, Ude S, Lenggoro IW, Fernandez de la Mora J. Mass analysis of water-soluble polymers by mobility measurement of charge-reduced ions generated by electrosprays. *Anal Chem*. 2004;76(4):1045–53.
36. Ude S, Fernandez de la Mora J, Thomson BA. Charge-induced unfolding of multiply charged polyethylene glycol ions. *J Am Chem Soc*. 2004;126(38):12184–90.
37. Muller R, Laschober C, Szymanski WW, Allmaier G. Determination of molecular weight, particle size, and density of high number generation PAMAM dendrimers using MALDI-TOF-MS and nES-GEMMA. *Macromolecules*. 2007;40(15):5599–605.
38. Dudkiewicz A, Wagner S, Lehner A, Chaudhry Q, Pietravalle S, Tiede K, et al. A uniform measurement expression for cross method comparison of nanoparticle aggregate size distributions. *Analyst*. 2015;140(15):5257–67.
39. Grombe R, Charoud-Got J, Emteborg H, Linsinger TP, Seghers J, Wagner S, et al. Production of reference materials for the detection and size determination of silica nanoparticles in tomato soup. *Anal Bioanal Chem*. 2014;406(16):3895–907.
40. Hinterwirth H, Wiedmer SK, Moilanen M, Lehner A, Allmaier G, Waitz T, et al. Comparative method evaluation for size and size-distribution analysis of gold nanoparticles. *J Sep Sci*. 2013;36(17):2952–61.
41. Kallinger P, Weiss VU, Lehner A, Allmaier G, Szymanski WW. Analysis and handling of bio-nanoparticles and environmental nanoparticles using electrostatic aerosol mobility. *Particuology*. 2013;11(1):14–9.
42. Weiss VU, Lehner A, Kerul L, Grombe R, Kratzmeier M, Marchetti-Deschmann M, et al. Characterization of cross-linked gelatin nanoparticles by electrophoretic techniques in the liquid and the gas phase. *Electrophoresis*. 2013;34(24):3267–76.
43. Tsai DH, DelRio FW, Pettibone JM, Lin PA, Tan J, Zachariah MR, et al. Temperature-programmed electrospray-differential mobility analysis for characterization of ligated nanoparticles in complex media. *Langmuir*. 2013;29(36):11267–74.
44. Havlik M, Marchetti-Deschmann M, Friedbacher G, Winkler W, Messner P, Perez-Burgos L, et al. Comprehensive size-determination of whole virus vaccine particles using gas-phase

- electrophoretic mobility macromolecular analyzer, atomic force microscopy, and transmission electron microscopy. *Anal Chem.* 2015;87(17):8657–64.
45. Wieland K, Ramer G, Weiss VU, Allmaier G, Lendl B, Centrone A. Nanoscale chemical imaging of individual chemotherapeutic cytarabine-loaded liposomal nanocarriers. *Nano Res.* 2019;12(1):197–203.
 46. Weiss VU, Wieland K, Schwaighofer A, Lendl B, Allmaier G. Native nano-electrospray differential mobility analyzer (nES GEMMA) enables size selection of liposomal nanocarriers combined with subsequent direct spectroscopic analysis. *Anal Chem.* 2019;91(6):3860–8.
 47. Engel NY, Weiss VU, Marchetti-Deschmann M, Allmaier G. nES GEMMA analysis of lectins and their interactions with glycoproteins - separation, detection, and sampling of noncovalent biospecific complexes. *J Am Soc Mass Spectrom.* 2017;28(1):77–86.
 48. Bacher G, Szymanski WW, Kaufman SL, Zollner P, Blaas D, Allmaier G. Charge-reduced nano electrospray ionization combined with differential mobility analysis of peptides, proteins, glycoproteins, noncovalent protein complexes and viruses. *J Mass Spectrom.* 2001;36(9):1038–52.
 49. Allmaier G, Laschober C, Szymanski WW. Nano ES GEMMA and PDMA, new tools for the analysis of nanobiotopes-protein complexes, lipoparticles, and viruses. *J Am Soc Mass Spectrom.* 2008;19(8):1062–8.
 50. Buck CB, Thompson CD. Production of papillomavirus-based gene transfer vectors. *Curr Protoc Cell Biol.* 2007. <https://doi.org/10.1002/0471143030.cb2601s37>.
 51. Tycova A, Prikryl J, Foret F. Reproducible preparation of nanospray tips for capillary electrophoresis coupled to mass spectrometry using 3D printed grinding device. *Electrophoresis.* 2016;37(7–8):924–30.
 52. van den Heuvel RH, van Duijn E, Mazon H, Synowsky SA, Lorenzen K, Versluis C, et al. Improving the performance of a quadrupole time-of-flight instrument for macromolecular mass spectrometry. *Anal Chem.* 2006;78:7473–83.
 53. Lorenzen K, Versluis C, van Duijn E, van den Heuvel RHH, Heck AJR. Optimizing macromolecular tandem mass spectrometry of large non-covalent complexes using heavy collision gases. *Int J Mass Spectrom.* 2007;268(2–3):198–206.
 54. Contino NC, Pierson EE, Keifer DZ, Jarrold MF. Charge detection mass spectrometry with resolved charge states. *J Am Soc Mass Spectrom.* 2013;24(1):101–8.
 55. Weiss VU, Kerul L, Kallinger P, Szymanski WW, Marchetti-Deschmann M, Allmaier G. Liquid phase separation of proteins based on electrophoretic effects in an electrospray setup during sample introduction into a gas-phase electrophoretic mobility molecular analyzer (CE-GEMMA/CE-ES-DMA). *Anal Chim Acta.* 2014;841:91–8.
 56. Wang Q, Kaltgrad E, Lin T, Johnson JE, Finn MG. Natural supra-molecular building blocks. Wild-type cowpea mosaic virus. *Chem Biol.* 2002;9(7):805–11.
 57. Catalina MI, van den Heuvel RH, van Duijn E, Heck AJ. Decharging of globular proteins and protein complexes in electrospray. *Chemistry.* 2005;11(3):960–8.
 58. Laschober C, Kaddis CS, Reischl GP, Loo JA, Allmaier G, Szymanski WW. Comparison of various nano-differential mobility analysers (nDMAs) applying globular proteins. *J Exp Nanosci.* 2007;2(4):291–301.

Publisher's note Springer Nature remains neutral with regard to jurisdictional claims in published maps and institutional affiliations.



Victor U. Weiss is an Assistant Professor in the research group “Mass Spectrometric Bio- and Polymer Analytics” at TU Wien, Institute of Chemical Technologies and Analytics, Vienna, Austria. In his research, he focusses on the characterization and detection of nanoparticle material (organic, inorganic, and biological, e.g., liposomes, viruses, and virus-like particles) by application of electrophoretic techniques (liquid-phase electrophoresis in the capillary and the chip format as well as gas-phase electrophoresis). Furthermore, he works on the on- and offline hyphenation of gas-phase electrophoresis to orthogonal analysis methods.



Ronja Pogan is a PhD student at Charlotte Uetrecht's lab at the Heinrich Pette Institute, Leibniz Institute for Experimental Virology in Hamburg, Germany. She studied biology in Hamburg. Her work within the Horizon 2020 project VIRUSCAN aims to characterize viral particles with mass spectrometry focusing on capsid assembly and stability.



Samuele Zoratto is a PhD student in the research group “Mass Spectrometric Bio- and Polymer Analytics” at TU Wien, Institute of Chemical Technologies and Analytics, Vienna, Austria. His current project focusses on methods development for the characterization of nano(bio)particles (i.e., virus-like particles) by means of gas-phase electrophoresis (nES GEMMA), atomic force microscopy (AFM), and native mass spectrometry (nMS).



Kevin M. Bond is a PhD candidate in Professor Martin F. Jarrold's research lab at Indiana University in Bloomington, Indiana. His research in the Jarrold group has primarily involved investigation of the assembly pathways and products of virus-like particles and the analysis of viral vaccines using charge detection mass spectrometry.



Nicholas Lykтей is a PhD candidate in Professor Martin F. Jarrold's research lab at Indiana University in Bloomington, Indiana. His research in the Jarrold group has primarily involved investigation of the gene therapy vector AAV as well as studies of micellular formation using charge detection mass spectrometry.



DNA into the host cell.

Pascale Boulanger is Head of the Team Bacteriophage T5 of the Institute for Integrative Biology of the Cell (I2BC) in Gif-sur-Yvette, France. She has been studying for many years the mechanisms of infection of bacteria by their natural predators, the bacteriophages, using both in vivo and in vitro approaches. She has been a major contributor in deciphering the structure of phage T5 particle as well as the molecular basis of phage/host recognition and delivery of viral



Dominik Pahl is a PhD student in the Institute of Cellular Virology in Münster, Germany. His work is focused on structural features of the human papillomavirus capsid during cell entry.



Martin F. Jarrold is Full Professor and Robert and Marjorie Mann Chair in the Chemistry Department at Indiana University in Bloomington, Indiana. His current research focusses on the development and applications of charge detection mass spectrometry.



Nicole Puffler graduated with her Master's from TU Wien where she studied "Technical Chemistry." She focused on analytical chemistry and wrote her bachelor and master thesis within the Institute of Chemical Technologies and Analytics (TU Wien, Vienna, Austria).



Mario Schelhaas is Director of the Institute of Cellular Virology at the University of Münster, Germany. His work is focussed on structural and cell biological aspects of virus entry (particularly of small non-enveloped DNA viruses) into host cells with a strong emphasis on imaging techniques.



Charlotte Uetrecht is Junior Group Leader at the Heinrich Pette Institute, Leibniz Institute for Experimental Virology, Hamburg, Germany, and guest scientist at the European XFEL GmbH, Schenefeld, Germany. Her research focuses on dynamics of viral structures using structural mass spectrometry. She studied biochemistry in Potsdam, Germany, obtained her PhD from Utrecht University in the lab of Albert Heck and did a postdoc in Uppsala, Sweden, and at

European XFEL.



Ekaterina Selivanovitch is a 4th year chemistry PhD student in the Douglas Lab at Indiana University. Her current research is based on the development of biomimetic materials using virus-like particles. She received a B.S. in chemistry from St. Francis College in Brooklyn, NY, and a M.S. in chemistry from St. John's University in Queens, NY.



Günter Allmaier is Full Professor of Analytical Chemistry in the research group "Mass Spectrometric Bio- and Polymer Analytics" at TU Wien, Institute of Chemical Technologies and Analytics, Vienna, Austria. Since the beginning of the 1980s, he has been working in the field of mass spectrometry and analysis of bioactive compounds with emphasis on therapeutic proteins and proteomics/lipidomics. During the last 15 years, he has also been engaged in the field of electrophoretic separation in the liquid and gas phase of various classes of biomolecules and nano(bio)particles.

eretic separation in the liquid and gas phase of various classes of biomolecules and nano(bio)particles.

Analytical and Bioanalytical Chemistry

Electronic Supplement Material

Virus-like particle size and molecular weight/mass determination applying gas-phase electrophoresis (native nES GEMMA)

Victor U. Weiss, Ronja Pogan, Samuele Zoratto, Kevin Bond, Pascale Boulanger,
Martin F. Jarrold, Nicholas Lykтей, Dominik Pahl, Nicole Puffler, Mario Schelhaas,
Ekaterina Selivanovitch, Charlotte Uetrecht, Günter Allmaier

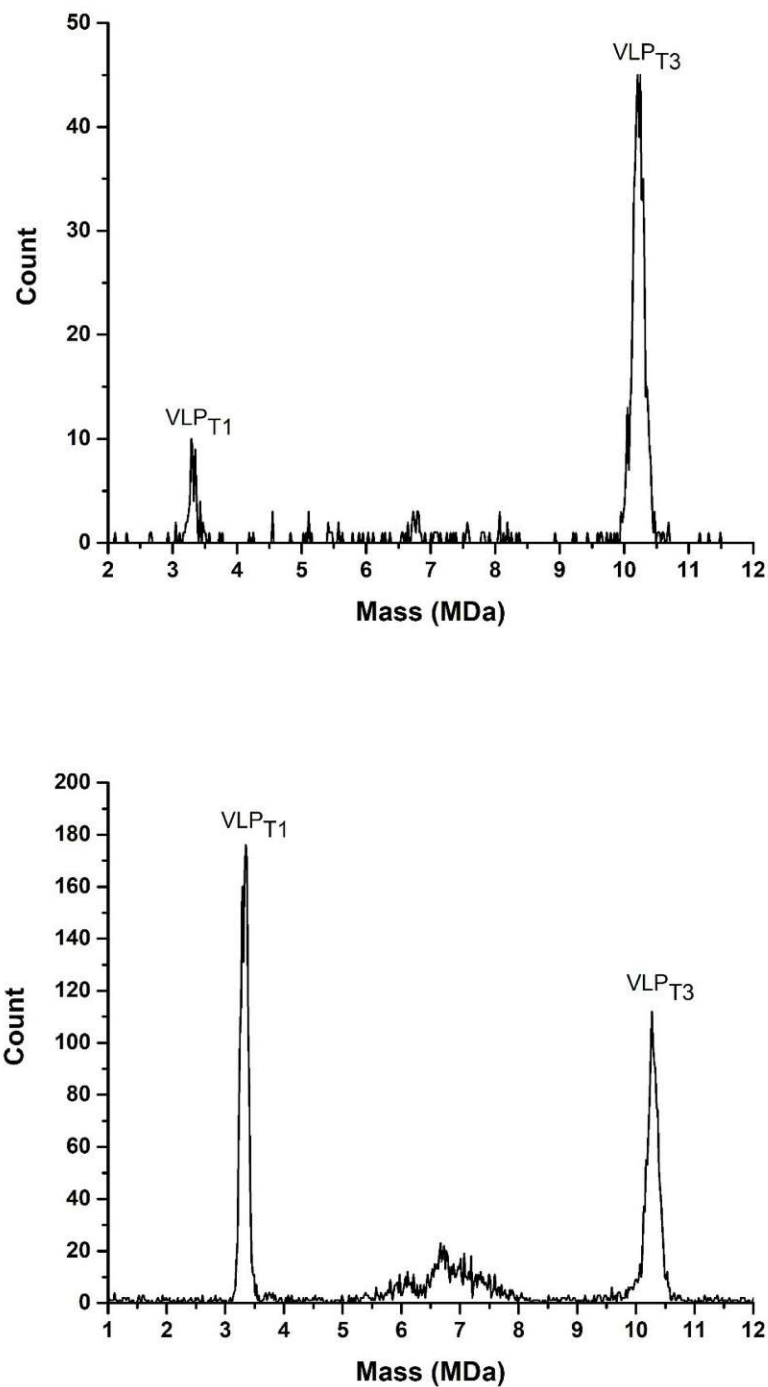


Fig. S1 CDMS spectrum of norovirus West Chester VLPs measured in 50 mM ammonium acetate, pH 6 (top) and 250 mM ammonium acetate, pH 6 (bottom) with peak fitting. 20 kDa bin size were used. Note the overall lower count in the top spectrum indicative of suboptimal spray, which could cause the altered ratios of T1 to T3. Moreover, it is well known that norovirus assembly is sensitive to ionic strength [1, 2]

References

1. Pogan R, Schneider C, Reimer R, Hansman G, Uetrecht C. Norovirus-like VP1 particles exhibit isolate dependent stability profiles. *J Phys Condens Matter*. 2018;30(6):064006.
2. Shoemaker GK, van Duijn E, Crawford SE, Uetrecht C, Baclayon M, Roos WH, Wuite GJ, Estes MK, Prasad BV, Heck AJ. Norwalk virus assembly and stability monitored by mass spectrometry. *Mol Cell Proteomics*. 2010;9(8):1742-51.

5 Conclusions

The field of gene therapy has witnessed remarkable advancements in recent years, largely due to the development and utilization of viral vectors. Among these, AAV8 VLP has emerged as a promising candidate, especially for its potential to deliver genetic material for therapeutic purposes without eliciting a strong immune response. However, despite its potential, a comprehensive understanding of AAV8's properties and behaviors remains a significant challenge, especially in the context of its application as a vector in gene therapy. This gap in knowledge poses a critical question: How can we effectively characterize AAV8 VLPs to optimize their use in gene therapy? Addressing this question is crucial for enhancing the efficacy of gene therapies and advancing our understanding of the behavior of these viral vectors in biological systems.

The present thesis aims to present a detailed exploration of AAV8 VLP, employing several analytical techniques to expand the scientific community's knowledge in this area. To achieve this, this thesis presents three peer-reviewed publications, each contributing unique insights into the properties and behaviors of AAV8 VLPs. A particular focus is given to gas-phase electrophoretic methods, i.e. nES GEMMA, which is instrumental in our analysis. Through this focused approach, this work seeks to provide a comprehensive understanding of the characteristics and behavior of AAV8 VLPs.

The first publication in this thesis aims to explore AAV8 VLPs with an array of analytical techniques. Central to this exploration is the use of nES GEMMA, a method that has proven particularly effective in determining the surface-dry particle size of VLPs. Indeed, with this method, the size of AAV8 VLPs can be precisely measured while maintaining their size characteristics in their native state at atmospheric pressure.

An important aspect for nES GEMMA analysis is the purity of the sample. Indeed, a critical step to ensure accurate measurements and remove nonvolatile buffer contaminants is the buffer exchange process. However, this process comes with a price, which is the potential loss of sample. From the nES GEMMA results, empty and filled AAV8 VLPs can be differentiated. Thus, it confirms the feasibility of nES GEMMA for these viral vectors and provides a hint of how genomic material influences VLP properties.

Complementing the results obtained from nES GEMMA, AF4 was employed for size-separation, enrichment, and collection of fractions of AAV8 VLPs previously exposed to environmental stressors (i.e., heat and shear stress). This technique has been employed for separating VLPs into different oligomeric states, offering valuable insights into their aggregation behavior under the investigated conditions.

Lastly, AFM was employed to provide high-resolution imaging of the different AF4 fractions of AAV8 VLPs. It's important to note that while dimers and trimers of AAV8 VLPs can be resolved using nES GEMMA, this technique encounters limitations in detecting larger oligomers. Due to their low abundance and heterogeneity, these oligomers present a challenge for nES GEMMA. However, AFM successfully bridges this gap by providing detailed images of these larger, more complex structures. This capability of AFM to visualize what nES GEMMA cannot, particularly in the context of oligomers, highlights the complementary nature of these analytical techniques in the comprehensive characterization of AAV8 VLPs.

Overall, the first publication presents a cross-platform analysis approach, combining nES GEMMA, AF4, and AFM to comprehensively characterize VLPs. This approach allowed for a deeper understanding of VLP behavior during analytical investigations, offering insights into particle size, purity, and aggregation states. The effectiveness of combining these multiple analytical techniques enriches our understanding of the structural integrity, robustness, and morphological characteristics of AAV8 VLPs.

Building upon the work of the first publication, the second publication in this thesis focuses on analyzing the molecular weight of empty and filled AAV8 VLPs. This study employs nES GEMMA and a modified nESI QRTOF MS for native mass spectrometry analysis. The former method is instrumental in determining the electrophoretic mobility diameter of such bio-nanoparticles, which can then be converted into molecular weight using a correlation formula. Although this demonstrates the technique's effectiveness in estimating the molecular weight of VLPs, for a more precise determination, native MS analysis is better suited. Hence, the employment of the latter method becomes necessary. This method, ideal for studying analytes in their native state, faces challenges due to the need for customized instrumental modifications, especially for analytes as large as AAV8 VLPs. Nonetheless, this study proves that nESI QRTOF MS, when combined with results from nES GEMMA, is capable of providing a precise estimation of the MW of AAV8 VLPs

Key findings from this study include the molecular weight of AAV8 VLPs lacking genomic cargo, estimated at 3670 ± 69 kDa, and those carrying an engineered genome, at 4751 ± 47 kDa. These results are not only significant for the field of gene therapy but also highlight the importance of advanced analytical techniques for the accurate measure of AAV8 VLPs. Such detailed characterization is crucial for expanding the knowledge of these viral vectors and supporting the ongoing development of gene therapy applications.

Lastly, the third manuscript in this thesis presents a detailed study of the response of empty and filled AAV8 VLPs to pH changes, employing nES GEMMA as the primary analytical tool. This research is crucial

for understanding the stability and behavior of VLPs in varying environments, a key aspect for their application in gene therapy. The study reveals that pH changes significantly impact the diameter and aggregation behavior of VLPs. Specifically, nES GEMMA shows that filled VLPs tend to aggregate under acidic conditions, while empty VLPs remain unaffected. Additionally, empty VLPs exhibit the greatest degree of diameter change across different pH levels, whereas filled VLPs remain stable with no significant diameter variation. This finding highlights the importance of considering environmental factors in the development and application of VLPs.

To corroborate these nES GEMMA observations, AFM and cryo-TEM analysis were incorporated. These techniques provide deeper insights into the shape and structural characteristics of VLPs. AFM, in particular, was applied to investigate filled VLPs at acidic pH, where it was suspected that large aggregates were forming. This phenomenon was challenging for nES GEMMA to detect due to the size and heterogeneity of these clusters, as indicated by the results of the first publication. Indeed, AFM results confirmed the formation of these large clusters. Additionally, cryo-TEM was employed to generate high-resolution images, illustrating the structural differences between filled and empty VLPs at both acidic and alkaline conditions. With its near-atomic resolution, native-like environmental conditions, and a robust statistical number of particles, cryo-TEM enabled diameter determination for both empty and filled VLPs, measured at 25.0 ± 0.1 nm and 25.9 ± 0.2 nm, respectively. This process of unbiased diameter determination was further enhanced by an in-house developed Python script, ensuring accuracy and reliability in the measurements. Contrary to the findings from nES GEMMA and AFM, cryo-TEM revealed that different pH levels did not affect the diameter of empty VLPs or the aggregation behavior for filled ones, suggesting that the observed changes in other methods are likely caused by their dry analytical environments.

Overall, these findings are crucial for understanding the stability and adaptability of AAV8 VLPs in different environments, a key aspect for their application in gene therapy. The unique behaviors of empty and filled VLPs, have profound implications for the analysis and manufacturing processes within the biopharmaceutical industry.

Moreover, this study points out how the analytical environment's conditions—dry for nES GEMMA and AFM, and wet for cryo-TEM—can influence these bio-nanoparticles' appearance and aggregation behavior. This critical observation highlights the importance of a cautious interpretation when relying on a single analytical technique.

The varying environmental conditions of these analytical methods can lead to different observations and conclusions, thereby emphasizing the need for a comprehensive analytical strategy that

incorporates multiple techniques. Such an approach is essential for a more accurate understanding of VLP behavior, particularly in the development and application of VLPs in gene therapy.

Throughout this thesis, the comprehensive exploration of AAV8 VLPs using advanced analytical techniques has significantly advanced our understanding of these viral vectors and their possible implications for gene therapy applications. Each of the three publications has contributed uniquely to this field, collectively providing a detailed picture of the physical, chemical, and environmental properties of AAV8 VLPs.

From the initial exploration of particle size, purity, and aggregation states in the first publication to the precise molecular weight determination in the second and the pH-responsive behavior in the third, this thesis demonstrates the complexity and versatility of AAV8 VLPs. The combined findings from these studies highlight the importance of employing a range of analytical methods to fully characterize VLPs, acknowledging that each technique brings its own strengths and limitations.

This thesis contributes important insights into AAV8 VLPs, enhancing the scientific community's understanding in a specialized area of gene therapy. The methodologies and findings presented here offer valuable advancements in characterizing such viral vectors, supporting the development of gene therapy applications. While the focus is specifically on AAV8 VLPs, this work highlights the importance of detailed analytical approaches and points out the potential for innovation in this dynamic field. It stresses the need for ongoing exploration and study, contributing to the discussion on using viral vectors for therapeutic purposes.

References

1. Wang, D.; Tai, P. W. L.; Gao, G., Adeno-associated virus vector as a platform for gene therapy delivery. *Nat Rev Drug Discov* **2019**, *18* (5), 358-378.
2. Bernaud, J.; Rossi, A.; Fis, A.; Gardette, L.; Aillot, L.; Buning, H.; Castelnovo, M.; Salvetti, A.; Faivre-Moskalenko, C., Characterization of AAV vector particle stability at the single-capsid level. *J Biol Phys* **2018**, *44* (2), 181-194.
3. Naso, M. F.; Tomkowicz, B.; Perry, W. L., 3rd; Strohl, W. R., Adeno-Associated Virus (AAV) as a Vector for Gene Therapy. *BioDrugs* **2017**, *31* (4), 317-334.
4. Rayaprolu, V.; Kruse, S.; Kant, R.; Venkatakrishnan, B.; Movahed, N.; Brooke, D.; Lins, B.; Bennett, A.; Potter, T.; McKenna, R.; Agbandje-McKenna, M.; Bothner, B., Comparative analysis of adeno-associated virus capsid stability and dynamics. *J Virol* **2013**, *87* (24), 13150-60.
5. Sant'Anna, T. B.; Araujo, N. M., Adeno-associated virus infection and its impact in human health: an overview. *J Virol* **2022**, *19* (1), 173.
6. Barnes, L. F.; Draper, B. E.; Chen, Y. T.; Powers, T. W.; Jarrold, M. F., Quantitative analysis of genome packaging in recombinant AAV vectors by charge detection mass spectrometry. *Mol Ther Meth Clin D* **2021**, *23*, 87-97.
7. Aschauer, D. F.; Kreuz, S.; Rumpel, S., Analysis of Transduction Efficiency, Tropism and Axonal Transport of AAV Serotypes 1, 2, 5, 6, 8 and 9 in the Mouse Brain. *PLoS one* **2013**, *8* (9).
8. Fu, Y.; Choudhary, D.; Liu, N.; Moon, Y.; Abdubek, P.; Sweezy, L.; Rosconi, M.; Palackal, N.; Pyles, E., Comprehensive biophysical characterization of AAV-AAVR interaction uncovers serotype- and pH-dependent interaction. *J Pharm Biomed Anal* **2023**, *234*, 115562.
9. Lins-Austin, B.; Patel, S.; Mietzsch, M.; Brooke, D.; Bennett, A.; Venkatakrishnan, B.; Van Vliet, K.; Smith, A. N.; Long, J. R.; McKenna, R.; Potter, M.; Byrne, B.; Boye, S. L.; Bothner, B.; Heilbronn, R.; Agbandje-McKenna, M., Adeno-Associated Virus (AAV) Capsid Stability and Liposome Remodeling During Endo/Lysosomal pH Trafficking. *Viruses* **2020**, *12* (6).
10. Worner, T. P.; Bennett, A.; Habka, S.; Snijder, J.; Friese, O.; Powers, T.; Agbandje-McKenna, M.; Heck, A. J. R., Adeno-associated virus capsid assembly is divergent and stochastic. *Nat Commun* **2021**, *12* (1), 1642.
11. Zincarelli, C.; Soltys, S.; Rengo, G.; Rabinowitz, J. E., Analysis of AAV serotypes 1-9 mediated gene expression and tropism in mice after systemic injection. *Mol Ther* **2008**, *16* (6), 1073-80.
12. He, Y.; Weinberg, M. S.; Hirsch, M.; Johnson, M. C.; Tisch, R.; Samulski, R. J.; Li, C., Kinetics of adeno-associated virus serotype 2 (AAV2) and AAV8 capsid antigen presentation in vivo are identical. *Hum Gene Ther* **2013**, *24* (5), 545-53.
13. Barnes, L. F.; Draper, B. E.; Chen, Y. T.; Powers, T. W.; Jarrold, M. F., Quantitative analysis of genome packaging in recombinant AAV vectors by charge detection mass spectrometry. *Mol Ther Meth Clin D* **2021**, *23*, 87-97.
14. Mietzsch, M.; Barnes, C.; Hull, J. A.; Chipman, P.; Xie, J.; Bhattacharya, N.; Sousa, D.; McKenna, R.; Gao, G.; Agbandje-McKenna, M., Comparative Analysis of the Capsid Structures of AAVrh.10, AAVrh.39, and AAV8. *J Virol* **2020**, *94* (6).
15. Wang, Q.; Dong, B.; Firrman, J.; Roberts, S.; Moore, A. R.; Cao, W.; Diao, Y.; Kapranov, P.; Xu, R.; Xiao, W., Efficient production of dual recombinant adeno-associated viral vectors for factor VIII delivery. *Hum Gene Ther Methods* **2014**, *25* (4), 261-8.
16. Zhao, L.; Yang, Z.; Zheng, M.; Shi, L.; Gu, M.; Liu, G.; Miao, F.; Chang, Y.; Huang, F.; Tang, N., Recombinant adeno-associated virus 8 vector in gene therapy: Opportunities and challenges. *Genes Dis* **2024**, *11* (1), 283-293.

17. Strasser, L.; Morgan, T. E.; Guapo, F.; Fussl, F.; Forsey, D.; Anderson, I.; Bones, J., A Native Mass Spectrometry-Based Assay for Rapid Assessment of the Empty:Full Capsid Ratio in Adeno-Associated Virus Gene Therapy Products. *Anal Chem* **2021**, *93* (38), 12817-12821.
18. Shen, W.; Liu, S.; Ou, L., rAAV immunogenicity, toxicity, and durability in 255 clinical trials: A meta-analysis. *Front Immunol* **2022**, *13*, 1001263.
19. Aponte-Ubillus, J. J.; Barajas, D.; Peltier, J.; Bardliving, C.; Shamlou, P.; Gold, D., Molecular design for recombinant adeno-associated virus (rAAV) vector production. *Appl Microbiol Biotechnol* **2018**, *102* (3), 1045-1054.
20. Aloor, A.; Zhang, J.; Gashash, E. A.; Parameswaran, A.; Chrzanowski, M.; Ma, C.; Diao, Y.; Wang, P. G.; Xiao, W., Site-Specific N-Glycosylation on the AAV8 Capsid Protein. *Viruses* **2018**, *10* (11).
21. Rieser, R.; Koch, J.; Faccioli, G.; Richter, K.; Menzen, T.; Biel, M.; Winter, G.; Michalakis, S., Comparison of Different Liquid Chromatography-Based Purification Strategies for Adeno-Associated Virus Vectors. *Pharmaceutics* **2021**, *13* (5).
22. Campbell, E. S. B.; Goens, M. M.; Cao, W.; Thompson, B.; Susta, L.; Banadyga, L.; Wootton, S. K., Recent Advancements in AAV-Vectored Immunoprophylaxis in the Nonhuman Primate Model. *Biomedicines* **2023**, *11* (8).
23. Penaud-Budloo, M.; Le Guiner, C.; Nowrouzi, A.; Toromanoff, A.; Chérel, Y.; Chenuaud, P.; Schmidt, M.; von Kalle, C.; Rolling, F.; Moullier, P.; Snyder, R. O., Adeno-associated virus vector Genomes persist as episomal chromatin in primate muscle. *J Virol* **2008**, *82* (16), 7875-7885.
24. Mohsen, M. O.; Bachmann, M. F., Virus-like particle vaccinology, from bench to bedside. *Cell Mol Immunol* **2022**, *19* (9), 993-1011.
25. Nooraei, S.; Bahrulolum, H.; Hoseini, Z. S.; Katalani, C.; Hajizade, A.; Easton, A. J.; Ahmadian, G., Virus-like particles: preparation, immunogenicity and their roles as nanovaccines and drug nanocarriers. *J Nanobiotech* **2021**, *19* (1), 59.
26. Tariq, H.; Batool, S.; Asif, S.; Ali, M.; Abbasi, B. H., Virus-Like Particles: Revolutionary Platforms for Developing Vaccines Against Emerging Infectious Diseases. *Front Microbiol* **2021**, *12*, 790121.
27. Fuenmayor, J.; Godia, F.; Cervera, L., Production of virus-like particles for vaccines. *N Biotechnol* **2017**, *39* (Pt B), 174-180.
28. Le, D. T.; Muller, K. M., In Vitro Assembly of Virus-Like Particles and Their Applications. *Life (Basel)* **2021**, *11* (4).
29. Frieze, K. M.; Peabody, D. S.; Chackerian, B., Engineering virus-like particles as vaccine platforms. *Curr Opin Virol* **2016**, *18*, 44-9.
30. Gupta, R.; Arora, K.; Roy, S. S.; Joseph, A.; Rastogi, R.; Arora, N. M.; Kundu, P. K., Platforms, advances, and technical challenges in virus-like particles-based vaccines. *Front Immunol* **2023**, *14*, 1123805.
31. Zhang, P.; Narayanan, E.; Liu, Q.; Tsybovsky, Y.; Boswell, K.; Ding, S.; Hu, Z.; Follmann, D.; Lin, Y.; Miao, H.; Schmeisser, H.; Rogers, D.; Falcone, S.; Elbashir, S. M.; Presnyak, V.; Bahl, K.; Prabhakaran, M.; Chen, X.; Sarfo, E. K.; Ambrozak, D. R.; Gautam, R.; Martin, M. A.; Swerczek, J.; Herbert, R.; Weiss, D.; Misamore, J.; Ciaramella, G.; Himansu, S.; Stewart-Jones, G.; McDermott, A.; Koup, R. A.; Mascola, J. R.; Finzi, A.; Carfi, A.; Fauci, A. S.; Lusso, P., A multiclade env-gag VLP mRNA vaccine elicits tier-2 HIV-1-neutralizing antibodies and reduces the risk of heterologous SHIV infection in macaques. *Nat Med* **2021**, *27* (12), 2234-2245.
32. Yang, Y.; Shi, W.; Abiona, O. M.; Nazzari, A.; Olia, A. S.; Ou, L.; Phung, E.; Stephens, T.; Tsybovsky, Y.; Verardi, R.; Wang, S.; Werner, A.; Yap, C.; Ambrozak, D.; Bylund, T.; Liu, T.; Nguyen, R.; Wang, L.; Zhang, B.; Zhou, T.; Chuang, G. Y.; Graham, B. S.; Mascola, J. R.; Corbett,

- K. S.; Kwong, P. D., Newcastle Disease Virus-Like Particles Displaying Prefusion-Stabilized SARS-CoV-2 Spikes Elicit Potent Neutralizing Responses. *Vaccines (Basel)* **2021**, *9* (2).
33. Chichester, J. A.; Green, B. J.; Jones, R. M.; Shoji, Y.; Miura, K.; Long, C. A.; Lee, C. K.; Ockenhouse, C. F.; Morin, M. J.; Streatfield, S. J.; Yusibov, V., Safety and immunogenicity of a plant-produced Pfs25 virus-like particle as a transmission blocking vaccine against malaria: A Phase 1 dose-escalation study in healthy adults. *Vaccine* **2018**, *36* (39), 5865-5871.
 34. Zeltins, A.; West, J.; Zabel, F.; El Turabi, A.; Balke, I.; Haas, S.; Maudrich, M.; Storni, F.; Engeroff, P.; Jennings, G. T.; Kotecha, A.; Stuart, D. I.; Foerster, J.; Bachmann, M. F., Incorporation of tetanus-epitope into virus-like particles achieves vaccine responses even in older recipients in models of psoriasis, Alzheimer's and cat allergy. *NPJ Vaccines* **2017**, *2*, 30.
 35. Chang, L. J.; Dowd, K. A.; Mendoza, F. H.; Saunders, J. G.; Sitar, S.; Plummer, S. H.; Yamshchikov, G.; Sarwar, U. N.; Hu, Z.; Enama, M. E.; Bailer, R. T.; Koup, R. A.; Schwartz, R. M.; Akahata, W.; Nabel, G. J.; Mascola, J. R.; Pierson, T. C.; Graham, B. S.; Ledgerwood, J. E.; Team, V. R. C. S., Safety and tolerability of chikungunya virus-like particle vaccine in healthy adults: a phase 1 dose-escalation trial. *Lancet* **2014**, *384* (9959), 2046-52.
 36. Kim, M. C.; Song, J. M.; O, E.; Kwon, Y. M.; Lee, Y. J.; Compans, R. W.; Kang, S. M., Virus-like particles containing multiple M2 extracellular domains confer improved cross-protection against various subtypes of influenza virus. *Mol Ther* **2013**, *21* (2), 485-92.
 37. Coates, E. E.; Edupuganti, S.; Chen, G. L.; Happe, M.; Strom, L.; Widge, A.; Florez, M. B.; Cox, J. H.; Gordon, I.; Plummer, S.; Ola, A.; Yamshchikov, G.; Andrews, C.; Curate-Ingram, S.; Morgan, P.; Nagar, S.; Collins, M. H.; Bray, A.; Nguyen, T.; Stein, J.; Case, C. L.; Kaltovich, F.; Wycuff, D.; Liang, C. J.; Carlton, K.; Vazquez, S.; Mascola, J. R.; Ledgerwood, J. E.; Team, V. R. C. S., Safety and immunogenicity of a trivalent virus-like particle vaccine against western, eastern, and Venezuelan equine encephalitis viruses: a phase 1, open-label, dose-escalation, randomised clinical trial. *Lancet Infect Dis* **2022**, *22* (8), 1210-1220.
 38. Qian, C.; Liu, X.; Xu, Q.; Wang, Z.; Chen, J.; Li, T.; Zheng, Q.; Yu, H.; Gu, Y.; Li, S.; Xia, N., Recent Progress on the Versatility of Virus-Like Particles. *Vaccines (Basel)* **2020**, *8* (1).
 39. Schmitz, N.; Dietmeier, K.; Bauer, M.; Maudrich, M.; Utzinger, S.; Muntwiler, S.; Saudan, P.; Bachmann, M. F., Displaying Fel d1 on virus-like particles prevents reactogenicity despite greatly enhanced immunogenicity: a novel therapy for cat allergy. *J Exp Med* **2009**, *206* (9), 1941-55.
 40. Wang, L.; Calcedo, R.; Nichols, T. C.; Bellinger, D. A.; Dillow, A.; Verma, I. M.; Wilson, J. M., Sustained correction of disease in naive and AAV2-pretreated hemophilia B dogs: AAV2/8-mediated, liver-directed gene therapy. *Blood* **2005**, *105* (8), 3079-86.
 41. Akache, B.; Grimm, D.; Pandey, K.; Yant, S. R.; Xu, H.; Kay, M. A., The 37/67-kilodalton laminin receptor is a receptor for adeno-associated virus serotypes 8, 2, 3, and 9. *J Virol* **2006**, *80* (19), 9831-6.
 42. Gao, G. P.; Alvira, M. R.; Wang, L.; Calcedo, R.; Johnston, J.; Wilson, J. M., Novel adeno-associated viruses from rhesus monkeys as vectors for human gene therapy. *Proc Natl Acad Sci U S A* **2002**, *99* (18), 11854-9.
 43. Pan, X.; Yue, Y.; Zhang, K.; Lostal, W.; Shin, J. H.; Duan, D., Long-term robust myocardial transduction of the dog heart from a peripheral vein by adeno-associated virus serotype-8. *Hum Gene Ther* **2013**, *24* (6), 584-94.
 44. Wang, A. Y.; Peng, P. D.; Ehrhardt, A.; Storm, T. A.; Kay, M. A., Comparison of adenoviral and adeno-associated viral vectors for pancreatic gene delivery in vivo. *Hum Gene Ther* **2004**, *15* (4), 405-13.
 45. Ayers, J. I.; Fromholt, S.; Sinyavskaya, O.; Siemienski, Z.; Rosario, A. M.; Li, A.; Crosby, K. W.; Cruz, P. E.; DiNunno, N. M.; Janus, C.; Ceballos-Diaz, C.; Borchelt, D. R.; Golde, T. E.;

Chakrabarty, P.; Levites, Y., Widespread and efficient transduction of spinal cord and brain following neonatal AAV injection and potential disease modifying effect in ALS mice. *Mol Ther* **2015**, *23* (1), 53-62.

46. Aronson, S. J.; Veron, P.; Collaud, F.; Hubert, A.; Delahais, V.; Honnet, G.; de Knecht, R. J.; Junge, N.; Baumann, U.; Di Giorgio, A.; D'Antiga, L.; Ginocchio, V. M.; Brunetti-Pierri, N.; Labrune, P.; Beuers, U.; Bosma, P. J.; Mingozzi, F., Prevalence and Relevance of Pre-Existing Anti-Adeno-Associated Virus Immunity in the Context of Gene Therapy for Crigler-Najjar Syndrome. *Hum Gene Ther* **2019**, *30* (10), 1297-1305.
47. Kruzik, A.; Fetahagic, D.; Hartlieb, B.; Dorn, S.; Koppensteiner, H.; Horling, F. M.; Scheiflinger, F.; Reipert, B. M.; de la Rosa, M., Prevalence of Anti-Adeno-Associated Virus Immune Responses in International Cohorts of Healthy Donors. *Mol Ther Methods Clin Dev* **2019**, *14*, 126-133.
48. Kruzik, A.; Koppensteiner, H.; Fetahagic, D.; Hartlieb, B.; Dorn, S.; Romeder-Finger, S.; Coulibaly, S.; Weber, A.; Hoellriegel, W.; Horling, F. M.; Scheiflinger, F.; Reipert, B. M.; de la Rosa, M., Detection of Biologically Relevant Low-Titer Neutralizing Antibodies Against Adeno-Associated Virus Require Sensitive In Vitro Assays. *Hum Gene Ther Methods* **2019**, *30* (2), 35-43.
49. Gross, D. A.; Tedesco, N.; Leborgne, C.; Ronzitti, G., Overcoming the Challenges Imposed by Humoral Immunity to AAV Vectors to Achieve Safe and Efficient Gene Transfer in Seropositive Patients. *Front Immunol* **2022**, *13*, 857276.
50. Chan, C.; Harris, K. K.; Zolotukhin, S.; Keeler, G. D., Rational Design of AAV-rh74, AAV3B, and AAV8 with Limited Liver Targeting. *Viruses* **2023**, *15* (11).
51. Dalwadi, D. A.; Calabria, A.; Tiyaaboonchai, A.; Posey, J.; Naugler, W. E.; Montini, E.; Grompe, M., AAV integration in human hepatocytes. *Mol Ther* **2021**, *29* (10), 2898-2909.
52. Martino, A. T.; Basner-Tschakarjan, E.; Markusic, D. M.; Finn, J. D.; Hinderer, C.; Zhou, S.; Ostrov, D. A.; Srivastava, A.; Ertl, H. C.; Terhorst, C.; High, K. A.; Mingozzi, F.; Herzog, R. W., Engineered AAV vector minimizes in vivo targeting of transduced hepatocytes by capsid-specific CD8+ T cells. *Blood* **2013**, *121* (12), 2224-33.
53. Dudek, A. M.; Zabaleta, N.; Zinn, E.; Pillay, S.; Zengel, J.; Porter, C.; Franceschini, J. S.; Estelien, R.; Carette, J. E.; Zhou, G. L.; Vandenberghe, L. H., GPR108 Is a Highly Conserved AAV Entry Factor. *Mol Ther* **2020**, *28* (2), 367-381.
54. van Lieshout, L. P.; Stegelmeier, A. A.; Rindler, T. N.; Lawder, J. J.; Sorensen, D. L.; Frost, K. L.; Booth, S. A.; Bridges, J. P.; Wootton, S. K., Engineered AAV8 capsid acquires heparin and AVB sepharose binding capacity but has altered in vivo transduction efficiency. *Gene Ther* **2023**, *30* (3-4), 236-244.
55. Cabanes-Creus, M.; Navarro, R. G.; Zhu, E.; Baltazar, G.; Liao, S. H. Y.; Drouyer, M.; Amaya, A. K.; Scott, S.; Nguyen, L. H.; Westhaus, A.; Hebben, M.; Wilson, L. O. W.; Thrasher, A. J.; Alexander, I. E.; Lisowski, L., Novel human liver-tropic AAV variants define transferable domains that markedly enhance the human tropism of AAV7 and AAV8. *Mol Ther Methods Clin Dev* **2022**, *24*, 88-101.
56. Havlik, L. P.; Simon, K. E.; Smith, J. K.; Klinc, K. A.; Tse, L. V.; Oh, D. K.; Fanous, M. M.; Meganck, R. M.; Mietzsch, M.; Kleinschmidt, J.; Agbandje-McKenna, M.; Asokan, A., Coevolution of Adeno-associated Virus Capsid Antigenicity and Tropism through a Structure-Guided Approach. *J Virol* **2020**, *94* (19).
57. Eichhoff, A. M.; Borner, K.; Albrecht, B.; Schafer, W.; Baum, N.; Haag, F.; Korbelin, J.; Trepel, M.; Braren, I.; Grimm, D.; Adriouch, S.; Koch-Nolte, F., Nanobody-Enhanced Targeting of AAV Gene Therapy Vectors. *Mol Ther Methods Clin Dev* **2019**, *15*, 211-220.
58. Kaufman, S. L.; Skogen, J. W.; Dorman, F. D.; Zarrin, F.; Lewis, K. C., Macromolecule analysis based on electrophoretic mobility in air: globular proteins. *Anal Chem* **1996**, *68* (11), 1895-904.

59. Weiss, V. U.; Frank, J.; Piplits, K.; Szymanski, W. W.; Allmaier, G., Bipolar Corona Discharge-Based Charge Equilibration for Nano Electrospray Gas-Phase Electrophoretic Mobility Molecular Analysis of Bio- and Polymer Nanoparticles. *Anal Chem* **2020**, *92* (13), 8665-8669.
60. Weiss, V. U.; Wieland, K.; Schwaighofer, A.; Lendl, B.; Allmaier, G., Native Nano-electrospray Differential Mobility Analyzer (nES GEMMA) Enables Size Selection of Liposomal Nanocarriers Combined with Subsequent Direct Spectroscopic Analysis. *Anal Chem* **2019**, *91* (6), 3860-3868.
61. Weiss, V. U.; Pogan, R.; Zoratto, S.; Bond, K. M.; Boulanger, P.; Jarrold, M. F.; Lykтей, N.; Pahl, D.; Puffler, N.; Schelhaas, M.; Selivanovitch, E.; Uetrecht, C.; Allmaier, G., Virus-like particle size and molecular weight/mass determination applying gas-phase electrophoresis (native nES GEMMA). *Anal Bioanal Chem* **2019**, *411* (23), 5951-5962.
62. Allmaier, G.; Weiss, V. U.; Engel, N. Y.; Marchetti-Deschmann, M.; Szymanski, W. W., Soft X-ray Radiation Applied in the Analysis of Intact Viruses and Antibodies by Means of Nano Electrospray Differential Mobility Analysis. *Nato Sci Peace Sec A* **2017**, 149-157.
63. Urey, C.; Weiss, V. U.; Gondikas, A.; von der Kammer, F.; Hofmann, T.; Marchetti-Deschmann, M.; Allmaier, G.; Marko-Varga, G.; Andersson, R., Combining gas-phase electrophoretic mobility molecular analysis (GEMMA), light scattering, field flow fractionation and cryo electron microscopy in a multidimensional approach to characterize liposomal carrier vesicles. *Int J Pharm* **2016**, *513* (1-2), 309-318.
64. Kapellios, E. A.; Karamanou, S.; Sardis, M. F.; Aivaliotis, M.; Economou, A.; Pergantis, S. A., Using nanoelectrospray ion mobility spectrometry (GEMMA) to determine the size and relative molecular mass of proteins and protein assemblies: a comparison with MALLS and QELS. *Anal Bioanal Chem* **2011**, *399* (7), 2421-33.
65. Weiss, V. U.; Bereszczak, J. Z.; Havlik, M.; Kallinger, P.; Gosler, I.; Kumar, M.; Blaas, D.; Marchetti-Deschmann, M.; Heck, A. J.; Szymanski, W. W.; Allmaier, G., Analysis of a common cold virus and its subviral particles by gas-phase electrophoretic mobility molecular analysis and native mass spectrometry. *Anal Chem* **2015**, *87* (17), 8709-17.
66. Weiss, V. U.; Subirats, X.; Pickl-Herk, A.; Bilek, G.; Winkler, W.; Kumar, M.; Allmaier, G.; Blaas, D.; Kenndler, E., Characterization of rhinovirus subviral A particles via capillary electrophoresis, electron microscopy and gas-phase electrophoretic mobility molecular analysis: Part I. *Electrophoresis* **2012**, *33* (12), 1833-41.
67. Kallinger, P.; Steiner, G.; Szymanski, W. W., Characterization of four different bipolar charging devices for nanoparticle charge conditioning. *Journal of Nanoparticle Research* **2012**, *14* (6).
68. Laschober, C.; Wruss, J.; Blaas, D.; Szymanski, W. W.; Allmaier, G., Gas-phase electrophoretic molecular mobility analysis of size and stoichiometry of complexes of a common cold virus with antibody and soluble receptor molecules. *Anal Chem* **2008**, *80* (6), 2261-4.
69. Bacher, G.; Szymanski, W. W.; Kaufman, S. L.; Zollner, P.; Blaas, D.; Allmaier, G., Charge-reduced nano electrospray ionization combined with differential mobility analysis of peptides, proteins, glycoproteins, noncovalent protein complexes and viruses. *J Mass Spectrom* **2001**, *36* (9), 1038-52.
70. Wiedensohler, A.; Fissan, H. J., Aerosol charging in high purity gases. *J Aerosol Sci* **1988**, *19* (7), 867-870.
71. Fuchs, N. A., On the stationary charge distribution on aerosol particles in a bipolar ionic atmosphere. *Pure Appl Geophys* **1963**, *56* (1), 185-193.
72. Flagan, R. C., Differential Mobility Analysis of Aerosols: A Tutorial. *KONA Powder Part J* **2008**, *26* (0), 254-268.
73. Intra, P.; Tippayawong, N., An overview of aerosol particle sensors for size distribution measurement. *Maejo Int J Sci Tech* **2007**, *1* (2), 120-136.

74. Allmaier, G.; Laschober, C.; Szymanski, W. W., Nano ES GEMMA and PDMA, new tools for the analysis of nanobioparticles-protein complexes, lipoparticles, and viruses. *J Mass Spectrom* **2008**, *19* (8), 1062-8.
75. Carazzone, C.; Raml, R.; Pergantis, S. A., Nanoelectrospray ion mobility spectrometry online with inductively coupled plasma-mass spectrometry for sizing large proteins, DNA, and nanoparticles. *Anal Chem* **2008**, *80* (15), 5812-5818.
76. Weiss, V. U.; Lehner, A.; Kerul, L.; Grombe, R.; Kratzmeier, M.; Marchetti-Deschmann, M.; Allmaier, G., Characterization of cross-linked gelatin nanoparticles by electrophoretic techniques in the liquid and the gas phase. *Electrophoresis* **2013**, *34* (24), 3267-76.
77. Incorporated, T., *Manual 3080 Electrostatic Classifier*. 2006.
78. Koropchak, J. A.; Sadain, S.; Yang, X.; Magnusson, L. E.; Heybroek, M.; Anisimov, M.; Kaufman, S. L., Nanoparticle detection technology for chemical analysis. *Anal Chem* **1999**, *71* (11), 386A-394A.
79. Kallinger, P.; Weiss, V. U.; Lehner, A.; Allmaier, G.; Szymanski, W. W., Analysis and handling of bio-nanoparticles and environmental nanoparticles using electrostatic aerosol mobility. *Particuology* **2013**, *11* (1), 14-19.
80. Havlik, M.; Marchetti-Deschmann, M.; Friedbacher, G.; Winkler, W.; Messner, P.; Perez-Burgos, L.; Tauer, C.; Allmaier, G., Comprehensive size-determination of whole virus vaccine particles using gas-phase electrophoretic mobility macromolecular analyzer, atomic force microscopy, and transmission electron microscopy. *Anal Chem* **2015**, *87* (17), 8657-64.
81. Engel, N. Y.; Weiss, V. U.; Marchetti-Deschmann, M.; Allmaier, G., nES GEMMA Analysis of Lectins and Their Interactions with Glycoproteins - Separation, Detection, and Sampling of Noncovalent Biospecific Complexes. *J Mass Spectrom* **2017**, *28* (1), 77-86.
82. Weiss, V. U.; Balantic, K.; Pittenauer, E.; Tripisciano, C.; Friedbacher, G.; Weber, V.; Marchetti-Deschmann, M.; Allmaier, G., Nano electrospray differential mobility analysis based size-selection of liposomes and very-low density lipoprotein particles for offline hyphenation to MALDI mass spectrometry. *J Pharm Biomed Anal* **2020**, *179*, 112998.
83. Allmaier, G.; Blaas, D.; Bliem, C.; Dechat, T.; Fedosyuk, S.; Gosler, I.; Kowalski, H.; Weiss, V. U., Monolithic anion-exchange chromatography yields rhinovirus of high purity. *J Virol Methods* **2018**, *251*, 15-21.
84. Pogan, R.; Weiss, V. U.; Bond, K.; Dulfer, J.; Krisp, C.; Lykтей, N.; Muller-Guhl, J.; Zoratto, S.; Allmaier, G.; Jarrold, M. F.; Munoz-Fontela, C.; Schluter, H.; Uetrecht, C., N-terminal VP1 Truncations Favor T = 1 Norovirus-Like Particles. *Vaccines (Basel)* **2021**, *9* (1).
85. Subirats, X.; Weiss, V. U.; Gösler, I.; Puls, C.; Limbeck, A.; Allmaier, G.; Kenndler, E., Characterization of rhinovirus subviral A particles via capillary electrophoresis, electron microscopy and gas phase electrophoretic mobility molecular analysis: Part II. *Electrophoresis* **2013**, *34* (11), 1600-1609.
86. Weiss, V. U.; Subirats, X.; Kumar, M.; Harutyunyan, S.; Gosler, I.; Kowalski, H.; Blaas, D., Capillary electrophoresis, gas-phase electrophoretic mobility molecular analysis, and electron microscopy: effective tools for quality assessment and basic rhinovirus research. *Methods Mol Biol* **2015**, *1221*, 101-28.
87. Zoratto, S.; Weiss, V. U.; Friedbacher, G.; Buengener, C.; Pletzenauer, R.; Foettinger-Vacha, A.; Graninger, M.; Allmaier, G., Adeno-associated Virus Virus-like Particle Characterization via Orthogonal Methods: Nanoelectrospray Differential Mobility Analysis, Asymmetric Flow Field-Flow Fractionation, and Atomic Force Microscopy. *Acs Omega* **2021**, *6* (25), 16428-16437.
88. Zoratto, S.; Weiss, V. U.; van der Horst, J.; Commandeur, J.; Buengener, C.; Foettinger-Vacha, A.; Pletzenauer, R.; Graninger, M.; Allmaier, G., Molecular weight determination of adeno-associate virus serotype 8 virus-like particle either carrying or lacking genome via native nES

gas-phase electrophoretic molecular mobility analysis and nESI QRTOF mass spectrometry. *J Mass Spectrom* **2021**, *56* (11).

89. Zoratto, S.; Heuser, T.; Friedbacher, G.; Pletzenauer, R.; Graninger, M.; Marchetti-Deschmann, M.; Weiss, V. U., Adeno-Associated Virus-like Particles' Response to pH Changes as Revealed by nES-DMA. *Viruses (Basel)* **2023**, *15* (6).
90. Fernandez-Garcia, J.; Compton, S.; Wick, D.; Fernandez de la Mora, J., Virus Size Analysis by Gas-Phase Mobility Measurements: Resolution Limits. *Anal Chem* **2019**, *91* (20), 12962-12970.
91. Martínez-Lozano, P.; de la Mora, J. F., Resolution improvements of a nano-DMA operating transonically. *J Aerosol Sci* **2006**, *37* (4), 500-512.
92. Perez-Lorenzo, L. J.; Khanna, V.; Meena, T.; Schmitt, J. J.; de la Mora, J. F., A high resolution DMA covering the 1-67 nm size range. *Aerosol Sci Technol* **2020**, *54* (1), 128-142.
93. Fernandez de la Mora, J., High-resolution mobility analysis of charge-reduced electrosprayed protein ions. *Anal Chem* **2015**, *87* (7), 3729-35.
94. Zoratto, S.; Heuser, T.; Friedbacher, G.; Pletzenauer, R.; Graninger, M.; Marchetti-Deschmann, M.; Weiss, V. U., Adeno-Associated Virus-like Particles' Response to pH Changes as Revealed by nES-DMA. *Viruses* **2023**, *15* (6).
95. Weiss, V. U.; Kerul, L.; Kallinger, P.; Szymanski, W. W.; Marchetti-Deschmann, M.; Allmaier, G., Liquid phase separation of proteins based on electrophoretic effects in an electrospray setup during sample introduction into a gas-phase electrophoretic mobility molecular analyzer (CE-GEMMA/CE-ES-DMA). *Anal Chim Acta* **2014**, *841*, 91-8.
96. Kuznetsov, Y. G.; McPherson, A., Atomic Force Microscopy in Imaging of Viruses and Virus-Infected Cells. *Microbiol Mol Biol R* **2011**, *75* (2), 268-285.
97. Baclayon, M.; Wuite, G. J. L.; Roos, W. H., Imaging and manipulation of single viruses by atomic force microscopy. *Soft Matter* **2010**, *6* (21), 5273-5285.
98. Dufrene, Y. F.; Ando, T.; Garcia, R.; Alsteens, D.; Martinez-Martin, D.; Engel, A.; Gerber, C.; Muller, D. J., Imaging modes of atomic force microscopy for application in molecular and cell biology. *Nat Nanotechnol* **2017**, *12* (4), 295-307.
99. Dufrêne, Y. F.; Viljoen, A.; Mignolet, J.; Mathelié-Guinlet, M., AFM in cellular and molecular microbiology. *Cell Microbiol.* **2021**, *23* (7), 12.
100. Muller, D. J.; Dufrene, Y. F., Atomic force microscopy: a nanoscopic window on the cell surface. *Trends Cell Biol* **2011**, *21* (8), 461-9.
101. Hughes, M. L.; Dougan, L., The physics of pulling polypeptides: a review of single molecule force spectroscopy using the AFM to study protein unfolding. *Rep. Prog. Phys.* **2016**, *79* (7), 40.
102. Sigdel, K. P.; Pittman, A. E.; Matin, T. R.; King, G. M., High-Resolution AFM-Based Force Spectroscopy. In *Nano Imag*, Lyubchenko, Y. L., Ed. Humana Press Inc: Totowa, 2018; Vol. 1814, pp 49-62.
103. Liu, S.; Wang, Y., Application of AFM in microbiology: a review. *Scanning* **2010**, *32* (2), 61-73.
104. Milhiet, P. E.; Dosset, P.; Godefroy, C.; Le Grimmellec, C.; Guigner, J. M.; Larquet, E.; Ronzon, F.; Manin, C., Nanoscale topography of hepatitis B antigen particles by atomic force microscopy. *Biochimie* **2011**, *93* (2), 254-9.
105. Chopinet, L.; Formosa, C.; Rols, M. P.; Duval, R. E.; Dague, E., Imaging living cells surface and quantifying its properties at high resolution using AFM in QI mode. *Micron* **2013**, *48*, 26-33.
106. Golek, F.; Mazur, P.; Ryszka, Z.; Zuber, S., AFM image artifacts. *Appl. Surf. Sci.* **2014**, *304*, 11-19.
107. Shen, J.; Zhang, D.; Zhang, F. H.; Gan, Y., AFM tip-sample convolution effects for cylinder protrusions. *Appl. Surf. Sci.* **2017**, *422*, 482-491.

108. Eleta-Lopez, A.; Calo, A., Key factors of scanning a plant virus with AFM in air and aqueous solution. *Microsc Res Techniq* **2017**, *80* (1), 18-29.
109. Meillan, M.; Ramin, M. A.; Buffeteau, T.; Marsaudon, S.; Odorico, M.; Chen, S. W. W.; Pellequer, J. L.; Degueil, M.; Heuze, K.; Vellutini, L.; Bennetau, B., Self-assembled monolayer for AFM measurements of Tobacco Mosaic Virus (TMV) at the atomic level. *Rsc Adv* **2014**, *4* (23), 11927-11930.
110. Negishi, A.; Chen, J.; McCarty, D. M.; Samulski, R. J.; Liu, J.; Superfine, R., Analysis of the interaction between adeno-associated virus and heparan sulfate using atomic force microscopy. *J Glycobiol* **2004**, *14* (11), 969-77.
111. Negishi, A.; Liu, J.; McCarty, D.; Samulski, J.; Superfine, R., An AFM imaging-based assay for viral binding: Heparan sulfate and adeno-associated virus. *J Glycobiol* **2003**, *13* (11), 851-851.
112. Negishi, A.; Liu, J.; McCarty, D. M.; Samulski, R. J.; Superfine, R., AFM binding study of adeno-associated virus type 2 to heparan sulfate. *J Biophys* **2004**, *86* (1), 479a-479a.
113. Chen, S. W. W.; Odorico, M.; Meillan, M.; Vellutini, L.; Teulon, J. M.; Parot, P.; Bennetau, B.; Pellequer, J. L., Nanoscale structural features determined by AFM for single virus particles. *Nanoscale* **2013**, *5* (22), 10877-10886.
114. Zhang, Q. R.; Yang, J. S.; Tillieux, S.; Guo, Z. Y.; Natividade, R. D.; Koehler, M.; Petitjean, S.; Cui, Z. Q.; Alsteens, D., Stepwise Enzymatic-Dependent Mechanism of Ebola Virus Binding to Cell Surface Receptors Monitored by AFM. *Nano Lett* **2022**, *22* (4), 1641-1648.
115. Ortega-Esteban, A.; Martin-Gonzalez, N.; Moreno-Madrid, F.; Llauro, A.; Hernando-Perez, M.; San Martin, C.; de Pablo, P. J., Structural and Mechanical Characterization of Viruses with AFM. *J Microsc* **2019**, *1886*, 259-278.
116. Liu, C. H.; Horng, J. T.; Chang, J. S.; Hsieh, C. F.; Tseng, Y. C.; Lin, S., Localization and force analysis at the single virus particle level using atomic force microscopy. *Biochem Biophys Res Commun* **2012**, *417* (1), 109-15.
117. Nam, Y. R.; Ju, H. H.; Lee, J.; Lee, D.; Kim, Y.; Lee, S. J.; Kim, H. K.; Jang, J. H.; Lee, H., Distinguishing between DNA-Loaded Full and Empty Capsids of Adeno-Associated Virus with Atomic Force Microscopy Imaging. *Langmuir* **2023**, *39* (19), 6740-6747.
118. Heldt, C. L.; Areo, O.; Joshi, P. U.; Mi, X.; Ivanova, Y.; Berrill, A., Empty and Full AAV Capsid Charge and Hydrophobicity Differences Measured with Single-Particle AFM. *Langmuir* **2023**, *39* (16), 5641-5648.
119. Xiao, P. J.; Li, C.; Neumann, A.; Samulski, R. J., Quantitative 3D tracing of gene-delivery viral vectors in human cells and animal tissues. *Mol Ther* **2012**, *20* (2), 317-28.
120. Delguste, M.; Koehler, M.; Alsteens, D., Probing Single Virus Binding Sites on Living Mammalian Cells Using AFM. *Nano Imag* **2018**, *1814*, 483-514.
121. Georgakaki, D.; Mitridis, S.; Sapalidis, A. A.; Mathioulakis, E.; Polatoglou, H. M., Calibration of tapping AFM cantilevers and uncertainty estimation: Comparison between different methods. *Measurement* **2013**, *46* (10), 4274-4281.
122. Wahlund, K. G.; Giddings, J. C., Properties of an Asymmetrical Flow Field-Flow Fractionation Channel Having One Permeable Wall. *Anal Chem* **1987**, *59* (9), 1332-1339.
123. Giddings, J. C.; Yang, F. J.; Myers, M. N., Flow-field-flow fractionation: a versatile new separation method. *Science* **1976**, *193* (4259), 1244-5.
124. Yohannes, G.; Jussila, M.; Hartonen, K.; Riekkola, M. L., Asymmetrical flow field-flow fractionation technique for separation and characterization of biopolymers and bioparticles. *J Chromatogr A* **2011**, *1218* (27), 4104-16.

125. Wagner, M.; Holzschuh, S.; Traeger, A.; Fahr, A.; Schubert, U. S., Asymmetric flow field-flow fractionation in the field of nanomedicine. *Anal Chem* **2014**, *86* (11), 5201-10.
126. Leeman, M.; Storm, M. U.; Nilsson, L., Practical Applications of Asymmetrical Flow Field-Flow Fractionation (AF4): A Review. *LC GC Eur.* **2015**, *28* (12), 642-651.
127. Litzen, A., Separation speed, retention, and dispersion in asymmetrical flow field-flow fractionation as function of channel dimension and flow-rates. *Anal Chem* **1993**, *65* (4), 461-470.
128. Fraunhofer, W.; Winter, G., The use of asymmetrical flow field-flow fractionation in pharmaceuticals and biopharmaceuticals. *Eur J Pharm Biopharm* **2004**, *58* (2), 369-83.
129. Roda, B.; Zattoni, A.; Reschiglian, P.; Moon, M. H.; Mirasoli, M.; Michelini, E.; Roda, A., Field-flow fractionation in bioanalysis: A review of recent trends. *Anal Chimica Acta* **2009**, *635* (2), 132-143.
130. Wahlund, K.-G.; Nilsson, L., *Flow FFF—basics and key applications*. Springer: 2012.
131. Ratanathanawongs Williams, S. K.; Lee, D., Field-flow fractionation of proteins, polysaccharides, synthetic polymers, and supramolecular assemblies. *J Sep Sci* **2006**, *29* (12), 1720-1732.
132. Messaud, F. A.; Sanderson, R. D.; Runyon, J. R.; Otte, T.; Pasch, H.; Williams, S. K. R., An overview on field-flow fractionation techniques and their applications in the separation and characterization of polymers. *Prog Polym Sci* **2009**, *34* (4), 351-368.
133. Pease, L. F., 3rd; Lipin, D. I.; Tsai, D. H.; Zachariah, M. R.; Lua, L. H.; Tarlov, M. J.; Middelberg, A. P., Quantitative characterization of virus-like particles by asymmetrical flow field flow fractionation, electrospray differential mobility analysis, and transmission electron microscopy. *Biotechnol Bioeng* **2009**, *102* (3), 845-55.
134. Eskelin, K.; Lampi, M.; Meier, F.; Moldenhauer, E.; Bamford, D. H.; Oksanen, H. M., Asymmetric flow field flow fractionation methods for virus purification. *J Chromatogr A* **2016**, *1469*, 108-119.
135. Eskelin, K.; Poranen, M. M.; Oksanen, H. M., Asymmetrical Flow Field-Flow Fractionation on Virus and Virus-Like Particle Applications. *Microorganisms* **2019**, *7* (11).
136. Chen, Y.; Zhang, Y.; Zhou, Y.; Luo, J.; Su, Z., Asymmetrical flow field-flow fractionation coupled with multi-angle laser light scattering for stability comparison of virus-like particles in different solution environments. *Vaccine* **2016**, *34* (27), 3164-3170.
137. Citkowicz, A.; Petry, H.; Harkins, R. N.; Ast, O.; Cashion, L.; Goldmann, C.; Bringmann, P.; Plummer, K.; Larsen, B. R., Characterization of virus-like particle assembly for DNA delivery using asymmetrical flow field-flow fractionation and light scattering. *Anal Biochem* **2008**, *376* (2), 163-72.
138. Zhang, X. Y.; Li, Y. Q.; Shen, S. G.; Lee, S.; Dou, H. Y., Field-flow fractionation: A gentle separation and characterization technique in biomedicine. *Anal Chem* **2018**, *108*, 231-238.
139. Wiedmer, S. K.; Riekkola, M. L., Field-flow fractionation - an excellent tool for fractionation, isolation and/or purification of biomacromolecules. *J Chromatogr A* **2023**, *1712*, 464492.
140. Griffiths, J., A brief history of mass spectrometry. *Anal Chem* **2008**, *80* (15), 5678-83.
141. Rostom, A. A.; Fucini, P.; Benjamin, D. R.; Juenemann, R.; Nierhaus, K. H.; Hartl, F. U.; Dobson, C. M.; Robinson, C. V., Detection and selective dissociation of intact ribosomes in a mass spectrometer. *Proc Natl Acad Sci U S A* **2000**, *97* (10), 5185-90.
142. Uetrecht, C.; Rose, R. J.; van Duijn, E.; Lorenzen, K.; Heck, A. J., Ion mobility mass spectrometry of proteins and protein assemblies. *Chem Soc Rev* **2010**, *39* (5), 1633-55.
143. Laganowsky, A.; Reading, E.; Allison, T. M.; Ulmschneider, M. B.; Degiacomi, M. T.; Baldwin, A. J.; Robinson, C. V., Membrane proteins bind lipids selectively to modulate their structure and function. *Nature* **2014**, *510* (7503), 172-175.

144. Leney, A. C.; Heck, A. J., Native Mass Spectrometry: What is in the Name? *J Mass Spectrom* **2017**, *28* (1), 5-13.
145. Siuzdak, G.; Bothner, B.; Yeager, M.; Brugidou, C.; Fauquet, C. M.; Hoey, K.; Chang, C. M., Mass spectrometry and viral analysis. *Chem Bio* **1996**, *3* (1), 45-48.
146. Wilm, M.; Mann, M., Analytical properties of the nanoelectrospray ion source. *Anal Chem* **1996**, *68* (1), 1-8.
147. Uetrecht, C.; Barbu, I. M.; Shoemaker, G. K.; van Duijn, E.; Heck, A. J., Interrogating viral capsid assembly with ion mobility-mass spectrometry. *Nat Chem* **2011**, *3* (2), 126-32.
148. Sharon, M.; Robinson, C. V., The role of mass spectrometry in structure elucidation of dynamic protein complexes. *Biochem* **2007**, *76*, 167-93.
149. Bothner, B.; Siuzdak, G., Electrospray ionization of a whole virus: analyzing mass, structure, and viability. *Chembiochem* **2004**, *5* (3), 258-60.
150. Fuerstenau, S. D.; Benner, W. H.; Thomas, J. J.; Brugidou, C.; Bothner, B.; Siuzdak, G., Mass Spectrometry of an Intact Virus. *Angew Chem* **2001**, *40* (3), 541-544.
151. Tamara, S.; den Boer, M. A.; Heck, A. J. R., High-Resolution Native Mass Spectrometry. *Chem Rev* **2022**, *122* (8), 7269-7326.
152. Snijder, J.; Rose, R. J.; Veessler, D.; Johnson, J. E.; Heck, A. J., Studying 18 MDa virus assemblies with native mass spectrometry. *Angew Chem* **2013**, *52* (14), 4020-3.
153. Dülfer, J.; Kadek, A.; Kopicki, J. D.; Krichel, B.; Uetrecht, C., Structural mass spectrometry goes viral. In *Adv Virus Res*, Rey, F. A., Ed. 2019; Vol. 105, pp 189-238.
154. Serrano, M. A. C.; Furman, R.; Chen, G. D.; Tao, L., Mass spectrometry in gene therapy: Challenges and opportunities for AAV analysis. *Drug Discov* **2023**, *28* (1), 1-10.
155. Pogan, R.; Schneider, C.; Reimer, R.; Hansman, G.; Uetrecht, C., Norovirus-like VP1 particles exhibit isolate dependent stability profiles. *J Condens Matter Phys* **2018**, *30* (6).
156. Snijder, J.; van de Waterbeemd, M.; Damoc, E.; Denisov, E.; Grinfeld, D.; Bennett, A.; Agbandje-McKenna, M.; Makarov, A.; Heck, A. J., Defining the stoichiometry and cargo load of viral and bacterial nanoparticles by Orbitrap mass spectrometry. *J Am Chem Soc* **2014**, *136* (20), 7295-9.
157. Serrano, M. A. C.; Furman, R.; Chen, G.; Tao, L., Mass spectrometry in gene therapy: Challenges and opportunities for AAV analysis. *Drug Discov* **2023**, *28* (1), 103442.
158. Lossl, P.; Snijder, J.; Heck, A. J., Boundaries of mass resolution in native mass spectrometry. *J Mass Spectrom* **2014**, *25* (6), 906-17.
159. Chernushevich, I. V.; Thomson, B. A., Collisional cooling of large ions in electrospray mass spectrometry. *Anal Chem* **2004**, *76* (6), 1754-60.
160. Uetrecht, C.; Versluis, C.; Watts, N. R.; Roos, W. H.; Wuite, G. J.; Wingfield, P. T.; Steven, A. C.; Heck, A. J., High-resolution mass spectrometry of viral assemblies: molecular composition and stability of dimorphic hepatitis B virus capsids. *Proc Natl Acad Sci* **2008**, *105* (27), 9216-9220.
161. Lorenzen, K.; Duijn, E. v., Native mass spectrometry as a tool in structural biology. *Curr Protoc Protein Sci* **2010**, *62* (1), 17.12. 1-17.12. 17.
162. van Duijn, E., Current limitations in native mass spectrometry based structural biology. *J Mass Spectrom* **2010**, *21* (6), 971-8.
163. Huiskonen, J. T., Image processing for cryogenic transmission electron microscopy of symmetry-mismatched complexes. *Bioscience Rep* **2018**, *38*.
164. Mielanczyk, L.; Matysiak, N.; Michalski, M.; Buldak, R.; Wojnicz, R., Closer to the native state. Critical evaluation of cryo-techniques for Transmission Electron Microscopy: preparation of biological samples. *Folia Histochem Cytobiol* **2014**, *52* (1), 1-17.

165. Milne, J. L.; Borgnia, M. J.; Bartesaghi, A.; Tran, E. E.; Earl, L. A.; Schauder, D. M.; Lengyel, J.; Pierson, J.; Patwardhan, A.; Subramaniam, S., Cryo-electron microscopy--a primer for the non-microscopist. *FEBS J* **2013**, *280* (1), 28-45.
166. Burrows, N. D.; Penn, R. L., Cryogenic Transmission Electron Microscopy: Aqueous Suspensions of Nanoscale Objects. *Micros Microanal* **2013**, *19* (6), 1542-1553.
167. Chang, J.; Liu, X.; Rochat, R. H.; Baker, M. L.; Chiu, W., Reconstructing virus structures from nanometer to near-atomic resolutions with cryo-electron microscopy and tomography. *Adv Exp Med Biol* **2012**, *726*, 49-90.
168. Grigorieff, N.; Harrison, S. C., Near-atomic resolution reconstructions of icosahedral viruses from electron cryo-microscopy. *Curr Opin Struct Biol* **2011**, *21* (2), 265-73.
169. Gonzalez-Dominguez, I.; Puente-Massaguer, E.; Cervera, L.; Godia, F., Quality Assessment of Virus-Like Particles at Single Particle Level: A Comparative Study. *Viruses (Basel)* **2020**, *12* (2).
170. Lua, L. H. L.; Connors, N. K.; Sainsbury, F.; Chuan, Y. P.; Wibowo, N.; Middelberg, A. P. J., Bioengineering Virus-Like Particles as Vaccines. *Biotech Bioeng* **2014**, *111* (3), 425-440.
171. Lindsay, B. J.; Bonar, M. M.; Costas-Cancelas, I. N.; Hunt, K.; Makarkov, A. I.; Chierzi, S.; Krawczyk, C. M.; Landry, N.; Ward, B. J.; Rouiller, I., Morphological characterization of a plant-made virus-like particle vaccine bearing influenza virus hemagglutinins by electron microscopy. *Vaccine* **2018**, *36* (16), 2147-2154.
172. Adrian, M.; Dubochet, J.; Lepault, J.; McDowell, A. W., Cryo-electron microscopy of viruses. *Nature* **1984**, *308* (5954), 32-6.
173. Chmielewski, D.; Schmid, M. F.; Simmons, G.; Jin, J.; Chiu, W., Chikungunya virus assembly and budding visualized in situ using cryogenic electron tomography. *Nat. Microbiol* **2022**, *7* (8), 1270.
174. Stass, R.; Ng, W. M.; Kim, Y. C.; Huiskonen, J. T., Structures of enveloped virions determined by cryogenic electron microscopy and tomography. In *Adv Virus Res*, Rey, F. A., Ed. Elsevier Academic Press Inc: San Diego, 2019; Vol. 105, pp 35-71.
175. Guo, F.; Jiang, W., Single particle cryo-electron microscopy and 3-D reconstruction of viruses. *Methods Mol Biol* **2014**, *1117*, 401-43.
176. Colomb-Delsuc, M.; Raim, R.; Fiedler, C.; Reuberger, S.; Lengler, J.; Nordstrom, R.; Ryner, M.; Folea, I. M.; Kraus, B.; Hernandez Bort, J. A.; Sintorn, I. M., Assessment of the percentage of full recombinant adeno-associated virus particles in a gene therapy drug using CryoTEM. *PLoS one* **2022**, *17* (6), e0269139.
177. Zhang, X.; Jin, L.; Fang, Q.; Hui, W. H.; Zhou, Z. H., 3.3 A cryo-EM structure of a nonenveloped virus reveals a priming mechanism for cell entry. *Cell* **2010**, *141* (3), 472-82.
178. Goetschius, D. J.; Lee, H.; Hafenstein, S., CryoEM reconstruction approaches to resolve asymmetric features. *Adv Virus Res* **2019**, *105*, 73-91.
179. Stagg, S. M.; Yoshioka, C.; Davulcu, O.; Chapman, M. S., Cryo-electron Microscopy of Adeno-associated Virus. *Chem Rev* **2022**, *122* (17), 14018-14054.
180. Meyer, N. L.; Chapman, M. S., Adeno-associated virus (AAV) cell entry: structural insights. *Trends Microbiol* **2022**, *30* (5), 432-451.
181. Khatwani, S. L.; Pavlova, A.; Piro, Z., Anion-exchange HPLC assay for separation and quantification of empty and full capsids in multiple adeno-associated virus serotypes. *Mol Ther Meth Clin D* **2021**, *21*, 548-558.

Abbreviations

AAV	Adeno-Associated Virus
AAV8	Adeno-Associated Virus serotype-8
AAV8 VLP	Adeno-Associated Virus 8 Virus-Like Particle
AF4	Asymmetrical Flow Field-Flow Fractionation
AFM	Atomic Force Microscopy
B/IC	Baculovirus-Insect Cell
CDMS	Charge Detection Mass Spectrometry
CPC	Condensation Particle Counter
Cryo-TEM	Cryogenic Transmission Electron Microscopy
CTL	CD8 ⁺ cytotoxic T lymphocyte
DMA	Differential Mobility Analyzer
EMA	European Medicine Agency
EMD	Electrophoretic Mobility Diameter
ENAS	Electrostatic Nanoparticle Sampler
eVLP	Enveloped VLP
FDA	U.S. Food and Drug Administration
HRV	Human Rhinovirus
HRV-A2	Human Rhinovirus serotype-2
ITRs	Inverted Terminal Repeats
LamR	Laminin Receptor
MacroIMS	Macro Ion Mobility Spectrometer
MS	Mass Spectrometry
MW	Molecular Weight
NAb	Neutralizing Antibody
nES	Nano Electrospray
nES GEMMA	Nano Electrospray Gas-Phase Electrophoretic Mobility Molecular Analysis
nES-DMA	nES Differential Mobility Analyzer
nESI	Nano Electrospray Ionization
nESI QRTOF MS	nESI Quadrupole Reflectron Time Of Flight MS
nMS	Native Mass Spectrometry
ORFs	Open Reading Frames
PLA2	Phospholipase A2
rAAV	Recombinant AAV
SMPS	Scanning Mobility Particle Sizer
VLP	Virus-Like Particle
VP	Viral Protein
wtAAV	Wild-type AAV

Curriculum Vitae

SAMUELE ZORATTO

Project Assistant, PhD Student

Six years of experience in mass spectrometry and nanoparticle analysis. Innovator, problem-solver, and thrilled to tackle the challenges of today and tomorrow.



samuele.zoratto@tuwien.ac.at ✉

+43-1-58801-740001 ☎

Vienna, Austria 📍

linkedin.com/in/samuelezoratto in

0000-0002-1491-3404 id

WORK EXPERIENCE

PhD Doctorate Program

Technical University of Wien (TU Wien)
Institute of Chemical Technologies and Analytics

CDL for Skin Multimodal Analytical Imaging of Aging and Senescence.

12/2020 – ongoing Vienna, Austria

Analytical characterization of viral vectors for gene therapy. In collaboration with Takeda Pharmaceuticals GmbH, Austria

12/2016 – ongoing Vienna, Austria

- Analysis of skin samples via MALDI FTICR MS for the generation of imaging experiments. Focus on lipid identification and characterization of known and unknown species.
- Developed analytical methodologies for the analyses of adeno-associated viruses (AAVs) via nES GEMMA instrumentation (TSI Inc.).
- Experience on orthogonal analytical techniques such as AF4, AFM, DESI and ESI MS, and MS ion mobility.
- Involved in the training of several students on operating the ScimaX FTICR (Bruker), nES GEMMA or the MALDI Synapt G2 (Waters).
- Developed solid and meaningful friendships with the members and heads of the team.

Native MS Collaboration

Warwick University

Dep. of Chemistry
02/2020 – 2 weeks Coventry, United Kingdom

- Native MS analysis of AAV samples with the Solarix FTICR

MS Vision

06/2018 – 2 weeks Almere, The Netherlands

- Native MS analysis of AAV samples with a modified Synapt G1 (Waters).

DESI MS Collaboration

Palacky University

Dept. of Analytical Chemistry – RCPTM
10/2015 – 2 weeks Olomouc, Czech Republic

- Analysis of peptaibols directly on alive fungi sample by means of a home-built DESI source.

Erasmus+ Traineeship Internship

Technical University of Wien (TU Wien)

Institute of Chemical Technologies and Analytics

01/2015 – 12/2015 Vienna, Austria

- Mastered on the MALDI Synapt G2: MALDI imaging MS (MSI), ion mobility MS (IMS), and the combination of both techniques.
- Characterization of the sequence of secondary metabolites via MALDI MS/MS, from fungi samples.
- Developed a protocol for the cultivation, sample preparation, MSI, IMS and MS/MS analyses of fungi samples.
- The traineeship was functional to the drafting of my master thesis: Profiling and Imaging of Fungal Metabolites by MALDI Ion Mobility MS

EDUCATION

PhD in Natural Science Tech. Chem.

Technical University of Wien

Ongoing Vienna, Austria

MSc in Industrial Biotechnology

University of Milano-Bicocca

10/2016 – GPA 3,6 Milan, Italy

CERTIFICATES

Hands-On Proteomics Workshop

Technical University of Wien

TEM Operator

Technical University of Wien

LANGUAGES

Italian
English
German



Samuele Zoratto – Résumé

Articles:

- **Adeno-Associated Virus-like Particles' Response to pH Changes as Revealed by nES-DMA**
Samuele Zoratto; Thomas Heuser; Gernot Friedbacher; Robert Pletzenauer; Michael Graninger; Martina Marchetti-Deschmann; Victor U. Weiss
Viruses 2023, 15(6):1361. DOI: 10.3390/v15061361
- **FT-ICR Mass Spectrometry Imaging at Extreme Mass Resolving Power Using a Dynamically Harmonized ICR Cell with 1ω or 2ω Detection**
Tiquet M; La Rocca R; Kirnbauer S; Zoratto S; Van Kruining D; Quinton L; Eppe G; Martinez-Martinez P; Marchetti-Deschmann M; De Pauw E et al.
Anal. Chem. 2022, 94(26):9316–9326. DOI: 10.1021/acs.analchem.2c00754
- **Research Techniques Made Simple: Lipidomic Analysis in Skin Research**
Michaela Sochorová, Kateřina Vávrová, Maria Fedorova, Zhixu Ni, Denise Slenter, Martina Kutmon, Egon L. Willighagen, Sophia Letsiou, Daniel Töröcsik, Martina Marchetti-Deschmann, Samuele Zoratto, Christopher Kremslehner, Florian Gruber
Journal of Investigative Dermatology 2022, 142(1):4–11.e1. DOI: 10.1016/j.jid.2021.09.017
- **Molecular Weight Determination of Adeno-Associate Virus serotype 8 Virus-like Particle either carrying or lacking genome via native nES Gas-phase Electrophoretic Molecular Mobility Analysis (GEMMA) and nESI QTOF Mass Spectrometry**
Zoratto S., Weiss V.U., Van der Horst J., Commandeur J., Buengener C., Foettinger-Vacha A., Pletzenauer R., Graninger M., Allmaier G.
Journal of Mass Spectrometry 2021, 56(11):e4786. DOI: 10.1002/jms.4786
- **Autophagy protects murine preputial glands against premature aging, and controls their sebum phospholipid and pheromone profile**
Rossiter H., Copic D., Direder M., Gruber F., Zoratto S., Marchetti-Deschmann M., Kremslehner C., Sochorová M., Nagelreiter I., Mlitz V., Buchberger M., Lengauer B., Golabi B., Suksee S., Mildner M., Eckhart L., Tschachler E.
Autophagy 2022, 18(5):1005–1019. DOI: 10.1080/15548627.2021.1966716
- **N-terminal VP1 Truncations Favor T = 1 Norovirus-Like Particles**
Pogan R, Weiss VU, Bond K, Dülfer J, Krisp C, Lykтей N, Müller-Guhl J, Zoratto S, Allmaier G, Jarrold MF, Muñoz-Fontela C, Schlüter H, Uetrecht C.
Vaccines (Basel) 2020, 9(1):8. DOI: 10.3390/vaccines9010008
- **Adeno-associated Virus Virus-like Particle Characterization via Orthogonal Methods: Nanoelectrospray Differential Mobility Analysis, Asymmetric Flow Field-Flow Fractionation, and Atomic Force Microscopy**
Zoratto S., Weiss V.U., Friedbacher G., Buengener C., Pletzenauer R., Foettinger-Vacha A., Graninger M., Allmaier G.
ACS Omega 2021, 6(25):16428–16437. DOI: 10.1021/acsomega.1c01443
- **Epilipidomics of Senescent Dermal Fibroblasts Identify Lysophosphatidylcholines as Pleiotropic Senescence-Associated Secretory Phenotype (SASP) Factors**
Narzt MS, Pils V, Kremslehner C, Nagelreiter IM, Schosserer M, Bessonova E, Bayer A, Reifschneider R, Terlecki-Zaniewicz L, Waidhofer-Söllner P, Mildner M, Tschachler E, Cavinato M, Wedel S, Jansen-Dürr P, Nanic L, Rubelj I, El-Ghalbzouri A, Zoratto S, Marchetti-Deschmann M, Grillari J, Gruber F, Lämmermann I.
J Invest Dermatol. 2021, 141:993–1006. DOI: 10.1016/j.jid.2020.11.020
- **Virus-like particle size and molecular weight/mass determination applying gas-phase electrophoresis (native nES GEMMA)**
Weiss VU, Pogan R, Zoratto S, Bond KM, Boulanger P, Jarrold MF, Lykтей N, Pahl D, Puffer N, Schelhaas M, Selivanovitch E, Uetrecht C, Allmaier G.
Anal Bioanal Chem. 2019, 411(23):5951–5962. DOI: 10.1007/s00216-019-01998-6

Application notes:

- **Tissue pathology of aging research revealed with lipid analysis using MRMS MALDI Imaging**
Zoratto S., Kremslehner C., Gruber F., Marchetti-Deschmann M.
Bruker Daltonics – MRMS 83 – Nov. 2023

Samuele Zoratto – Résumé

Oral Presentations:

- Age-related N-glycan changes in human skin biopsies identified by MALDI FTICR imaging
ASMS 2023- Houston TX, USA
- ESI and MALDI FTICR MS analysis of skin-relevant lipids after exposure to long wavelength UV radiation
IMSC 2022 Maastricht, The Netherlands
- A systematic study of lipids – from ESI analysis to MALDI Imaging using a 7T FT-ICR instrument
Mass Spec Forum 2022 – UniWien Vienna, Austria
- The benefit of mass spectrometry imaging for skin research – a study of lipids and their oxidation products
Austrian Cluster for Tissue Regeneration – ACTR 2022 Vienna, Austria
- Characterization of Adeno-associated Virus-like Particles via nES GEMMA and Orthogonal Techniques
Moderne Analytische Chemie – TU Wien 2021 Vienna, Austria
- Analysis of UV-exposed skin sections via MALDI Imaging Mass Spectrometry
19th Congress of the European Society for Photobiology - 2021 Salzburg, Austria
- Nano electrospray differential mobility analysis and molecular weight determination of aerosolized adeno-associated viruses
European Aerosol Conference – EAC2021 Virtual event
- Nano electrospray differential mobility analysis of adeno-associated viruses as gene therapy platform
15th ASAC JunganalytikerInnen-Forum 2019 Linz, Austria
- Analysis of UV-exposed skin sections via MALDI Imaging Mass Spectrometry
19th Congress of the European Society for Photobiology - 2021 Salzburg, Austria




Posters presentation:

- Quantifying the distribution of endogenous lipids in skin – bridging the gap between MS imaging and Lipidomic
IMSIS 2023 Montreal, Canada
- Targeting N-glycan changes in skin tissue by MALDI FT-ICR MSI
Anakon 2023 – TU Wien Vienna, Austria
- The influence of pH for the analysis of adeno-associated virus by nES GEMMA
Anakon 2023 – TU Wien Vienna, Austria
- Integration of MALDI FTICR MSI data with the open-source software Cytomine
COMULIS 2022 Nicosia, Cyprus
- Lipid oxidation induced by UV exposure as observed in skin
Ourcon 2021 Sheffield, UK
- Investigation of skin-relevant lipids and their oxidized state after UVA exposure via ESI and MALDI FTICR MS
ASMS 2021 Virtual event
- Molecular weight determination of an adeno-associated virus based virus-like particle
ASMS 2020 Virtual event
- Nano electrospray differential mobility analysis of adeno-associated viruses as gene therapy platform
ASMS 2018 San Diego, CA, USA

SKILLS

 Teamwork  Decision Making  Flexibility  Public Speaking  Coding  3D Printing

INTERESTS

 Technology  Photography  Fix and Improve  Cooking  Boardgames

Samuele Zoratto – Résumé

Acknowledgments

This thesis couldn't have been made without the support of those who guided my steps and fueled my passion. I stand before you, filled with gratitude, to express my most profound appreciation to the people who have shaped my academic journey and made this work possible.

If **you** are reading this, **you** have been part of this journey somehow. Whether you have been a mentor, friend, family member, or supporter, your presence has enriched my life and contributed to my journey.

My heart swells with gratitude for my esteemed professor, Günter Allmaier. His insightful guidance and expertise have been my lighthouse, leading me through the maze of research. His legacy lives on, not just in the pages of this work but in the hearts of all who knew him and were inspired by his kindness and brilliance.

I extend my deepest gratitude to my mentors, Victor U. Weiss, Martina Marchetti-Deschmann, and Ernst Pittenauer, pillars of support and wisdom who have been my companions throughout this journey. I am forever grateful for their mentorship and friendship, which have enriched my academic and personal life in countless ways.

My heart overflows with gratitude for my circle of loved ones, who have been my unwavering support system and confidantes throughout this journey. Their encouragement and support have been a source of strength and inspiration. I am incredibly grateful for their presence in my life, which has enriched me in ways I could never have imagined.

I am also deeply grateful to the team members of Takeda who were part of this project: Elisabeth Müller, Robert Pletzenauer, Michael Graninger, Juan Hernandez Bort, Carsten Buengener, Roman Raim, and Alexandra Foettinger-Vacha. I am honored to have been a part of such a collaborative and passionate team.

I offer my heartfelt thanks to all who have contributed to this thesis, showering me with their wisdom, encouragement, and unwavering support. Your presence in my life has been a blessing, and I am forever indebted to your generosity and compassion.

